Neural Plasticity

# Peripheral Nerve Injury and Repair: Plasticity from Muscle to Brain

Lead Guest Editor: Jianguang Xu
Guest Editors: Xu-Yun Hua, Mou-Xiong Zheng, Jia-Jia Wu, and Zhongyu Li

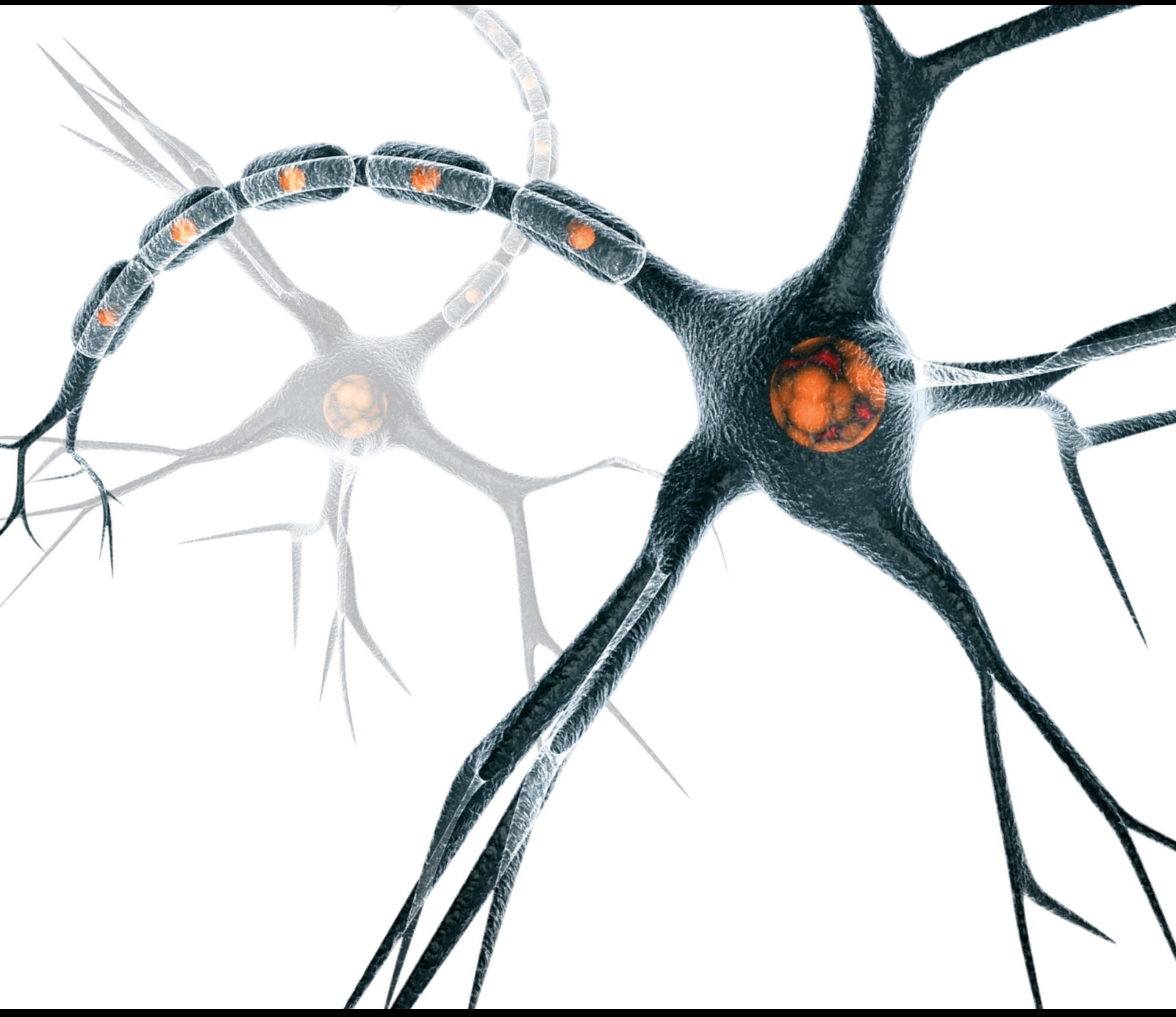

# Peripheral Nerve Injury and Repair: Plasticity from Muscle to Brain

Neural Plasticity

# Peripheral Nerve Injury and Repair: Plasticity from Muscle to Brain

Lead Guest Editor: Jianguang Xu
Guest Editors: Xu-Yun Hua, Mou-Xiong Zheng, Jia-Jia Wu, and Zhongyu Li

# Contents

**Celecoxib-Loaded Electrospun Fibrous Antiadhesion Membranes Reduce COX-2/$PGE_2$ Induced Inflammation and Epidural Fibrosis in a Rat Failed Back Surgery Syndrome Model**
Wei Wang, Yunhao Wang, Tengfei Lou, Mingqian Ding, Juehong Li, Hao Xiong, Zhixiao Yao, Yingying Ma, Huajiang Chen, and Shenghe Liu
Research Article (8 pages), Article ID 6684176, Volume 2021 (2021)

**Predicting Upcoming Events Occurring in the Space Surrounding the Hand**
Maria L. Rangel, Lidiane Souza, Erika C. Rodrigues, José M. Oliveira, Michelle F. Miranda, Antonio Galves, and Claudia D. Vargas
Research Article (10 pages), Article ID 6649135, Volume 2021 (2021)

**Impaired Limb Functional Outcome of Peripheral Nerve Regeneration Is Marked by Incomplete Recovery of Paw Muscle Atrophy and Brain Functional Connectivity in a Rat Forearm Nerve Repair Model**
Qiyuan Bao, Qi Liu, Jun Wang, Yuhui Shen, and Weibin Zhang
Research Article (8 pages), Article ID 6689476, Volume 2021 (2021)

**Altered Topological Properties of Grey Matter Structural Covariance Networks in Complete Thoracic Spinal Cord Injury Patients: A Graph Theoretical Network Analysis**
Wen-Li Wang, Yu-Lin Li, Mou-Xiong Zheng, Xu-Yun Hua, Jia-Jia Wu, Fei-Fei Yang, Nan Yang, Xia He, Li-Juan Ao, and Jian-Guang Xu
Research Article (11 pages), Article ID 8815144, Volume 2021 (2021)

**Why It Is Necessary to Use the Entire Root rather than Partial Root When Doing Contralateral C7 Nerve Transfer: Cortical Plasticity Also Matters besides the Amount of Nerve Fibers**
Jinding Guo, Xin Zhao, Jie Lao, and Kaiming Gao
Research Article (12 pages), Article ID 8819380, Volume 2021 (2021)

**Exosomes Derived from CXCR4-Overexpressing BMSC Promoted Activation of Microvascular Endothelial Cells in Cerebral Ischemia/Reperfusion Injury**
Xutong Li, Ye Zhang, Yong Wang, Dan Zhao, Chengcheng Sun, Shaoting Zhou, Dongsheng Xu, and Jing Zhao
Research Article (13 pages), Article ID 8814239, Volume 2020 (2020)

**Comparison of Different In Vivo Animal Models of Brachial Plexus Avulsion and Its Application in Pain Study**
Hang Xian, Rougang Xie, Ceng Luo, and Rui Cong
Review Article (9 pages), Article ID 8875915, Volume 2020 (2020)

Hindawi
Neural Plasticity
Volume 2021, Article ID 9923537, 12 pages
https://doi.org/10.1155/2021/9923537

*Research Article*

# Microglial Activation of GLP-1R Signaling in Neuropathic Pain Promotes Gene Expression Adaption Involved in Inflammatory Responses

**Le Ma,[1,2] Peijun Ju,[1] Wei Wang,[1] Jinbao Wei,[1,2] Weidi Wang,[1] Mengjing Zhao,[2] Khalil Ali Ahmad,[2] Yongxiang Wang,[2] and Jinghong Chen[1]**

[1]*Shanghai Key Laboratory of Psychotic Disorders, Shanghai Mental Health Center, Shanghai Jiao Tong University, School of Medicine, School of Pharmacy, Shanghai 200240, China*
[2]*King's Lab, Shanghai Jiao Tong University School of Pharmacy, Shanghai 200240, China*

Correspondence should be addressed to Yongxiang Wang; yxwang@sjtu.edu.cn and Jinghong Chen; chenjh_008@hotmail.com

Le Ma and Peijun Ju contributed equally to this work.

Received 10 March 2021; Revised 7 July 2021; Accepted 4 August 2021; Published 1 September 2021

Academic Editor: Jianguang Xu



*Background*. Neuropathic pain is a common chronic pain, which is related to hypersensitivity to stimulus and greatly affects the quality of life of patients. Maladaptive gene changes and molecular signaling underlie the sensitization of nociceptive pathways. We previously found that the activation of microglial glucagon-like peptide 1 receptor (GLP-1R) could potently relieve formalin-, bone cancer-, peripheral nerve injury-, and diabetes-induced pain hypersensitivity. So far, little is known about how the gene profile changes upon the activation of GLP-1R signaling in the pathophysiology of neuropathic pain. *Methods*. Spinal nerve ligation (SNL) was performed to induce neuropathic pain in rats. Mechanical allodynia was assessed using von Frey filaments. The expression of IL-10, $\beta$-endorphin, and $\mu$-opioid receptor (MOR) was examined by real-time quantitative polymerase chain reaction (qPCR) and whole-cell recording. Measurements of cellular excitability of the substantia gelatinosa (SG) neurons by whole-cell recording were carried out. R packages of differential gene expression analysis based on the negative binomial distribution (DESeq2) and weighted correlation network analysis (WGCNA) were used to analyze differential gene expression and the correlated modules among GLP-1R clusters in neuropathic pain. *Results*. The GLP-1R agonist, exenatide, has an antiallodynic effect on neuropathic pain, which could be reversed by intrathecal injections of the microglial inhibitor minocycline. Furthermore, differential gene expression analysis (WGCNA) indicated that intrathecal injections of exenatide could reverse the abnormal expression of 591 genes in the spinal dorsal horn induced by nerve injury. WGCNA revealed 58 modules with a close relationship between the microglial GLP-1R pathway and features of nerve injuries, including pain, ligation, paw withdrawal latency (PWL), and anxiety. The brown module was identified as the highest correlated module, and the Kyoto Encyclopedia of Genes and Genomes (KEGG) analysis indicated that inflammatory responses were most correlated with PWL. To further unravel the changes of hyperalgesia-related neuronal electrophysiological activity mediated by microglia GLP-1 receptors, whole-cell recording identified that MOR agonism stimulated a robust outward current in the sham groups compared with the spinal nerve ligation (SNL) groups. This inhibitory effect on the SNL group was more sensitive than that of the sham group after bath application of $\beta$-endorphin. *Conclusions*. Our results further confirmed that the GLP-1R pathway is involved in alleviating pain hypersensitivity mediated by spinal microglia activation, and inflammatory responses were the most correlated pathway associated with PWL changes in response to exenatide treatment. We found that the identification of gene regulation in response to GLP-1R activation is an effective strategy for identifying new therapeutic targets for neuropathic pain. Investigation for the activation of spinal microglial GLP-1R which might ameliorate inflammatory responses through gene expression and structural changes is providing a potential biomarker in pain management.

## 1. Introduction

Unbalanced inflammation in the nervous system may contribute to the initiation and maintenance of persistent pain [1]. Cytokines, chemokines, etc., could be released during an inflammatory response and promote maladaptive synaptic plasticity [2, 3]. Additionally, the inflammatory mediators would directly or indirectly regulate the release of neurotransmitters such as glutamate, $\gamma$-aminobutyric acid, and glycine as well as postsynaptic transmitters, followed by long-term deleterious plastic changes of nerve activity [4]. Neuroinflammation facilitates pain signal transduction and the reconstruction of the nerve loop in the central nervous system (CNS). Furthermore, imbalanced excitability and inhibitory neurotransmission lead to hyperalgesia. Therefore, changes in inflammation and neurotransmission are closely related to the occurrence and maintenance of neuropathic pain. Targeting excessive inflammation could be seen as a therapy for neuropathic pain.

Microglia are the major source of multiple inflammatory cytokines in CNS, and increasing evidence inferred that microglia could drive central sensitization and pain hypersensitivity via a microglial mediator [5]. However, direct targeting of microglial activation and neuroinflammation via inhibition of microglia may produce side effects such as infection and inflammation [6]. Strategies that could control abnormal microglial activation and excessive neuroinflammation as well as promote a return to neural homeostasis for relieving pain should be considered.

Glucagon-like peptide 1 receptor (GLP-1R) signaling, which is specifically expressed in the microglia of the spinal dorsal horn, was found to be involved in a number of biological processes, including inflammation, neuroprotection, and synaptic plasticity [7–10]. Cumulative studies from our laboratory illustrated that GLP-1R agonism could effectively relieve pain hypersensitivity through increasing the biomarkers of M2 in microglia associated with expression of IL-10, CD206, IL-4, and Arg1 [10–13]. Specifically, intrathecal injection of exenatide completely abolished the pain states of bone cancer-, peripheral nerve injury-, formalin-, and diabetes-induced hypersensitivity through IL-10 and $\beta$-endorphin expression [11]. Furthermore, bath application of GLP-1R agonism abolished spinal glutamatergic transmission, and those inhibitory effects could be reversed by microglial inhibitor minocycline [13]. Moreover, exenatide showed antiallodynic effects by stimulating cAMP, p-protein kinase A (PKA), p-p38, and p-cyclic adenosine monophosphate (cAMP) response element binding protein (CREB) in a dose-dependent manner. Genetical knockdown of p38$\alpha$ or inhibition of PKA suppressed exenatide-induced p38/$\beta$-endorphin expression [14]. Morroniside, which was extracted from traditional medicinal herbs, was identified as the agonist of GLP-1R and could suppress peripheral nerve injury-induced hypersensitivity mediated by microglial autocrine IL-10 and $\beta$-endorphin expression [8, 12, 15]. These data collectively demonstrate that the antinociceptive pathway of GLP-1 in the microglia plays a crucial role in the pathophysiological condition of neuropathic pain in the CNS. However, the large scale of mechanisms linking GLP-1R in neuropathic pain remains largely unraveled. Untargeted approaches may be required to highlight GLP-1R agonist-mediated differences in global signaling networks.

In our study, we aim to determine the gene expression profiles that contributed to neuropathic pain before and after activation of the spinal dorsal horn microglial GLP-1R signaling by RNA sequencing. We found that the microglial GLP-1R agonist, exenatide, rescued the expression of 591 genes in the dorsal spinal cord with spinal nerve injury, and WGCNA identifies critical brown modules correlating with the GLP-1R pathway in neuropathic pain. Our results further illustrated that GLP-1R-induced antiallodynia was correlated with inflammatory responses in neuropathic pain. Furthermore, the GLP-1R pathway was critically involved in spinal synaptic plasticity in pain as verified with electrophysiological recordings. The application of MOR agonists showing inhibitory effect on neuronal excitability was less likely abolished in rats with neuropathic pain, suggesting the involvement of GLP-1R/IL-10/$\beta$-endorphin in the neuronal plasticity of pain. Taken together, our study reveals that GLP-1R signaling, stimulating IL-10/$\beta$-endorphin expression, has potential to inhibit the excitability of lamina II neurons of the substantia gelatinosa (SG) after pharmacological blocking of the MOR.

## 2. Materials and Methods

*2.1. Chemicals and Reagents.* Exenatide was synthesized from Dan Gang Peptides Co. (Hangzhou, China); [D-Ala2, N-Me-Phe4, Gly5-ol]-enkephalin (DAMGO) was obtained from Phoenix (Burlingame, CA, USA), while minocycline was purchased from Yuanye Biotech (Shanghai, China). D-Phe-Cys-Tyr-D-Trp-Arg-Thr-Pen-Thr-NH2 (CTAP) were purchased from Abcam.

*2.2. Animals.* Male Wistar rats were raised in a controlled temperature ($23 \pm 1^{\circ}$C) and humid environment on a 12 h light/dark cycle with lights on at 7:00 AM. Food and water were provided *ad libitum*. All experiments were performed in accordance with the Animal Care and Welfare Committee of Shanghai Jiao Tong University and followed the animal care guidelines of the National Institutes of Health.

*2.3. Spinal Nerve Ligation and Behavioural Testing.* Rats (200-250 g) were anaesthetized by intraperitoneal injection of pentobarbital sodium (50 mg/kg), the left L5 paralleled to the spinal cord was gently dissected with a man-made glass hook, and the nerves were gently ligated with 6-0 silk sutures. The L6 nerve, vertical to the spinal cord and looking more thinner than L5, was operated identically. The sham rats were operated identically without ligations of L5 and L6. After those procedures, the wound was sutured before giving broad antibiotics preventing infections. The rats were allowed to recover for 14 days, and the spinal nerve ligation (SNL) rats developed significant hypersensitivity to mechanical stimuli on the operated side with paw withdrawal thresholds < 8 g. No motor impairments were excluded from this study.

For mechanical threshold testing, all rats were handled by the investigators for 4 days [16]. The rats were randomly divided into groups and blinded to the investigators. The rats

were individually placed in a plastic box and acclimated for 30 min before the tests. Mechanical threshold testing was performed with 2290 CE electrical von Frey hair (IITC Life Science, Woodland Hills, CA, USA) ranging from 0.1 to 90 g. The upward force stimulated suddenly withdrew from operated hind paws including withdrew, lifting, and licking, while the lowest force was recorded as the threshold. The procedure was repeated three times at 1 min intervals. The average of the recorded thresholds was determined as the mechanical threshold.

*2.4. Intrathecal Catheterization and Injection in Rats.* Before ligation of L5 and L6, a catheter (0.28 nm inner diameter and 0.61 nm outer diameter, PE-10, Clay Adams, Parsippany, NJ, USA) was placed in the lumbar spine of the rats, and the typical whipping was observed under inhaled isoflurane anaesthesia. Two joints in the catheter were used tightly located near the ilium and neck to prevent displacement. The following day, intrathecal injection of 10 $\mu$L of 4% lidocaine in artificial cerebrospinal fluid (ACSF: 125 mM NaCl, 3 mM KCl, 1.25 mM $NaH_2PO_4$, 26 mM $NaHCO_3$, 1 mM $MgCl_2$, 2 mM $CaCl_2$, and 10 mM D-glucose, pH 7.3) was administered, followed by bilateral paralysis and claudication, while the other rats were excluded from this study. For intrathecal delivery, 10 $\mu$L of the drug solution was administered through a 50 $\mu$L microinjector followed by a 15 $\mu$L artificial cerebrospinal fluid (ACSF) flush. In our study, 100 $\mu$g minocycline and 100 ng exenatide were intrathecally injected.

*2.5. RNA Isolation and Quantitative Reverse Transcription PCR (qRT-PCR).* The ipsilateral spinal enlargements L3-L5 of the sham and SNL groups from 4 rats in each group were gently isolated into cold ACSF. Total RNA was extracted using TRIzol, and the ratio of 260/280 > 1.8 was chosen for further experiments. Using the First Strand cDNA Synthesis Kit (Thermal, K1622), 1 $\mu$g mRNA was used for cDNA synthesis. The primers used were as follows: proopiomelanocortin (POMC) (exon 2–3) forward primer: CCTATCGGGTGGAGCACTTC and reverse primer: TGGCTCTTCTCGGAGGTCAT, IL-10 forward primer: GGCTCAGCA CTGCTATGTTGCC and reverse primer: AGCATGTGGGTCTGGCTGACTG, and GAPDH forward primer: CCAAGGTCATCCATGACGAC and TCCACAGTCTTCTGAGTGGC. All primers were manufactured according to a previous study [11]. Real-time quantitative PCR was performed using Roche SYBR qPCR Mix and identified to be specific as assessed by a melting curve. The relative expression of IL-10 and POMC was calculated using the $2^{-\Delta\Delta CT}$ method after normalization to GAPDH.

*2.6. Spinal Slice Preparation.* The L3-L5 spinal cord was quickly separated under inhaled isoflurane anaesthesia and transferred into ice-cold high-sucrose ACSF containing 234 mM sucrose, 3.6 mM KCl, 1.2 mM $MgCl_2$, 1.2 mM $NaH_2PO_4$, 12 mM glucose, 2.5 mM $CaCl_2$, and 25 mM $NaHCO_3$ for 90 s. The spinal slices were cut using a Leica VT-1200S vibratome (Wetzlar, Germany), the velocity was 0.06 mm/s, and the amplitude was 1.00 mm. The 400 $\mu$m slices were transferred to 32°C oxygenated ACSF for 30 min and cooled to room temperature.

*2.7. Whole-Cell Recordings.* Whole-cell recording was conducted in the ipsilateral dorsal horn neurons of the substantia gelatinosa with a 4-5 M$\Omega$ pipette (1.0 mm outer diameter, 0.5 mm inner diameter; Sutter Instruments, Novato, CA, USA). The excitability of spinal neurons from lamina II was recorded before and after bath application of 1 $\mu$mol $\beta$-endorphin or 1 $\mu$mol DAMGO using pipettes containing an internal solution (135 mM K-gluconate, 0.5 mM $CaCl_2$, 2 mM $MgCl_2$, 5 mM EGTA, 5 mM HEPES, and 5 mM Mg-ATP, pH 7.3) under current clamp conditions. All the neurons were clamped at −70 mV, and current injections were given with step intervals of 20 pA from -80 to 400 pA over a period of 500 ms. The spike numbers were calculated as the excitability according to the currents injected into the neurons by Clampfit 10.7.

*2.8. RNA Extraction and Sequencing.* The spinal dorsal horn was rapidly dissected on ice from the fresh spinal cord. Total RNA was extracted from 11 samples using the RNeasy Mini kit (Qiagen) for further library preparation and sequencing by Illumina NovaSeq 6000 PE150. Bioinformatic analyses of mRNA sequencing raw reads were performed by FASTQCT. The reads were mapped to the ensemble database of rat norvegicus (Rat (Rnor_6.0)). Normalized gene counts for identifying distinct genes affected by different treatments were chosen for bioinformatic analyses. Differential expression analyses were conducted using R package DESeq2 ($\log_2$ (fold change) > $\log_2$ (1.5) and $p$adj < 0.05).

*2.9. Weighted Gene Coexpression Network Analysis (WGCNA).* The coexpression network was analyzed using weighted gene coexpression network analysis (WGCNA), reshape2, and stringr packages in R version 4.0.4 (2021-02-15). The coexpression network was calculated by transforming the gene coexpression correlation matrix into the adjacency matrix and subsequently transferring it into the topological overlap matrix (TOM). When TOM = 0, there is no correlation between gene expression and other gene expressions. Based on the principle of data dissimilarity, WGCNA further polished TOM data and divided gene expression into gene modules. The cluster dendrogram was obtained by merging highly similar data sets. Highly similar expression relationships were grouped and divided into modules. Each module was identified and correlated with behavioural phenotypes such as ligation, nerve injury, pain, anxiety, and paw withdrawal latency.

*2.10. Data Evaluation and Statistics.* GraphPad Prism 7.0 (GraphPad Software) was used for data analysis. The data were analyzed using two independent sample Student's $t$ -test and one-way or repeated-measures two-way ANOVA, followed by Tukey's post hoc tests for multiple comparisons. Data are summarized as the mean SEM. Statistical significance was set at $p < 0.05$. All data were processed using CorelDraw 2019.

## 3. Results

*3.1. Intrathecal Delivery of Exenatide Inhibited Mechanical Allodynia in Neuropathic Pain via Microglial GLP-1R Activation.* The analgesic effects of the GLP-1R agonist exenatide were assessed in rats with spinal nerve ligation-induced neuropathic pain, and sham rats were identically operated on without ligation (Figure 1(a)). The rats from the SNL and sham groups were individually administered vehicle (10 $\mu$L), exenatide (100 ng), or the microglial metabolic inhibitor minocycline (100 $\mu$g). Mechanical thresholds were tested with noninvasive monofilament stimulus on operated hind paws before and at 0.5, 1, 2, and 4 h. Intrathecal injection of exenatide significantly suppressed mechanical allodynia after 1 h of incubation, without affecting the basal thresholds in the sham group. Pretreatment with minocycline (100 $\mu$g) dramatically inhibited microglial functions in neuropathic pain and exhibited completely abolished exenatide-induced analgesic effects 1 h later. In the sham group, exenatide or minocycline did not affect the basal thresholds of the sham groups at 4 h (Figure 1(b)). These results confirmed that activation of microglia GLP-1R is specifically effective in alleviating pain hypersensitivity states.

*3.2. Microglial GLP-1R Agonist Exenatide Ameliorated Abnormal Cellular Signaling in Neuropathic Pain.* To examine gene expression profiles in neuropathic pain via the regulation of microglial GLP-1R signaling, RNA sequencing (RNA-seq) analysis of GLP-1R signaling in neuropathy was performed using an Illumina NovaSeq 6000 PE150 platform and analyzed using R packages (Figure 2(a)). A multidimensional scaling analysis (principal component analysis, PCA) revealed a clear separation between the sham group and the SNL group, and the exenatide-treated group showed a tendency towards the sham group (Figure 2(b)). We then analyzed differentially expressed genes across the three groups by comparison. Of the 24416 detected mRNA genes profiled, 591 (2.42%) were involved in the spinal dorsal horn following SNL (Figure 2(c)). Nerve injury induced a large scale of dysfunctions of genes; more importantly, exenatide induced a recovery towards the sham group, which was consistent with the distribution of PCA. To investigate the potential cell signaling pathways associated with differential gene expression in GLP-1R signaling, pathway interactions were constructed (Figure 2(d)). The Kyoto Encyclopedia of Genes and Genomes (KEGG) analyses revealed that nerve injury triggered more than 20 signaling genes involved, including NF-$\kappa$B signaling, TNF-$\alpha$, Toll-like receptor, and cytokine-cytokine receptor interaction, and this signaling was associated with inflammation and the inflammation-induced sensitization of synaptic transmission (Figure 2(e)). The NF-$\kappa$B pathway was associated enriched in the KEGG when the intrathecal injection of exenatide through the large scales of RNA expression was compared with the sham group (Figures 2(f) and 2(g)).

*3.3. WGCNA Identifies Critical Modules that Correlate with the GLP-1R Pathway in Neuropathic Pain.* To explore the relationship between critical gene models of GLP-1R clusters and modules in neuropathic pain, WGCNA was carried out. The connections of the phenotype and variations in gene expression were then tested to summarize the associated modules. The neuropathic pain model was characterized by ligation, nerve injury, pain, anxiety, and paw withdrawal latency. Based on these phenotypes, highly correlated gene expression was calculated using the R package of WGCNA, and a sample dendrogram associated with traits was established (Figure 3(a)). The topological overlap matrix (TOM) plot of the weighted network shows high similarity in network construction (Figure 3(b)). Highly similar modules were separated by clustering and grouped together (Figure 3(c)). Our data identified 58 modules with one large module and several smaller modules in neuropathic pain by WGCNA (Figures 3(a)–3(c)). Of the 58 modules correlated with behavioural tests and operation in neuropathic pain, the relationships were qualified by R packages, which thoroughly concluded the interactions (Figure 3(d)). The correlation of each module is shown in a heatmap (Figure 3(e)). The largest gene modules (brown) strongly correlated with paw withdrawal latency indicated that paw withdrawal latency was significantly associated with gene expression in neuropathic pain. Based on the most correlated module with paw withdrawal latency, the brown module was further illustrated. We found the brown module enriched for inflammatory responses including response to lipopolysaccharide, NF-$\kappa$B signaling pathway, innate immunity, innate immune response, inflammatory responses, and cytokine-cytokine receptor interaction by the KEGG analysis (Figure 3(f)).

*3.4. Microglial GLP-1R Signaling Is Associated with the Excitability of Neurons in SG through MOR.* Neuropathic pain arises from the dysfunction of neuronal circuits of noxious and nociceptive information; however, the direct evidence of neuroplasticity in the GLP-1R pathway has been debated. A previous study from our laboratory revealed that the microglial GLP-1R agonist exenatide exerted antiallodynia by stimulating the twofold expression of IL-10/$\beta$-endorphin. To our knowledge, $\beta$-endorphin binds to $\mu$-receptor which showed inhibitory effects on neurons and was associated with neural plasticity. However, this pathway could not be distinguished from the RNA-seq data. To highlight the direct association between GLP-1R/IL-10/$\beta$-endorphin signaling and neural plasticity, neuronal excitability was assayed by application of MOR ligands, $\beta$-endorphin or DAMGO. Indeed, the mRNA expression level of IL-10 and $\beta$-endorphin was not significantly changed in the SNL group, as compared with the sham group (Figure 4(a)), while the functions of MOR are under debate. Activation of MOR induced an outward current when bath application of DAMGO (1 $\mu$mol) and $\beta$-endorphin (1 $\mu$mol) and pretreatment with CTAP (1 $\mu$mol) completely reversed these currents in both the sham and SNL groups. Moreover, the currents were more obviously inhibited in the SNL group compared with the sham group (Figures 4(b) and 4(c)). MOR was associated with the excitability of neurons in SG. Current clamp recordings of spikes were generated by direct intracellular current injections and used to assess the excitability of neurons. Increased spikes were generated in the SNL group compared to the sham group (Figure 4(d)). In

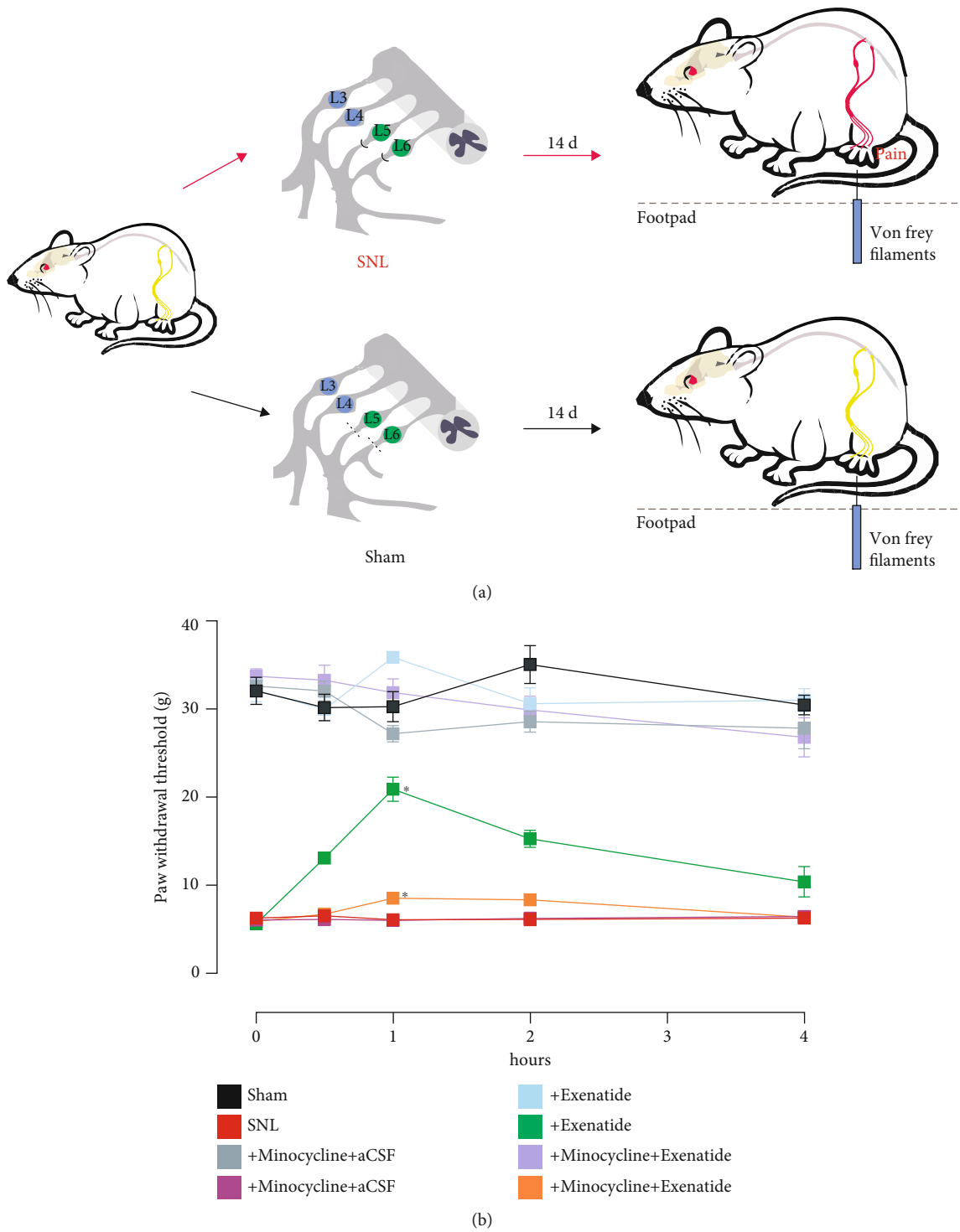


Figure 1: Schematic diagram of the rat operation and behavioural testing (a). Effects of glucagon-like peptide 1 receptor agonist exenatide in the activation of microglia in SNL-induced rats (b). Rats with spinal nerve ligation-induced neuropathy, received intrathecal injections of vehicle, exenatide (100 ng), or pretreatment of minocycline (100 $\mu$g) 4 h. Data are presented as means ± SEM ($N = 5$ per group). $^{*}p < 0.05$, analyzed by the repeated measures two-way ANOVA followed by the Tukey post hoc test.

the sham group, current injection induced declined spikes when using the bath application of $\beta$-endorphin, while this inhibitory effect was more likely abolished in the SNL group, indicating that activation of MOR is more likely to inhibit the excitability of the sham group and downregulation of MOR-coupled signaling due to nerve injury (Figures 4(e) and 4(f)).

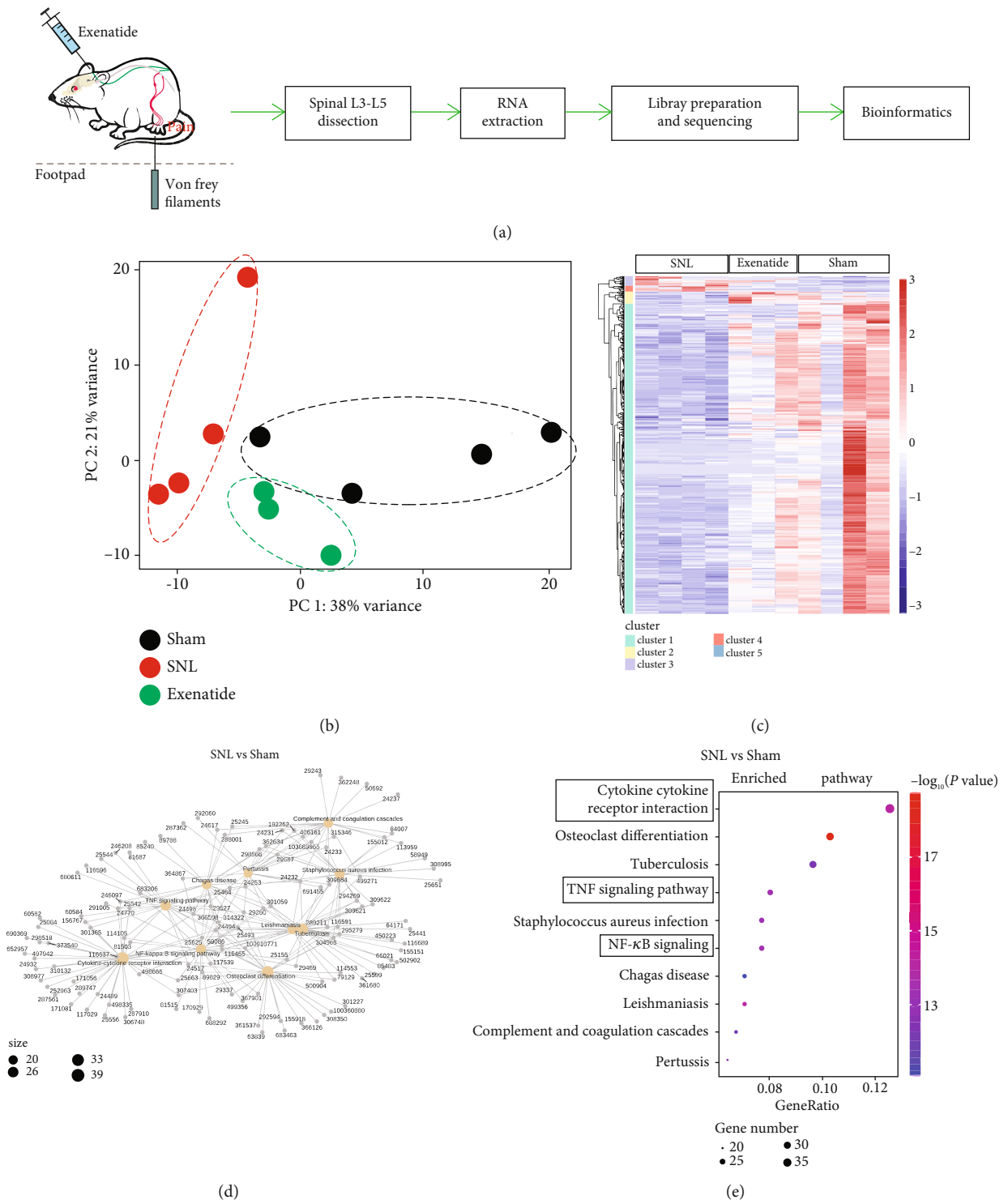


Figure 2: Continued.

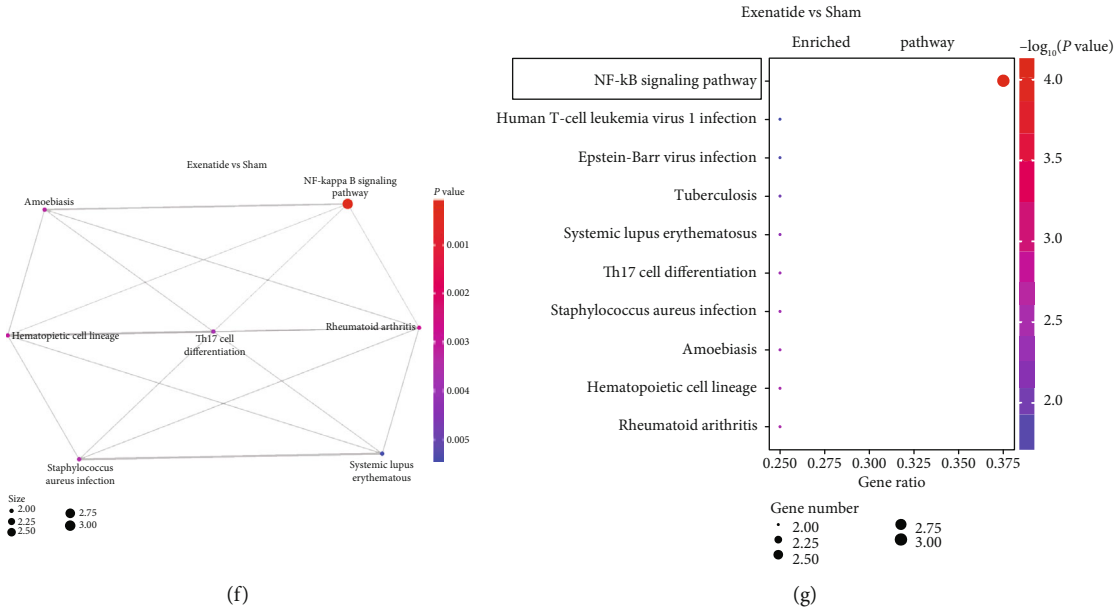


Figure 2: Schematic diagram of the operational process (a). RNA-seq analysis of glucagon-like peptide 1 receptor agonism exenatide induced responses after spinal nerve ligation. Unbiased principal component analysis (b) and heat map (c) of mRNA transcriptome in the spinal ipsilateral dorsal horn. The network of genes (d) and the Kyoto Encyclopedia of Genes and Genomes pathways (e) differentially enriched in the SNL and sham groups. The network of genes (f) and signaling (g) differentially enriched in the exenatide and sham groups ($p < 0.05$). Gene number: number of target genes in each pathway. Rich factor: the ratio of the number of target genes divided by the number of all the genes in each pathway.

## 4. Discussion

Neuropathic pain is characterized by abnormal neural circuits [17, 18]. Crosstalk between the microglia and neurons has gained more attention in pain. Manipulation of the microglial functions has shown great potential in antiallodynia. Our data supported that activation of spinal microglial GLP-1R signaling reversed nerve injury followed by comprehensive transcriptional changes. Specifically, inflammatory responses were identified as the highest-correlated signaling pathway with paw withdrawal latency.

Neuropathic pain is a widespread disease worldwide, and it is important to discover and illustrate new targets and pathways. Our previous study revealed that microglial GLP-1R agonism inhibited various pain states through autocrine IL-10/STAT3 and cAMP/PKA/p38$\beta$/CREB signaling in primary microglia cultures [10, 19]. At the early stage, microglial-derived inflammatory factors contribute to abnormal neural circuits in pain. Recently, we demonstrated that microglia are promising targets for antinociception and neuroprotection. A previous study demonstrated that the GLP-1R agonist exenatide suppressed mechanical allodynia in a dosage- and time-dependent manner in vivo, and a primary culture study also demonstrated that exenatide stimulated $\beta$-endorphin expression in vitro.

To study GLP-1R signaling in a more comprehensive way, the RNA-seq was performed. Compared with the previous study, bioinformaticians could provide independently and reliably transcriptional information. The large-scale mRNA screening by next-generation sequencing identified 591 genes involved in pain, and our results highlighted that intrathecal delivery of exenatide rescued the abnormal gene expression. However, nerve injury triggered the activation of microglia with upregulation of IL-6, IL-1$\beta$, and TNF-$\alpha$, which modulate neuronal receptors and channels, resulting in hypersensitivity. As shown in Figure 2, the KEGG analysis showed that inflammatory signaling of TNF-$\alpha$, Toll-like receptor, and cytokine-cytokine receptor interaction were enriched. However, intrathecal administration of exenatide shifted towards the sham group; the KEGG analysis found that NF-$\kappa$B signaling is mainly enriched and also demonstrated that GLP-1R signaling completely inhibited pain through a large scale of gene expression. Our results highlight the broad significance of GLP-1R signaling in the regulation of pain states.

WGCNA uncovered 58 modules in our data in accordance with the pathological traits in our operation. In our rodent model of neuropathic pain, the SNL model was operated by ligation of spinal L5 and L6, and after 14 days, the microglial-derived inflammatory response accelerated nerve injury and developed to pain states [20, 21]. In human and animal studies, many studies have found that patients with pain are more likely to develop anxiety-like behaviours [22–26]. Periphery nerve injury sensitized spinally mediated transmission of messengers of pain to a higher brain control center, including lateral parabrachial area, caudal ventrolateral medulla, and periaqueductal grey matter. Considering the comorbidity of anxiety with pain, anxiety was selected as one element in WGCNA [27]. For further analysis, pathological traits of ligation, nerve injury, pain, anxiety, and paw withdrawal latency were chosen. More

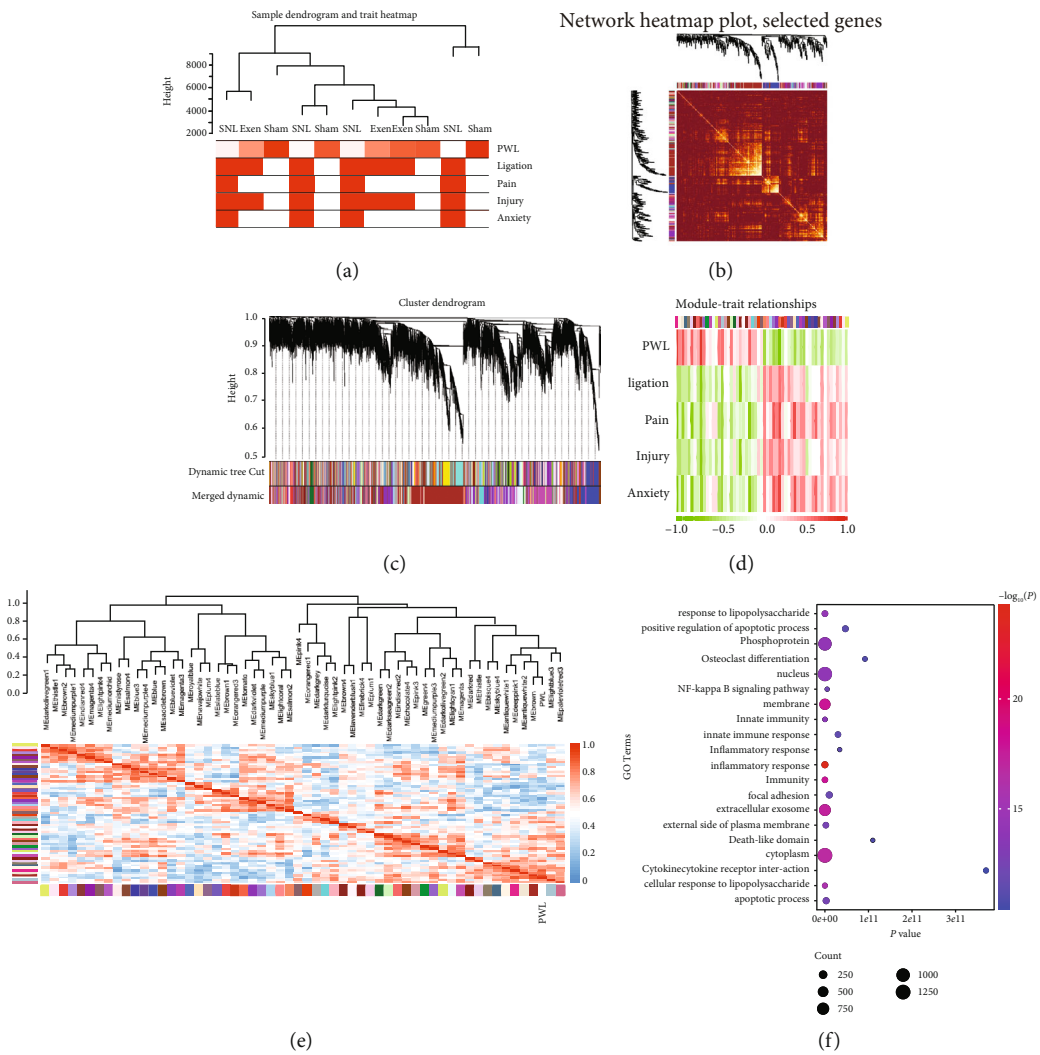


Figure 3: Weighted gene coexpression network analysis of microglial glucagon-like peptide 1 receptor signaling, hierarchical clustering dendrogram of the samples based on paw withdrawal latency, ligation, injury, pain, and anxiety (a), topological overlap matrix (TOM) among identified genes (b), average linkage hierarchical clustering dendrogram of the genes. Input was the TOM based on dissimilarity. Modules, designated by color code, are the branches of the clustering tree (c), correlation between module character and pathological traits. Each color represents the correlated degree. The values are presented as "Pearson $r$ ($p$ value)," and color-coded by the degree of the correlation (red = positive correlation; green = negative correlation) (d), unsupervised hierarchical clustering heat map, color-coded by the degree of the correlation (red = positive correlation; blue = negative correlation) (e), pathway analysis using the Kyoto Encyclopedia of Genes and Genomes showing the top pathways enriched in the gene sets of the brown, distance between nodes is determined by $p$ value and gene counts (f).

importantly, paw withdrawal latency is an objective assessment compared with pathological traits of ligation, nerve injury, pain, and anxiety [28, 29]. We found 58 modules in exenatide-induced antiallodynia by WGCNA. Activation of microglia and astrocytes accelerate the release of inflammatory factors, which in turn is considered a key element in neuropathic pain [30, 31]. All the modules were associated with parameters of behavioural hypersensitivity which may further support the promising mechanism of inhibition of inflammation in pain and the strategy employed in drug development. Interestingly, a previous study on RNA-seq found that nerve injury was characterized by inflammatory responses and highlighted response to lipopolysaccharide, inflammatory response, immune response, and cellular response to lipopolysaccharide signaling [32]. The application of the GLP-1R agonist exenatide inhibited hypersensitivity; meanwhile, response to lipopolysaccharide, inflammatory response, immune response, and cellular response to lipopolysaccharide pathway were the most correlated signaling pathways in exenatide-induced neuroprotection. This finding revealed that anti-inflammatory therapy could be an effective approach for neuropathic pain treatment.

Nerve injury is associated with glial inflammation, leading to maladaptive response. Inflammatory factors (TNF-$\alpha$ and IL-1$\beta$) contribute to neuronal dysfunction associated with ion channel activity, subunits of channels, and phosphorylation of kinases which in turn may regulate the excitability of SG neurons, consistent with RNA-seq data of

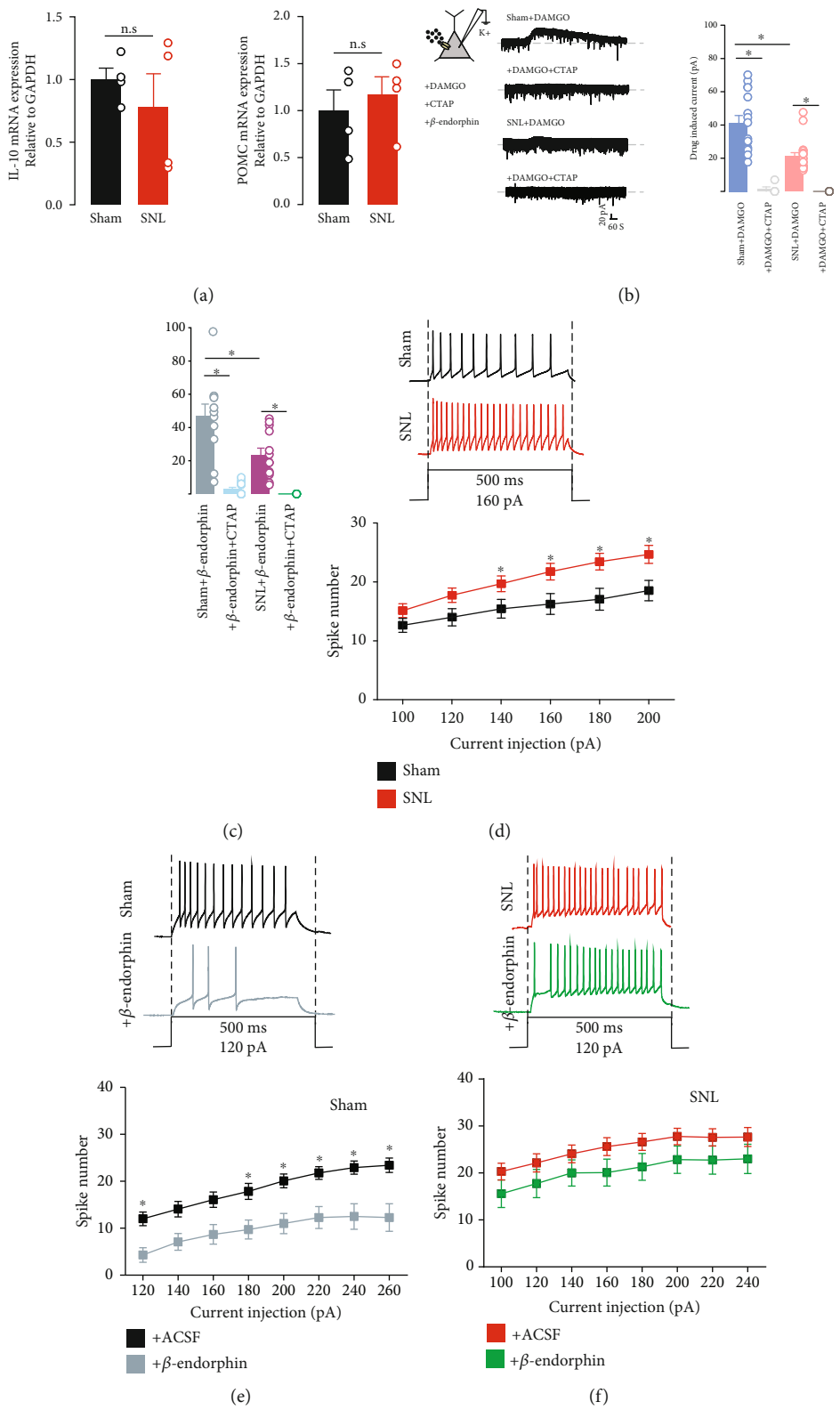


Figure 4: Expression of glucagon-like peptide 1 receptor/IL-10/$\beta$-endorphin/$\mu$-opioid receptor (MOR) in the ipsilateral side. IL-10 and $\beta$-endorphin mRNA (a), MOR agonist DAMGO (b), and $\beta$-endorphin (c) induced outward currents, excitability (d), and inhibitory effect of $\beta$-endorphin on the sham (e) and SNL (f) groups. Rats were induced with neuropathy by the ligation of spinal nerves. Neurons were obtained from the lamina II spinal dorsal horn neurons. The data are presented as the means ± SEM ($n$ = 5-6 animals). $^{*}p < 0.05$, by one-way ANOVA followed by the Tukey post hoc test.

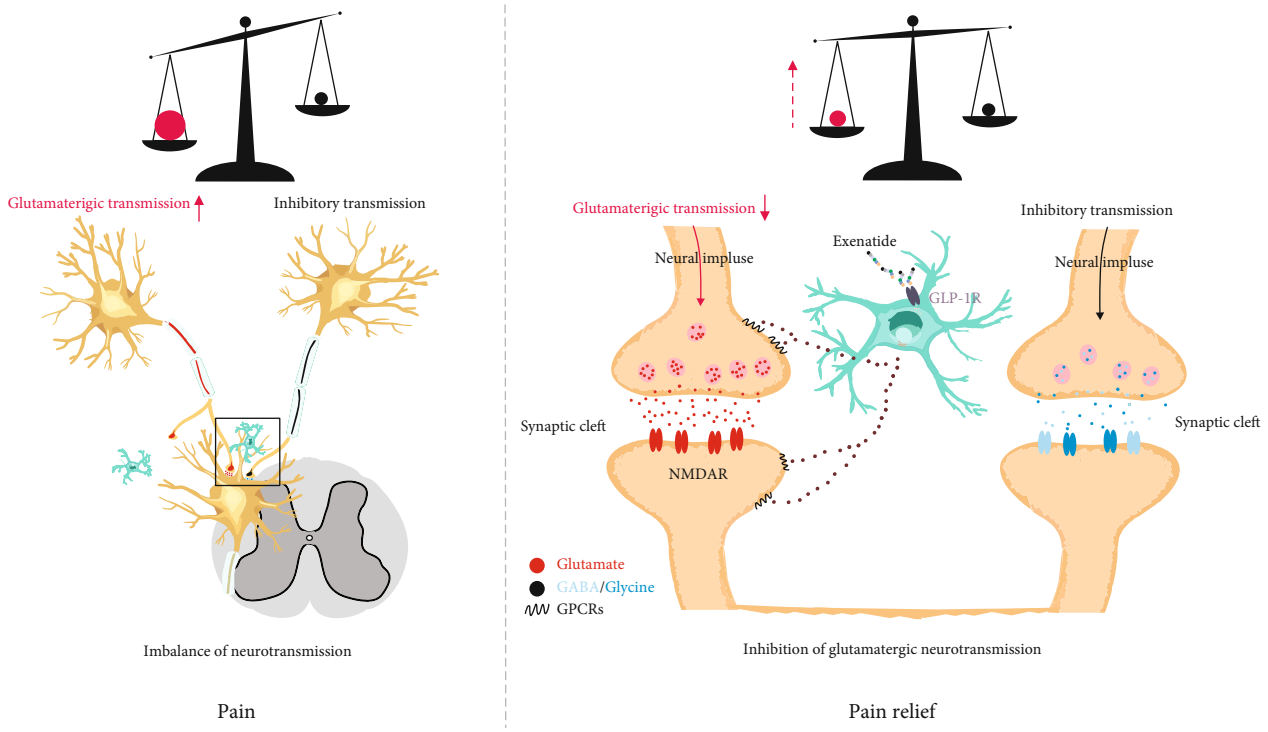


Figure 5: Schematic diagram showing that microglial glucagon-like peptide 1 receptor agonist exenatide prevented peripheral spinal nerve injury-induced mechanical allodynia and glutamatergic transmission and rescued 591 gene expressions associated with a spinal microglial-mediated mechanism.

inflammatory reaction [33, 34]. Many studies have highlighted that microglia is crucial for maintaining synaptic plasticity in neuropathic pain [35, 36] and demonstrated that the modulation of microglial receptors or functions also inhibits pain states [36–38]. Interestingly, our previous study verified that microglial GLP-1R agonist exenatide suppressed various pain states, and pretreatment of IL-10 antiserum and $\beta$-endorphin antiserum completely reversed the inhibition of allodynia [10, 11]. Another previous study from our laboratory found that microglial autocrine IL-10 suppressed hypersensitivity in neuropathic pain and was separated from inflammatory responses [19]. Intrathecal administration of IL-10 stimulates POMC expression and binding to presynaptic neurons to mitigate nerve injury-induced hypersensitivity in the spinal dorsal horn of the SG [19, 39]. IL-10 suppressed LPS-induced TNF-$\alpha$, IL-1$\beta$, or IL-6 expression without affecting mechanical allodynia during the inhibition of MOR. In addition, siRNA/Bcl3 and Socs3, responsible for IL-10 suppressing the anti-inflammatory cytokine expression, totally inhibited TNF-$\alpha$, IL-1$\beta$, and IL-6 expression but not mechanical allodynia [19]. Intrathecal administration of spinal microglial GLP-1R agonist suppressed hypersensitivity, and WGCNA also indicated that exenatide totally abolished inflammatory responses, which further supports our previous research on the separation between pain and inflammation. Moreover, microglial GLP-1R signaling interrupts abnormal nociceptive information transmission of glutamatergic transmission mediated by autocrine IL-10 and $\beta$-endorphin expression, which in turn abolished nociceptive circuits from peripheral receptors to the brain mediated by the spinal cord mediated by MOR [10, 13, 19]. Those data supported that microglial GLP-1R signaling exhibited neuroprotection through binding to neuronal expressed inhibitory MOR.

Intrinsic plasticity refers to changes in the excitability of neurons during pain. Changes in neuronal excitability are a major feature of hypersensitivity and are still disputed when activating GLP-1R signaling. As we know, MOR was the typical opioid in neuropathic pain and is associated with the excitability of neurons. In order to illustrate the role of GLP-1R/IL-10/$\beta$-endorphin signaling modulating neuronal excitability, MOR agonism $\beta$-endorphin and DAMGO were applied. Bath application of MOR agonist $\beta$-endorphin and DAMGO stimulated outward currents in the SG neurons [39], and this inhibitory function was damaged after nerve injury, consistent with our study, showing that the excitability of neurons in the sham group was more sensitive to $\beta$-endorphin compared with the SNL group. In that line, MOR intervention yielded several mechanisms, including balance of the neural circuits, mainly GABAergic and glycinergic neurons in the spinal cord, and reduction of the inhibition of secondary GABAergic interneurons [40].

In summary, behavioural tests and whole-cell recording of the sham, SNL, and exenatide groups indicated strong connections between GLP-1R and neuronal excitability, mechanical allodynia, hypersensitivity, and neuropathic pain. It is worth noting that the intrathecal delivery of exenatide prevented nerve injury-induced damage. WGCNA highlighted a strong correlation between gene expression and functional changes including ligation, hypersensitivity, and anxiety, which

established the microglial GLP-1R pathway in pain management, and highlighted key elements of pain-associated targets of spinal microglial GLP-1R in future pharmaceutical development, as shown in Figure 5.

## Abbreviations

SNL: Spinal nerve ligation
GLP-1: Glucagon-like peptide-1
ACSF: Artificial cerebrospinal fluid
mEPSC: Miniature excitatory postsynaptic current
SG: Substantia gelatinosa
DESeq2: Differential gene expression analysis based on the negative binomial distribution
WGCNA: Weighted correlation network analysis
KEGG: Kyoto Encyclopedia of Genes and Genomes.

## Data Availability

All data, models, or figures generated or used during the study are available from the corresponding authors.

## Ethical Approval

This study was carried out in accordance with the recommendations of the Experimental Animal Committee of Shanghai Jiao Tong University School of Medicine. The protocol was approved by the Animal Care Guidelines of the National Institutes of Health.

## Conflicts of Interest

The authors declare that there are no competing financial interests in this work.

## Authors' Contributions

YXW, JHC, LM, and PJJ conceived and designed the experiments; LM, SYP, JBW, MJZ, and KAA performed the experiments; LM, PJJ, and YXW analyzed the data; and PJJ and LM prepared the paper. Le Ma and Peijun Ju contributed equally to this work.

## Acknowledgments

We thank Shiyu Peng for their help during data collection and management. The study was funded by the Feixiang Personnel Training Program of Shanghai Mental Health Center (grant number 2018-FX-02) and the National Natural Science Foundation of China (81571326).

## References

[1] A. Ellis and D. L. Bennett, "Neuroinflammation and the generation of neuropathic pain," *British Journal of Anaesthesia*, vol. 111, no. 1, pp. 26–37, 2013.

[2] M. Calvo, J. M. Dawes, and D. L. Bennett, "The role of the immune system in the generation of neuropathic pain," *The Lancet Neurology*, vol. 11, no. 7, pp. 629–642, 2012.

[3] F. Marchand, M. Perretti, and S. B. McMahon, "Role of the immune system in chronic pain," *Nature Reviews Neuroscience*, vol. 6, no. 7, pp. 521–532, 2005.

[4] X. Navarro, M. Vivo, and A. Valero-Cabre, "Neural plasticity after peripheral nerve injury and regeneration," *Progress in Neurobiology*, vol. 82, no. 4, pp. 163–201, 2007.

[5] G. Chen et al., "Microglia in pain: detrimental and protective roles in pathogenesis and resolution of pain," *Neuron*, vol. 100, no. 6, pp. 1292–1311, 2018.

[6] C.-Y. Liu, X. Wang, C. Liu, and H.-L. Zhang, "Pharmacological targeting of microglial activation: new therapeutic approach," *Frontiers in Cellular Neuroscience*, vol. 13, 2019.

[7] T. Sato, T. Shimizu, H. Fujita et al., "GLP-1 receptor signaling differentially modifies the outcomes of sterile vs viral pulmonary inflammation in male mice," *Endocrinology*, vol. 161, no. 12, 2020.

[8] Y. Jia, N. Gong, T.-F. Li, B. Zhu, and Y.-X. Wang, "Peptidic exenatide and herbal catalpol mediate neuroprotection via the hippocampal GLP-1 receptor/$\beta$-endorphin pathway," *Pharmacological Research*, vol. 102, pp. 276–285, 2015.

[9] C. Rebosio, M. Balbi, M. Passalacqua, R. Ricciarelli, and E. Fedele, "Presynaptic GLP-1 receptors enhance the depolarization-evoked release of glutamate and GABA in the mouse cortex and hippocampus," *Biofactors*, vol. 44, no. 2, pp. 148–157, 2018.

[10] H.-Y. Wu, X.-Q. Tang, X.-F. Mao, and Y.-X. Wang, "Autocrine interleukin-10 mediates glucagon-like peptide-1 receptor-induced spinal microglial $\beta$-Endorphin expression," *The Journal of Neuroscience*, vol. 37, no. 48, pp. 11701–11714, 2017.

[11] N. Gong, Q. Xiao, B. Zhu et al., "Activation of spinal glucagon-like peptide-1 receptors specifically suppresses pain hypersensitivity," *Journal of Neuroscience*, vol. 34, no. 15, pp. 5322–5334, 2014.

[12] Z.-Y. Wang, Q.-Q. Han, M.-Y. Deng et al., "Lemairamin, isolated from the _Zanthoxylum_ plants, alleviates pain hypersensitivity via spinal $\alpha$7 nicotinic acetylcholine receptors," *Biochemical and Biophysical Research Communications*, vol. 525, no. 4, pp. 1087–1094, 2020.

[13] S. P. Le Ma, J. Wei, M. Zhao, K. A. Ahmad, J. Chen, and Y.-. X. Wang, "Spinal microglial $\beta$-endorphin signaling mediates IL-10 and exenatide-induced inhibition of synaptic plasticity in neuropathic pain," *CNS Neuroscience & Therapeutics*, 2021.

[14] H.-Y. Wu, X.-F. Mao, H. Fan, and Y.-X. Wang, "p38$\beta$Mitogen-Activated protein kinase signaling mediates exenatide-stimulated Microglial$\beta$-Endorphin expression," *Molecular Pharmacology*, vol. 91, no. 5, pp. 451–463, 2017.

[15] B. Zhu, N. Gong, H. Fan et al., "Lamiophlomis rotata, an orally available Tibetan herbal painkiller, specifically reduces pain hypersensitivity states through the activation of spinal glucagon-like peptide-1 receptors," *Anesthesiology*, vol. 121, no. 4, pp. 835–851, 2014.

[16] R. M. Deacon, "Housing, husbandry and handling of rodents for behavioral experiments," *Nature Protocols*, vol. 1, no. 2, pp. 936–946, 2006.

[17] L. Sivilotti and C. J. Woolf, "The contribution of GABAA and glycine receptors to central sensitization: disinhibition and touch-evoked allodynia in the spinal cord," *Journal of Neurophysiology*, vol. 72, no. 1, pp. 169–179, 1994.

[18] S.-B. Zhang, S.-Y. Lin, M. Liu et al., "CircAnks1a in the spinal cord regulates hypersensitivity in a rodent model of neuropathic pain," *Nature Communications*, vol. 10, no. 1, 2019.

[19] H.-Y. Wu, X.-F. Mao, X.-Q. Tang et al., "Spinal interleukin-10 produces antinociception in neuropathy through microglial $\beta$-endorphin expression, separated from antineuroinflammation," *Brain, Behavior, and Immunity*, vol. 73, pp. 504–519, 2018.

[20] T. L. Yaksh, "Behavioral and autonomic correlates of the tactile evoked allodynia produced by spinal glycine inhibition: effects of modulatory receptor systems and excitatory amino acid antagonists," *Pain*, vol. 37, no. 1, pp. 111–123, 1989.

[21] E. C. Burgard and J. J. Hablitz, "NMDA receptor-mediated components of miniature excitatory synaptic currents in developing rat neocortex," *Journal of Neurophysiology*, vol. 70, no. 5, pp. 1841–1852, 1993.

[22] G.-Q. Wang, C. Cen, C. Li et al., "Deactivation of excitatory neurons in the prelimbic cortex via Cdk5 promotes pain sensation and anxiety," *Nature Communications*, vol. 6, 2015.

[23] H.-Y. Liang, Z.-J. Chen, H. Xiao et al., "nNOS-expressing neurons in the vmPFC transform pPVT-derived chronic pain signals into anxiety behaviors," *Nature Communications*, vol. 11, no. 1, p. 2501, 2020.

[24] H. Li, B. Zhang, Q. Hu et al., "Altered heartbeat perception sensitivity associated with brain structural alterations in generalised anxiety disorder," *General Psychiatry*, vol. 33, no. 1, 2020.

[25] H. Shen, M. Chen, and D. Cui, "Biological mechanism study of meditation and its application in mental disorders," *General Psychiatry*, vol. 33, no. 4, 2020.

[26] F. S. Lodhi, A. M. Elsous, S. Irum, A. A. Khan, and U. Rabbani, "Psychometric properties of the Urdu version of the Hospital Anxiety and Depression Scale (HADS) among pregnant women in Abbottabad, Pakistan," *General Psychiatry*, vol. 33, no. 5, article e100276, 2020.

[27] A. Baker, N. Simon, A. Keshaviah et al., "Anxiety Symptoms Questionnaire (ASQ): development and validation," *General Psychiatry*, vol. 32, no. 6, 2019.

[28] B. Yang, J. Wei, P. Ju, and J. Chen, "Effects of regulating intestinal microbiota on anxiety symptoms: a systematic review," *General Psychiatry*, vol. 32, no. 2, 2019.

[29] S. H. Kim and J. M. Chung, "An experimental model for peripheral neuropathy produced by segmental spinal nerve ligation in the rat," *Pain*, vol. 50, no. 3, pp. 355–363, 1992.

[30] K. Inoue, S. Koizumi, M. Tsuda, and Y. Shigemoto-Mogami, "Signaling of ATP receptors in glia-neuron interaction and pain," *Life Sciences*, vol. 74, no. 2-3, pp. 189–197, 2003.

[31] I. Bettoni, F. Comelli, C. Rossini et al., "Glial TLR4 receptor as new target to treat neuropathic pain: efficacy of a new receptor antagonist in a model of peripheral nerve injury in mice," *Glia*, vol. 56, no. 12, pp. 1312–1319, 2008.

[32] W. Sun, D. Kou, Z. Yu et al., "A transcriptomic analysis of neuropathic pain in rat dorsal root ganglia following peripheral nerve injury," *NeuroMolecular Medicine*, vol. 22, no. 2, pp. 250–263, 2020.

[33] Y. Kawasaki, L. Zhang, J.-K. Cheng, and R.-R. Ji, "Cytokine mechanisms of central sensitization: distinct and overlapping role of interleukin-1beta, interleukin-6, and tumor necrosis factor-alpha in regulating synaptic and neuronal activity in the superficial spinal cord," *Journal of Neuroscience*, vol. 28, no. 20, pp. 5189–5194, 2008.

[34] B. Viviani, S. Bartesaghi, F. Gardoni et al., "Interleukin-1beta enhances NMDA receptor-mediated intracellular calcium increase through activation of the Src family of kinases," *The Journal of Neuroscience*, vol. 23, no. 25, pp. 8692–8700, 2003.

[35] Y. Hayashi, S. Morinaga, J. Zhang et al., "BK channels in microglia are required for morphine-induced hyperalgesia," *Nature Communications*, vol. 7, no. 1, 2016.

[36] T. Yu, X. Zhang, H. Shi et al., "P2Y12 regulates microglia activation and excitatory synaptic transmission in spinal lamina II neurons during neuropathic pain in rodents," *Cell Death & Disease*, vol. 10, no. 3, p. 165, 2019.

[37] M.-C. Hsieh, Y.-C. Ho, C.-Y. Lai et al., "Spinal TNF-$\alpha$ impedes Fbxo45-dependent Munc13-1 ubiquitination to mediate neuropathic allodynia in rats," *Cell Death & Disease*, vol. 9, no. 8, p. 811, 2018.

[38] X. Yan, F. Li, D. W. Maixner et al., "Interleukin-1beta released by microglia initiates the enhanced glutamatergic activity in the spinal dorsal horn during paclitaxel-associated acute pain syndrome," *Glia*, vol. 67, no. 3, pp. 482–497, 2019.

[39] T. Kohno, R.-R. Ji, N. Ito et al., "Peripheral axonal injury results in reduced $\mu$ opioid receptor pre- and post-synaptic action in the spinal cord☆," *Pain*, vol. 117, no. 1, pp. 77–87, 2005.

[40] T. Yasaka, G. Kato, H. Furue et al., "Cell-type-specific excitatory and inhibitory circuits involving primary afferents in the substantia gelatinosa of the rat spinal dorsal horn in vitro," *The Journal of Physiology*, vol. 581, no. 2, pp. 603–618, 2007.

Hindawi
Neural Plasticity
Volume 2021, Article ID 9961145, 8 pages
https://doi.org/10.1155/2021/9961145

*Research Article*

# Therapeutic Efficacy of Ultrasound-Guided High-Voltage Long-Duration Pulsed Radiofrequency for Pudendal Neuralgia

**Feng Ji**,[1] **Shuzhuan Zhou**,[2] **Caixia Li**,[1] **Yongyan Zhang**,[1] **and Hua Xu**[1]

[1]*Department of Anesthesiology, Yueyang Hospital of Integrated Traditional Chinese and Western Medicine Affiliated to Shanghai University of Traditional Chinese Medicine, Shanghai 200437, China*
[2]*Department of Anesthesiology, Marine Corps Hospital of PLA, Chaozhou 521000, Guangdong Province, China*

Correspondence should be addressed to Hua Xu; pshhuaxu@163.com

Received 11 March 2021; Revised 14 June 2021; Accepted 17 July 2021; Published 31 July 2021

Academic Editor: Xu-Yun Hua



Pudendal neuralgia (PN) is a complex disease with various clinical characteristics, and there is no treatment showing definite effectiveness. This study is aimed at evaluating the clinical efficacy of ultrasound-guided high-voltage long-duration pulsed radiofrequency (PRF) for PN. Two cadavers (one male, one female) were dissected to provide evidence for localization of the pudendal nerve. Patients diagnosed as PN who failed or were intolerant in regular medication were screened for diagnostic local anesthesia block of the pudendal nerve before recruitment. Twenty PN patients were enrolled in this study. In the PRF procedure, the needle tip was inserted medially into the internal pudendal artery under ultrasound guidance. The position of the PRF needle tip was then adjusted by the response of the pudendal nerve to the electrical stimulation within the pudendal area (42°C, a series of 2 Hz, and 20 ms width pulses that lasted for 900 s). Alleviation of pain was assessed by the visual analogue scale (VAS) and sitting time pretreatment and on 7 d, 14 d, 1 m, 2 m, 3 m, and 6 m posttreatment in outpatient follow-up or by telephone interview. Two patients were lost due to intervention-irrelevant reasons. Patients showed significantly decreased VAS scores on 7 d after RFP, compared with pretreatment status ($7.0 \pm 0.9$ vs. $3.2 \pm 1.7$, $P < 0.001$). The efficacy remained steady till the end of 6 months, with a final remission rate of 88.9%. Sitting time also significantly lengthened following PRF (7 d, 14 d, 1 m, 2 m, 3 m, and 6 m vs. pretreatment, all $P < 0.05$). Only short-term ipsilateral involuntary convulsion of the lower extremity was reported in one patient, who recovered within 12 h. Six patients were treated with nonsteroidal drugs for a short time. All patients stopped taking medication finally. In conclusion, the ultrasound-guided high-voltage long-duration PRF approach not only reduced the pelvic pain caused by PN but also improved the quality of life by extending sitting time without nerve injury.

## 1. Introduction

Pudendal neuralgia (PN) refers to neuropathic pain in the pudendal nerve innervation region, which may occur in the entire perineal region or in one of its branches, and is often accompanied by symptoms such as rectal and anal foreign body sensation, distension, frequency and urgency of urination, and sexual dysfunction [1, 2]. According to the survey by the International Pudendal Neuropathy Association, the incidence of PN in the general population is about 1/100,000 [3]. However, Spinosa et al. [4] documented the incidence at 1% in the general population, which is higher in females than in males, with more unilateral cases [3]. PN patients present a variety of clinical symptoms and usually need multidisciplinary treatment. In addition, due to the pain in private parts, patients tend to have a longer course of disease and more severe symptoms before willing to visit the doctor, which would seriously affect their quality of life. However, there is still a lack of definite treatment because of its unclear pathogenesis.

Radiofrequency has been used to treat pain for nearly a century. It is widely applied to regions including the head, neck, chest, waist, and sacral region [5–9]. However, with the extensive application of continuous radiofrequency treatment, clinicians found that the heat or improper operation would cause unacceptable compilations due to permanent nerve injury, such as continuous numbness and fecal incontinence [10]. Since the emergence of the pulsed

Table 1: Diagnostic criteria for pudendal neuralgia (Nantes criteria).

| Essential criteria | Complementary diagnostic criteria | Exclusion criteria |
|---|---|---|
| Pain in the territory of the pudendal nerve<br>Pain is predominantly experienced while sitting<br>The pain does not wake the patient at night<br>Pain with no objective sensory impairment<br>Pain relieved by diagnostic pudendal nerve block | Burning, shooting, and stabbing pain, numbness<br>Allodynia or hyperpathia<br>Rectal or vaginal foreign body sensation (sympathalgia)<br>Worsening of pain during the day<br>Predominantly unilateral pain<br>Pain triggered by defecation<br>Presence of exquisite tenderness on palpation of the ischial spine<br>Clinical neurophysiology findings in men or nulliparous women | Exclusively coccygeal, gluteal, pubic, or hypogastric pain<br>Pruritus<br>Exclusively paroxysmal pain<br>Imaging abnormalities able to account for the pain |

radiofrequency (PRF) technique, these situations can be mostly avoided because of its lower temperature (no more than 50°C) during treatment [11, 12]. It has been increasingly used in the treatment of chronic pain, including PN. Studies reported that CT-guided pudendal nerve PRF treatment through the sacrotuberous ligament puncture to the pudendal canal could obviously relieve the symptoms of PN [13, 14]. CT-guided high-voltage long-duration PRF treatment was also applied to reduce the pain in patients with postherpetic neuralgia, as well as PN [15, 16]. However, radiation in CT scan may limit its further clinical application.

Compared with other image-guided technology, ultrasound is playing an increasingly important role in pain diagnosis and treatment due to its advantages of radiation-free, convenient, and real-time positioning guidance [17–19]. Ultrasound-guided PRF treatment at the ischial spine was reported effective for PN [18]. Its clinical efficacy and safety have also been confirmed by a randomized controlled clinical study [19]. However, the application of ultrasound-guided high-voltage long-duration PRF in the treatment of PN has not been reported yet. In the present study, we investigated the anatomical position of the pudendal nerve at the transverse section of the ischial spine and its adjacent relationship with the surrounding tissue. Eligible patients were then selected to receive ultrasound-guided high-voltage long-duration PRF treatment at the ischial spine. Its clinical efficacy and especially improvement in the quality of life were observed. It may provide a new option for PN treatment.

## 2. Materials and Methods

*2.1. Anatomical Study.* Two adult cadavers (one male and one female) formalin embalmed and fixed were used (provided by the Human Anatomy Teaching and Research Department of the Basic Department of Naval Military Medical University). The cadaver specimens had intact pelvis and pelvic organs. The subcutaneous tissues and muscles of the buttock were opened layer by layer to expose the subgluteal space, the sacrospinous ligament, and its adjacent vessels and nerves. The anatomical relationship between the sacrospinous ligament and the pudendal nerve was confirmed.

*2.2. Patients.* Patients diagnosed as PN who received treatment were recruited from the pain center of Changhai Hospital from Sep 1, 2015, to Oct 31, 2016. The PN diagnosis was based on the Nantes criteria (Table 1) [1]. They were unresponsive to medication therapy (12 patients) or intolerant to the side effects (8 patients) at recruitment. This study was approved by the Ethics Committee of Changhai Hospital Affiliated to the Naval Military Medical University.

Inclusion criteria are as follows: (1) aged from 18 to 80 years old and no sex limitation; (2) patients who were not satisfied with conservative treatment or intolerant to the side effects; and (3) be able to sign an informed consent form. Exclusion criteria are as follows: (1) patients with pelvic organic disease that may also cause pain in the pudendal region; (2) patients with malignant or autoimmune diseases that cause pain; (3) pregnant women; (4) patients with any coagulation disorder; and (5) patients who are unable to complete the outpatient or telephone interview.

*2.3. Diagnostic Block of the Pudendal Nerve.* Effective pudendal nerve block is an essential approach for the inclusion of patients. The patient was in the prone position, and a low-frequency curved-array probe (C251/1~5 MHz, Hitachi Noblus, Japan) was used to scan from the posterior superior iliac spine downwards to the transverse section of the ischial spine (Figures 1(a) and 1(b)). The internal pudendal artery above the ischial spine was identified in color Doppler mode (Hitachi Noblus, Japan) (Figure 2). Outside of the ultrasound probe, a nerve block needle (Pajunk, 21 G ∗ 100 m, Germany) penetrates the skin near the internal pudendal artery by the in-plane technique (the pudendal nerve mostly located in the medial part of the internal pudendal artery). The nerve stimulator (Braun Stimuplex, Germany) was applied to detect movement of the patient's pain site, and the needle tip position was adjusted accordingly. When the current is less than 0.4 mA and the pain site movement was induced, an injection of 5 ml 1% lidocaine was applied with 10 min observation. In bilateral cases, diagnostic block should be applied to bilateral pudendal nerves. Numbness and pain relief of more than half indicated the effectiveness of the diagnostic block and eligibility for recruitment of PRF treatment.

*2.4. PRF Procedure.* In the PRF procedure, the patient was placed in the prone position on a sterilized sheet with routine disinfection. A 20 G radiofrequency needle (Cosman) was used for puncture, and the puncture process was the same as the diagnostic block of PN (Figures 3(a) and 3(b)).

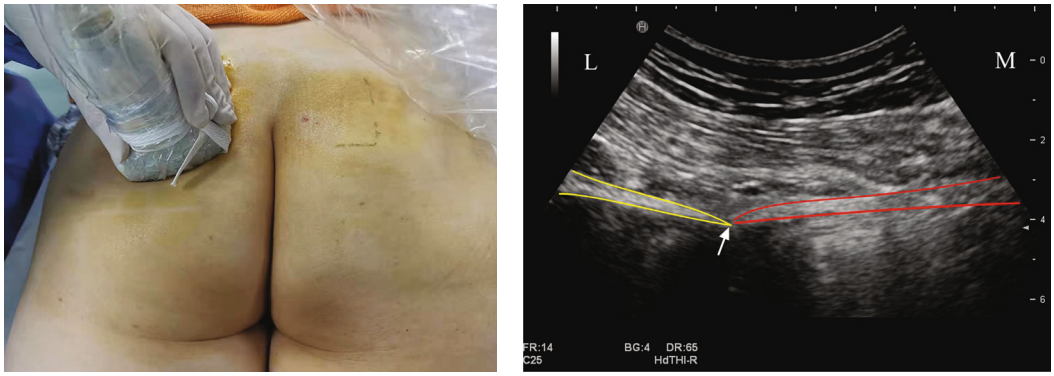


(a) (b)

Figure 1: Diagnostic block of the pudendal nerve under ultrasound guidance. (a) Position and direction of the ultrasonic probe. (b) Transverse section of the ultrasound image in the ischial spine. Red outline: sacrospinous ligament; yellow outline: ischium; white arrow: ischial spine. L: lateral; M: medial.

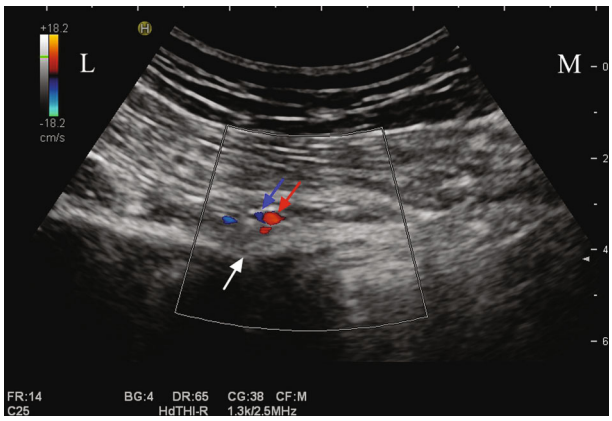


Figure 2: Internal pudendal artery presented in color Doppler. White arrow: ischium spine; red arrow: internal pudendal artery; blue arrow: internal pudendal vein. L: lateral; M: medial.

*2.4.1. Test Parameters.* In the sensory test (50 Hz), when the voltage was 0.3-0.5 V, the patient could feel the tingling sensation at the pain site, which indicated that the puncture needle tip was around the pudendal nerve. When the voltage was higher than 2 V in the motor test (2 Hz), the lower limb movement of the same side was not induced, indicating that the puncture needle tip was far from the sciatic nerve. During PRF, the radiofrequency instrument was set as the manual pulse treatment mode, and the RF parameters were set as follows: temperature 42°C, stimulation frequency 2 Hz, pulse width 20 ms, and duration 900 s; the field intensity began at 40 V and gradually increased until the patient has an intolerable abnormal sensation (such as burning sensation) in the pain site (the intensity was not more than 80 V to avoid nerve damage caused by high temperature). Patients with bilateral pain were treated with bilateral PRF. The procedure was performed with the radiofrequency therapeutic apparatus (Baylis, Canada).

*2.5. Outcome Measures.* Through outpatient or telephone follow-up, the pain intensity of patients was evaluated before intervention and on 7 d, 14 d, 1 month, 2 months, 3 months, and 6 months after high-voltage long-duration PRF treatment. The visual analogue scale (VAS) was applied for pain assessment, with 0 indicating no pain, 1-3 mild pain, 4-6 moderate pain, and above 7 severe pain. The patients' maximum sitting time before the onset of pain (i.e., sitting time) was evaluated according to the assessment method and criteria of previous studies [20, 21]. Briefly, the assessment was performed in the afternoon, and the patient was asked to sit in a comfortable position while the sitting time was recorded as the maximum time when the patient reported being too painful to keep on sitting. The sitting time of patients before treatment and on 7 d, 14 d, 1 month, 2 months, 3 months, and 6 months after treatment was evaluated in the outpatient follow-up by the same physician. However, if the patients were unable to come for the outpatient follow-up, self-assessed results were obtained through telephone interview under the guidance of the same physician instead (Supplement Table 3).

*2.6. Statistical Analysis.* The measurement data were expressed in terms of mean ± standard deviation ($X \pm \mathrm{SD}$). Repeated-measures one-way ANOVA was used for within-group comparison and Bonferroni's test for between-group comparison. $P < 0.05$ was considered statistically significant. SPSS 22.0 software was used in the statistical analysis.

## 3. Results

*3.1. Anatomical Study.* Two cadaver specimens (embalmed) were examined, including one Asian man (death age 76, height 172 cm, and BMI 25.7 kg/m$^2$) and one Asian woman (death age 86, height 158 cm, and BMI 19.2 kg/m$^2$).

As indicated by a previous study [22], the course of bilateral pudendal nerves in two specimens was between the lesser sciatic foramen composed of the sacrospinal ligament and sacrospinal ligament. The pudendal nerve was located on the surface of the sacrospinal ligament, medially to the sciatic spine and adjacent to the internal pudendal artery (Figure 4).

At the cross of the sciatic spine in the male cadaver, the pudendal nerve was 13 mm medial to the sciatic spine, and the internal pudendal artery was 6 mm lateral to the

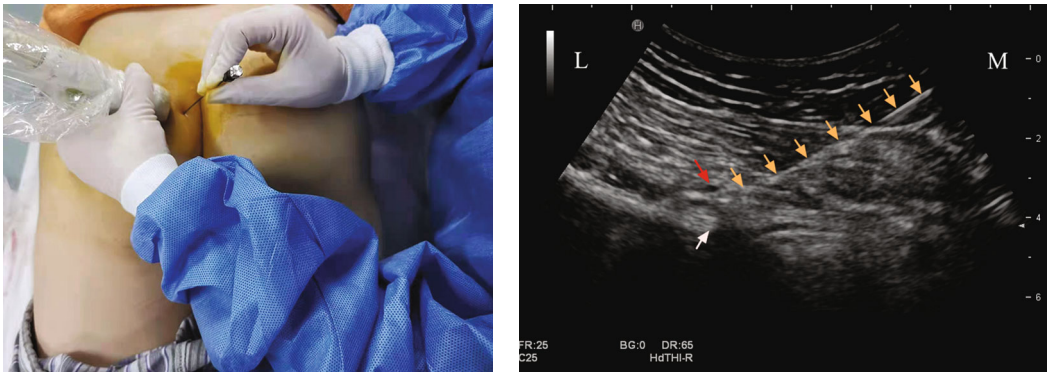


(a) (b)

Figure 3: Procedure of pulsed radiofrequency. (a) The relationship between the location of the PRF needle and the position of the ultrasonic probe. (b) The track of the PRF needle and the position of the needle tip. Orange arrow: radiofrequency puncture needle; red arrow: internal pudendal artery; white arrow: ischium spine. L: lateral; M: medial.

pudendal nerve. In the female cadaver, the pudendal nerve was 11 mm medial to the sciatic spine, and the internal pudendal artery was 6 mm lateral to the pudendal nerve (Table 2). Anatomical results provided a position landmark for ultrasound-guided PRF at the ischial spine.

*3.2. Patients.* A total of twenty patients were finally enrolled, including six males and fourteen females, aged 42~68 yrs (57 ± 4.7 yrs) (Table 3, Supplement Table 1). Seven patients reported pain in the genitals and five in the anus, while the rest (eight) covering the anus, genitals, and perineum. Twelve patients reported unilateral pain, and eight patients were bilaterally involved. Patients were informed of the risks, and a written informed consent form was provided. Eighteen patients completed the 6-month postoperative follow-up, and two patients were lost because they could not be contacted by phone or were unwilling to participate in outpatient follow-up after treatment. Finally, sixteen patients stopped taking medication immediately after PRF. Four patients still reported short-term pain in the initial stage after PRF, took tramadol+pregabalin intermittently for a short time, and stopped taking medication at final visits.

*3.3. VAS Score.* All the patients reported moderate or severe pain, with VAS scores of 7.0 ± 0.9 points before treatment. The VAS score on day 7 after the treatment (3.2 ± 1.7) was significantly lower than that before treatment ($P < 0.05$). The VAS score did not significantly change since day 14 after treatment (all $P > 0.05$, Figure 5). The remission rate was 88.9% at the end of 6 months, with only two reporting no obvious relief of pain.

*3.4. Sitting Time.* As many patients were unable to come for each outpatient follow-up due to intervention-irrelevant reasons (e.g., lived too far away from the center), part of the assessments was completed under the guidance of the same physician through telephone interview. Compared with pretreatment (30 ± 15 min), sitting time significantly prolonged on 7 d (62 ± 20 min), 1 m (81 ± 34 min), 2 m (83 ± 36 min), 3 m (84 ± 39 min), and 6 m (85 ± 37 min) after treatment was significantly longer than that before treatment (30 ± 15 min). However, there was no significant difference in the sitting time among 7 d, 14 d, 1 m, 2 m, 3 m, and 6 m after treatment ($P > 0.05$, Figure 6).

*3.5. Adverse Events.* No serious adverse event was reported. No infection occurred following PRF. One patient reported ipsilateral involuntary convulsion of the lower extremity immediately after treatment and recovered within 12 h. Six patients complained of pain at the puncture site, which alleviated shortly with the application of nonsteroidal drugs. Three patients reported mild skin herpes in the perineum within 3 days after treatment and recovered thereafter, which was considered irrelevant to the intervention (Supplement Table 2).

## 4. Discussion

The etiology of PN is complex, and the mechanism is largely unclear. It may be due to the entrapment and mechanical injury of the pudendal nerve. The common entrapment sites are the sciatic foramen and pudendal canal between the sacrotuberous ligament and the sacrospinal ligament, especially the sciatic spine [23, 24]. However, the mechanical injury of the pudendal nerve is often associated with pregnancy, delivery, and pelvic surgery. In addition, the pathological changes of the pudendal nerve may also lead to PN, such as herpes zoster neuralgia and diabetic peripheral neuralgia. In this study, one patient reported herpes zoster neuralgia in the pudendal innervation region, and two patients had diabetic peripheral neuropathy.

For these reasons, conservative treatment (e.g., oral medicine, nerve block therapy, and physical therapy) is usually ineffective. With the continuous development of image-guided technology, interventional treatment has been increasingly performed by clinicians, especially by pain practitioners. Interventional treatment (such as nerve block, radiofrequency, and electrical stimulation treatment) has been applied in the treatment of PN [13, 20], and the efficacy was quite promising.

Radiofrequency technology is a novel technology to treat chronic pain. Traditional continuous radiofrequency

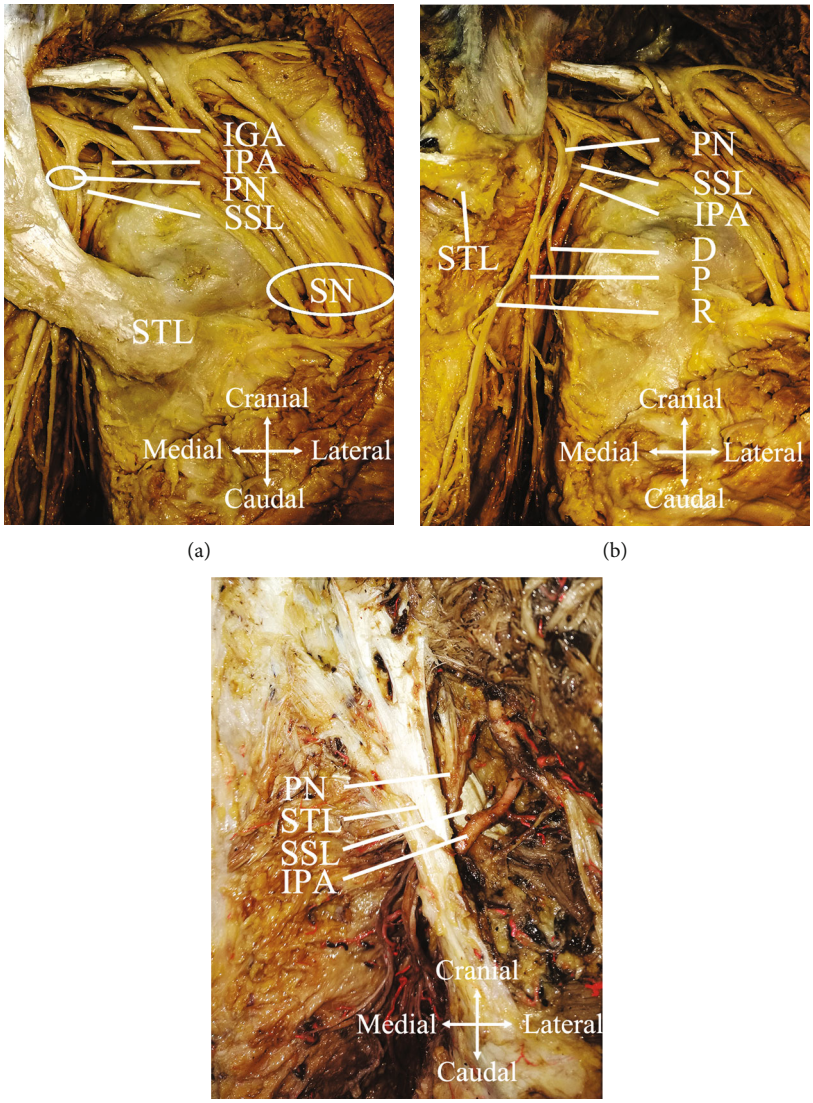


Figure 4: Anatomical study of the pudendal nerve in cadavers. (a) Pudendal nerve and its adjacent tissues. (b) Pudendal nerve and its branches of a male cadaver (dissection of the sacrotuberous ligament). (c) Pudendal nerve and its adjacent tissue in a female cadaver. STL: sacrotuberous ligament; SSL: sacrospinous ligament; IPA: internal pudendal artery; IGA: inferior gluteal artery; PN: pudendal nerve; SN: sciatic nerve; D: dorsal nerve of the penis; P: perineal nerve; R: inferior rectal nerve.

Table 2: Distance of the pudendal nerve to the sciatic spine and the pudendal nerve to the internal pudendal artery in the cadavers.

| | Distance between the pudendal nerve and the sciatic spine | Distance between the pudendal nerve and the internal pudendal artery |
|---|---|---|
| Male | 13 mm | 6 mm |
| Female | 11 mm | 6 mm |

technology damages nerves to treat pain in the dominant area, which would inevitably lead to permanent nerve injury and serious side effects. Compared with traditional continuous radiofrequency thermocoagulation technology, pulsed radiofrequency is a nonneurodegenerative radiofrequency technology. The temperature of the electrode tip does not exceed 42°C, which will not cause irreversible tissue damage, in which situation the sensorimotor functions of the nerve could be largely preserved.

However, the underlying mechanism of pulsed radiofrequency in the treatment of neuropathic pain is mostly unknown. Some studies suggested that low-temperature pulsed radiofrequency can form a field effect around the lesion, thus regulating the transmission of pain signals [12]. Compared with continuous radiofrequency thermocoagulation, the PRF procedure shows a similar therapeutic effect and fewer complications [25]. In a typically standard PRF procedure (42°C), the intensity of the electric field is fixed and the efficacy would last for a period of time. In the continuous RF, however, heat effect (as high as 80°C) was used to damage the nerve; thus, the defecation function would be injured as well. Some studies indicated that the electric field

Table 3: Demographic characteristics of patients.

| Characteristic | Content | Value |
|---|---|---|
| Numbers ($n$) | | 20 |
| Sex ($n$) | Male | 6 |
| | Female | 14 |
| BMI | Range | 18.9-31.70 |
| | Mean ± SD | 23.7 ± 3.1 |
| Age (years) | Range | 42-68 |
| | Mean ± SD | 57 ± 8 |
| Pain site | Anus | 5 |
| | Genitals | 7 |
| | Anus, genitals, and perineum | 8 |
| Unilateral and bilateral pain | Unilateral | 12 |
| | Bilateral | 8 |
| Baseline VAS (points) | Range | 5-9 |
| | Mean ± SD | 7.0 ± 0.9 |
| Baseline of sitting time (min) | Range | 5-52 |
| | Mean ± SD | 30 ± 15 |
| Duration of pain | <1 year | 5 |
| | 1-5 years | 10 |
| | >5 years | 5 |
| Pain characteristics | Stabbing pain | 5 |
| | Burning pain | 11 |
| | Aching pain | 4 |
| | Throbbing pain | 2 |

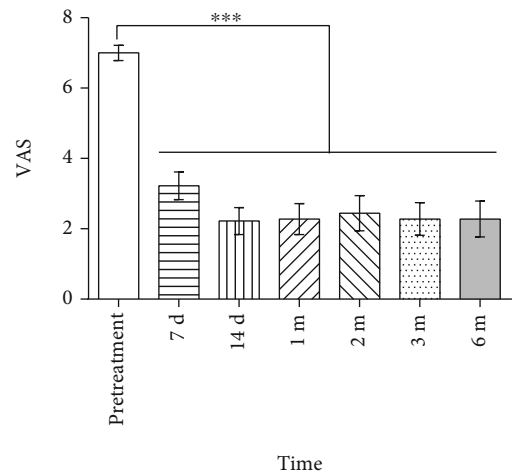


Figure 5: Results of the visual analogue scale (VAS) before and after high-voltage long-duration pulsed radiofrequency (PRF) treatment. VAS significantly decreased on 7 d after treatment and remained steady till 6 months. There was no significant difference among all the time points after treatment (pretreatment vs. 7 d, 14 d, 1 m, 2 m, 3 m, and 6 m posttreatment; $^{***}P < 0.001$).

effect can inhibit the transmission of excitatory neurotransmitters, activate the immune system, and reduce the chronic inflammatory response [26, 27]. Some researchers suggested that the therapeutic effect of neuropathic pain treatment was based on the electric field [28, 29]. Recently, high-voltage long-duration PRF was reported rewarding for the treatment of chronic pain (e.g., trigeminal neuralgia and postherpetic neuralgia) without obvious nerve injury [15, 30, 31]. It has also been applied in the treatment of PN with the guidance of CT scan [16]. But few studies have reported the therapeutic effect of the ultrasound-guided PRF procedure in PN except for some cases and a small randomized controlled clinical study [18, 19]. It may show a better therapeutic effect than pudendal nerve block only. The application of ultrasound-guided high-voltage long-duration PRF has not been reported in the treatment of PN, as well as anatomical studies and patients' quality of life. Compared with the study reported by Fang et al. [19], we used modified RF parameters. In Fang et al.'s report, the standard radiofrequency ablation mode with 42°C and 120 s pulse consisting of two cycles was used. In our study, a high-voltage (started from 40 V and no more than 80 V) and long-duration (2 Hz of 20 ms width pulses that lasted for 900 s) PRF mode under US guidance was used. As for the outcome measure, VAS and PHQ-9 were used in Fang et al.'s study, while VAS and sitting time were used for the assessment of the efficacy in the present study. According to our clinical experience and patients' reports, sitting time was considered an important subjective index for pain-related quality of life. Studies have shown that sitting time in patients with pudendal neuralgia or chronic pelvic pain will be significantly shortened, and relevant treatment measures can significantly delay the onset time of sitting pain so as to improve the satisfaction of treatment [20, 21, 32]. In a report by Buffenoir et al., sitting time was also used as an evaluation index for pudendal neuralgia [20]. For patients with reduced time of comfortable sitting caused by pain, longer comfortable sitting time not only improved patients' satisfaction with the treatment but also reduced the impact of disease and brought overall well-being and quality of life [21]. The present study indicated that high-voltage long-term PRF treatment can significantly alleviate pain over 6 months and prolong sitting time at least 2 weeks in patients with PN without obvious side effects, suggesting that it can be used as an effective method of PN treatment.

Anatomically, the pudendal nerve goes tortuously and is largely varied. A study showed that before entering the pudendal canal, the branch of the pudendal nerve, the inferior rectum nerve, often runs inward and downward [33]. Even under the guidance of X-ray or CT, there is still the possibility of inaccurate positioning. A report revealed that the pudendal nerve trunk is fixed relative to the surface of the sacrospinous ligament and medial to the ischial spine, and it was adjacent to the internal pudendal artery [22]. It is consistent with the results of our anatomical study (Figures 4(a) and 4(c), Table 3). We further verified the results by cutting off the sacrotuberous ligament (Figure 4(b)). Ultrasound could be a helpful tool to locate the internal pudendal artery and ischial spine in the guidance of the puncturing approach due to its capability of identifying the blood vessel (i.e., internal pudendal artery) and bone landmark (i.e., ischial spine). As a real-time positioning and radiation-free technology,

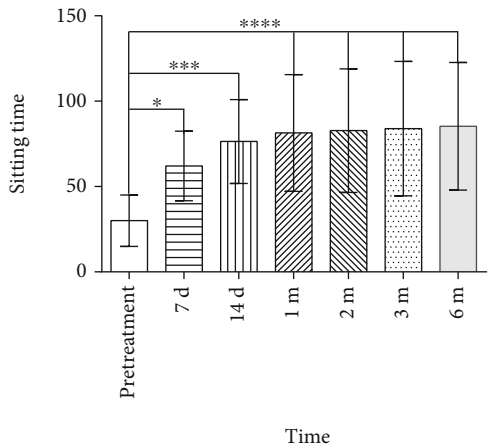


Figure 6: Comparison of sitting time before and after pulsed radiofrequency treatment. The sitting time significantly increased since day 7 after treatment (pretreatment vs. 7 d, $^{*}P < 0.05$; pretreatment vs. 14 d, $^{***}P < 0.001$; and pretreatment vs. 1 m, 2 m, 3 m, or 6 m, $^{****}P < 0.0001$). There was no significant difference in the sitting time among 7 d, 14 d, 1 m, 2 m, 3 m, and 6 m after treatment ($P > 0.05$).

ultrasound-guided PRF avoids vascular damage and is easier and more flexible for operators.

With the internal pudendal artery companied, the pudendal nerve is located on the surface of the sacrospinal ligament. When it goes down into the pudendal canal, its branches are more dispersed, and its relative location to the internal pudendal artery may be varied. Therefore, the pudendal nerve is more accessible in the transverse section of the sciatic spine. Previous studies suggested that the pudendal nerve is adjacent to the sciatic nerve above the cross-section of the sciatic spine, which indicated that the sciatic nerve and even the sacral plexus could be involved if penetrating above the cross-section of the sciatic spine. Therefore, punctuation is recommended to locate at the entrance of the pudendal nerve canal. This provided important information for improving ultrasound-guided treatment for PN [34].

Brusciano et al. reported a novel approach, the dynamic transperineal ultrasound (DTU), in the assessment of the pudendal nerve motility [35, 36]. By this method, pelvic floor neuromuscular integrity such as displacement of puborectalis muscle could be identified. Other pelvic neuromuscular diseases could also be identified, such as ilioinguinal nerve-, genitofemoral nerve-, and obturator nerve-related pelvic pain. In our future study, DTU and electrophysiology examination could be included in the diagnostic process of pudendal neuropathy before application of PRF treatment. The quality of life and pain impact questionnaires also need to be further investigated to evaluate a global response to the intervention in future studies. The sample size of this study was relatively small. A randomized controlled study with a larger sample is needed to draw a final conclusion. High requirement of ultrasound operators also limits the application of this approach. The role and underlying mechanisms of PRF in the treatment of PN still remain to be further explored.

## 5. Conclusions

The present study suggested that high-voltage long-duration PRF treatment can alleviate the pain of patients with pudendal neuralgia and improve their quality of life by prolonging the sitting time without obvious severe adverse events. Ultrasound-guided PRF could be a safe and rewarding treatment for PN patients.

## Data Availability

The data used to support the findings of this study are available from the corresponding author upon request.

## Conflicts of Interest

All authors claim that there are no conflicts of interest.

## Authors' Contributions

Feng Ji and Shuzhuan Zhou contributed equally to this work.

## Acknowledgments

This work was supported by the National Natural Science Foundation of China (NSFC) (Grant No. 82074288).

## Supplementary Materials

Supplement Table 1: information of all patients. Supplement Table 2: adverse events. Supplement Table 3: follow-up assessments of all patients. *(Supplementary Materials)*

## References

[1] J.-J. Labat, T. Riant, R. Robert, G. Amarenco, J.-P. Lefaucheur, and J. Rigaud, "Diagnostic criteria for pudendal neuralgia by pudendal nerve entrapment (Nantes criteria)," *Neurourology& Urodynamics*, vol. 27, no. 4, pp. 306–310, 2010.

[2] K. Waseem and H. Douglass, "Pudendal neuralgia," *Obstetrics & Gynecology Clinics of North America*, vol. 41, no. 3, pp. 443–452, 2014.

[3] M. Hibner, N. Desai, L. J. Robertson, and M. Nour, "Pudendal neuralgia," *Journal of Minimally Invasive Gynecology*, vol. 17, no. 2, pp. 148–153, 2010.

[4] J. P. Spinosa, E. D. Bisschop, and J. Laurençon, "Sacral staged reflexes to localize the pudendal compression: an anatomical validation of the concept," *Revue Médicale Suisse*, vol. 2, no. 84, pp. 2416–2418, 2006.

[5] H. A. V. Suijlekom, M. V. Kleef, G. A. M. Barendse, M. E. Sluijter, and W. E. J. Weber, "Radiofrequency cervical zygapophyseal joint neurotomy for cervicogenic headache: a prospective study of 15 patients," *Functional Neurology*, vol. 13, no. 4, pp. 297–303, 1998.

[6] G. A. S. Miguel, G. J. Hordijk, and K. P. J. M. Van Gisbergen, "Effects of radiofrequency thermocoagulation of the sphenopalatine ganglion on headache and facial pain: correlation with diagnosis," *Journal of Orofacial Pain*, vol. 26, no. 1, p. 59, 2012.

[7] L. Niemistö, E. Kalso, A. Malmivaara, S. Seitsalo, and H. Hurri, "Radiofrequency denervation for neck and back pain: a systematic review within the framework of the Cochrane

Collaboration Back Review Group," *Spine*, vol. 28, no. 16, pp. 1877–1888, 2003.

[8] R. J. Stolker, A. C. M. Vervest, and G. J. Groen, "The treatment of chronic thoracic segmental pain by radiofrequency percutaneous partial rhizotomy," *Journal of Neurosurgery*, vol. 80, no. 6, pp. 986–992, 1994.

[9] J. N. S. Juch, E. T. Maas, R. W. J. G. Ostelo et al., "Effect of radiofrequency denervation on pain intensity among patients with chronic low back pain: the MINT randomized clinical trials," *JAMA*, vol. 318, no. 1, pp. 68–81, 2017.

[10] M. Hammer and W. Meneese, "Principles and practice of radiofrequency neurolysis," *Current Review of Pain*, vol. 2, no. 4, pp. 267–278, 1998.

[11] C. Ojango, M. Raguso, R. Fiori, and S. Masala, "Pulse-dose radiofrequency treatment in pain management-initial experience," *Skeletal Radiology*, vol. 47, no. 5, pp. 609–618, 2018.

[12] E. E. Rhame, K. A. Levey, and C. G. Gharibo, "Successful treatment of refractory pudendal neuralgia with pulsed radiofrequency," *Pain Physician*, vol. 12, no. 3, pp. 633–638, 2009.

[13] S. Masala, E. Calabria, A. Cuzzolino, M. Raguso, M. Morini, and G. Simonetti, "CT-guided percutaneous pulse-dose radiofrequency for pudendal neuralgia," *CardioVascular&Interventional Radiology*, vol. 37, no. 2, pp. 476–481, 2014.

[14] V. Petrov-Kondratov, A. Chhabra, and S. Jones, "Pulsed radiofrequency ablation of pudendal nerve for treatment of a case of refractory pelvic pain," *Pain Physician*, vol. 20, no. 3, 2017.

[15] T. Song, "Bipolar high-voltage, long-duration pulsed radiofrequency improves pain relief in postherpetic neuralgia," *Pain Physician*, vol. 19, no. 5, 2016.

[16] C. Wang and T. Song, "The clinical efficacy of high-voltage long-range pulsed radiofrequency treatment in pudendal neuralgia," *Chinese Journal of Pain Medicine*, vol. 25, no. 8, pp. 43–47, 2019.

[17] I. M. Ajeena, R. H. Al-Saad, A. Al-Mudhafar, N. R. Hadi, and S. H. Al-Aridhy, "Ultrasonic assessment of females with carpal tunnel syndrome proved by nerve conduction study," *Neural Plasticity*, vol. 2013, Article ID 754564, 6 pages, 2013.

[18] M.-J. Hong, Y.-D. Kim, J.-K. Park, and H.-J. Hong, "Management of pudendal neuralgia using ultrasound-guided pulsed radiofrequency: a report of two cases and discussion of pudendal nerve block techniques," *Journal of Anesthesia*, vol. 30, no. 2, pp. 1–4, 2015.

[19] H. Fang, J. Zhang, Y. Yang, and X. W. Le Ye, "Clinical effect and safety of pulsed radiofrequency treatment for pudendal neuralgia: a prospective, randomized controlled clinical trial," *Journal of Pain Research*, vol. Volume 11, pp. 2367–2374, 2018.

[20] K. Buffenoir, B. Rioult, O. Hamel, J.-J. Labat, T. Riant, and R. Robert, "Spinal cord stimulation of the conus medullaris for refractory pudendal neuralgia: a prospective study of 27 consecutive cases," *Neurourology&Urodynamics*, vol. 34, no. 2, pp. 177–182, 2015.

[21] M. Hibner, M. E. Castellanos, D. Drachman, and J. Balducci, "Repeat operation for treatment of persistent pudendal nerve entrapment after pudendal neurolysis," *Journal of Minimally Invasive Gynecology*, vol. 19, no. 3, pp. 325–330, 2012.

[22] P. A. Maldonado, K. Chin, A. A. Garcia, and M. M. Corton, "Anatomic variations of pudendal nerve within pelvis and pudendal canal: clinical applications," *American Journal of Obstetrics & Gynecology*, vol. 213, no. 5, pp. 727.e1–727.e6, 2015.

[23] R. Robert, J.-J. Labat, M. Bensignor et al., "Decompression and transposition of the pudendal nerve in pudendal neuralgia: a randomized controlled trial and long-term evaluation," *European Urology*, vol. 47, no. 3, pp. 403–408, 2005.

[24] S. Ploteau, M. A. Perrouin-Verbe, and J. J. Labat, "Anatomical variants of the pudendal nerve observed during a transgluteal surgical approach in a population of patients with pudendal neuralgia," *Pain Physician*, vol. 20, no. 1, 2017.

[25] R. Vallejo, R. M. Benyamin, and L. Aliaga, "Radiofrequency vs. pulse radiofrequency: the end of the controversy," *Techniques in Regional Anesthesia& Pain Management*, vol. 14, no. 3, pp. 128–132, 2010.

[26] L. Todorov, "Pulsed radiofrequency of the sural nerve for the treatment of chronic ankle pain," *Pain Physician*, vol. 14, no. 3, pp. 301–304, 2011.

[27] O. Rohof, "Intradiscal pulsed radiofrequency application following provocative discography for the management of degenerative disc disease and concordant pain: a pilot study," *Pain Practice*, vol. 12, no. 5, pp. 342–349, 2012.

[28] A. Teixeira and M. E. Sluijter, "Intradiscal high-voltage, long-duration pulsed radiofrequency for discogenic pain: a preliminary report," *Pain Medicine*, vol. 7, no. 5, pp. 424–428, 2006.

[29] A. Cahana, J. Van Zundert, L. Macrea, M. Van Kleef, and M. Sluijter, "Pulsed radiofrequency: current clinical and biological literature available," *Pain Medicine*, vol. 7, no. 5, pp. 411–423, 2006.

[30] L. Fang, W. Tao, L. Jingjing, and J. Nan, "Comparison of high-voltage- with standard-voltage pulsed radiofrequency of Gasserian ganglion in the treatment of idiopathic trigeminal neuralgia," *Pain Practice*, vol. 15, no. 7, pp. 595–603, 2015.

[31] C. Wan, D. S. Dong, and T. Song, "High-voltage, long-duration pulsed radiofrequency on Gasserian ganglion improves acute/subacute zoster-related trigeminal neuralgia: a randomized, double-blinded, controlled trial," *Pain Physician*, vol. 22, no. 4, pp. 361–368, 2019.

[32] J.-M. Louppe, J.-P. Nguyen, R. Robert et al., "Motor cortex stimulation in refractory pelvic and perineal pain: report of two successful cases," *Neurourology and Urodynamics*, vol. 32, no. 1, pp. 53–57, 2013.

[33] T. I. Montoya, L. Calver, K. S. Carrick, J. Prats, and M. M. Corton, "Anatomic relationships of the pudendal nerve branches," *American Journal of Obstetrics & Gynecology*, vol. 205, no. 5, pp. 504.e1–504.e5, 2011.

[34] T. F. Bendtsen, T. Parras, B. Moriggl et al., "Ultrasound-guided pudendal nerve block at the entrance of the pudendal (Alcock) canal," *Regional Anesthesia and Pain Medicine*, vol. 41, no. 2, pp. 140–145, 2016.

[35] L. Brusciano, C. Gambardella, B. Roche et al., "Dynamic transperineal ultrasonography correlates with prolonged pudendal nerve latency in female with fecal incontinence," *Updates in Surgery*, vol. 72, no. 4, pp. 1187–1194, 2020.

[36] L. Brusciano, C. Gambardella, S. Tolone et al., "An imaginary cuboid: chest, abdomen, vertebral column and perineum, different parts of the same whole in the harmonic functioning of the pelvic floor," *Techniques in Coloproctology*, vol. 23, no. 6, pp. 603–605, 2019.

Hindawi
Neural Plasticity
Volume 2021, Article ID 9959103, 8 pages
https://doi.org/10.1155/2021/9959103

*Research Article*

# Diabetic Peripheral Neuropathy Affects Pinch Strength and Hand Dexterity in Elderly Patients

**Qi Zhang,[1] Yifang Lin,[1] Xinhua Liu,[1] Li Zhang,[1] Yan Zhang,[2] Dong Zhao,[2] Qi Lu,[2] and Jie Jia[1,3]**

[1]*Department of Rehabilitation Medicine, Huashan Hospital, Fudan University, China*
[2]*Jiaozuo People's Hospital, Henan Province, China*
[3]*National Clinical Research Center for Aging and Medicine, Huashan Hospital, Fudan University, China*

Correspondence should be addressed to Jie Jia; shannonjj@126.com

Received 10 March 2021; Revised 24 May 2021; Accepted 3 July 2021; Published 21 July 2021

Academic Editor: Jia-Jia Wu



*Objective*. Diabetic peripheral neuropathy (DPN) is one of the most common chronic complications of diabetes, leading to disability and decreased quality of life. In past research and clinical studies, the lower limb function of DPN patients was often the principal subject of research, with little attention given to the upper limb and hand. Our goal was to assess and compare hand function between elderly diabetic patients with DPN and without DPN. *Methods*. A total of 52 diabetic patients were registered and underwent hand function assessments and electrodiagnostic tests. Dynamometer, pinch meter, Semmes Weinstein monofilaments, and the Purdue Pegboard Test (PPT) were used to assess the patients' grip strength, pinch strength, tactile sensory threshold, and hand dexterity. *Results*. Compared with the non-DPN group, the elderly DPN group showed worse thumb-middle fingertip pinch strength and thumb-little fingertip pinch strength in the dominant hand (3.50 (2.50, 4.25) vs. 4.50 (3.00, 5.00), $p = 0.019$; 1.50 (1.00, 2.00) vs. 2.50 (2.00, 3.00), $p < 0.001$); the elderly DPN group displayed worse thumb-middle fingertip pinch strength, thumb-ring fingertip pinch strength, and thumb-little fingertip pinch strength in the nondominant hand (3.50 (2.00, 4.50) vs. 4.00 (3.00, 5.00), $p = 0.013$; 2.50 (1.25, 3.00) vs. 3.00 (2.50, 3.50), $p = 0.033$; 1.00 (0.75, 2.25) vs. 2.50 (2.00, 2.50), $p < 0.001$). The elderly DPN group scored lower than the non-DPN group on the PPT test of assembly ($13.96 \pm 5.18$ vs. $16.96 \pm 4.61$, $t = 2.212$, $p = 0.032$). *Conclusion*. Motor function limitation is the principal hand dysfunction in elderly patients with DPN, which is mainly manifested as a decline in fingertip pinch strength and a decrease in hand dexterity. This trial is registered with Clinical Trial Registry no. ChiCTR1900025358.

## 1. Introduction

China has the largest number of diabetes mellitus cases and the highest annual increases in cases in the world, with 116 million cases nationwide in 2019 [1, 2]. Diabetic peripheral neuropathy (DPN) is one of the most common chronic complications of diabetes, leading to disability and decreased quality of life, and its incidence increases with the duration of diabetes [3]. Approximately 10% to 15% of patients have signs of neuropathy when they are diagnosed with diabetes, and 50% of diabetics will eventually develop DPN, which could affect 236 million people worldwide by 2030 [4, 5]. DPN can affect both sensory neurons and motor neurons and is characterized by decreases in tactile sensitivity, nerve conduction velocity, and motor function in the advanced stages of the disease, which may eventually lead to foot ulcers, amputation, and disability [6, 7]. The major symptom of DPN is symmetrical sensory pain affecting the lower limbs [8]. Other manifestations include atypical pain, numbness, and pins-and-needles and hot or burning sensations. Other signs of neuromotor dysfunction include muscle weakness, poor balance, and a tendency to fall [9, 10].

With the increasing prevalence of diabetes and the prolongation of the life span of diabetic patients, the prevalence

of diabetes in the elderly is rising [11]. Therefore, elderly people are also the main population affected by DPN. Previous researchers have focused on the lower limbs of patients with DPN but ignored the impact of DPN on the hands. A few studies have reported pain, numbness, and even ulcers in the hands of parents with DPN [12, 13]. Evidence has suggested that hand function, especially pinch and grip strength, decreases in type 2 diabetes mellitus compared with healthy controls [14]. However, limited studies have focused on sensory and motor function in the hands of elderly patients with DPN. Based on previous studies, we assume that elderly DPN patients have decreased sensory and motor function compared to non-DPN patients. The aim of this study was to document the monofilament tactile sensation, grip strength, pinch strength, and dexterity of the hands of the elderly patients with DPN and to explore the rehabilitation strategies for hand function in DPN patients.

## 2. Research Design and Methods

*2.1. Study Design and Participants.* Data were collected in Jiaozuo People's Hospital, Henan Province, China. The inclusion criteria were as follows: (1) participants were age 65 years or older with a previous diagnosis of type 2 diabetes for more than 5 years; (2) their blood glucose control was basically stable, and there was no acute complications of diabetes; and (3) informed consent was obtained from all participants. The exclusion criteria included the following: (1) history of stroke, Parkinson's disease, and other central system diseases; (2) history of peripheral nervous system diseases such as carpal tunnel syndrome; (3) hands with ulcers, gout, and disability; (4) new fractures and severe muscle atrophy in the hands; (5) habit/history of alcohol abuse; (6) participants with no education; and (7) participants with severe cognitive impairment (Montreal Cognitive Assessment (MoCA) score ≤ 18). This study was approved by the Ethics Committee of Huashan Hospital Affiliated to Fudan University (NO.2019M-006) and the Ethics Committee of Jiaozuo People's Hospital (NO.2019001) and was registered in the China Clinical Trial Registration Center (ChiCTR1900025358). A total of 52 participants who met the above criteria were included (Figure 1). All participants were included in strict accordance with our standards, and general information, hand function assessment, and electrophysiological diagnosis were gathered from all participants who met the standards in accordance with specific procedures (Figure 2). All participants were divided into two groups according to whether they had DPN: elderly diabetic patients with DPN (DPN+) and elderly diabetic patients without DPN (DPN-).

*2.2. General Information.* Data on all participants included age, sex, height, weight, waist circumference, hip circumference, diabetes duration, and medical history.

*2.3. Monofilament Tactile Sensation Assessment.* Semmes Weinstein monofilament examination (SWME) is often used to assess the tactile sensation function of the hands and feet in patients with DPN [15]. All participants were asked to wear eye masks for the Semmes Weinstein monofilament assessment (Touch Test Complete Hand Kit, North Coast Medical Inc., USA) following a standard testing protocol [16]. We assessed the area innervated by the median, ulnar, and radial nerves: the dorsal area of the first and second metacarpal bones (SWME-1), the tip of the index finger (SWME-2), and the tip of the little finger (SWME-3). Each part was assessed three times, and the minimum tactile threshold that the participant could feel was recorded (Figure 3).

*2.4. Grip and Pinch Strength Assessment of Hands.* Grip strength of the participants was assessed using a hydraulic hand dynamometer (Exacta, North Coast Medical Inc., Gilroy, CA, USA) with participants seated with the shoulder adducted and neutrally rotated, the elbow flexed at 90 degrees, and the forearm in the neutral position. We used a mechanical pinch-strength meter (B&L Engineering, CA, United States) to measure the pinch strength between the thumb and the remaining four fingers. The measurement methods were as follows: (1) thumb-index fingertip pinch strength (Pinch-I), (2) thumb-middle fingertip pinch strength (Pinch-M), (3) thumb-ring fingertip pinch strength (Pinch-R), and (4) thumb-little fingertip pinch strength (Pinch-L). Each was measured three times, and the maximum value was recorded.

*2.5. Assessment of Hand Dexterity.* Hand dexterity is an important manifestation of upper limb motor function. We also assessed fine-motor-skill performance using the previously validated Purdue Pegboard Test (PPT, model 32020, Lafayette Instruments, Lafayette, IN, USA) following a standard testing protocol [17]. Participants were asked to complete four tests: (1) fill in the holes with pegs within 30 seconds with the dominant hand, (2) fill in the holes with pegs within 30 seconds with the nondominant hand, (3) fill in the holes with pegs within 30 seconds with the both hands, and (4) assemble in sequence a peg, a washer, a collar, and finally another washer within 60 seconds. The number of parts completed by participants was recorded.

*2.6. Nerve Conduction Studies.* Nerve conduction studies (NCS) are the current gold standard for the diagnosis of DPN [18]. All participants underwent NCS using a standard electromyography (EMG) device (KOHDEN, MEB-9200K, Japan). Testing was performed by a professional technician with more than 10 years of clinical experience in the EMG room, and the entire process was conducted in a special shielded room. There were 32 variables recorded: sensory nerve conduction velocity (SNCV) and sensory nerve action potential (SNAP) in the median, ulnar, sural, and superficial peroneal nerves on both sides; motor nerve conduction velocity (MNCV) and compound muscle action potential (CMAP) in the median, ulnar, peroneal, and tibial nerves on both sides. We used NCS to diagnose DPN using the criteria for electrodiagnostic confirmation of DPN: an abnormality of any attribute of nerve conduction in two separate nerves, one of which must be a nerve in the lower limbs [19, 20].

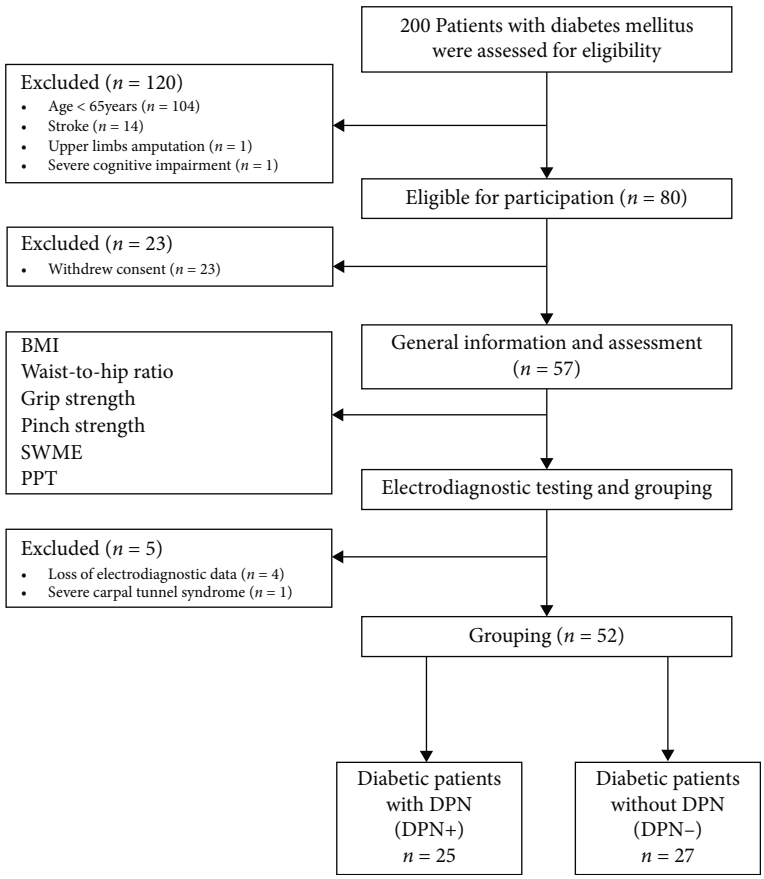


Figure 1: Participant inclusion criteria and research procedure. SWME: Semmes Weinstein monofilament examination; PPT: Purdue Pegboard Test.


Figure 2: Illustration of hand function assessment.

*2.7. Statistical Analysis.* Statistical analysis was performed using SPSS for Windows, version 21.0 (SPSS, Chicago, IL). All statistics were tested for normal distribution. The continuous data of normal distribution were expressed as mean ± standard deviation, and categorical variables were presented as numbers and percentages (%). An independent sample $t$-test was used to compare the means of two groups, and a chi-square test was used to compare the percentages. Data of skewed distribution were presented as the median (25th-75th percentile) and tested with the Mann–Whitney $U$ test. A value of $p < 0.05$ was considered statistically significant.

## 3. Results

*3.1. Baseline Characteristics of DPN and Non-DPN Groups.* A total of 52 participants were included in our study. The DPN group had 25 participants (12 males, 13 females) with an average age of 73.0 ± 5.3 years. The body mass index (BMI) was 25.6 ± 3.0 kg/m$^2$, the waist-to-hip ratio was 0.93 ± 0.07, and the diabetes duration was 15.0 (9.5, 21.0) years. The percentage of participants who self-reported smoking, drinking, and coronary heart disease was 28.0%, 24.0%, and 40.0%, respectively. The non-DPN group had 27 participants (8 males, 19 females) with an average age of 72.1 ± 5.5 years. The BMI was 25.5 ± 3.6 kg/m$^2$, the waist-to-hip ratio was 0.90 ± 0.07, and the diabetes duration was 12.0 (6.0, 16.0) years. The percentage of participants who self-reported smoking, drinking, and coronary heart disease was 11.1%,

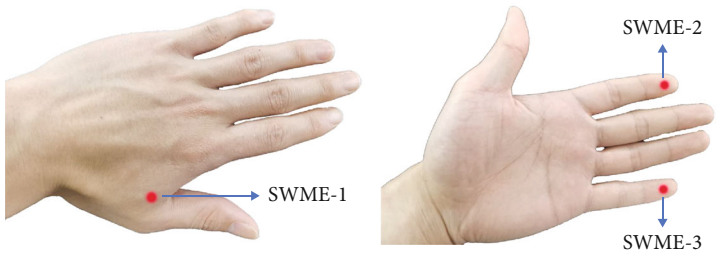


Figure 3: The assessment sites for the Semmes Weinstein monofilament examination.

Table 1: Characteristics of the DPN group (DPN+) and the non-DPN group (DPN-).

| | DPN group (DPN+) | Non-DPN group (DPN-) | $t/X^2/Z$ | $p$ |
|---|---|---|---|---|
| $N$ | 25 | 27 | | |
| Age (years) | 73.0 ± 5.3 | 72.1 ± 5.5 | -0.568 | 0.573 |
| Male/female (number) | 12/13 | 8/19 | 1.851 | 0.174 |
| BMI (kg/m$^2$) | 25.6 ± 3.0 | 25.5 ± 3.6 | -0.123 | 0.903 |
| Waist-to-hip ratio | 0.93 ± 0.07 | 0.90 ± 0.07 | -1.587 | 0.119 |
| Diabetes duration (years) | 15.0 (9.5, 21.0) | 12.0 (6.0, 16.0) | -1.714 | 0.086 |
| Current smoker, $n$ (%) | 7 (28.0%) | 3 (11.1%) | 2.384 | 0.123 |
| Current drinker, $n$ (%) | 6 (24.0%) | 3 (11.1%) | 1.507 | 0.220 |
| Coronary heart disease, $n$ (%) | 10 (40.0%) | 10 (37.0%) | 0.048 | 0.826 |

Data are expressed as the mean ± standard deviation, %, or median (25th-75th percentile). BMI: body mass index. A $p$ value > 0.05 was considered as not indicating statistical significance.

11.1%, and 37.0%, respectively. There were no significant differences in baseline data between the two groups ($p > 0.05$) (Table 1).

*3.2. NCS and Monofilament Tactile Threshold Analysis.* In the NCS results, there were significant differences in the nerve conduction velocities in both hands between the DPN group and the non-DPN group. The results showed that the conduction velocities in the median sensory nerve, median motor nerve, and ulnar sensory nerve in the dominant hand in the DPN group were lower than those in the non-DPN group ($p < 0.05$). The conduction velocities in the median sensory nerve and median motor nerve in the nondominant hand in the DPN group were lower than those in the non-DPN group ($p < 0.05$). There were significant differences in four nerve conduction velocities in the lower limbs between the two groups ($p < 0.05$). The results showed that the median sensory nerve action potential, the peroneal nerve compound muscle action potential, and the tibial nerve compound muscle action potential in the dominant hand/lower limb in the DPN group were lower than those in the non-DPN group ($p < 0.05$). The median sensory nerve action potential, the median nerve compound muscle action potential, the ulnar sensory nerve action potential, and the peroneal nerve compound muscle action potential in the nondominant hand/lower limb in the DPN group were lower than those of the non-DPN group ($p < 0.05$). There were no significant differences in the SWME threshold between the two groups ($p > 0.05$) (Table 2).

*3.3. Analysis of Hand Grip and Pinch Strength.* Analysis of hand grip strength of all participants showed no significant differences between the two groups ($p > 0.05$). The results showed that the thumb-middle fingertip pinch strength and thumb-little fingertip pinch strength of the DPN group were lower than those of the non-DPN group in the dominant hand ($p < 0.05$). There were no significant differences in the thumb-index fingertip pinch strength and thumb-ring fingertip pinch strength between the two groups in the dominant hand ($p > 0.05$). The thumb-middle fingertip pinch strength, thumb-ring fingertip pinch strength, and thumb-little fingertip pinch strength of the DPN group were lower than those of the non-DPN group in the nondominant hand ($p < 0.05$) (Table 3; Figure 4).

*3.4. Analysis of Hand Dexterity.* Table 4 shows PPT differences in the dominant hand, nondominant hand, both hands, and assembly between the DPN group and the non-DPN group. There were no significant differences between the two groups of participants in the PPT test of dominant hand, nondominant hand, and both hands ($p > 0.05$). The results showed that the DPN group scored lower than the non-DPN group in PPT test of assembly (13.96 ± 5.18 vs. 16.96 ± 4.61, $t = 2.212$, $p = 0.032$) (Table 4; Figure 5).

Table 2: Comparison of nerve conduction studies and Semmes Weinstein monofilament examination threshold between the two groups.

| | Dominant hand/lower limb | | | | Nondominant hand/lower limb | | | |
|---|---|---|---|---|---|---|---|---|
| | DPN+ | DPN- | $t/Z$ | $p$ | DPN+ | DPN- | $t/Z$ | $p$ |
| M-SNCV (m/s) | 46.4 ± 6.4 | 49.8 ± 4.8 | 2.100 | 0.041* | 45.5 ± 6.8 | 52.0 ± 4.9 | 3.836 | <0.001* |
| M-MNCV (m/s) | 49.1 ± 4.7 | 52.2 ± 4.2 | 2.458 | 0.018* | 50.1 ± 5.8 | 53.7 ± 4.9 | 2.357 | 0.023* |
| U-SNCV (m/s) | 47.2 ± 4.5 | 49.9 ± 3.0 | 2.537 | 0.014* | 47.7 ± 5.2 | 50.2 ± 4.3 | 1.849 | 0.071 |
| U-MNCV (m/s) | 53.6 ± 7.3 | 56.2 ± 4.9 | 1.509 | 0.138 | 55.1 ± 6.9 | 56.1 ± 5.1 | 0.619 | 0.539 |
| S-SNCV (m/s) | 42.2 ± 4.8 | 46.7 ± 4.1 | 3.451 | 0.001* | 42.0 ± 6.1 | 46.6 ± 5.0 | 2.840 | 0.007* |
| SP-SNCV (m/s) | 41.5 ± 6.1 | 46.4 ± 4.3 | 3.189 | 0.003* | 41.1 ± 6.3 | 45.3 ± 3.7 | 2.869 | 0.006* |
| P-MNCV (m/s) | 41.0 ± 4.8 | 44.6 ± 4.1 | 2.880 | 0.006* | 40.2 ± 5.4 | 43.7 ± 2.9 | 2.858 | 0.006* |
| T-MNCV (m/s) | 40.2 ± 3.7 | 43.1 ± 3.1 | 3.025 | 0.004* | 39.6 ± 4.6 | 43.5 ± 2.9 | 3.655 | 0.001* |
| M-SNAP ($\mu$V) | 4.9 ± 3.9 | 9.5 ± 7.7 | 2.762 | 0.009* | 6.7 ± 5.4 | 12.2 ± 5.3 | 3.681 | 0.001* |
| M-CMAP (mV) | 8.1 ± 4.4 | 9.0 ± 2.9 | 0.926 | 0.359 | 8.4 ± 4.3 | 10.7 ± 3.3 | 2.136 | 0.038* |
| U-SNAP ($\mu$V) | 7.4 ± 5.9 | 9.4 ± 6.8 | 1.125 | 0.266 | 5.8 ± 4.9 | 9.8 ± 6.2 | 2.530 | 0.015* |
| U-CMAP (mV) | 11.5 ± 4.1 | 12.1 ± 2.9 | 0.578 | 0.566 | 10.7 ± 4.2 | 12.2 ± 2.2 | 1.704 | 0.095 |
| S-SNAP ($\mu$V) | 8.8 ± 9.8 | 12.1 ± 9.5 | 1.222 | 0.228 | 8.9 ± 12.3 | 8.6 ± 4.7 | -0.136 | 0.893 |
| SP-SNAP ($\mu$V) | 6.1 ± 9.3 | 11.0 ± 10.4 | 1.784 | 0.080 | 6.9 ± 10.6 | 11.4 ± 8.5 | 1.645 | 0.107 |
| P-CMAP (mV) | 3.8 ± 2.2 | 6.5 ± 2.6 | 4.106 | <0.001* | 3.8 ± 2.7 | 6.9 ± 3.6 | 3.547 | 0.001* |
| T-CMAP (mV) | 10.7 ± 6.7 | 14.9 ± 7.2 | 2.161 | 0.036* | 9.9 ± 5.2 | 12.9 ± 6.4 | 1.858 | 0.069 |
| SWME-1 | 2.83 (2.44, 3.61) | 2.83 (2.36, 3.61) | -0.751 | 0.453 | 2.83 (2.36, 3.22) | 2.83 (2.36, 3.22) | -0.308 | 0.758 |
| SWME-2 | 3.61 (2.83, 3.73) | 2.83 (2.44, 3.61) | -1.074 | 0.283 | 2.83 (2.44, 3.61) | 2.83 (2.44, 3.22) | -0.981 | 0.327 |
| SWME-3 | 3.22 (2.83, 3.73) | 2.83 (2.44, 3.22) | -1.453 | 0.146 | 2.83 (2.44, 3.61) | 2.83 (2.44, 3.22) | -1.377 | 0.168 |

Data are expressed as the mean ± standard deviation or median (25th-75th percentile). M-SNCV: median sensory nerve conduction velocity; M-MNCV: median motor nerve conduction velocity; U-SNCV: ulnar sensory nerve conduction velocity; U-MNCV: ulnar motor nerve conduction velocity; S-SNCV: sural sensory nerve conduction velocity; SP-SNCV: superficial peroneal sensory nerve conduction velocity; P-MNCV: peroneal motor nerve conduction velocity; T-MNCV: tibial motor nerve conduction velocity; M-SNAP: median sensory nerve action potential; M-CMAP: median nerve compound muscle action potential; U-SNAP: ulnar sensory nerve action potential; U-CMAP: ulnar nerve compound muscle action potential; S-SNAP: sural sensory nerve action potential; SP-SNAP: superficial peroneal sensory nerve action potential; P-CMAP: peroneal nerve compound muscle action potential; T-CMAP: tibial nerve compound muscle action potential. *A $p$ value < 0.05 was considered to indicate statistical significance.

Table 3: Comparison of grip and pinch strength between the two groups.

| | Dominant hand | | | | Nondominant hand | | | |
|---|---|---|---|---|---|---|---|---|
| | DPN+ | DPN- | $Z$ | $p$ | DPN+ | DPN- | $Z$ | $p$ |
| Grip strength (kg) | 16.00 (12.50, 26.50) | 17.00 (14.00, 24.00) | -0.340 | 0.734 | 15.00 (8.50, 23.00) | 16.00 (12.00, 21.00) | -0.468 | 0.640 |
| Pinch-I (kg) | 4.50 (3.50, 5.50) | 5.00 (4.00, 6.50) | -1.482 | 0.138 | 3.50 (2.75, 5.25) | 4.50 (3.50, 6.00) | -1.821 | 0.069 |
| Pinch-M (kg) | 3.50 (2.50, 4.25) | 4.50 (3.00, 5.00) | -2.341 | 0.019* | 3.50 (2.00, 4.50) | 4.00 (3.00, 5.00) | -2.489 | 0.013* |
| Pinch-R (kg) | 2.50 (1.50, 3.50) | 3.00 (2.50, 4.00) | -1.878 | 0.060 | 2.50 (1.25, 3.00) | 3.00 (2.50, 3.50) | -2.134 | 0.033* |
| Pinch-L (kg) | 1.50 (1.00, 2.00) | 2.50 (2.00, 3.00) | -4.046 | <0.001* | 1.00 (0.75, 2.25) | 2.50 (2.00, 2.50) | -3.689 | <0.001* |

Data are expressed as the median (25th-75th percentile). Pinch-I: thumb-index fingertip pinch strength; Pinch-M: thumb-middle fingertip pinch strength; Pinch-R: thumb-ring fingertip pinch strength; Pinch-L: thumb-little fingertip pinch strength. *A $p$ value < 0.05 was considered to indicate statistical significance.

## 4. Discussion

The study showed that elderly patients with DPN displayed worse fingertip pinch strength, especially in thumb-middle fingertip pinch strength, thumb-ring fingertip pinch strength, and thumb-little fingertip pinch strength in both dominant and nondominant hands. Weakness in pinch strength may affect the dexterity of the patient's hands.

Sensory function is an important part of hand function. In the past reports, DPN caused sensory impairments such as pain, decreased vibration sensation, and loss of tactile sensation [21, 22]. Sensory function is closely related to peripheral nerves. SWME is often used to assess the tactile sensation in patients with DPN [23]. In our study, there were no significant differences between the SWME assessment results of the DPN group and the non-DPN group. A

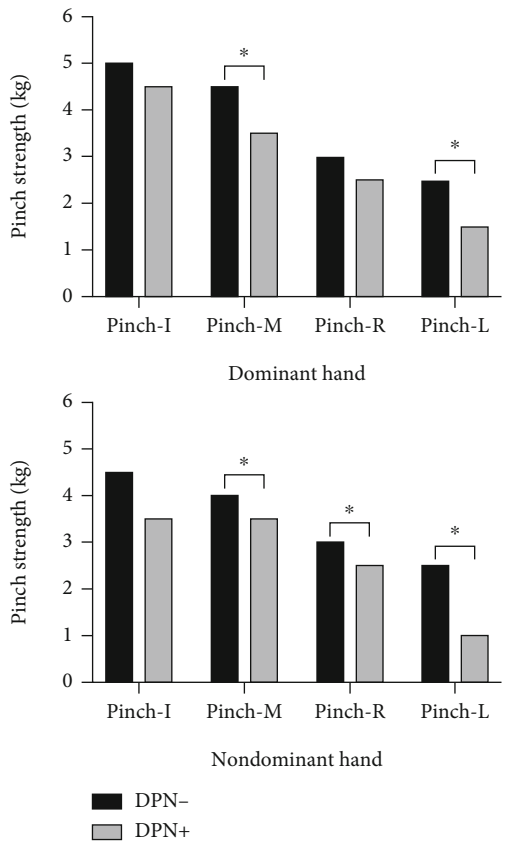


Figure 4: Differences in pinch strength between the thumb and the other four fingers in both hands. Pinch-I: thumb-index fingertip pinch strength; Pinch-M: thumb-middle fingertip pinch strength; Pinch-R: thumb-ring fingertip pinch strength; Pinch-L: thumb-little fingertip pinch strength. *A $p$ value < 0.05 was considered to indicate statistical significance.

possible explanation for this might be that the degree of upper and lower limb nerve damage was not consistent. Liu et al. performed EMG assessment on 700 DPN patients and found that the nerve conduction abnormality in the lower limbs was more serious than that in the upper limbs [24]. In our study, we found that peripheral nerves in the lower limbs seem to be more likely to be affected (Table 2). This suggests that peripheral neuropathy in the upper limbs of DPN patients was not serious compared with that in the lower limbs. Moreover, the tactile sensation assessed by SWME pertains to large-fiber function [23]. In the early stage of DPN development, the small fibers of the peripheral nerves are damaged first, followed by gradual damage in the large fibers of the nerve [25, 26]. This also may explain why SWME could not accurately assess the hand tactile sensation in DPN patients.

Grip strength is a measure of upper limb performance and is closely related to muscle strength, which is considered an important component of physical fitness and a convenient but powerful predictor of disability, morbidity, and mortality in the elderly population [27–29]. The results of this study showed no significant differences in hand grip strength between the DPN group and the non-DPN group. This is consistent with the results of Lima et al., which showed that mild to moderate DPN had no significant effect on maximum hand grip strength [30]. The reason for this result might be due to factors such as the older age and the longer diabetes duration in the two groups. In addition, sarcopenia, which is caused by risk factors such as diabetes, high blood pressure, and dyslipidemia, leads to a decrease in skeletal muscle mass, muscle strength, and physical function in older adults [31]. Compared with DPN, sarcopenia might have a greater impact on grip strength.

Pinch strength is the most frequently used hand motor function in activities of daily living, and it is also an important part of hand function. Good pinch strength is conducive to the fine motor movements of the hands. In this study, a fingertip-type pinch strength measurement method was used, and it was found that the hand pinch strength performance of the DPN group was worse than that of the non-DPN group, especially the thumb-middle fingertip pinch strength, thumb-ring fingertip pinch strength, and thumb-little fingertip pinch strength in both hands (Figure 4). This difference might be due to skeletal muscle atrophy caused by distal peripheral neuropathy, which may lead to the decrease in hand pinch strength in DPN patients. In a prior study, Anderson et al. performed MRI on the lower leg muscles of DPN patients and found that distal muscle atrophy was the most obvious [32]. This kind of skeletal muscle atrophy caused by peripheral neuropathy may be present not only in the lower limbs but also in the upper limbs and hands.

Reduced hand dexterity will directly affect the hand function of the elderly and indirectly lead to the decline in activities of daily living. In this study, we tested hand dexterity using PPT and found no differences between the two groups when DPN patients performed relatively simple hole-filling tasks. When patients performed assembly activities, the DPN group was worse than the non-DPN group (Figure 5). This result might be explained by the fact that the pinch strength of the patient's hand was decreased, which affected the fine movement and dexterity of the DPN patients' hands. In addition, there is evidence that the cognitive function of DPN patients is worse, mainly in executive function, which may affect the patient's left-right coordination [33]. Because the PPT test requires the patient to have a certain level of cognitive function (executive function) to complete the assembly, the assembly task performance of the DPN group was worse.

In our clinical work, although the lower limb dysfunction of DPN patients was prominent, function problems in the upper limbs and hands could not be ignored. In the future rehabilitation training, the sensory and motor functions of the hands of patients with DPN deserve clinical attention by therapists. In particular, focusing on the patient's hand muscle strength and dexterity may improve the patient's quality of life. There are some limitations in this study. The sample is small and a cross-sectional study with a single source of cases. Therefore, the results obtained may be biased and relatively limited. In the future, large-sample, multicenter research will need to be carried out, and a control group will be set up. In addition, sensory assessment was relatively narrow. We focused only on the tactile sensation of DPN

Table 4: Comparison of the scores on the Purdue Pegboard Test (PPT) between the two groups.

| | DPN group (DPN+) | Non-DPN group (DPN-) | $t$ | $p$ |
|---|---|---|---|---|
| PPT (dominant hand) | 8.88 ± 1.90 | 9.37 ± 2.05 | 0.890 | 0.378 |
| PPT (nondominant hand) | 8.56 ± 2.22 | 9.04 ± 1.56 | 0.903 | 0.371 |
| PPT (both hands) | 5.04 ± 1.59 | 5.63 ± 1.52 | 1.364 | 0.179 |
| PPT (assembly) | 13.96 ± 5.18 | 16.96 ± 4.61 | 2.212 | 0.032* |

Data were expressed the mean ± standard deviation. *A $p$ value < 0.05 was considered to indicate statistical significance.

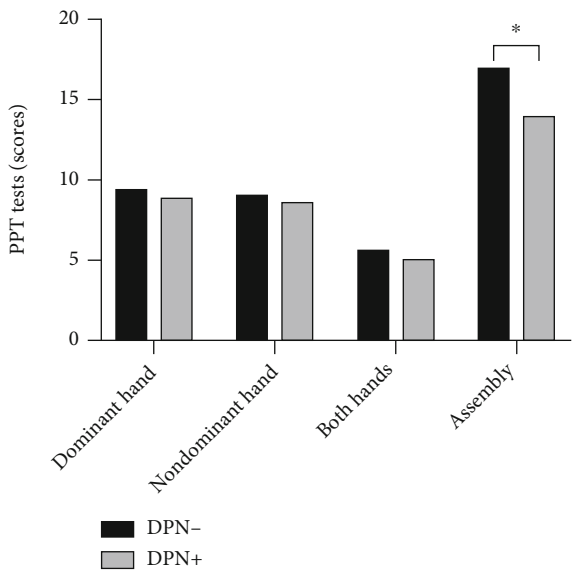


Figure 5: Differences between the two Purdue Pegboard Tests (PPT). *A $p$ value < 0.05 was considered to indicate statistical significance.

patients and did not assess patients' temperature sensation, vibration sensation, and two-point discrimination.

## 5. Conclusions

In the elderly, limited motor function is the main hand dysfunction in patients with DPN, which is mostly manifested as a decline of fingertip pinch strength and decrease in hand dexterity.

## Data Availability

Datasets analyzed during the current study are available from the corresponding author on reasonable request.

## Conflicts of Interest

The authors declare that they have no conflicts of interest.

## Authors' Contributions

Yifang Lin has equal contribution as the first author.

## Acknowledgments

We would like to thank all volunteers for their participation in the study. The study was supported by the National Key Research & Development Program of the Ministry of Science and Technology of the People's Republic of China (Grant numbers 2018YFC2002300 and 2018YFC2002301) and the National Natural Science Foundation of China Major Research Programs (Grant numbers 9194830003 and 82021002).

## References

[1] P. Saeedi, I. Petersohn, P. Salpea et al., "Global and regional diabetes prevalence estimates for 2019 and projections for 2030 and 2045: results from the International Diabetes Federation Diabetes Atlas, 9th edition," *Diabetes Research and Clinical Practice*, vol. 157, p. 107843, 2019.

[2] R. C. W. Ma, "Epidemiology of diabetes and diabetic complications in China," *Diabetologia*, vol. 61, no. 6, pp. 1249–1260, 2018.

[3] Z. Iqbal, S. Azmi, R. Yadav et al., "Diabetic peripheral neuropathy: epidemiology, diagnosis, and pharmacotherapy," *Clinical Therapeutics*, vol. 40, no. 6, pp. 828–849, 2018.

[4] L. L. Määttä, M. Charles, D. R. Witte et al., "Prospective study of neuropathic symptoms preceding clinically diagnosed diabetic polyneuropathy: addition-Denmark," *Diabetes Care*, vol. 42, no. 12, pp. 2282–2289, 2019.

[5] S. Tesfaye and D. Selvarajah, "Advances in the epidemiology, pathogenesis and management of diabetic peripheral neuropathy," *Diabetes/Metabolism Research and Reviews*, vol. 28, pp. 8–14, 2012.

[6] P. J. Watkins and P. K. Thomas, "Diabetes mellitus and the nervous system," *Journal of Neurology, Neurosurgery & Psychiatry*, vol. 65, no. 5, pp. 620–632, 1998.

[7] N. Ramji, C. Toth, J. Kennedy, and D. W. Zochodne, "Does diabetes mellitus target motor neurons?," *Neurobiology of Disease*, vol. 26, no. 2, pp. 301–311, 2007.

[8] R. H. Dworkin, A. B. O. Connor, M. Backonja et al., "Pharmacologic management of neuropathic pain: evidence-based recommendations," *Pain*, vol. 132, no. 3, pp. 237–251, 2007.

[9] M.-M. Backonja and B. Stacey, "Neuropathic pain symptoms relative to overall pain rating," *The Journal of Pain*, vol. 5, no. 9, pp. 491–497, 2004.

[10] M. R. Khdour, "Treatment of diabetic peripheral neuropathy: a review," *Journal Of Pharmacy And Pharmacology*, vol. 72, no. 7, pp. 863–872, 2020.

[11] S. Kalra and S. K. Sharma, "Diabetes in the elderly," *Diabetes Therapy*, vol. 9, no. 2, pp. 493–500, 2018.

[12] C. Wang, L. Lv, X. Wen et al., "A clinical analysis of diabetic patients with hand ulcer in a diabetic foot centre," *Diabetic Medicine*, vol. 27, no. 7, pp. 848–851, 2010.

[13] M. M. T. M. Win, K. Fukai, H. H. Nyunt, Y. Hyodo, and K. Z. Linn, "Prevalence of peripheral neuropathy and its impact on activities of daily living in people with type 2 diabetes mellitus," *Nursing & Health Sciences*, vol. 21, no. 4, pp. 445–453, 2019.

[14] S. Gundmi, A. G. Maiya, A. K. Bhat, N. Ravishankar, M. H. Hande, and K. V. Rajagopal, "Hand dysfunction in type 2 diabetes mellitus: systematic review with meta-analysis," *Annals of physical and rehabilitation medicine*, vol. 61, no. 2, pp. 99–104, 2018.

[15] S. L. Ennis, M. P. Galea, D. N. O. Neal, and M. J. Dodson, "Peripheral neuropathy in the hands of people with diabetes mellitus," *Diabetes Research and Clinical Practice*, vol. 119, pp. 23–31, 2016.

[16] K. Bell, J. Tomancik, and E. Tomancik, "The Repeatability of Testing with Semmes-Weinstein Monofilaments," *The Journal of Hand Surgery*, vol. 12, no. 1, pp. 151–161, 1987.

[17] C.-J. Yang, H.-Y. Hsu, C.-H. Lu, Y.-L. Chao, H.-Y. Chiu, and L.-C. Kuo, "The associations among hand dexterity, functional performance, and quality of life in diabetic patients with neuropathic hand from objective-and patient-perceived measurements," *Quality of Life Research*, vol. 24, no. 1, pp. 213–221, 2015.

[18] D. Selvarajah, D. Kar, K. Khunti et al., "Diabetic peripheral neuropathy: advances in diagnosis and strategies for screening and early intervention," *The Lancet Diabetes & Endocrinology*, vol. 7, no. 12, pp. 938–948, 2019.

[19] J. D. England, G. S. Gronseth, G. Franklin et al., "Distal symmetrical polyneuropathy: a definition for clinical research. A report of the American Academy of Neurology, the American Association of Electrodiagnostic Medicine, and the American Academy of Physical Medicine and Rehabilitation," *Archives Of Physical Medicine And Rehabilitation*, vol. 86, no. 1, pp. 167–174, 2005.

[20] I. Höliner, "Validity of the neurological examination in diagnosing diabetic peripheral neuropathy," *Pediatric Neurology*, vol. 49, no. 3, pp. 171–177, 2013.

[21] T. S. Jensen, "New perspectives on the management of diabetic peripheral neuropathic pain," *Diabetes and Vascular Disease Research*, vol. 3, no. 2, pp. 108–119, 2006.

[22] T. R. M. Santos, J. V. Melo, N. C. Leite, G. F. Salles, and C. R. L. Cardoso, "Usefulness of the vibration perception thresholds measurement as a diagnostic method for diabetic peripheral neuropathy: results from the Rio De Janeiro type 2 diabetes cohort study," *Journal of Diabetes and its Complications*, vol. 32, no. 8, pp. 770–776, 2018.

[23] N. Kamei, K. Yamane, S. Nakanishi et al., "Effectiveness of Semmes-Weinstein monofilament examination for diabetic peripheral neuropathy screening," *Journal of Diabetes and its Complications*, vol. 19, no. 1, pp. 47–53, 2005.

[24] M. S. Liu, B. L. Hu, L. Y. Cui, X. F. Tang, H. Du, and B. H. Li, "Clinical and neurophysiological features of 700 patients with diabetic peripheral neuropathy," *Zhonghua Nei Ke Za Zhi*, vol. 44, no. 3, pp. 173–176, 2005.

[25] R. Pop-Busui, "Diabetic neuropathy: a position statement by the American Diabetes Association," *Diabetes Care*, vol. 40, no. 1, pp. 136–154, 2017.

[26] I. N. Petropoulos, G. Ponirakis, A. Khan, H. Almuhannadi, H. Gad, and R. A. Malik, "Diagnosing diabetic neuropathy: something old, something new," *Diabetes & Metabolism Journal*, vol. 42, no. 4, pp. 255–269, 2018.

[27] M. Visser, A. B. Newman, M. C. Nevitt et al., "Reexamining the sarcopenia hypothesis: muscle mass versus muscle strength," *Annals of the New York Academy of Sciences*, vol. 904, no. 1, pp. 456–461, 2000.

[28] A. J. Mayhew, L. E. Griffith, A. Gilsing, M. K. Beauchamp, A. Kuspinar, and P. Raina, "The association between self-reported and performance-based physical function with activities of daily living disability in the Canadian Longitudinal Study on Aging," *The Journals of Gerontology: Series A*, vol. 75, no. 1, pp. 147–154, 2020.

[29] D. Vancampfort, B. Stubbs, J. Firth, and A. Koyanagi, "Handgrip strength, chronic physical conditions and physical multimorbidity in middle-aged and older adults in six low- and middle income countries," *European Journal of Internal Medicine*, vol. 61, pp. 96–102, 2019.

[30] A. Limade, K. Carvalho, L. D. S. Borges, E. Hatanaka, L. C. Rolim, and P. B. de Freitas, "Grip force control and hand dexterity are impaired in individuals with diabetic peripheral neuropathy," *Neuroscience Letters*, vol. 659, pp. 54–59, 2017.

[31] L.-K. Chen, J. Woo, P. Assantachai et al., "Asian Working Group for Sarcopenia: 2019 Consensus update on sarcopenia diagnosis and treatment," *Journal of the American Medical Directors Association*, vol. 21, pp. 300–307, 2020.

[32] H. Andersen, P. C. Gadeberg, B. Brock, and J. Jakobsen, "Muscular atrophy in diabetic neuropathy: a stereological magnetic resonance imaging study," *Diabetologia*, vol. 40, no. 9, pp. 1062–1069, 1997.

[33] J. L. Rucker, S. D. Jernigan, J. M. McDowd, and P. M. Kluding, "Adults with diabetic peripheral neuropathy exhibit impairments in multi-tasking and other executive functions," *Journal of neurologic physical therapy: JNPT*, vol. 38, no. 2, pp. 104–110, 2014.

Hindawi
Neural Plasticity
Volume 2021, Article ID 6678863, 8 pages
https://doi.org/10.1155/2021/6678863

*Research Article*

# Restoration of Deafferentation Reduces Tinnitus, Anxiety, and Depression: A Retrospective Study on Cochlear Implant Patients

**Juanmei Yang**,[1,2,3,4] **Jing Song**,[1,2,3,4] **Xiang Zhao**,[5] **Carol Pang**,[6] **Ning Cong**,[2,3,4] **and Zhao Han**[7]

[1]*Department of Otology and Skull Base Surgery, Eye Ear Nose and Throat Hospital, Fudan University, Shanghai 200031, China*
[2]*Shanghai Clinical Medical Center of Hearing Medicine, Shanghai 200031, China*
[3]*Key Laboratory of Hearing Medicine of National Health Commission of the People's Republic of China, Shanghai 20031, China*
[4]*Research Institute of Otolaryngology, Fudan University, Shanghai 200031, China*
[5]*Department of Traditional Chinese Medicine, Shandong Zaozhuang Municipal Hospital, Shandong Zaozhuang 277100, China*
[6]*Audiology, Speech & Medical Research Institute, Nurotron Biotechnology Co., Ltd, Hangzhou 310011, China*
[7]*Department of Otorhinolaryngology, Huadong Hospital Affiliated with Fudan University, 200040, No. 221 West Yan'an Road, Jing An District, Shanghai, China*

Correspondence should be addressed to Ning Cong; congningent@126.com and Zhao Han; sfhanzao@163.com

Received 31 October 2020; Revised 7 May 2021; Accepted 15 June 2021; Published 25 June 2021

Academic Editor: Jianguang Xu



Patients with profound bilateral deafness (BD) are prone to suffering from tinnitus, which further leads to psychological comorbidities and makes it more difficult for patients to communicate with people. This study was aimed at investigating the effect of cochlear implants (CIs) on tinnitus distress and psychological comorbidities in patients with profound BD. This multicenter retrospective study reviewed 51 patients with severe postlingual BD who underwent cochlear implantation; 49 patients underwent unilateral cochlear implantation, and 2 patients underwent bilateral cochlear implantation. The patients were asked to complete all the questionnaires, including the tinnitus handicap inventory (THI), the visual analog scale (VAS) score, the Hospital Anxiety and Depression Scale Questionnaire (HADS), the Categories of Auditory Performance (CAP), and the Speech Intelligibility Rating (SIR), at least 4 months after implantation when the CI was on or off, in approximately May-June 2019. In our study, 94% (48/51) of BD patients suffered from tinnitus before CI, and 77% (37/48) of them suffered from bilateral tinnitus. In addition, 50.9% (26/51) of the CI patients were suffering from anxiety, 52.9% (27/51) of them were suffering from depression (score ≥ 8), and 66.7% (34/51) (27/51) of them were suffering from anxiety or depression. Cochlear implantation could reduce tinnitus more obviously when the CI was on than when the CI was off. Cochlear implantation also reduced anxiety/depression severity. There were significantly positive correlations between tinnitus severity and anxiety/depression severity before and after surgery. Moreover, hearing improvement is positively correlated with reduction level of tinnitus, the better hearing, and the lesser severity of tinnitus. Thus, along with effective restoration of deafferentation, cochlear implantation shows positive therapeutic effects on tinnitus and psychological comorbidities, providing a reference for future clinical and research work.

## 1. Introduction

Tinnitus, which literally means "ringing in the ears," is defined by the perception of sound or noise in the absence of an external physical sound source. The prevalence of tinnitus in adults is 10-15%. In the affected subgroup of patients, it causes extreme distress with far-reaching consequences for daily activities and quality of life [1]. In addition, tinnitus can cause an overall perceived handicap that can include hearing difficulties, anxiety, depression, inability to relax, and sleep difficulties [2]. In sensorineural hearing-impaired patients, tinnitus has a higher prevalence, but this association is not simple or straightforward because some people with troublesome tinnitus have audiometrically normal hearing;

conversely, many people with hearing loss do not report tinnitus [1, 3].

Cochlear damage is a trigger factor for tinnitus. Tinnitus is generated by a series of changes in central auditory pathways, such as the cochlear nucleus (CN), inferior colliculus (IC), the medial geniculate body (MGB), and auditory cortex (AC) to compensate for the loss of this input when the electrical input of the cochlea decreases or disappears [4]. Based on the tinnitus mechanism by which injury to the peripheral auditory system induces plasticity in the auditory central system, many treatment algorithms, including sound therapy, try to recorrect plasticity and restore hearing loss with hearing aids to reduce tinnitus [1, 5]. Cochlear implantation involves the surgical placement of an electrode array within the cochlea to stimulate spiral ganglion cells electrically to convey auditory information [6]. Recently, cochlear implants have been used more frequently to restore deafferentation in profound single-side or bilateral postlingual deafness patients [7–11]. The prevalence rates of tinnitus in postlingual profound BD patients in previous studies are different, ranging from 67% to 86% in cochlear implant (CI) candidates ([7, 10–14]). Although many reports have explored the relationships between CI and tinnitus/depression/anxiety, it is still controversial whether CI may induce or reduce tinnitus distress [11, 12, 15]. This study was aimed at investigating the influence of restoring deafferentation with cochlear implants (CIs) on tinnitus distress and psychological comorbidities in profound BD patients. Fifty-one CI participants with postlingually acquired profound BD were involved in this retrospective study. We investigated the severity of tinnitus, anxiety, and depression before and after CI surgery according to different questionnaires to explore the response of postlingually profound BD patients who receive cochlear implants which will provide clues regarding the tinnitus mechanism and provide directions for the treatment of tinnitus.

## 2. Patients and Methods

This study was performed at multiple centers over a period of approximately 6 years (2013.9.16-2019.6.6). Fifty-one adult patients with acquired bilateral profound deafness were enrolled in the study, which was approved by the local ethics committee. The main inclusion criteria were adult CI patients with profound bilateral hearing loss, intact auditory nerves, and no obvious malformation of the cochlea.

The patients were asked to complete all the questionnaires at least 4 months after implantation. There were 24 males and 27 females. The mean age at the time of implantation was $41.0 \pm 17.0$ years (range 19.0–74.0 years). The mean duration of deafness before implantation was $8.0 \pm 7.2$ years (range 0.5–27 years). The mean time post-CI at the moment of completing the questionnaire was $18.0 \pm 16.7$ months (range 3–69 months). The cochlear type for every patient was the Nurotron (CS-10A). Two of the patients (2/51) received bilateral CIs (49/51), and the others received unilateral CIs. A postoperative X-ray was taken to verify successful intracochlear electrode insertion for each patient. Thirty-two patients had worn hearing aids before CI (15 bilaterally and 17 unilaterally). Nineteen patients had not worn hearing aids before CI. Student's $t$-test and ANOVA were used to assess VAS, THI, HAD, CAP, and SIR scores before and after CI. Statistical significance was defined as $^{*}p < 0.05$ and $^{**}p < 0.01$. The relationship between hearing ability and scores from the questionnaires was tested using Spearman's correlation test.

*2.1. Tinnitus Handicap Inventory (THI) and Visual Analog Scale (VAS) Score.* The THI is an internationally validated tinnitus scoring questionnaire developed by Newman et al. in 1996 [16]. It consists of 25 questions with the purpose of evaluating the functional, emotional, and catastrophic effects of tinnitus. The three choices for each question are "Yes," "Occasionally," and "No," and scores of 4, 2, and 0 are applied to the choices. The CI recipients were required to select one choice among the three recipients. They were also asked to complete the THI to assess their tinnitus impact on their psychology and activities of daily living. There were five tinnitus severity levels determined by the total score: slight (0–16), mild (18–36), moderate (38–56), severe (58–76), or catastrophic (78–100).

The VAS was used to evaluate the severity of tinnitus at the same time as the THI was assessed [17]. The patients were asked to complete both questionnaires with the CI device on and off. Patients were asked to mark a single point between 0 and 10 to indicate their feelings. For example, the question of satisfaction for CI sounds was evaluated for whether tinnitus interfered with the listening effect of the CI. A score of 10 on the scale was identified as "too noisy and annoying," and a score of 0 suggested "absolutely clear and satisfying."

*2.2. Hospital Anxiety and Depression Scale Questionnaire (HADS).* A hearing handicap and chronic tinnitus can be associated with depressive symptoms such as anxiety or emotions such as helplessness. We used the translated and validated Dutch version of the Hospital Anxiety and Depression Scale (HADS). The HADS questionnaire assessed the presence and severity of mild and even subsyndrome degrees of anxiety and depression [18, 19]. The questionnaire contains 14 items, i.e., 7 about anxiety and 7 about depression. Patients answered the questions on a scale of 0–3. Subscale scores can be calculated for anxiety and depression. Scores below 7 indicate neither an anxiety nor a depression problem, scores between 8 and 10 suggest a potential anxiety or depression disorder, and scores beyond 11 indicate definite cases of anxiety or depression. The scores of the two subscales of anxiety and depression were as follows: 0-7 was negative; 8-10 was mild; 11-14 was classified as moderate; and 15-21 was classified as severe. Studies have found that the HADS has good reliability and validity. Taking 9 points as the critical value of anxiety and depression yielded good sensitivity and specificity. Therefore, the use of this critical point is recommended.

*2.3. Categories of Auditory Performance (CAP) and Speech Intelligibility Rating (SIR).* Categories of Auditory Performance (CAP) and the Speech Intelligibility Rating (SIR) were

developed by the University of Nottingham for the assessment of children's daily auditory and speech ability [20] and have been widely used in the assessment of the effect of speech rehabilitation after cochlear implantation in young children [21]. In this study, we used this tool to evaluate adult patients. For each patient, the measures were assessed at least 4 months after CI surgery. The higher the score, the better the auditory comprehension and the better the speech recognition.

*2.4. Statistical Analyses.* All data were analyzed using SPSS 18.0 (SPSS Inc., Chicago, IL, USA). Normal distribution of the data was verified with the Kolmogorov–Smirnov test. Student's $t$-test and ANOVA were used to assess the VAS, THI, HAD, CAP, and SIR scores before and after CI with the device on and off. Statistical significance was defined as $^{*}p < 0.05$ and $^{**}p < 0.01$. The relationships between hearing ability and scores from the questionnaires were tested using Spearman's correlation test.

## 3. Results

*3.1. Characteristics of the CI Patients.* Fifty-one postlingual profound BD patients (27 women, 24 men) in this study were implanted with a multichannel cochlear implant manufactured by Nurotron. Surgeries were performed between 2013 and 2019. The mean age at the time of implantation was 41.0 ± 17.0 years old (range 19.0-74.0 years old). The mean duration of deafness before implantation was 8.0 ± 7.2 years (range 0.5-27 years). The mean time post-CI at the moment of completing the questionnaire was 18.0 ± 16.7 months (range 3-69 months). The other preoperative characteristics are shown in Table 1 and Figure 1.

*3.2. Most of the Profound BD CI Candidates with Tinnitus Also Suffered from Anxiety and Depression Distress before CI.* According to our results, 94% (48/51) of the CI patients suffered from tinnitus before CI surgery, and 77.1% (37/48) of them had bilateral tinnitus. The average THI scores were 48.3 ± 22.2 in males and 57.3 ± 29.9 in females, and there was no significant difference between the male and female patients ($p = 0.24$). The THI scores showed that 2% of them (1/48) were suffering from only slight tinnitus (0-16), 25.5% (14/48) were suffering from mild tinnitus (18-36), 19.6% (10/48) were suffering from moderate tinnitus (38-56), 23.5% (12/48) were suffering from severe tinnitus (58-76), and 21.6% (11/48) were suffering from catastrophic tinnitus (78-100). The proportion of CI patients with severe and catastrophic tinnitus before CI surgery was 45.1%. The etiology of deafness of CI candidates includes drug induced (27%, 14/51), sudden hearing loss (16%, 8/51), presbycusis (6/51, 12%), infective (3/51, 6%), hereditary (2/51, 4%), traumatic (1/51, 2%), congenital (1/51, 2%), sound exposure (1/51, 2%), and unknown reason (15/51, 29%) shown in Figure 1.

In addition, according to our results, 50.9% (26/51) of the CI patients suffered from anxiety before CI surgery (≥8), 84.6% (22/26) were at a mild level (8-10), and 15.4% (4/26) were at a moderate level (11-14). Overall, 52.9% (27/51) of the CI patients were suffering from depression before CI surgery, with 51.9% (14/27) of them exhibiting mild depression (8-10), 44.4% (12/27) moderate depression (11-14), and 3.4% (1/27) severe depression (15-21); 37.2% (19/51) of CI candidates experienced both anxiety and depression. The detailed characteristics are shown in Table 1.

Table 1: Preoperative characteristics of CI candidates.

| Preoperative characteristics | |
|---|---|
| Characteristics | Sum $n = 51$ |
| Male : female, No. | 24 : 27 |
| Age at CI | 41.0 ± 17.0 (19-74) |
| Hearing aid use proportion before CI (%) | 60.8% (31/51) |
| Mean duration of severe deafness before CI (years) | 8.0 ± 7.2 (0.5-27) |
| Tinnitus proportion before CI (%) | 94.1% (48/51) |
| Catastrophic (78–100) | 22.9% (11/48) |
| Severe (58–76) | 25% (12/48) |
| Moderate (38–56) | 20.8% (10/48) |
| Mild (18–36) | 29.2% (14/48) |
| Light (0–16) | 2% (1/48) |
| Anxiety proportion before CI ($A \geq 8$) | 51% (26/51) |
| Depression proportion before CI ($D \geq 8$) | 52.9% (27/51) |
| Anxiety or depression proportion before CI ($D \geq 8$) | 66.6% (34/51) |

*3.3. The Relationships between Depression/Anxiety Levels and Tinnitus Severity Levels.* Pearson's relative statistic was used to test the relationships between tinnitus severity levels and depression/anxiety levels. The results showed that the THI score was positively correlated with depression and anxiety scores before CI surgery ($p < 0.01$, $n = 51$, bilateral), and the THI score was positively correlated with depression scores after CI surgery ($p < 0.01$, $n = 51$, bilateral). However, there was no correlation between the THI score and the anxiety score after CI surgery ($p = 0.06$) (Table 2).

*3.4. Tinnitus, Depression, and Anxiety Could Be Suppressed in Profound BD Patients after CI.* The tinnitus prevalence rates of CI patients were 94% (48/51) before CI and 98% (50/51) after CI when the device is off and 94% (48/51) when the device is on. It is worth noting that tinnitus disappeared after CI in 3 patients when the CI device is on (CI on) and in 1 patient when the CI device is off (CI off). We also found that 3 patients without tinnitus before surgery suffered from tinnitus after CI.

The preoperative average THI score was 53.1 ± 27.5, and the postoperative average THI scores were 43.2 ± 26.2 (CI off) and 29.1 ± 21.3 (CI on). For the average THI score, there was no significant difference between preoperative and CI-off scores ($p = 0.06$), but there was a significant difference between preoperative and CI-on scores ($p < 0.01$). Additionally, there was a significant difference between CI-on and CI-off scores ($p < 0.01$). In other words, tinnitus improvements of all CI patients were more obvious when the CI was on than off (see Table 3).

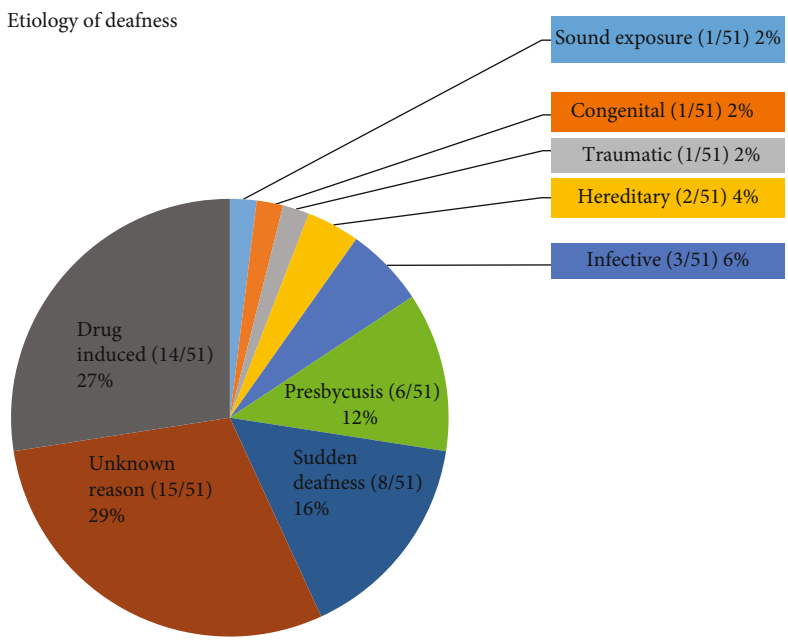


Figure 1: Etiology of deafness of CI candidates.

Table 2

| Relationships between depression/anxiety level and tinnitus level | | | | | |
|---|---|---|---|---|---|
| Pre-CI | THI | *A* | Post-CI | THI | *A* |
| Pearson relative | 1 | 0.576** | Pearson relative | 1 | 0.264 |
| *p* | 0.001** | | *p* | 0.061 | |
| Pre-CI | THI | *D* | Post-CI | THI | *D* |
| Pearson relative | 1 | 0.622** | Pearson relative | 1 | 0.377** |
| *p* | 0.001** | | *p* | 0.006** | |

**Significant correlation at the 0.01 level (bilateral).

To obtain more details, further comparisons among patients were conducted according to different levels of tinnitus. For patients with catastrophic tinnitus, the average THI score decreased from $90.4 \pm 7.1$ preoperatively to $66.7 \pm 31.4$ with the CI off and $39.8 \pm 32.2$ with the CI on. There was a significant difference between the THI score of preoperative and CI-on conditions ($p < 0.01$) and between the preoperative and CI-off conditions ($p = 0.02$). There was no significant difference between CI-on and CI-off conditions ($p = 0.06$) (see Table 3).

For the patients with severe tinnitus, the average THI score decreased from $67.7 \pm 6.1$ preoperatively to $54.8 \pm 21.1$ postoperatively with the CI off and $35.8 \pm 20.1$ with the CI on. There was a significant difference between the THI score of preoperative and CI-on conditions ($p < 0.01$), and there was a significant difference between the CI-on and CI-off conditions ($p = 0.03$). However, there was no significant difference between the preoperative and postoperative scores of CI-off condition ($p = 0.06$) (see Table 3).

For the patients with moderate tinnitus, the average THI score decreased from $48.4 \pm 6.1$ preoperatively to $42.4 \pm 8.1$ postoperatively with the CI off and $32.6 \pm 12.9$ with the CI on. For the THI score, there was a significant difference between the preoperative and CI-on conditions ($p < 0.01$), there was no significant difference between the CI-on and CI-off conditions ($p = 0.06$), and there was no significant difference between the preoperative and postoperative CI groups when the CI was off ($p = 0.08$) (see Table 3).

For the patients with mild tinnitus, the average THI score decreased from $29.0 \pm 5.0$ preoperatively to $18.6 \pm 9.1$ postoperatively when the CI was off; when the CI was on, the average THI score was $13.8 \pm 8.4$. For the THI score, there was a significant difference between the preoperative and CI-on conditions ($p < 0.01$), there was no significant difference between the CI-on and CI-off conditions ($p = 0.1$), and there was a significant difference between the preoperative and postoperative CI groups when the CI was off ($p < 0.01$) (see Table 3).

For patients with slight tinnitus or no tinnitus (4/48) before surgery, the THI score increased from 12 preoperatively to 20 postoperatively when the CI was off and to 28 when the CI was on in one of the patients; for the other 3 patients without tinnitus before CI, the THI score increased from 0 to 12, 38, and 58, respectively, when the CI was off

Table 3

| Type (%) | THI and VAS scores before and after CI | | | |
|---|---|---|---|---|
| | Pre-CI (A) (%) | Post-CI off (B) (%) | Post-CI on (C) (%) | $p^{*}$ $p^{**}$ |
| Overall THI | 53.1 ± 27.5<br>94% (48/51) | 43.2 ± 26.2<br>98% (50/51) | 29.1 ± 21.3<br>94% (48/51) | A&B $p = 0.06$<br>B&C $p < 0.01^{**}$<br>A&C $p < 0.01^{**}$ |
| Catastrophic (78–100) | 90.4 ± 7.1<br>22.9% (11/48) | 66.7 ± 31.4<br>12% (6/50) | 39.8 ± 32.2<br>4.2% (2/48) | A&B $p = 0.02^{*}$<br>B&C $p = 0.06$<br>A&C $p < 0.01^{**}$ |
| Severe (58–76) | 67.7 ± 6.1<br>25% (12/48) | 54.8 ± 21.1<br>24% (12/50) | 35.8 ± 20.1<br>12.5% (6/48) | A&B $p = 0.06$<br>B&C $p = 0.03^{*}$<br>A&C $p < 0.01^{**}$ |
| Moderate (38–56) | 48.4 ± 6.1<br>20.8% (10/48) | 42.4 ± 8.1<br>20% (10/50) | 32.6 ± 12.9<br>14.6% (7/48) | A&B $p = 0.08$<br>B&C $p = 0.056$<br>A&C $p < 0.01^{**}$ |
| Mild (18-36) | 29.0 ± 5.0<br>29.2% (14/48) | 18.6 ± 9.1<br>22% (11/50) | 13.8 ± 8.4<br>35.4% (17/48) | A&B $p < 0.01^{**}$<br>B&C $p = 0.1$<br>A&C $p < 0.01^{**}$ |
| Light (0-16) | 12<br>2% (1/48) | 32 ± 38.2<br>22% (11/50) | 26 ± 10.7<br>33.3% (16/48) | A&B $p = 0.03^{*}$<br>B&C $p = 0.62$<br>A&C $p < 0.01^{**}$ |
| VAS | 3.9 ± 3.1 | 2.6 ± 2.8 | 1.7 ± 2.2 | A&B $p = 0.06$<br>B&C $p = 0.02^{*}$<br>A&C $p < 0.01^{**}$ |

and to 12, 26, and 38, respectively, when the CI was on (see Table 3).

Although the prevalence rate of tinnitus is similar before and after CI, the tinnitus severity level decreased significantly after CI. The proportion of catastrophic tinnitus in the patients was reduced from 22.9% (11/48) preoperatively to 12% (6/50) when CI device was off and to 4.2% (2/48) when CI device was on. The proportion of severe tinnitus in the patients was reduced from 25% (12/48) preoperatively to 24% (12/50) when CI device was off and to 12% (5/48) when CI device was on. The proportion of moderate tinnitus in the patients was 20.8% (10/48) preoperatively and to 20% (10/50) when CI device was off and to 14.6% (7/48) when CI device was on. The proportion of mild tinnitus in the patients was 29.2% (14/48) preoperatively and to 22% (11/50) when CI device was off and to 35.4% (17/48) when CI device was on. The proportion of slight tinnitus in the patients was 2% (1/48) preoperatively and to 22% (11/50) when CI device was off and to 33.3% (16/48) when CI device was on.

According to the VAS results, the preoperative average VAS score was 3.9 ± 3.1, and the postoperative average VAS scores were 2.6 ± 2.8 when the CI device was off and 1.7 ± 2.2 when the CI device was on. There was no significant difference between the CI-off group and the preoperative group ($p = 0.06$). Meanwhile, there was a significant difference between the CI-on group and the preoperative group ($p < 0.01$), and there was a significant difference between the CI-on group and the CI-off group ($p = 0.02$) (see Table 3).

*3.5. CI Could Reduce Anxiety and Depression Levels in Profound BD Patients.* Before CI surgery, 50.9% (26/48) of the CI patients suffered from anxiety, and 52.9% (27/48) of them suffered from depression. After CI surgery, 73.1% (19/26) of patients who suffered from anxiety preoperatively reported anxiety scores within negative (no anxiety) range ($A < 8$), and 63% (17/27) of patients reported depression scores within negative (no depression) range ($D < 8$). According to our HADS results, the preoperative average anxiety score was 7.2 ± 2.5, and the postoperative average anxiety scores were 5.6 ± 2.6 when the CI device was off and 4.5 ± 2.4 when the CI device was on. There were significant differences between the CI-off group and the preoperative group ($p = 0.003$), the CI-on group and the preoperative group ($p < 0.01$), and the CI-on group and the CI-off group ($p = 0.03$) (see Table 4).

The preoperative average depression score was 7.5 ± 3.7, and the postoperative average anxiety scores were 5.9 ± 3.2

Table 4

| Score | Anxiety and depression scores before and after CI<br>Pre-CI<br>(A) | Post-CI off<br>(B) | Post-CI on<br>(C) | $p^*$<br>$p^{**}$ |
|---|---|---|---|---|
| Anxiety score | 7.2 ± 2.5 | 5.6 ± 2.6 | 4.5 ± 2.4 | A&B $p < 0.01^{**}$<br>B&C $p = 0.03^*$<br>A&C $p < 0.01^{**}$ |
| Depression score | 7.5 ± 3.7 | 5.9 ± 3.2 | 5.3 ± 3.3 | A&B $p = 0.03^*$<br>B&C $p = 0.33$<br>A&C $p < 0.01^{**}$ |

*A*: anxiety score; *D*: depression score.

when the CI device was off and 5.3 ± 3.3 when the CI device was on. There were significant differences between the CI-off group and the preoperative group ($p = 0.02$) and between the CI-on group and the preoperative group ($p = 0.002$). There was no significant difference between the CI-on group and the CI-off group ($p = 0.33$) (see Table 4).

*3.6. The Degree of Hearing Improvement after CI Is Correlated with the Degree of Tinnitus Reduction when the CI Device Is On but Is Not Correlated with Anxiety or Depression.* According to the results summarized in Table 5, the CAP scores were 1.3 ± 1.3 before CI and 4.3 ± 1.3 after CI. There was a significant difference ($p < 0.01$), meaning that hearing was significantly improved after CI. Pearson's relative statistic was used to test the relationship between the hearing improvement degree (CAP) after CI and the tinnitus reduction degree (THI). The degree of hearing improvement after CI was correlated with the degree of tinnitus reduction when the CI device was on ($p < 0.01$), but when the CI was off, there was no significant difference ($p = 0.6$). Thus, the better the hearing improvement was, the less severe the tinnitus. However, there was no relationship between the degree of hearing improvement and the degree of anxiety/depression reduction. For the SIR, there was no difference before and after surgery.

*3.7. Other Relative Relationships.* Pearson's relative statistic was also used to determine the relationship between the Categories of Auditory Performance (CAP) and Speech Intelligibility Rating (SIR), CAP and tinnitus level, CAP and depression/anxiety level, CAP and hearing aid wearing duration, and SIR and hearing aid wearing duration. There were no relationships between these potentially related factors.

Table 5

(a)

| Score | CAP and SIR scores before and after CI<br>Pre-CI | Post-CI on | $p^*, p^{**}$ |
|---|---|---|---|
| CAP | 1.3 ± 1.3 | 4.3 ± 1.3 | $p < 0.01^{**}$ |
| SIR | 4.4 ± 0.8 | 4.5 ± 0.7 | $p = 0.6$ |

(b)

| CAP | Correlation between CAP improve degree and tinnitus reduce degree<br>THI | Pearson relative $r$ | $p$ |
|---|---|---|---|
| (Post- CI -P re-CI) | (Post-CI on- P re-CI) | 0.387 | $p = 0.093^{**}$ |
| (Post- CI -P re-CI) | (Post-CI off - P re-CI) | 0.011 | $p = 0.939$ |

$^{**}$Significant correlation at the 0.01 level.

## 4. Discussion

Patients with profound or severe bilateral deafness have difficulty communicating with others, and some of them suffer from tinnitus, anxiety, and depressive stress. Cochlear implantation is a common treatment for patients with bilateral sensorineural hearing loss, which not only improves hearing but also relieves tinnitus, anxiety, and depression stress [7, 8, 10–15, 22]. Recently, customized music therapy has been shown to be an effective treatment for relieving severity level of chronic tinnitus, but the effect for relieving anxiety and depress is not clear [8].

In this retrospective study, we investigated the influence of cochlear implants on patients with profound bilateral deafness. According to our results, 94% of the CI patients suffered from tinnitus before CI surgery, and 77.1% of them had bilateral tinnitus, which is consistent with previous reports ([7, 12, 22]). The proportion of patients with severe and catastrophic tinnitus before CI surgery was 45.1%. Meanwhile, the proportion of profound BD CI candidates with anxiety and depression was high; 50.9% of them suffered from anxiety before CI surgery, 52.9% of them suffered from depression before CI surgery, and 66.7% of the CI candidates suffered from depression and anxiety. Thus, these factors greatly affect the physical and mental health of bilateral profoundly or severely deaf patients. Therefore, we focused on tinnitus distress and psychological comorbidities in the study.

Regarding the mechanism of tinnitus, it is generally agreed that tinnitus is generated within the brain in response to a reduction in auditory nerve fiber input from the cochlea to the brain. However, deafferentation appears

to be necessary, but not sufficient, to produce tinnitus [5, 24, 25]. Deafferentation can result in tinnitus from the cochlear nucleus (CN) accompanied by homeostatic and timing-dependent plasticity. Thus, the mechanism of tinnitus explains why most tinnitus patients suffer from varying degrees of unilateral or bilateral hearing loss and why many patients with hearing loss do not have tinnitus clinically.

In previous reports, an additional benefit of unilateral cochlear implantation was subjective reduction of tinnitus [7, 10, 12, 22]. Similarly, according to our results, the THI and VAS scores were reduced significantly after CI surgery when the CI device was on. It is also interesting that although 77.1% of CI candidates had bilateral tinnitus, one-sided CI could suppress both unilateral and bilateral tinnitus symptoms. This phenomenon could be explained by the auditory conduction pathway and contributes to the understanding of the lateralization of tinnitus. The CN is the first brain station that receives input from the cochlea and is believed to be the origin of tinnitus. After auditory afferent input to the cochlear nucleus, most of the input signal is transmitted to the contralateral inferior colliculus (IC), and some is transmitted to the ipsilateral IC [5]. Therefore, unilateral CI can reduce tinnitus on both sides (i.e., the contralateral and ipsilateral sides).

Although the reduction in tinnitus was more significant in the CI-on state, we still observed that tinnitus distress was suppressed even when the CI device was off. This is a very interesting phenomenon that provides some clues to the mechanism of tinnitus treatment. Restored deafferentation could explain the reduction in tinnitus in the CI-on state. Auditory input by a CI device could offset deafferentation immediately and reduce tinnitus. After the CI device works repeatedly for a period of time, this counteraction might slowly remodel the auditory center. Therefore, some people may be able to partially compensate, and the plasticity in the auditory center is in a state of homeostasis when even the CI device is turned off. For CI patients with chronic tinnitus that has lasted for decades, their tinnitus could decrease immediately when the CI is on, which gives us great inspiration that we can treat tinnitus even if it has be present for a long time. In our study, 3 BD patients had no tinnitus before CI but had slight or moderate tinnitus after CI, which is also consistent with previous reports that CI could induce tinnitus [12]. For these patients, restored deafferentation may induce remodeled plasticity in the auditory center and then tinnitus. Overall, most CI candidates experience a reduced burden of tinnitus.

In this study, we also investigated the influence of CI on the psychological comorbidities of BD patients. According to our results, 73.1% of patients with anxiety showed suppression of symptoms after CI surgery, and 63% of patients with depression showed suppression of symptoms after CI surgery. It is obvious that CI can suppress anxiety and depression levels. One reason for these changes is that the patients can hear sound and can speak more fluently than before CI surgery; another reason might be that the tinnitus distress is decreased. According to our results, there is a positive correlation between the severity level of anxiety/depression and tinnitus before CI surgery. The postoperative situation is more complicated. There was a positive correlation between the severity level of depression and tinnitus, but there was no correlation between the severity level of anxiety and tinnitus ($p = 0.06$). Tinnitus and anxiety or depression are comorbidities that influence each other. This provided us an important point in the clinical treatment of tinnitus, as we need to treat tinnitus and symptoms of anxiety or depression, including insomnia, at the same time.

In addition, we also explored the relationship between the degree of hearing improvement (CAP) and the degree of tinnitus reduction. Hearing was significantly improved after CI, and the better the hearing improvement was, the less severe the tinnitus. Thus, better restoration of auditory deafferentation could reduce tinnitus severity.

For the SIR, there was no difference before and after CI surgery, which may be because these patients were postlingually deafened. In addition, we also explored the relationships between SIR and tinnitus severity, SIR and depression/anxiety severity, CAP and hearing aid wearing duration, and SIR and hearing aid wearing duration. There were no relationships between these potentially related factors, which may be due to the limited number of candidates included in this study.

## 5. Conclusion

There is a high prevalence of patients with bilateral profound or severe deafness suffering from severe tinnitus, anxiety, and depressive stress, which seriously affect quality of life. Cochlear implantation is an effective treatment not only for improving hearing but also for relieving tinnitus, anxiety, and depressive distress. Cochlear implantation could reduce unilateral and bilateral tinnitus more obviously with the CI on than off. For some patients, even if the CI device is off, tinnitus distress could be reduced. There was a significantly positive correlation between tinnitus severity and anxiety/depression severity. Although CI could induce tinnitus for some CI candidates without tinnitus, most CI candidates experienced a reduced burden of tinnitus. Hearing was significantly improved after CI, and the better the hearing improvement was, the less severe the tinnitus. The repair of deafferentation with cochlear implantation might be responsible for the improvement of all the above symptoms in addition to hearing loss, which is important for future clinical and research work.

## Data Availability

The data that support the findings of this study are available on request from the corresponding author. The data are not publicly available due to privacy or ethical restrictions.

## Conflicts of Interest

The authors declare that they have no conflicts of interest.

## Authors' Contributions

Juanmei Yang and Jing Song contributed equally to the study.

## Acknowledgments

This work was supported by the Shanghai Natural Science Fund, China (No. 18ZR1406100), to Z.H. and the Natural Science Foundation of Shanghai (grant number 19ZR1408700) to J.Y.

## References

[1] D. Baguley, D. McFerran, and D. Hall, "Tinnitus," *Lancet*, vol. 382, no. 9904, pp. 1600–1607, 2013.

[2] K. Izuhara, K. Wada, K. Nakamura et al., "Association between tinnitus and sleep disorders in the general Japanese population," *The Annals of Otology, Rhinology, and Laryngology*, vol. 122, no. 11, pp. 701–706, 2013.

[3] T. Michikawa, Y. Nishiwaki, Y. Kikuchi et al., "Prevalence and factors associated with tinnitus: a community-based study of Japanese elders," *Journal of Epidemiology*, vol. 20, no. 4, pp. 271–276, 2010.

[4] J. J. Eggermont and L. E. Roberts, "Tinnitus: animal models and findings in humans," *Cell and Tissue Research*, vol. 361, no. 1, pp. 311–336, 2015.

[5] S. E. Shore and C. Wu, "Mechanisms of noise-induced tinnitus: insights from cellular studies," *Neuron*, vol. 103, no. 1, pp. 8–20, 2019.

[6] M. F. Dorman, P. C. Loizou, and J. Fitzke, "The identification of speech in noise by cochlear implant patients and normal-hearing listeners using 6-channel signal processors," *Ear and Hearing*, vol. 19, no. 6, pp. 481–484, 1998.

[7] F. J. J. Kloostra, J. Verbist, R. Hofman, R. H. Free, R. Arnold, and P. van Dijk, "A prospective study of the effect of cochlear implantation on tinnitus," *Audiology & Neuro-Otology*, vol. 23, pp. 356–363, 2019.

[8] C. Poncet-Wallet, E. Mamelle, B. Godey et al., "Prospective multicentric follow-up study of cochlear implantation in adults with single-sided deafness: tinnitus and audiological outcomes," *Otology & Neurotology*, vol. 41, no. 4, pp. 458–466, 2020.

[9] A. K. Punte, K. Vermeire, A. Hofkens, M. De Bodt, D. De Ridder, and P. Van de Heyning, "Cochlear implantation as a durable tinnitus treatment in single-sided deafness," *Cochlear Implants International*, vol. 12, no. sup1, pp. S26–S29, 2011.

[10] N. Quaranta, S. Wagstaff, and D. M. Baguley, "Tinnitus and cochlear implantation," *International Journal of Audiology*, vol. 43, no. 5, pp. 245–251, 2004.

[11] A. van Zon, Y. E. Smulders, G. G. Ramakers et al., "Effect of unilateral and simultaneous bilateral cochlear implantation on tinnitus: a prospective study," *Laryngoscope*, vol. 126, no. 4, pp. 956–961, 2016.

[12] G. G. Ramakers, A. van Zon, I. Stegeman, and W. Grolman, "The effect of cochlear implantation on tinnitus in patients with bilateral hearing loss: a systematic review," *Laryngoscope*, vol. 125, no. 11, pp. 2584–2592, 2015.

[13] G. G. J. Ramakers, G. A. van Zanten, H. Thomeer, R. J. Stokroos, M. W. Heymans, and I. Stegeman, "Development and internal validation of a multivariable prediction model for tinnitus recovery following unilateral cochlear implantation: a cross-sectional retrospective study," *BMJ Open*, vol. 8, no. 6, article e021068, 2018.

[14] Q. Wang, J. N. Li, G. X. Lei et al., "Interaction of tinnitus suppression and hearing ability after cochlear implantation," *Acta Oto-Laryngologica*, vol. 137, no. 10, pp. 1077–1082, 2017.

[15] G. G. J. Ramakers, V. J. C. Kraaijenga, Y. E. Smulders et al., "Tinnitus after simultaneous and sequential bilateral cochlear implantation," *Frontiers in Surgery*, vol. 4, p. 65, 2017.

[16] C. W. Newman, G. P. Jacobson, and J. B. Spitzer, "Development of the tinnitus handicap inventory," *Archives of Otolaryngology – Head & Neck Surgery*, vol. 122, no. 2, pp. 143–148, 1996.

[17] D. Raj-Koziak, E. Gos, W. Swierniak et al., "Visual analogue scales as a tool for initial assessment of tinnitus severity: psychometric evaluation in a clinical population," *Audiology & Neuro-Otology*, vol. 23, no. 4, pp. 229–237, 2018.

[18] P. Spinhoven, J. Ormel, P. P. Sloekers, G. I. Kempen, A. E. Speckens, and A. M. Van Hemert, "A validation study of the Hospital Anxiety and Depression Scale (HADS) in different groups of Dutch subjects," *Psychological Medicine*, vol. 27, no. 2, pp. 363–370, 1997.

[19] A. S. Zigmond and R. P. Snaith, "The hospital anxiety and depression scale," *Acta Psychiatrica Scandinavica*, vol. 67, no. 6, pp. 361–370, 1983.

[20] D. Han, N. Zhou, Y. Li, X. Chen, X. Zhao, and L. Xu, "Tone production of Mandarin Chinese speaking children with cochlear implants," *International Journal of Pediatric Otorhinolaryngology*, vol. 71, no. 6, pp. 875–880, 2007.

[21] S. Liu, F. Wang, P. Chen et al., "Assessment of outcomes of hearing and speech rehabilitation in children with cochlear implantation," *Journal of Otology*, vol. 14, no. 2, pp. 57–62, 2019.

[22] R. H. Pierzycki, C. Corner, C. A. Fielden, and P. T. Kitterick, "Effects of tinnitus on cochlear implant programming," *Trends in Hearing*, vol. 23, article 2331216519836624, 2019.

[23] D. He, Z. Shu, and Z. Han, "Clinical efficacy of web-based personalized music therapy for tinnitus," *Chinese Journal of Otology*, vol. 18, no. 4, pp. 704–707, 2020.

[24] A. N. Heeringa, C. Wu, C. Chung et al., "Glutamatergic projections to the cochlear nucleus are redistributed in tinnitus," *Neuroscience*, vol. 391, pp. 91–103, 2018.

[25] K. L. Marks, D. T. Martel, C. Wu et al., "Auditory-somatosensory bimodal stimulation desynchronizes brain circuitry to reduce tinnitus in guinea pigs and humans," *Science Translational Medicine*, vol. 10, no. 422, p. eaal3175, 2018.

Hindawi
Neural Plasticity
Volume 2021, Article ID 5513224, 9 pages
https://doi.org/10.1155/2021/5513224

*Research Article*

# Model-Based Analysis of Muscle Strength and EMG-Force Relation with respect to Different Patterns of Motor Unit Loss

**Chengjun Huang,[1,2,3] Maoqi Chen,[4] Yingchun Zhang,[5] Sheng Li,[2,3] and Ping Zhou[4]**

[1]*Guangdong Work Injury Rehabilitation Center, Guangzhou, China*
[2]*Department of Physical Medicine and Rehabilitation, University of Texas Health Science Center at Houston, TX, USA*
[3]*TIRR Memorial Hermann Research Center, Houston, TX, USA*
[4]*Institute of Rehabilitation Engineering, University of Health and Rehabilitation Sciences, Qingdao, China*
[5]*Department of Biomedical Engineering, University of Houston, Houston, TX, USA*

Correspondence should be addressed to Ping Zhou; dr.ping.zhou@outlook.com

Received 12 February 2021; Revised 2 May 2021; Accepted 1 June 2021; Published 23 June 2021

Academic Editor: Mou-Xiong Zheng



This study presents a model-based sensitivity analysis of the strength of voluntary muscle contraction with respect to different patterns of motor unit loss. A motor unit pool model was implemented including simulation of a motor neuron pool, muscle force, and surface electromyogram (EMG) signals. Three different patterns of motor unit loss were simulated, including (1) motor unit loss restricted to the largest ones, (2) motor unit loss restricted to the smallest ones, and (3) motor unit loss without size restriction. The model outputs including muscle force amplitude, variability, and the resultant EMG-force relation were quantified under two different motor neuron firing strategies. It was found that motor unit loss restricted to the largest ones had the most dominant impact on muscle strength and significantly changed the EMG-force relation, while loss restricted to the smallest motor units had a pronounced effect on force variability. These findings provide valuable insight toward our understanding of the neurophysiological mechanisms underlying experimental observations of muscle strength, force control, and EMG-force relation in both normal and pathological conditions.

## 1. Introduction

Voluntary muscle activation is mainly controlled by motor unit recruitment and rate modulation. Neurological disorders can influence motor unit properties, contributing to muscle atrophy, contracture, weakness, unstable force output, and altered electromyogram- (EMG-) force relationship. For example, previous studies have revealed various changes in motor unit properties of poststroke patients, such as loss of functional motor units [1–6], impaired motor unit control properties (reduced motor unit peak firing rates and compressed ranges of motor unit recruitment) [7–10], and altered motor unit morphological features [11–13]. These factors significantly impair muscle force generation and the EMG-force relation. Muscle strength of hemispheric stroke patients is profoundly weaker for the paretic side compared with the contralateral side or neurologically intact subjects. The slope of the EMG-force relation of the paretic first dorsal interosseous and biceps brachii muscles was reported to be significantly greater in hemiparetic stroke survivors compared with the contralateral or neurologically intact muscles [7, 14].

By using an experimental approach, it is difficult to quantify the relative contribution of each of the various motor unit property alterations to muscle weakness and the EMG-force relation. To overcome this difficulty, a classic motor neuron pool model, developed by Fuglevand et al. [15], has been widely used to better understand the experimental observations of the force and EMG signals and explore the mechanisms of motor impairment [16–18]. For example, Shin et al. [19] and Zhou et al. [20] have used the model to explore the effect of motor unit control property (recruitment and firing rate) changes on muscle weakness and the EMG-force relation.

Among different motor unit properties, loss of functional motor units plays a very important role in influencing muscle strength, force variability, and the EMG-force relation. Some

studies reported that small motor units (with low recruitment thresholds) were more affected after a neurological injury [13], while others found that large motor units (with high recruitment thresholds) were more susceptible to atrophy [21]. It still remains unclear whether motor unit loss occurred randomly or in a specific pattern. Therefore, the objective of this study was to explore the effects of different patterns of motor unit loss on muscle strength, force variability, and the EMG-force relation. This was performed by varying the model input with three different patterns of motor unit loss, including motor unit loss restricted to the largest ones, motor unit loss restricted to the smallest ones, and motor unit loss without any size restriction.

The Fuglevand model [15] was used in this study. Each pattern of motor unit loss was simulated under two different motor neuron firing strategies. The resultant muscle force amplitude, force variability, and the EMG-force relation under different conditions were compared. The findings of this study can help better understand experimental muscular force and surface EMG recordings in both healthy and pathological conditions and facilitate identification of specific motor unit mechanisms underlying observed alterations in overall muscle force and EMG activities. Such analyses in turn can help design appropriate rehabilitation strategies to improve muscle function by targeting the identified motor unit alterations.

## 2. Methods

There are three main components contained in the motor unit pool model used in this study: a motor neuron pool model, a force generation model, and a surface EMG model [15].

*2.1. Motor Neuron Pool Model.* A motor neuron pool innervating 120 motor units was simulated. Each motor unit had a recruitment threshold (RTE), which is the minimum excitatory drive needed to trigger the motor unit to discharge. The RTE was expressed as an exponential function as Equation (1). In Equation (1), RR is the range of recruitment threshold between the first and last motor units in the pool, $i$ is an index identifying each motor unit, and ln is the natural logarithm. According to Equation (1), most of the motor units would be recruited at relatively lower excitation levels. In our study, once the excitatory drive exceeded the RTE, the motor unit started to discharge at a minimum firing rate (MFR) of 8 Hz. RR of the motor unit pool was assigned to be 40% excitation (i.e., the last motor neuron was recruited at 40% maximum excitation).

$$\mathrm{RTE}(i) = e^{(\ln \mathrm{RR}/n)\bullet i}. \tag{1}$$

The firing rate (FR) of each motor unit was modeled to increase linearly until the peak firing rate (PFR) was reached. To simulate the stochastic nature of motor neuron discharge, the interspike interval of the motor unit firing was modeled as a random process with a Gaussian probability distribution function. The standard deviation of the interspike interval was fixed for all motor units at 20% of the mean interspike interval as used in the original model [15]. Two motor neuron firing rate patterns were simulated. The first pattern is called the "onion skin" pattern, in which the PFR of each motor unit was inversely proportional to its RTE. Therefore, the PFRs of later recruited large motor units were lower than the early recruited small ones. On the contrary, the other pattern is called the reverse "onion skin" pattern, meaning that the PFRs of large motor units were assigned to be higher than the small motor units. In both firing strategies, the gain between the firing rate and excitatory input was set to be the same for all motor units. The FR of each motor unit at a given time was governed by Equation (2) until it reached its PFR, where $E(t)$ was the excitatory drive. Figure 1 shows the two different motor neuron firing patterns.

$$\mathrm{FR}i = \mathrm{gain} * [E(t) - \mathrm{RTE(i)}] + \mathrm{MFR}\ E(t) \geq \mathrm{RTE}(i). \tag{2}$$

*2.2. Force Model.* A motor unit twitch was modelled as a second-order critically damped impulse response (Equation (3)), where $g_{i,j}$ is the force gain for discharge $j$ in the $i$th motor unit, $P_i$ is the peak twitch force, and $T_i$ is the contraction time of the $i$ th motor unit. For each motor unit, $P_i$ was varied over a wide range and associated with the motor unit recruitment threshold as in Equations (4) and (5). RP is the range of peak twitch force across all the motor units, RT is the range of contraction time, ln is the natural logarithm, $i$ is an index identifying each motor unit, $n$ is the number of motor units, and $T_L$ represents the longest contraction time. In this study, RP and RT were assigned to 100 and 3, respectively. Most motor units had lower and longer twitch forces, and a few had higher and shorter twitch forces as shown in Figure 1(c). Peak twitch force varied over a 100-fold range, and contraction time varied over 3-fold range. The highest threshold (of the last recruited motor unit) was assigned the largest force and shortest duration time.

The gain $g_{i,j}$ was nonlinearly changed based on the motor unit contraction time and the interspike interval (ISI) of the discharge $j$. The gain was assigned a value of 1 when $T_i/\mathrm{ISI}_j < 0.4$ and then was determined as in Equation (6) when $T_i/\mathrm{ISI}_j > 0.4$. As stated in the original model [15], the greatest gain in motor unit force occurs when the ISI is equivalent to the twitch contraction time. When the motor unit firing rate exceeds a certain level, there will be no more increase in the force output. The total muscle contraction force was calculated as the linear summation of each motor unit force output.

$$f_{i,j}(t) = g_{i,j} * \frac{P_i \bullet t}{T_i} \bullet e^{1-t/T_i}, \tag{3}$$

$$P(i) = e^{(\ln \mathrm{RP}/n)\bullet i}, \tag{4}$$

$$T(i) = T_L \left(\frac{1}{P(i)}\right)^{1/\log_{\mathrm{RT}}\mathrm{RP}}, \tag{5}$$

$$g_{i,j} = \frac{1 - e^{-2\left(T_i/\mathrm{ISI}_j\right)^3}}{T_i/\mathrm{ISI}_j} \text{ when } \frac{T_i}{\mathrm{ISI}_j} > 0.4. \tag{6}$$

*2.3. Surface EMG Model.* The muscle simulated in this study was cylindrical in shape, and the radius was 8 mm. The

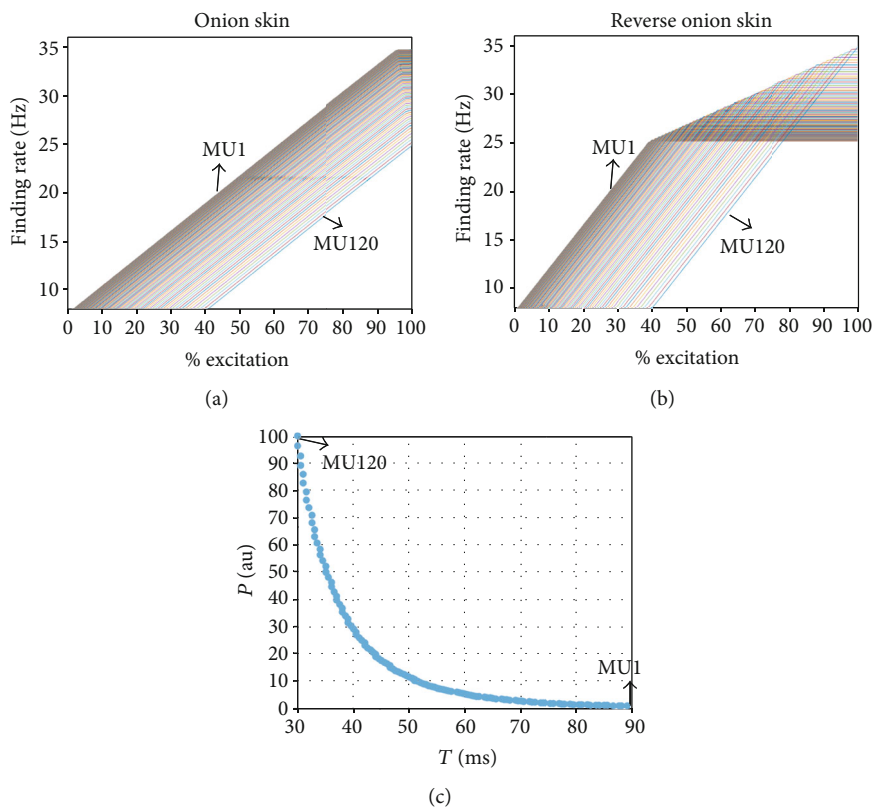


Figure 1: (a) The simulated relation between the excitation level and the motor unit firing rate for the "onion skin" firing strategy. (b) The simulated relation between the excitation level and the motor unit firing rate for the reverse "onion skin" firing strategy. (c) The twitch parameter assignment for the entire pool of 120 motor units.

thickness of fat and skin layers was set to be 2.5 mm. There were totally 70,000 muscle fibers innervated by all the 120 motor neurons, which were randomly scattered in a circular territory and distributed in parallel. The density of the territory was approximately 20 fibers/mm$^2$. Following an exponential function, the number of muscle fibers per motor unit was simulated to have the same range (100-fold) as the twitch force [15]. The smallest motor unit innervated 28 fibers, and the largest one innervated 2,728 fibers. The average innervation ratio was 598 fibers/motor unit. The conduction velocity was correlated to the diameter of fibers as described in [22].

A tripole model described in [23] was used to simulate the individual fiber action potentials in a three-dimensional muscle volume. Briefly, two action potentials generated by a fiber, modeled as two current tripoles, were originated at the innervation zone, propagated in opposite directions, and were extinct at the fiber-tendon endings (Figure 2). The monopolar signal detected by the electrode is the summation of the contribution from each of the tripoles. A motor unit action potential (MUAP) was simulated as the sum of its constituent muscle fiber action potentials.

The surface EMG signal $x(t)$ was then generated as a sparse combination of MUAP waveforms from all $N$ active motor units [24, 25], as described in Equation (7):

$$x(t) = \sum_{j=1}^{N} \sum_{\tau=0}^{L-1} a_j(\tau) s_j(t-\tau), \tag{7}$$

where $a_j$ is the MUAP waveform of the $j$th motor unit and $L$ is the length of the waveform. $s_j(t) = \sum_k \delta(t - T_j(k))$ indicates whether the $j$th motor unit discharges at a specific time $t$, where $T_j(k)$ is the $k$th discharge time of the $j$th motor unit and $\delta$ represents Dirac Delta function.

*2.4. Procedures.* To investigate the effect of motor unit loss on muscle strength and the EMG-force relation, each of the parameters describing these properties was adjusted. Each time when one parameter was adjusted, the other parameters remained the same as their initial assignments.

The percentage of motor unit loss was set to be 20%, 40%, and 60%, respectively. Three motor unit loss patterns were simulated in this study, including the following: (1) motor unit loss restricted to the largest ones, (2) motor unit loss restricted to the smallest ones, and (3) motor unit loss without any size restriction. The force and EMG outputs at 10 excitation levels were simulated. As demonstrated in Figure 3(a), during each excitation level, the excitation drive increased linearly in the first 2 seconds and then held at a steady level for 5 seconds. The steady state excitation level ranged from 10% to 100% of maximum excitation with 10% increments. An example of simulated force and surface EMG signals is shown in Figures 3(b) and 3(c). The first 2-second transient force or EMG output was excluded from analysis, and only the steady state force and EMG signals were analyzed. The coefficient of variation (COV) of the

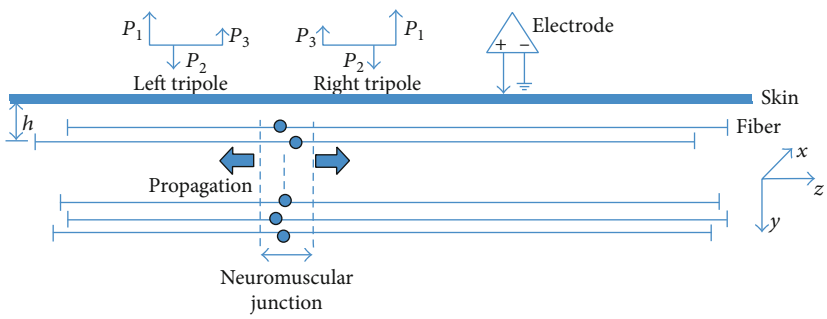


Figure 2: The simulated muscle fiber action potential generation and the detection system. All the muscle fibers are uniformly distributed in a cylinder at different depths $h$ ($y$ axis). The left or right current tripole originates from the neuromuscular junction and propagates along the direction of $z$ axis, to the fiber-tendon termination.

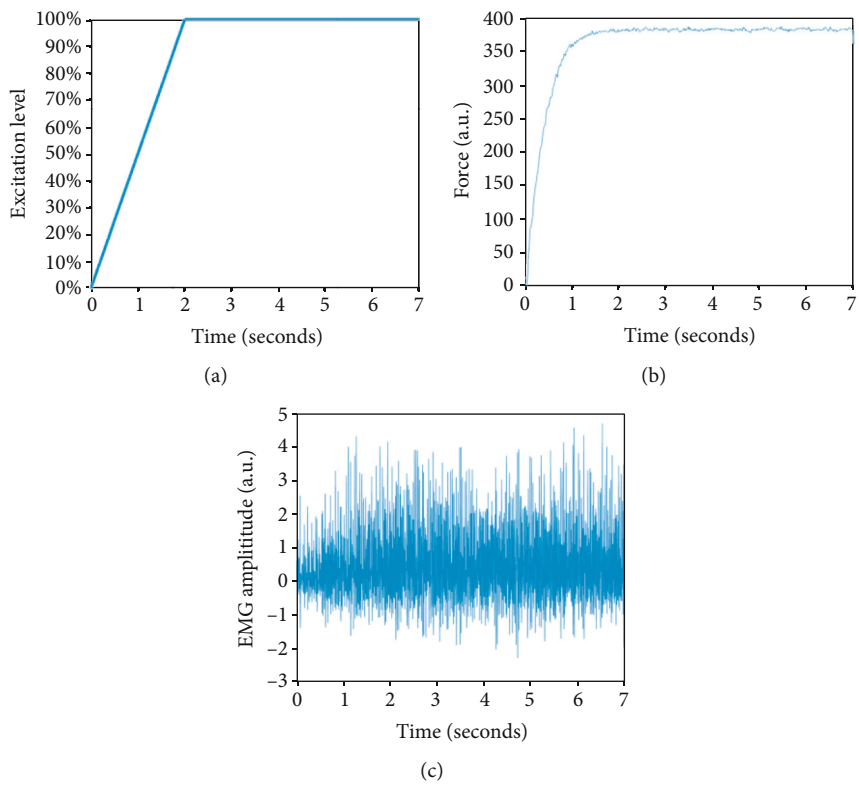


Figure 3: An example of (a) the excitation input simulation when the level was at 100% excitation and (b) the muscle force and (c) surface EMG outputs of the model.

generated force signals was calculated to estimate the force variability. The averaged rectified value (ARV) of surface EMG signals was calculated. As the force and EMG output may vary slightly because of the randomized firing time of each motor unit, 10 repetitions were simulated for each excitation level and each situation of motor unit loss. Then, the mean value of all the repetitions was calculated for each of the output parameters, including force amplitude, force COV, and ARV of surface EMG. For the EMG-force relation, the force value and surface EMG amplitude were normalized to their maximum levels. Because the variation of the simulation outcomes from different repetitions was very small, as observed in previous studies [19, 20] and confirmed in the current study, only the mean value of the 10 repetitions was reported for each simulation condition.

The model was implemented in MATLAB (MathWorks Inc., Natick, MA, USA). On average, it took approximately 10 to 15 minutes to complete simulation of one motor unit loss pattern under one firing strategy across all the excitation levels. The simulation can be run on a normal desktop or laptop computer.

## 3. Results

*3.1. Strength of Muscle Activation.* Compared with the default condition (120 motor units), motor unit loss led to reduction

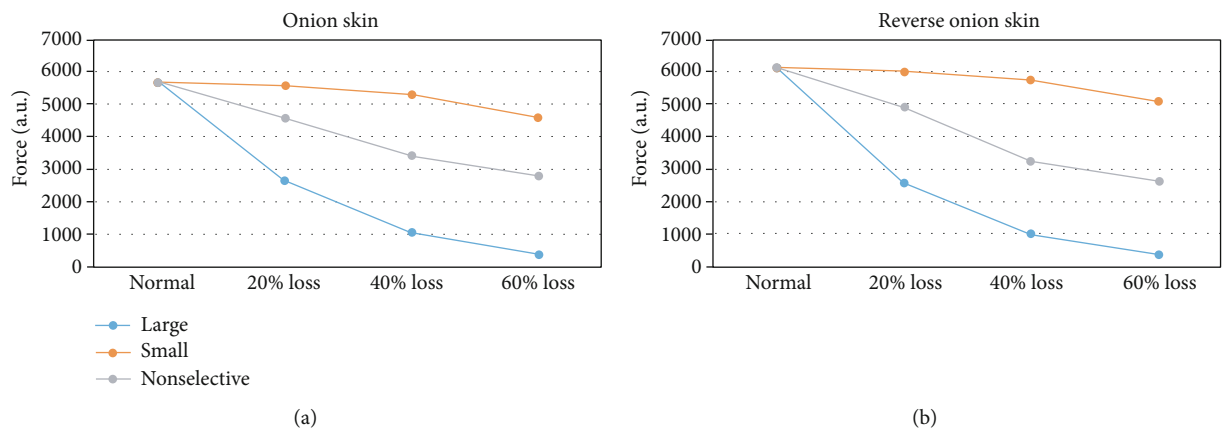


Figure 4: The simulated muscle force generation capacity (i.e., at 100% excitation) for different patterns and levels of motor unit loss in (a) the "onion skin" and (b) reverse "onion skin" motor unit firing strategies.

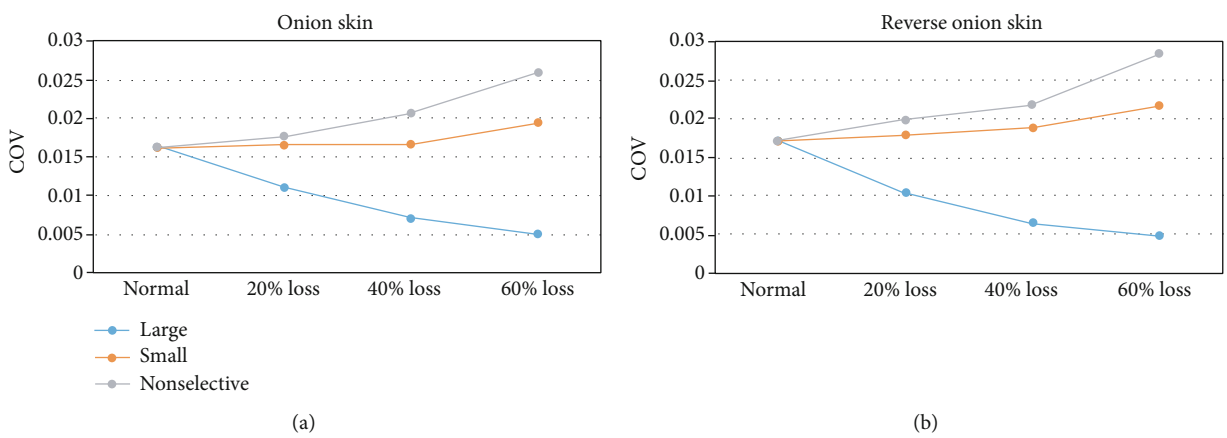


Figure 5: The coefficient of variation (COV) of the simulated maximum muscle force output (i.e., at 100% excitation) for different patterns and levels of motor unit loss in (a) the "onion skin" and (b) reverse "onion skin" motor unit firing strategies.

in muscle strength, the extent of which was related to each of the examined parameters. The muscle strength reduction caused by loss of large motor units was the greatest compared with the other two motor unit loss patterns. To examine the force capacity of the muscle, the maximum voluntary contraction force (i.e., the 100% excitation drive) was compared for different motor unit loss patterns. As shown in Figure 4, for the loss of 60% motor units restricted to the largest ones, the maximum muscle force was reduced from 5685 arbitrary units (au) to 382 au (an approximately 93.3% reduction) when the motor units followed the "onion skin" firing strategy and reduced from 6133 au to 380 au (an approximately 93.8% reduction), when the motor units followed the reverse "onion skin" firing strategy. By contrast, for the loss of 60% motor units restricted to the smallest ones, the maximum muscle force was only reduced from 5685 au to 4624 au (an approximately 18.7% reduction) when the motor units followed the "onion skin" firing strategy and reduced from 6133 au to 5090 au (an approximately 17% reduction), when the motor units followed the reverse "onion skin" firing strategy. It is worth noting that the force capacity under the motor unit reverse "onion skin" firing strategy was higher than the "onion skin" strategy.

*3.2. Force Variability.* The COV of the output force decreased substantially with increasing excitation drive under all conditions. Compared with the default condition (120 motor units), loss restricted to the largest motor units could lead to smaller COV, while motor unit loss restricted to the smallest ones or without any size restriction could lead to larger COV across all excitation levels. This was the case for both "onion skin" and reverse "onion skin" motor unit firing strategies.

The COV of the maximum voluntary contraction force (i.e., the 100% excitation drive) was compared for different motor unit loss patterns. As shown in Figure 5(a), for the loss of 60% motor units restricted to the largest ones, the COV of the maximum muscle force was reduced by 71.4% when the motor units followed the "onion skin" firing strategy. By contrast, for the loss of 60% motor units restricted to the smallest ones or without any size restriction, the COV of the maximum muscle force was increased by 23.5% and 64.7%, respectively. The COV of the maximum muscle force followed a similar trend when motor units followed the reverse "onion skin" firing strategy, as shown in Figure 5(b).

*3.3. EMG-Force Relation.* Figure 6 shows the simulated EMG-force relation for different patterns and degrees of

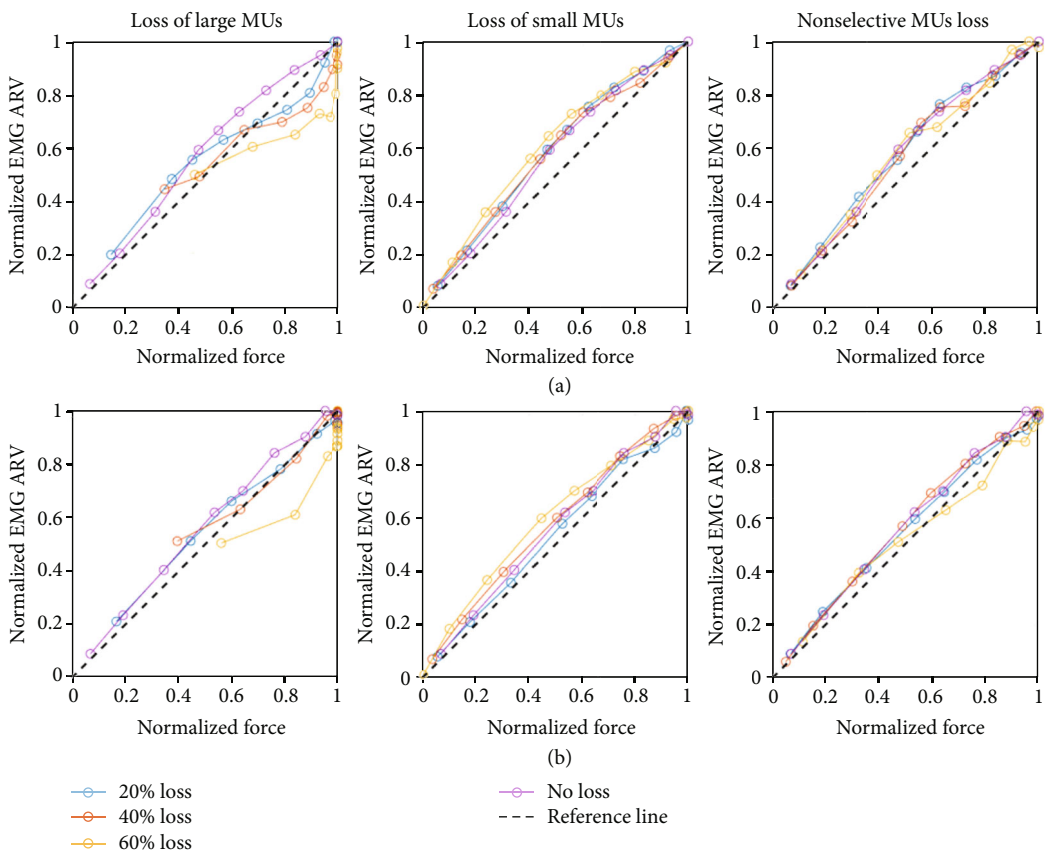


Figure 6: The simulated EMG-force relation for different patterns and levels of motor unit loss in (a) the "onion skin" and (b) reverse "onion skin" motor unit firing strategies.

motor unit loss, under two motor unit firing strategies. For each constructed relation, the force and EMG were normalized to their respective maximum values at the simulated situation. For the default condition (120 motor units), the EMG-force relation could be well fit by a linear line for both motor unit firing strategies. This linear fitting of the EMG-force relation was well maintained in the situations of motor unit loss restricted to the smallest ones or without any size restriction, regardless of the degree of motor unit loss. A similar slope of the fitted line was observed for different degrees of motor unit loss restricted to the smallest ones or without any size restriction. By contrast, motor unit loss restricted to the largest ones tended to drive the approximately linear EMG-force relation to a nonlinear form, with the EMG amplitude increasing faster than force, as shown in Figure 6. This was observed for both "onion skin" and reverse "onion skin" motor unit firing strategies.

## 4. Discussion

This study implemented a model to estimate the effect of different patterns of motor unit loss on muscle force strength, variability, and the EMG-force relation. The force and EMG outputs were simulated at different levels of excitation. It was found that loss restricted to the largest motor units had the most pronounced impact on muscle strength and the EMG-force relation, while motor unit loss restricted to the smallest ones had the most pronounced impact on force variability. This was observed for both motor unit firing strategies used in the simulation.

*4.1. Strength of Muscle Activation.* As documented in previous motor unit number estimation investigations [26], progressive motor unit loss occurs after neuromuscular diseases such as amyotrophic lateral sclerosis and spinal muscular atrophy [27–29]. Transsynaptic motor neuron degeneration has also been reported in neurological injuries, causing different degrees of motor unit loss in affected muscles [1–6, 30, 31]. Motor axon degeneration following various neuropathies can also be quantified by estimating motor unit number changes [32–35]. Loss of functional motor units, especially those large ones, has a dramatic effect on muscle strength. Based on the model, twitch forces were distributed exponentially across the motor unit pool with the smallest motor unit (MU 1) assigned the smallest twitch force and the largest motor unit (MU 120) assigned the largest twitch force. Therefore, the twitch forces of one-half the motor unit population (i.e., from MU 1 to MU 60) were less than 10% of the largest motor unit's twitch force. As a result, the loss restricted to the largest motor units could cause severe muscle weakness compared with the other two motor unit loss patterns.

It was observed that for the reverse "onion skin" motor neuron firing strategy, motor unit loss restricted to the largest ones could lead more severe muscle weakness than the

"onion skin" firing strategy. This is because the reverse "onion skin" firing strategy more ideally matches the motor unit contractile properties. As the excitation level increases, the discharge rate of almost all the motor units would be progressively closer to the fusion frequency, being able to reach the maximum motor unit force. However, in the "onion skin" firing strategy, the discharge rates of the largest motor units can be far below their fusion frequency even at the maximum excitation, thus compromising the maximum motor unit force generation. Consequently, the relative contribution of the largest motor units to the muscle force output is greater in the reverse "onion skin" strategy compared with the "onion skin" strategy. This results in a more severe muscle weakness if large motor units are lost in the reverse "onion" skin firing strategy.

*4.2. Muscle Force Variability.* Similar to a previous simulation study [36], the coefficient of variation (COV) of the force output decreased substantially with increasing excitation level in all simulated conditions. At submaximal excitation levels, the early recruited motor units would discharge at relatively low rates, which are below their fusion frequency. Therefore, there would be substantial ripples in the resultant motor unit force. As the excitation level increases, the motor unit firing rates start to increase, closer to the fusion frequency, gradually reducing the ripples of the individual motor unit forces. This can result in a more stable force, as suggested by the decreased COV with increasing excitation level.

Compared with the default condition, under both firing strategies, motor unit loss restricted to the largest ones could lead to a decrease in force COV, while motor unit loss restricted to the smallest ones could lead to an increase in force COV. When the lost motor units were primarily large ones, the generated force was only from small motor units even at the maximum excitation level. Given that the fusion frequency of the small motor units is low, there would be fewer ripples in the generated motor unit forces, as suggested by a decreased COV. On the other hand, when the lost motor units were primary small ones, increasing the excitation level could only activate the large motor units, whose fusion frequency is relatively high and difficult to reach. The generated force, therefore, would show more ripples as suggested by an increased COV.

*4.3. EMG-Force Relation.* The EMG-force relation has been extensively investigated in the past. A linear relation between force and the surface EMG amplitude has been reported for muscles with narrow motor unit recruitment ranges [15, 37, 38]. In the present simulation study, with the recruitment threshold set at 40% excitation, a linear EMG-force relation was also observed for both motor unit firing strategies. Interestingly, this linear relation remained in the case of motor unit loss restricted to the smallest ones or without any size restriction. If the lost motor units were primarily small ones, with increase of the excitation level, larger motor units were progressively recruited. Given relatively high fusion frequencies for the large motor units, their motor unit force continued to increase with increase of the firing rates. On the other hand, although there was an effect of EMG phase cancellation, the overall EMG amplitude also continued to increase since large MUAPs were generated with recruitment of large motor units. As a result of both force and EMG increase with excitation drive, an approximate linear EMG-force relation was maintained. There was a similar scenario for motor unit loss without size restriction since large motor units were still recruited with increase of the excitation, contributing to both force and EMG signals.

By contrast, our simulation results indicate that motor unit loss restricted to the largest ones tended to drive the EMG-force relation from a linear to nonlinear form, with EMG increasing faster than force. This is due to the fact that the remaining small motor units were assigned longer contraction time (i.e., low fusion frequency), so further increasing the motor unit firing rate with increased excitation level would not have an influence on force given that those motor units had already reached the maximum force output, and meanwhile, no larger motor units could be recruited. The increased number of MUAPs, however, increased surface EMG amplitude even there was an effect of phase cancellation. As a result, a nonlinear EMG-force relation was observed. It is worth noting that in the simulation, it was assumed that the excitation capacity still remained intact, while after a neurological injury, the excitation capacity could be impaired and consequently compromise the motor unit peak firing rates and alter the resultant EMG-force relation.

*4.4. Limitations.* As a simulation study with many assumptions used in the model, the limitations should be acknowledged. For example, the muscle fibers of each motor unit were simulated as widely scattered throughout the whole muscle, and the muscle fiber diameters of the small and large motor units were assigned the same mean value. However, motor units might locate in different regions of a muscle, with small and large motor units having different depth [39]. The size and type composition of muscle fibers belonging to small and large motor units of a muscle can also be different. Three simplified motor unit loss patterns were simulated while in real world, there is often a variable mixture of motor unit loss. A range of neurophysiological factors were not considered in the simulation, such as the excitatory and inhibitory central drive upon lower motor neurons, the interneurons input, motor unit synchronization [40], possible nonlinear effect of the individual motor unit force summation [41], and resistance to fatigue of different motor units. Of particular note, muscle fiber reinnervation as a possible compensatory process after motor unit loss was not considered in the simulation [42]. There are some other physiological changes that need to be considered in a practical situation, such as muscle atrophy, compression of motor unit recruitment range, and reduction in motor unit firing rate. All these factors may collectively alter muscle force and surface EMG signals. To address these issues, a more delicate or complicated model is required in a future study [43].

Nonetheless, by simulating three different motor unit loss patterns using the current model, we have observed their different effects on muscle weakness and changes in EMG-force relation. Motor unit loss restricted to the largest ones had the most dominant impact on the total force output and

significantly changed the EMG-force relation, while loss restricted to the smallest motor units had a pronounced effect on force variability. These findings provide valuable clues for understanding experimental observations of muscle strength, force control, and EMG-force relation, especially their alterations with pathological neural or muscular changes.

## Data Availability

No experimental datasets were generated or analyzed during the current study. The simulated datasets are available from the corresponding author (PZ) on request.

## Conflicts of Interest

The authors declare that they have no competing interests.

## Acknowledgments

This study was supported in part by the Natural Science Foundation of Shandong Province under Grant ZR2020KF012 and in part by the Guangzhou Science and Technology Program under Grant 201704030039.

## References

[1] X. Li, J. Liu, S. Li, Y.-C. Wang, and P. Zhou, "Examination of hand muscle activation and motor unit indices derived from surface EMG in chronic stroke," *IEEE Transactions on Biomedical Engineering*, vol. 61, no. 12, pp. 2891–2898, 2014.

[2] X. Li, M. Fisher, W. Z. Rymer, and P. Zhou, "Application of the F-response for estimating motor unit number and amplitude distribution in hand muscles of stroke survivors," *IEEE Transactions on Neural Systems and Rehabilitation Engineering*, vol. 24, no. 6, pp. 674–681, 2016.

[3] Y. Hara, Y. Masakado, and N. Chino, "The physiological functional loss of single thenar motor units in the stroke patients: when does it occur? Does it progress?," *Clinical Neurophysiology*, vol. 115, no. 1, pp. 97–103, 2004.

[4] K. Arasaki, O. Igarashi, Y. Ichikawa et al., "Reduction in the motor unit number estimate (MUNE) after cerebral infarction," *Journal of the Neurological Sciences*, vol. 250, no. 1–2, pp. 27–32, 2006.

[5] I. Kouzi, E. Trachani, E. Anagnostou et al., "Motor unit number estimation and quantitative needle electromyography in stroke patients," *Journal of Electromyography and Kinesiology*, vol. 24, no. 6, pp. 910–916, 2014.

[6] I. S. Choi, J. H. Kim, J. Y. Han, and S. G. Lee, "The correlation between F-wave motor unit number estimation (F-MUNE) and functional recovery in stroke patients," *Journal of Korean Medical Science*, vol. 22, no. 6, pp. 1002–1006, 2007.

[7] J. J. Gemperline, S. Allen, D. Walk, and W. Z. Rymer, "Characteristics of motor unit discharge in subjects with hemiparesis," *Muscle & Nerve*, vol. 18, no. 10, pp. 1101–1114, 1995.

[8] X. Li, A. Holobar, M. Gazzoni, R. Merletti, W. Z. Rymer, and P. Zhou, "Examination of poststroke alteration in motor unit firing behavior using high-density surface EMG decomposition," *IEEE Transactions on Biomedical Engineering*, vol. 62, no. 5, pp. 1242–1252, 2015.

[9] A. Rosenfalck and S. Andreassen, "Impaired regulation of force and firing pattern of single motor units in patients with spasticity," *Journal of Neurology, Neurosurgery, and Psychiatry*, vol. 43, no. 10, pp. 907–916, 1980.

[10] X. Hu, A. K. Suresh, W. Z. Rymer, and N. L. Suresh, "Assessing altered motor unit recruitment patterns in paretic muscles of stroke survivors using surface electromyography," *Journal of Neural Engineering*, vol. 12, no. 6, article 066001, 2015.

[11] B. Yao, C. S. Klein, H. Hu, S. Li, and P. Zhou, "Motor unit properties of the first dorsal interosseous in chronic stroke subjects: concentric needle and single fiber EMG analysis," *Frontiers in Physiology*, vol. 9, p. 1587, 2018.

[12] R. Dattola, P. Girlanda, G. Vita et al., "Muscle rearrangement in patients with hemiparesis after stroke: an electrophysiological and morphological study," *European Neurology*, vol. 33, no. 2, pp. 109–114, 1993.

[13] X. Li, L. Li, H. Shin, S. Li, and P. Zhou, "Electrical impedance myography for evaluating paretic muscle changes after stroke," *IEEE Transactions on Neural Systems and Rehabilitation Engineering*, vol. 25, no. 11, pp. 2113–2121, 2017.

[14] P. Zhou, X. Li, and W. Zev Rymer, "EMG-force relations during isometric contractions of the first dorsal interosseous muscle after stroke," *Topics in Stroke Rehabilitation*, vol. 20, no. 6, pp. 537–543, 2013.

[15] A. J. Fuglevand, D. A. Winter, and A. E. Patla, "Models of recruitment and rate coding organization in motor-unit pools," *Journal of Neurophysiology*, vol. 70, no. 6, pp. 2470–2488, 1993.

[16] P. Zhou and W. Z. Rymer, "Factors governing the form of the relation between muscle force and the EMG: a simulation study," *Journal of Neurophysiology*, vol. 92, no. 5, pp. 2878–2886, 2004.

[17] W. Yao, R. J. Fuglevand, and R. M. Enoka, "Motor-unit synchronization increases EMG amplitude and decreases force steadiness of simulated contractions," *Journal of Neurophysiology*, vol. 83, no. 1, pp. 441–452, 2000.

[18] X. Li, W. Z. Rymer, and P. Zhou, "A simulation-based analysis of motor unit number index (MUNIX) technique using motoneuron pool and surface electromyogram models," *IEEE Transactions on Neural Systems and Rehabilitation Engineering*, vol. 20, no. 3, pp. 297–304, 2012.

[19] H. Shin, N. L. Suresh, W. Z. Rymer, and X. Hu, "Relative contribution of different altered motor unit control to muscle weakness in stroke: a simulation study," *Journal of Neural Engineering*, vol. 15, no. 1, article 016014, 2018.

[20] P. Zhou, N. L. Suresh, and W. Z. Rymer, "Model based sensitivity analysis of EMG–force relation with respect to motor unit properties: applications to muscle paresis in stroke," *Annals of Biomedical Engineering*, vol. 35, no. 9, pp. 1521–1531, 2007.

[21] M. Lukács, L. Vécsei, and S. Beniczky, "Large motor units are selectively affected following a stroke," *Clinical Neurophysiology*, vol. 119, no. 11, pp. 2555–2558, 2008.

[22] J. Duchene and J.-Y. Hogrel, "A model of EMG generation," *IEEE Transactions on Biomedical Engineering*, vol. 47, no. 2, pp. 192–201, 2000.

[23] R. Merletti, L. Lo Conte, E. Avignone, and P. Guglielminotti, "Modeling of surface myoelectric signals. I. Model implementation," *IEEE Transactions on Biomedical Engineering*, vol. 46, no. 7, pp. 810–820, 1999.

[24] A. Holobar and D. Zazula, "Multichannel blind source separation using convolution kernel compensation," *IEEE Transactions on Signal Processing*, vol. 55, no. 9, pp. 4487–4496, 2007.

[25] M. Chen and P. Zhou, "A novel framework based on FastICA for high density surface EMG decomposition," *IEEE Transactions on Neural Systems and Rehabilitation Engineering*, vol. 24, no. 1, pp. 117–127, 2016.

[26] A. J. McComas, "Invited review: motor unit estimation: methods, results, and present status," *Muscle & Nerve*, vol. 14, no. 7, pp. 585–597, 1991.

[27] F. Fatehi, A.-M. Grapperon, D. Fathi, E. Delmont, and S. Attarian, "The utility of motor unit number index: a systematic review," *Neurophysiologie Clinique*, vol. 48, no. 5, pp. 251–259, 2018.

[28] C. L. G. Harati Yadollah, "Motor unit number estimation, ALS and clinical trials," *Amyotrophic Lateral Sclerosis and Other Motor Neuron Disorders*, vol. 1, no. 2, pp. 71–82, 2000.

[29] B. T. H. M. Sleutjes, C. A. Wijngaarde, R. I. Wadman et al., "Assessment of motor unit loss in patients with spinal muscular atrophy," *Clinical Neurophysiology*, vol. 131, no. 6, pp. 1280–1286, 2020.

[30] L. Li, X. Li, J. Liu, and P. Zhou, "Alterations in multidimensional motor unit number index of hand muscles after incomplete cervical spinal cord injury," *Frontiers in Human Neuroscience*, vol. 9, p. 238, 2015.

[31] X. Li, F. Jahanmiri-Nezhad, W. Z. Rymer, and P. Zhou, "An examination of the motor unit number index (MUNIX) in muscles paralyzed by spinal cord injury," *IEEE Transactions on Information Technology in Biomedicine*, vol. 16, no. 6, pp. 1143–1149, 2012.

[32] N. Garg, J. Howells, C. Yiannikas et al., "Motor unit remodelling in multifocal motor neuropathy: the importance of axonal loss," *Clinical Neurophysiology*, vol. 128, no. 10, pp. 2022–2028, 2017.

[33] A. DiAntonio, "Axon degeneration: mechanistic insights lead to therapeutic opportunities for the prevention and treatment of peripheral neuropathy," *Pain*, vol. 160, no. 1, pp. S17–S22, 2019.

[34] A. G. Kristensen, K. S. Khan, H. Bostock et al., "MScanFit motor unit number estimation and muscle velocity recovery cycle recordings in diabetic polyneuropathy," *Clinical Neurophysiology*, vol. 131, no. 11, pp. 2591–2599, 2020.

[35] R. A. Lewis, J. Li, D. R. Fuerst, M. E. Shy, and K. Krajewski, "Motor unit number estimate of distal and proximal muscles in Charcot-Marie-Tooth disease," *Muscle & Nerve*, vol. 28, no. 2, pp. 161–167, 2003.

[36] X. Hu, W. Z. Rymer, and N. L. Suresh, "Motor unit firing rate patterns during voluntary muscle force generation: a simulation study," *Journal of Neural Engineering*, vol. 11, no. 2, article 026015, 2014.

[37] H. S. Milner-Brown and R. B. Stein, "The relation between the surface electromyogram and muscular force," *The Journal of Physiology*, vol. 246, no. 3, pp. 549–569, 1975.

[38] J. H. Lawrence and C. J. De Luca, "Myoelectric signal versus force relationship in different human muscles," *Journal of Applied Physiology*, vol. 54, no. 6, pp. 1653–1659, 1983.

[39] C. A. Knight and G. Kamen, "Superficial motor units are larger than deeper motor units in human vastus lateralis muscle," *Muscle & Nerve*, vol. 31, no. 4, pp. 475–480, 2005.

[40] C. J. De Luca, A. M. Roy, and Z. Erim, "Synchronization of motor-unit firings in several human muscles," *Journal of Neurophysiology*, vol. 70, no. 5, pp. 2010–2023, 1993.

[41] E. J. Perreault, S. J. Day, M. Hulliger, C. J. Heckman, and T. G. Sandercock, "Summation of forces from multiple motor units in the cat soleus muscle," *Journal of Neurophysiology*, vol. 89, no. 2, pp. 738–744, 2003.

[42] S. D. Nandedkar, D. B. Sanders, and E. V. Stålberg, "EMG of reinnervated motor units: a simulation study," *Electroencephalography and Clinical Neurophysiology*, vol. 70, no. 2, pp. 177–184, 1988.

[43] J. W. Robertson and J. A. Johnston, "Modifying motor unit territory placement in the Fuglevand model," *Medical & Biological Engineering & Computing*, vol. 55, no. 11, pp. 2015–2025, 2017.

Hindawi
Neural Plasticity
Volume 2021, Article ID 6690414, 9 pages
https://doi.org/10.1155/2021/6690414

*Research Article*

# Potential Alterations of Functional Connectivity Analysis in the Patients with Chronic Prostatitis/Chronic Pelvic Pain Syndrome

**Shengyang Ge,[1] Qingfeng Hu,[1] Yijun Guo,[2] Ke Xu,[1] Guowei Xia,[1] and Chuanyu Sun[1]**

[1]*Department of Urology, Huashan Hospital, Fudan University, 12 Central Urumqi Rd, Shanghai 200040, China*
[2]*Department of Urology, Jing'an District Center Hospital of Shanghai, 259 Xikang Rd, Shanghai 200040, China*

Correspondence should be addressed to Guowei Xia; xiaguoweihuashan@sina.com and Chuanyu Sun; zhugexianglong@163.com

Received 29 December 2020; Revised 13 March 2021; Accepted 25 April 2021; Published 7 May 2021

Academic Editor: Xu-Yun Hua



*Background*. Chronic prostatitis/chronic pelvic pain syndrome (CP/CPPS) is one of the most common diseases in urology, but its pathogenesis remains unclear. As a kind of chronic pain which the patients suffered for more than 3 months, we investigated the influence on patients' brain functional connectivity in resting state. *Methods*. We recruited a cohort of 18 right-handed male patients with CP/CPPS and 21 healthy male right-handed age-matched controls. Their resting-state fMRI data and structural MRI data were preprocessed and processed by RESTPlus V1.22. To assess the integrity of the default mode network (DMN), we utilized the voxel-wised analysis that we set medial prefrontal cortex (mPFC) and posterior cingulate gyrus (PCC) as seed points to compare the global functional connectivity (FC) strength. *Results*. Compared with healthy control, the FC strength between left mPFC and posterior DMN decreased in the group of CP/CPPS ($P < 0.05$, GFR correction, voxel $P < 0.01$, cluster $P < 0.05$), and the FC strength between the left anterior cerebellar lobe and posterior DMN increased ($P < 0.05$, GFR correction, voxel $P < 0.01$, cluster $P < 0.05$). In the patient group, there was a positive correlation between the increased FC strength and the score of the Hospital Anxiety and Depression Scale (HADS) anxiety subscale ($r = 0.5509$, $P = 0.0178$) in the left anterior cerebellar lobe, a negative correlation between the decreased FC strength and the score of the National Institutes of Health Chronic Prostatitis Symptom Index ($r = -0.6281$, $P = 0.0053$) in the area of left mPFC, and a negative correlation between the decreased FC strength and the score of HADS anxiety subscale ($r = -0.5252$, $P = 0.0252$). *Conclusion*. Patients with CP/CPPS had alterations in brain function, which consisted of the default mode network's compromised integrity. These alterations might play a crucial role in the pathogenesis and development of CP/CPPS.

## 1. Introduction

In the urological clinic, chronic prostatitis/chronic pelvic pain syndrome (CP/CPPS) occurs in 5% to 10% of the male population [1]. According to the category of National Institutes of Health, CP/CPPS was defined as urological pain or discomfort in the pelvic region sustaining for no less than 3 months during the preceding 6 months that is associated with lower urinary symptoms and not in consort with a urinary tract bacterial infection [2]. Also, it is regularly connected with negative cognitive, sexual, behavioral, or emotional consequences [3].

The pathogenesis of CP/CPPS is still unidentified. The former studies suggested a specific role for immunological, neurological, endocrine, and psychological factors [4]. About 78% of the men with CP/CPPS are found to be fighting with psychological stress [5]. CP/CPPS is a kind of chronic pain disorder. Thus, CP/CPPS should be recognized as the compound, including a combination of spontaneous visceral and referred somatic pain characteristics (i.e., pelvic visceral and referred perineal pain) and the involvement of central sensitization in the spinal cord and brain [6].

Functional magnetic resonance imaging (fMRI) and higher magnetic field strengths could enable scientists to investigate the brain accurately and noninvasively. Based on hemodynamics, resting state in fMRI can assess functional connectivity reflecting synchronous ultraslow frequency oscillation between brain areas, which provides insight into how brain areas work together to produce pain and how these networks may be modified due to chronic pain [7]. The effect of blood oxygen level-dependent (BOLD) originates from an increase in metabolic

activity and blood flow in activating parts of the central nervous system [8]. Functional connectivity (FC) describes the temporal synchrony or interregional cooperation between two or more spatially separate regions [9]. Previous studies showed FC between the motor cortex and the posterior insula may be among the most significant markers of altered brain function in men with CP/CPPS and may represent changes in the integration of viscerosensory and motor processing [10]. However, the extent of other FC changes in CP/CPPS and how deep the RSN reorganization would be specific/standard across this particular disease remains mostly unclear.

Many patients with CP/CPPS complained that the disease affected their life when they were in a state of relaxation and resting instead of concentrating, working, and physical exercise. Coincidentally, the default mode network (DMN), which was initially identified as the "task-negative network," was originally recognized as domains that consistently showed synchronized deactivation during tasks and prominent activation in the resting state [11]. The DMN, based on the medial prefrontal cortex (mPFC) and posterior cingulate gyrus (PCC), exhibits higher metabolic activity at rest than during the performance of externally oriented cognitive tasks [12].

We hypothesized that due to chronic pain, the long-term hemodynamic changes in the brain that endure CP/CPPS do have diverse brain activity regions distinguished by resting-state fMRI. To figure out the profound mechanism of CP/CPPS, we utilized the BOLD fMRI method to investigate the FC alterations of CP/CPPS in patients with spontaneous pelvic pain during resting state.

## 2. Materials and Methods

*2.1. Characteristics of Participants.* The Ethics Committee approved the Jingan District Centre Hospital data collection, Shanghai (Ethical Approval Code: no. 2020-05). We collected data from 18 right-handed male patients with CP/CPPS and 21 healthy right-handed age and gender-matched controls (Table 1). To reduce the potential impact of senile brain atrophy, aged from 20 to 50 years male volunteers were required. Consistent with the definition of CP/CPPS, this disease was diagnosed by exclusion. The diagnosis was based on the chief complaint, medical history, routine urine, prostatic fluid examination, prostate ultrasound, and urinary system ultrasound to exclude acute or chronic bacterial prostatitis, prostate cancer, benign prostate hyperplasia, and other related diseases among the pelvic. All the patients had not taken any medications before, and they denied the other discomforts. The participants would be excluded if they got any acute or chronic infectious disease, other chronic pain diseases, internal organic diseases, history of malignant tumors, and chronic diseases that might contribute to peripheral nerve injury like diabetes mellitus and hypertension. We instantly took them to get the fMRI scan after their diagnosis through standardized clinical procedures, so all the patients of CP/CPPS were performed MRI examination only when they showed symptoms. Since we considered some clinical symptoms of the CP/CPPS involved in the lower urinary tract symptoms, all the participants were required to empty their urine bladders before entering the fMRI. After obtaining the written informed consent, all of the participants were requested to finish one National Institutes of Health Chronic Prostatitis Symptom Index (NIH-CPSI) scale [13] and one Hospital Anxiety and Depression Scale (HADS) [14]. The numerical rating scale (NRS) score was used to measure patients' spontaneous pain and eliminated potential pain patients in healthy control [15]. Then, we instructed the patients to take regular drug therapy according to their symptoms in case of delay in diagnosis. The acquisition, processing, and analysis of fMRI data were evaluated by a senior neuroradiologist together with our urologists.

*2.2. Resting-State fMRI Data Acquisition.* As shown in Figure 1, we primarily recruited a cohort of health control (22 persons) and patients (22 persons). After we eliminated unqualified candidates, fMRI data were obtained from 18 patients with chronic prostatitis/chronic pelvic pain syndrome rated spontaneous pain and also from 21 healthy control as participants inside the scanner. The resting-state fMRI data were obtained using a 3.0T GE MR750 MRI scanner with an eight-channel phased-array head coil at the Jingan District Centre Hospital, Shanghai. Whole resting-state fMRI data were acquired, using a gradient-recalled echo-planar imaging pulse sequence (repetition time (TR)/echo time (TE) = 2, 000/30 ms, FA = 90°, acquisition matrix = 64 × 64, field of view (FOV) = 22 × 22 $cm^2$, slice thickness = 4 mm, no gap, 43 slices, and total 240 time points). The high resolution T1-weighted magnetic resonance images were collected by a three-dimensional fast spoiled gradient-echo dual-echo sequence (TR = 8100 ms, TE = 3.1 ms, FA = 8 deg, matrix = 256 × 256, FOV = 25.6 × 25.6 $cm^2$, slice thickness = 1 mm, no gap, and 156 slices). To classify individual participants, the authors approached personal information during or after data collection. All the participants were required to keep their eyes closed, reduce thinking, maintain calm, and avoid falling asleep. In this step, the data would be eliminated if the senior neuroradiologist found any possible space-occupying lesion and vascular malformation in the brain.

*2.3. Data Preprocessing Analysis.* All the DICOM files in format were converted to NIFTI files by MRIconvert (http://lcni.uoregon.edu/jolinda/MRIConvert/). The resting-state fMRI data were also preprocessed using SPM12 (https://www.fil.ion.ucl.ac.uk/spm/) and RESTPlus V1.22 (http://www.restfmri.net). To avoid statistic errors, all the scans were examined before preprocessed. The preprocessing steps included as follows: (1) discarding the first 10 time points for reaching a steady-state magnetization and allowing all the participants to adapt to scanning noise, and the remaining 190 time points of image were processed in our following study; (2) slice timing correction, slice order could be Matlab formula: [1 : 2 : 43 2 : 2 : 42]; (3) head motion correction; (4) normalization, transforming the brain images to reduce the variability between individuals and allowing meaningful group analyses by using T1 image unified segmentation, with bounding box [-90, -126, -72; 90, 90, 108] and isotropic voxel size [3, 3, 3]; (5) spatial smoothing, by the convolution of the three-dimensional image with a three-dimensional Gaussian kernel with a full width at half maximum (FWHM) of 6 mm;

Table 1: The characteristics of participants.

| | CP/CPPS patients ($n = 18$) | Healthy controls ($n = 21$) | $P$ value |
|---|---|---|---|
| Gender | Male | Male | — |
| Age/years | 30.92 ± 7.69 | 37.56 ± 7.86 | 0.0626 |
| Duration of illness/months | 20.00 ± 8.49 | 0 | <0.001 |
| NIH-CPSI score (1 + 2 + 3 + 4 + 5 + 6 + 7 + 8 + 9) | 17.33 ± 4.40 | 0 | <0.001 |
| Pain and discomforts (1 + 2 + 3 + 4) | 11.55 ± 2.16 | 0 | <0.001 |
| Lower urinary tract symptoms (5 + 6) | 1.22 ± 0.78 | 0 | <0.001 |
| Impact on quality of life (7 + 8 + 9) | 4.55 ± 2.63 | 0 | <0.001 |
| NRS (4) | 2.44 ± 0.50 | 0 | <0.001 |
| Severity of symptoms (1 + 2 + 3 + 4 + 5 + 6) | 12.77 ± 2.34 | 0 | <0.001 |
| HADS (anxiety) | 8.11 ± 2.02 | 0.90 ± 1.22 | <0.001 |
| HADS (depression) | 3.22 ± 0.79 | 0.33 ± 0.47 | <0.001 |

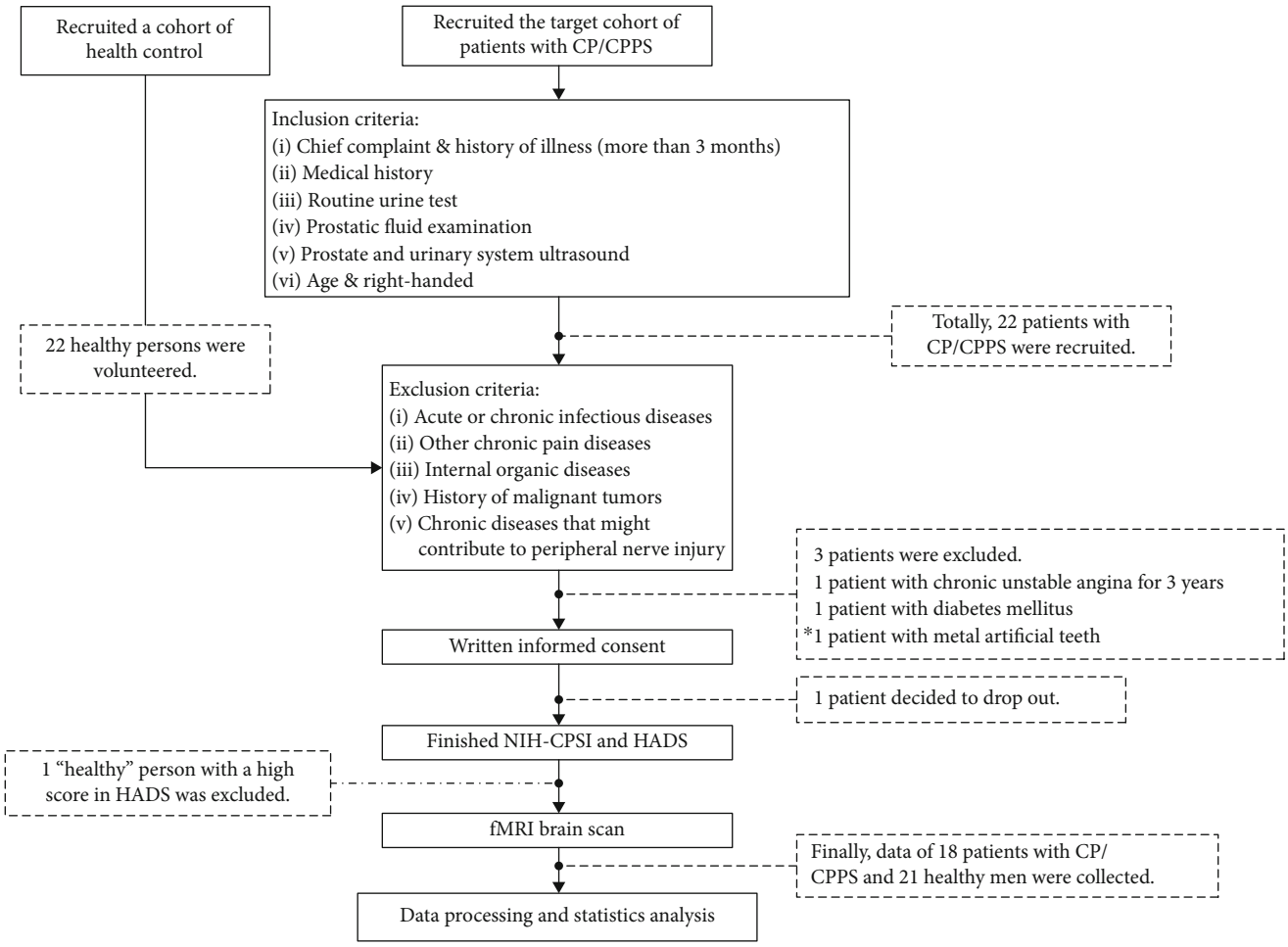


Figure 1: Study design flow chart. We initially recruited a cohort of health control (22 persons) and patients (22 persons). However, 1 person in health control and 4 persons in patient cohort were excluded. Their detailed reasons were demonstrated in the flow chart.

(6) removing the linear trend of the time series caused by warming of the scanner or adaptation of the participants, with the time accumulation; and (7) nuisance covariable regression, including 6 head motion parameters, the cerebrospinal flow signals, and white matter signals. The mean value of the time series of each voxel was not added back in this step. After preprocessing in RESTPlus, the linear trend was removed. The fMRI data were temporally band-pass filtered

Table 2: The details of differentiated FC in brain region.

| Brain region | MNI coordinates | | | Voxel numbers | Peak intensity |
|---|---|---|---|---|---|
| | *X* | *Y* | *Z* | | |
| Left cerebellum anterior lobe | -9 | -51 | -3 | 7 | 7.12 |
| Left mPFC | -6 | 51 | -3 | 13 | -7.40 |

(0.01-0.08 Hz) to decrease the very low-frequency drift and high-frequency noise from the cardiac and respiratory systems.

*2.4. Voxel-Wised FC Analysis.* FC analysis was performed using the RESTplus V1.22 after data preprocessing. Recognized as the core regions of the anterior and posterior DMN, the mPFC and the PCC were selected as seed points for analysis. Their Montreal Neurological Institute (MNI) coordinates are (-6, 52, -2) and (-8, -56, 26), respectively [16]. A sphere with a radius of 6 mm was selected as the region of interest (ROI). The average time series of all the voxels in ROI were extracted and calculated. Then, Pearson's correlation analysis was performed on the time series of each voxel in the whole brain. Thus, the functional connection diagram of mPFC and PCC with the whole brain was obtained. Pearson correlation analysis was performed on the time series of each voxel. The functional connection value was expressed by the correlation coefficient ($r$ value), and then, it was converted to $Z$ value by Fisher's to conform to the normal distribution.

*2.5. Statistics Analysis.* The results of characteristics of participants, NRS scores, NIH-CPSI scores, and HADS scores were compared using SPSS 17.0. A two-sample $t$-test was conducted based on the measurement data (age, duration of illness, NRS scores, NIH-CPSI scores, and HADS scores), and outcomes were listed as $\bar{X} \pm S$ (Table 1). A two-sample $t$-test was conducted based on the zFC values by the RESTplus software based on SPM12. Gaussian random field (GFR) theory, as multiple comparison correction, corrected functional connection values (voxel $P < 0.01$, cluster $P < 0.05$). The brain regions of increased or decreased FC values were taken as ROIs, and the values of each ROIs were extracted as independent variables by RESTplus. Pearson regression analysis was conducted with SPSS 11.0 as dependent variables to NIH-CPSI scores and HADS scores. The significant difference was set at $P < 0.05$. Activities larger than 5 voxels were displayed in pseudo-color on the calibrated standard brain map, and their MNI coordinates, positions, and voxel sizes of peak intensity were listed in a table (Table 2). The results of Pearson regression analysis were presented by GraphPad 5.0.

## 3. Results and Discussion

*3.1. The Characteristics of Participants.* We evaluated a male, dextromanual, and age-matched observational cohort ($P = 0.0626$). In the patient line (Table 1), the duration of the illness was about 20 months, accurately as defined. To avoid the abnormal results triggered by senile atrophy of the brain, we recruited volunteers aged between 20 and 50 years old. The score of NIH-CPSI revealed the patients suffered from CP/CPPS in the situation between moderate and severe edge, for a score above 18 means severe chronic prostatitis. Because the score of HADS would be meaningful when the score is more than 7, the main feature characteristic of patients in our study was anxiety as the score of HADS anxiety subscale was $8.11 \pm 2.02$ while the score of HADS depression subscale was $3.22 \pm 0.79$. Therefore, we paid our emphasis on the correlation between chronic pelvic pain caused by CP/CPPS and anxiety as a psychological symptom. The score of NRS was recognized as mild spontaneous pain that does not interfere with sleep.

*3.2. The Abnormal Brain Regions by FC Analysis.* In our study (see in Figure 2 and Table 2), when we set the PCC as the seed point, we found the noticeably lower intensity of mPFC (peak intensity: -7.40) and the ascending intensity of posterior DMN regions like anterior lobe of cerebellum (peak intensity: 7.12). Simultaneously, although we also put the mPFC as the seed point, there was no statistical difference in zFC, which indicated that the anterior and posterior DMN showed a dissociation pattern.

*3.3. The Correlation of Abnormal Brain Regions and Clinical Scale Scores.* As shown in Figure 3, in the patient cohort of CP/CPPS, the zFC strength of the negative activated area in the left mPFC was negatively correlated with the score of NIH-CPSI scale ($r = -0.6281$, $P = 0.0053$). The zFC strength of negative activated area in the left mPFC was negatively correlated with the score of HADS anxiety subscale ($r = -0.5252$, $P = 0.0252$) while the zFC strength of positive activated area in the left cerebellum anterior lobe was positively correlated with the score of HADS anxiety subscale ($r = 0.5509$, $P = 0.0178$). In contrast, there was no statistical difference between the zFC strength of this area and the score of NIH-CPSI scale ($P = 0.3821$). Additionally, the correlation between the NRS scores and abnormal zFC strength revealed no statistical difference, which is possibly due to the limited sample size.

## 4. Discussion

The default mode network (DMN), identified as the "task-negative network," was initially recognized as domains that consistently showed synchronized deactivation during tasks and prominent activation in the resting state [11]. According to the actual functional and anatomical classification of DMN, it is mainly subdivided into two parts, the anterior DMN and the posterior DMN, but both of these parts are responsible for spontaneous or self-generated cognition [17]. It has been proved that chronic pain is related to

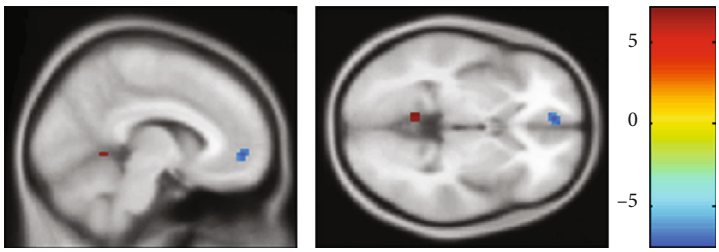


Figure 2: The differentiated brain regions with abnormal zFC values: (a) sagittal view; (b) axial view. The red region was positively activated, and the blue region was negatively activated ($P < 0.05$, voxel ≥ 5, GFR correction, voxel $P < 0.01$, cluster $P < 0.05$). Compared to the healthy control group, the patient cohort of CP/CPPS had differentiated brain regions with abnormal zFC values when we set the PCC as the seed point.

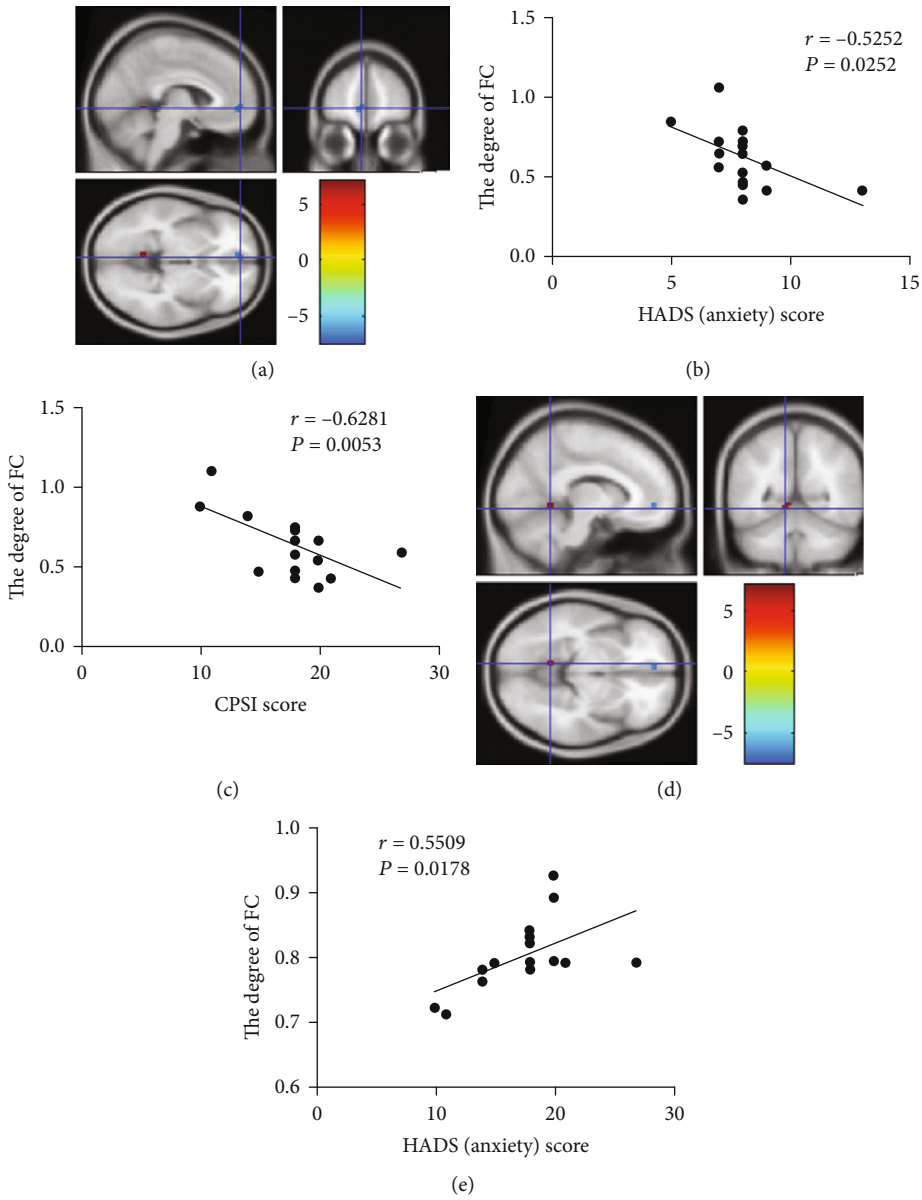


Figure 3: The differentiated brain regions with abnormal zFC values and their correlation with HADS anxiety subscale scores and NIH-CPSI scores. (a) Negatively activated clusters. (b) The correlation between the HADS (anxiety) score and the degree of FC in area of negatively activated clusters. (c) The correlation between the CPSI score and the degree of FC in area of negatively activated clusters. (d) Positively activated clusters. (e) The correlation between the HADS (anxiety) score and the degree of FC in area of positively activated clusters.

dysregulation within the DMN, and this dysregulation may help explain the mechanism of chronic pain syndromes [18, 19].

PCC is a part of the posterior medial cortex [20]. Its main functional characteristic in DMN is its central status [21]. PCC is a highly connected and metabolically active brain region, and its primary function is to integrate the central system, regulate the flow of information around the brain, and thus regulate attention and cognition to balance internal and external thinking [22]. The activity of PCC changes with arousal state and its interactions with other brain networks may be necessary for consciousness. The previous studies of fMRI indicated that a series of neurological and mental diseases like schizophrenia, autism, depression, and attention deficit hyperactivity disorder attribute to the abnormality of PCC [23, 24]. Chronic pain requires attention and competes for cognitive resource stimuli, so the internal functional alternatives in DMN might be the basis for the changes in attention and cognition during pain [16]. The previous study has proved that the FC strength within DMN of patients with chronic pain was connected to pain rumination that was a measure of an individual's constant attention to their pain and its potential negative consequences [25]. The internal changes of connectivity within the DMN may reduce the aptitude of other stimuli to attract the individual's attention away from the pain.

The mPFC plays an imperative role in both executive function and pain processing, and the mPFC undergoes a major reorganization in chronic pain [26]. Deactivation of mPFC output is causally correlated with both the cognitive and the sensory components of neuropathic pain [27]. The mPFC could serve dual, opposing roles in pain: (1) it mediates antinociceptive effects, due to its connections with other cortical areas as the main source of cortical afferents to the PAG for modulation of pain; (2) it could induce pain chronification via its corticostriatal projection, possibly depending on the level of dopamine receptor activation (or lack of) in the ventral tegmental area-nucleus accumbens reward pathway [28]. Painful stimuli may affect cognition—the mPFC and the mediodorsal nucleus of the thalamus form interconnected neural circuits that are important for spatial cognition and memory, and in chronic pain states, the mPFC is deactivated, and mPFC-dependent tasks such as attention and working memory are impaired [29]. Additionally, the functional and structural connectivity of mPFC-PAG might be associated with the individual differences in the tendency to self-concerns about pain [30]. So, due to the individual differences, it is possible to explain the phenomenon that there is no statistical difference between the patient group and the health control when we set the mPFC as the seed point, which may request to be further verified by subsequent large sample size experiments.

In the DMN, the changes of FC in the mPFC were also associated with self-reported anxiety levels [31]. The patients with chronic pain would not only feel anxiety but also get the fear related to the pain [32]. mPFC played a pivotal role in the brain circuits of fear, and the alternatives of the DMN might be the tractive force in this process. The fear related to the pain would promote the side effects of cognition and behavior [33]. More importantly, the fear of pain, which was motivated by the anticipation of pain, was a prognostic factor affecting the treatment of chronic pain [34]. Consequently, the clinical doctors must apprehend the strong impact of the cognitive process on the fear of pain, which even brings about avoidance behavior. In the clinic, many patients with CP/CPPS display poor compliance, i.e., they fail to take medicine on time and make psychological confrontation with the doctor. These patients should be carefully communicated and instructed. The main treatable processes conclude (1) to eliminate fear, explaining the idea "pain does not an equal injury"; (2) helping patients set realistic and reasonable expectations of treatment; (3) to improve self-efficacy and reduce self-catastrophizing, encouraging self-monitoring of patients; and (4) demanding the patients to the mental health department if the patients express a severe fear [35]. Otherwise, the anxiety, fear-avoidance, and density of chronic pain of the patients would aggravate each other. In similar studies, like chronic low back pain, complex regional pain syndrome, and knee osteoarthritis, there was decreased connectivity between mPFC and posterior DMN, and at the same time, there is increasing connectivity between mPFC and insular cortex, which is in proportion to pain intensity [18, 19]. These consequences were similar to the results in our study that there was decreased connectivity between mPFC and posterior DMN, and its zFC values negatively correlated to the prostatitis-like symptom scale scores, which also prompted that we should put emphasis on the alteration of the insular cortex in the patients with CP/CPPS in further study.

The cerebellum had anatomical connections to multiple regions of the frontal cortex and limbic region, critical for its involvement in visual and auditory processing, motion perception, cognition, and pain processing [36]. Yet, the specific function of the cerebellum in the process of pain and its role in pain disorders were still unclear [37]. The anterior cerebellum was also known as the old cerebellum, mainly involving motion control and body balance regulation [36]. Earlier studies had found anatomical connections between the cerebellum and the prefrontal cortex, which are also involved in motor function and somatic balance [36, 38]. A study had found that pain experiences were organized by somatization, and the cerebellum, activated by desomatization, indirectly accepted the information to engage in processing situational and emotional states partly through the cortex and subcortical connections [39]. During painful thermal stimulation, the bilateral frontal lobes of the cerebellum were active, which indicated the frontal lobes of the cerebellum might respond to motor control in response to painful stimuli after pain activation [39]. One study suggested that the cerebellum plays a vital role in the localizing of painful stimuli [40]. Because of the lack of relative evidence, it was speculated that the cerebellum is an integrator of multiple effector systems, including emotional processing, pain regulation, and sensorimotor processing [41, 42].

In this study, we speculated that the anterior cerebellum might respond to pain by motor control. Since the activated cerebellar motor regions were correlated with the anxiety levels in patients with CP/CPPS, it was also possible that multiple effector systems got involved in pain integration. There

were still differentiated functional subregions in the anterior cerebellum lobe, which their precise mechanism of structure and function were unclear. Further investigation was required. In a study of chronic low back pain, the dysfunction of mPFC might lead to the possibility of unconscious pain behavior controlled by the cerebellum [43]. In another study of chronic migraine, it revealed that the cerebellum was not only involved in the pain process of migraine but also played a significant role in the prognosis of migraine [44]. There was increasing connectivity between the cerebellum and corpus callosum cortex, temporal lobe in the patients of chronic migraine, and decreasing connectivity between the cerebellum and prefrontal lobe, which correlated with the poor prognosis [44].

So, it illustrated that in addition to motor control, the frontal cerebellum might also affect the patient's mood through its emotional processing capacity or get through structural connections with the prefrontal lobe. It was also proved that the clinical treatment of CP/CPPS should take a measure of mind-body therapy [45, 46]. The aim of cognitive reappraisal to the patients was to reverse maladaptive cognition evaluation of their own [47, 48]. Through mindfulness meditation, there is a particular therapeutic effect as well [26, 49].

The degree of reorganization within DMN depends on the intensity and duration of chronic pain, mainly after more than 10 years of chronic pain [19, 50]. We hypothesized that as time went on, the functional connectivity of posterior DMN and mPFC would be decreased, and its connectivity to the anterior cerebellum lobe would be increased, which reflected the influence of the clinical symptoms of CP/CPPS gradually improved from emotion to more fear of pain. The fear of pain progressively changed the behavior of patients, while the avoidance would deepen the anxiety and distraction of DMN. Owing to the anatomical affiliation between the cerebellum and the prefrontal lobe, whether the anterior cerebellum and mPFC had the same or similar FC changes or structural reconstruction remained to be investigated in the future.

Consequently, patients with CP/CPPS had changes in brain function, which consisted of the compromised integrity of the default mode network. These changes may play a crucial role in the pathogenesis and development of CP/CPPS. Chronic pain should be best managed by using a multidisciplinary, biopsychosocial approach. With the development of the research on etiology and mechanisms of CP/CPPS, we would broaden our mind to expand our etiological treatment, provide new targets for therapeutic trials, and improve patients' quality of life.

Nevertheless, there might be some limitations in this research. The cohort of participants was relatively small. In the patients of CP/CPPS, the main alteration of emotion and psychology was anxiety, while they seldom revealed symptoms of depression, which may be because the duration of illness perhaps was a little shorter than other researches of chronic pain. This study was an observational study without intervention. Therefore, based on current findings, well-designed clinical therapeutic cohorts are needed to investigate further. Additionally, the tool fMRI could only describe macroscopic changes in the patients' brain function and structure. It has been proved that chronic pain may be related to neural plasticity, and the deeper cytological mechanism needs to be explored by other methods.

## 5. Conclusions

Patients with CP/CPPS had some alterations in functional connectivity of the brain, which mainly included the broken integrity of the default mode network. These changes may participate in the pathogenesis and progression of CP/CPPS.

## Data Availability

The datasets used and analyzed in the current study are available from the corresponding author on reasonable request.

## Conflicts of Interest

There is no conflict of interest regarding the publication of this paper.

## Acknowledgments

We thank Dr. Fen and Dr. Wu for kindly providing valuable support during the research, especially in the fMRI data processing and analysis. Both of them kindly provided almost all of their experience in these procedures as senior researchers in fMRI. We appreciated the outstanding assistance of Dr. Huaping Sun, who came from Department of Radiology, Huashan Hospital, Fudan University, in the fMRI data acquisition. We could not get any data only if we were under his direction. This study was supported by grants from the National Natural Science Foundation of China (No. 81372316), the Chenguang Program of Shanghai Municipal Education Commission (No. 158554), the Chinese traditional medicine project of Shanghai Health Commission (No. 2020LP020), and the Health research project of Jing 'an District, Shanghai (No. 2020MS04).

## References

[1] H. Schneider, M. Ludwig, H. M. Hossain, T. Diemer, and W. Weidner, "The 2001 Giessen Cohort Study on patients with prostatitis syndrome–an evaluation of inflammatory status and search for microorganisms 10 years after a first analysis," *Andrologia*, vol. 35, no. 5, pp. 258–262, 2003.

[2] J. N. Krieger, L. Nyberg Jr., and J. C. Nickel, "NIH consensus definition and classification of prostatitis," *JAMA*, vol. 282, no. 3, pp. 236-237, 1999.

[3] M. B. Passavanti, V. Pota, P. Sansone, C. Aurilio, L. De Nardis, and M. C. Pace, "Chronic pelvic pain: assessment, evaluation, and objectivation," *Pain Research and Treatment*, vol. 2017, Article ID 9472925, 15 pages, 2017.

[4] M. A. Pontari and M. R. Ruggieri, "Mechanisms in prostatitis/-chronic pelvic pain syndrome," *The Journal of Urology*, vol. 179, 5 Suppl, pp. S61–S67, 2008.

[5] J. K. Kwon and I. H. Chang, "Pain, catastrophizing, and depression in chronic prostatitis/chronic pelvic pain syndrome," *International Neurourology Journal*, vol. 17, no. 2, pp. 48–58, 2013.

[6] J. D. Loeser and R. Melzack, "Pain: an overview," *Lancet*, vol. 353, no. 9164, pp. 1607–1609, 1999.

[7] K. D. Davis and M. Moayedi, "Central mechanisms of pain revealed through functional and structural MRI," *Journal of Neuroimmune Pharmacology*, vol. 8, no. 3, pp. 518–534, 2013.

[8] J. P. Bach, M. Lupke, P. Dziallas et al., "Auditory functional magnetic resonance imaging in dogs–normalization and group analysis and the processing of pitch in the canine auditory pathways," *BMC Veterinary Research*, vol. 12, no. 1, p. 32, 2016.

[9] Y. C. Chen, W. Xia, B. Luo et al., "Frequency-specific alternations in the amplitude of low-frequency fluctuations in chronic tinnitus," *Frontiers in Neural Circuits*, vol. 9, p. 67, 2015.

[10] J. J. Kutch, M. S. Yani, S. Asavasopon et al., "Altered resting state neuromotor connectivity in men with chronic prostatitis/chronic pelvic pain syndrome: a Mapp: research network neuroimaging study," *NeuroImage: Clinical*, vol. 8, pp. 493–502, 2015.

[11] M. E. Raichle and A. Z. Snyder, "A default mode of brain function: a brief history of an evolving idea," *NeuroImage*, vol. 37, no. 4, pp. 1083–1090, 2007.

[12] J. R. Andrews-Hanna, J. S. Reidler, J. Sepulcre, R. Poulin, and R. L. Buckner, "Functional-anatomic fractionation of the brain's default network," *Neuron*, vol. 65, no. 4, pp. 550–562, 2010.

[13] M. S. Litwin, M. McNaughton-Collins, F. FJ Jr. et al., "The National Institutes of Health chronic prostatitis symptom index: development and validation of a new outcome MEASURE," *The Journal of Urology*, vol. 162, no. 2, pp. 369–375, 1999.

[14] R. P. Snaith, "The hospital anxiety and depression scale," *Health and Quality of Life Outcomes*, vol. 1, no. 1, p. 29, 2003.

[15] F. A. Andrade, L. V. Pereira, and F. A. Sousa, "Pain measurement in the elderly: a review," *Revista Latino-Americana de Enfermagem*, vol. 14, no. 2, pp. 271–276, 2006.

[16] Z. Alshelh, K. K. Marciszewski, R. Akhter et al., "Disruption of default mode network dynamics in acute and chronic pain states," *NeuroImage: Clinical*, vol. 17, pp. 222–231, 2018.

[17] P. C. Mulders, P. F. van Eijndhoven, A. H. Schene, C. F. Beckmann, and I. Tendolkar, "Resting-state functional connectivity in major depressive disorder: a review," *Neuroscience and Biobehavioral Reviews*, vol. 56, pp. 330–344, 2015.

[18] M. N. Baliki, P. Y. Geha, A. V. Apkarian, and D. R. Chialvo, "Beyond feeling: chronic pain hurts the brain, disrupting the default-mode network dynamics," *Journal of Neuroscience*, vol. 28, no. 6, pp. 1398–1403, 2008.

[19] M. N. Baliki, A. R. Mansour, A. T. Baria, and A. V. Apkarian, "Functional reorganization of the default mode network across chronic pain conditions," *PLoS One*, vol. 9, no. 9, article e106133, 2014.

[20] P. Hagmann, L. Cammoun, X. Gigandet et al., "Mapping the structural core of human cerebral cortex," *PLoS Biology*, vol. 6, no. 7, article e159, 2008.

[21] M. D. Greicius, K. Supekar, V. Menon, and R. F. Dougherty, "Resting-state functional connectivity reflects structural connectivity in the default mode network," *Cerebral Cortex*, vol. 19, no. 1, pp. 72–78, 2009.

[22] R. Leech and D. J. Sharp, "The role of the posterior cingulate cortex in cognition and disease," *Brain*, vol. 137, no. 1, pp. 12–32, 2014.

[23] R. L. Buckner, J. R. Andrews-Hanna, and D. L. Schacter, "The brain's default network," *Annals of the New York Academy of Sciences*, vol. 1124, no. 1, pp. 1–38, 2008.

[24] D. Zhang and M. E. Raichle, "Disease and the brain's dark energy," *Nature Reviews Neurology*, vol. 6, no. 1, pp. 15–28, 2010.

[25] A. Kucyi, M. Moayedi, I. Weissman-Fogel et al., "Enhanced medial prefrontal-default mode network functional connectivity in chronic pain and its association with pain rumination," *Journal of Neuroscience*, vol. 34, no. 11, pp. 3969–3975, 2014.

[26] L. Hilton, S. Hempel, B. A. Ewing et al., "Mindfulness meditation for chronic pain: systematic review and meta-analysis," *Annals of Behavioral Medicine*, vol. 51, no. 2, pp. 199–213, 2017.

[27] D. Radzicki, S. L. Pollema-Mays, A. Sanz-Clemente, and M. Martina, "Loss of M1 receptor dependent cholinergic excitation contributes to mPFC deactivation in neuropathic pain," *Journal of Neuroscience*, vol. 37, no. 9, pp. 2292–2304, 2017.

[28] W. Y. Ong, C. S. Stohler, and D. R. Herr, "Role of the prefrontal cortex in pain processing," *Molecular Neurobiology*, vol. 56, no. 2, pp. 1137–1166, 2019.

[29] M. Kunz, V. Mylius, K. Schepelmann, and S. Lautenbacher, "Loss in executive functioning best explains changes in pain responsiveness in patients with dementia-related cognitive decline," *Behavioural Neurology*, vol. 2015, Article ID 878157, 7 pages, 2015.

[30] Y. Du, G. D. Pearlson, Q. Yu et al., "Interaction among subsystems within default mode network diminished in schizophrenia patients: a dynamic connectivity approach," *Schizophrenia Research*, vol. 170, no. 1, pp. 55–65, 2016.

[31] S. Elsenbruch and O. T. Wolf, "Could stress contribute to pain-related fear in chronic pain?," *Frontiers in Behavioral Neuroscience*, vol. 9, p. 340, 2015.

[32] J. W. Vlaeyen and S. J. Linton, "Fear-avoidance and its consequences in chronic musculoskeletal pain: a state of the art," *Pain*, vol. 85, no. 3, pp. 317–332, 2000.

[33] M. T. Tseng, Y. Kong, F. Eippert, and I. Tracey, "Determining the neural substrate for encoding a memory of human pain and the influence of anxiety," *Journal of Neuroscience*, vol. 37, no. 49, pp. 11806–11817, 2017.

[34] C. J. Stoodley and J. D. Schmahmann, "Evidence for topographic organization in the cerebellum of motor control versus cognitive and affective processing," *Cortex*, vol. 46, no. 7, pp. 831–844, 2010.

[35] D. C. Turk and H. D. Wilson, "Fear of pain as a prognostic factor in chronic pain: conceptual models, assessment, and treatment implications," *Current Pain and Headache Reports*, vol. 14, no. 2, pp. 88–95, 2010.

[36] O. Baumann, R. J. Borra, J. M. Bower et al., "Consensus paper: the role of the cerebellum in perceptual processes," *Cerebellum*, vol. 14, no. 2, pp. 197–220, 2015.

[37] T. Bocci, G. De Carolis, R. Ferrucci et al., "Cerebellar transcranial direct current stimulation (Ctdcs) ameliorates phantom limb pain and non-painful phantom limb sensations," *Cerebellum*, vol. 18, no. 3, pp. 527–535, 2019.

[38] J. D. Schmahmann and D. N. Pandya, "Anatomic organization of the basilar pontine projections from prefrontal cortices in rhesus monkey," *Journal of Neuroscience*, vol. 17, no. 1, pp. 438–458, 1997.

[39] F. H. S. M. Welman, A. E. Smit, J. L. M. Jongen, D. Tibboel, J. N. van der Geest, and J. C. Holstege, "Pain experience is

somatotopically organized and overlaps with pain anticipation in the human cerebellum," *Cerebellum*, vol. 17, no. 4, pp. 447–460, 2018.

[40] H. L. Fields, "Pain modulation: expectation, opioid analgesia and virtual pain," *Progress in Brain Research*, vol. 122, pp. 245–253, 2000.

[41] D. Borsook, E. A. Moulton, S. Tully, J. D. Schmahmann, and L. Becerra, "Human cerebellar responses to brush and heat stimuli in healthy and neuropathic pain subjects," *Cerebellum*, vol. 7, no. 3, pp. 252–272, 2008.

[42] E. A. Moulton, J. D. Schmahmann, L. Becerra, and D. Borsook, "The cerebellum and pain: passive integrator or active participator?," *Brain Research Reviews*, vol. 65, no. 1, pp. 14–27, 2010.

[43] Y. Nakamura, K. Nojiri, H. Yoshihara et al., "Significant differences of brain blood flow in patients with chronic low back pain and acute low back pain detected by brain SPECT," *Journal of Orthopaedic Science*, vol. 19, no. 3, pp. 384–389, 2014.

[44] H.-Y. Liu, P.-L. Lee, K.-H. Chou et al., "The cerebellum is associated with 2-year prognosis in patients with high-frequency migraine," *Journal of Headache and Pain*, vol. 21, no. 1, p. 29, 2020.

[45] T. V. Salomons, M. Moayedi, N. Erpelding, and K. D. Davis, "A brief cognitive-behavioural intervention for pain reduces secondary hyperalgesia," *Pain*, vol. 155, no. 8, pp. 1446–1452, 2014.

[46] A. Yoshino, Y. Okamoto, G. Okada et al., "Changes in resting-state brain networks after cognitive-behavioral therapy for chronic pain," *Psychological Medicine*, vol. 48, no. 7, pp. 1148–1156, 2018.

[47] J. D. Greenwald and K. M. Shafritz, "An integrative neuroscience framework for the treatment of chronic pain: from cellular alterations to behavior," *Frontiers in Integrative Neuroscience*, vol. 12, p. 18, 2018.

[48] D. A. Seminowicz, M. Shpaner, M. L. Keaser et al., "Cognitive-behavioral therapy increases prefrontal cortex gray matter in patients with chronic pain," *The Journal of Pain*, vol. 14, no. 12, pp. 1573–1584, 2013.

[49] J. Kabat-Zinn, L. Lipworth, and R. Burney, "The clinical use of mindfulness meditation for the self-regulation of chronic pain," *Journal of Behavioral Medicine*, vol. 8, no. 2, pp. 163–190, 1985.

[50] H. Yang, X. Y. Long, Y. Yang et al., "Amplitude of low frequency fluctuation within visual areas revealed by resting-state functional MRI," *NeuroImage*, vol. 36, no. 1, pp. 144–152, 2007.

Hindawi
Neural Plasticity
Volume 2021, Article ID 8831379, 13 pages
https://doi.org/10.1155/2021/8831379

*Research Article*

# Changes in Temporal and Spatial Patterns of Intrinsic Brain Activity and Functional Connectivity in Upper-Limb Amputees: An fMRI Study

**Bingbo Bao,[1] Lei Duan,[2] Haifeng Wei,[1] Pengbo Luo,[1] Hongyi Zhu,[1] Tao Gao,[1] Xiaoer Wei,[3] Jing Li,[3] Yuehua Li,[3] Yimin Chai,[1] Changqing Zhang,[1] and Xianyou Zheng[1]**

[1]*Department of Orthopedic Surgery, Shanghai Jiao Tong University Affiliated Sixth People's Hospital, Shanghai 200233, China*
[2]*Department of Orthopedic Surgery, Yueyang Hospital, Shanghai University of Traditional Chinese Medicine, Shanghai 200437, China*
[3]*Institute of Diagnostic and Interventional Radiology, Shanghai Jiao Tong University Affiliated Sixth People's Hospital, Shanghai 200233, China*

Correspondence should be addressed to Xianyou Zheng; zhengxianyou@126.com

Received 30 August 2020; Revised 4 January 2021; Accepted 5 April 2021; Published 24 April 2021

Academic Editor: Carlo Cavaliere



*Background*. Amputation in adults is a serious procedure or traumatic outcome, one that leads to a possible "remapping" of limb representations (somatotopy) in the motor and sensory cortex. The temporal and spatial extent underlying reorganization of somatotopy is unclear. The aim of this study was to better understand how local and global structural plasticity in sensory-motor cortical networks changes temporally and spatially after upper-limb amputation. *Methods*. We studied 8 healthy nonamputee control subjects and 16 complete upper-limb amputees. Resting-state MRI (rs-fMRI) was used to measure local and large-scale relative differences (compared to controls) in both the amplitude of low-frequency fluctuations (ALFF) and degree of centrality (DC) at 2 months, 6 months, and 12 months after traumatic amputation. *Results*. In amputees, rs-fMRI scans revealed differences in spatial patterns of ALFF and DC among brain regions over time. Significant relative increases in ALFF and DC were detected not only in the sensory and motor cortex but also in related cortical regions believed to be involved in cognition and motor planning. We observed changes in the magnitude of ALFFs in the pre- and postcentral gyrus and primary sensory cortex, as well as in the anterior cingulate, parahippocampal gyrus, and hippocampus, 2 months after the amputation. The regional distribution of increases/decreases in ALFFs and DC documented at 2-month postamputation was very different from those at 6 and 12-month postamputation. *Conclusion*. Local and wide-spread changes in ALFFs in the sensorimotor cortex and cognitive-related brain regions after upper-limb amputation may imply dysfunction not only in sensory and motor function but also in areas responsible for sensorimotor integration and motor planning. These results suggest that cortical reorganization after upper extremity deafferentation is temporally and spatially more complicated than previously appreciated, affecting DC in widespread regions.

## 1. Introduction

Not only is complete traumatic limb amputation in adults an emotionally disturbing wound, but it can also develop into a serious medical condition. The traumatic amputation event often causes widespread damage and destruction of skin, tendons, muscles, bones, vasculature, and nerves at the trauma site, and because nerves are axotomized, afferent neurons degenerate, terminal swelling ensues, and regenerative sprouting of the severed axons forms neuromas in the limb stump. This deafferentation also leads to structural and physiological changes in the spinal cord, and some previous studies suggest that a remapping, or reorganization, of limb representations (somatotopy) eventually occurs at the cortical level in motor

and sensory networks. These changes are often accompanied by altered perceptual sensations reported by the patient.

Alterations in the sensorimotor cortex of limb amputees have been extensively investigated with various electrophysiological and neuroimaging techniques [1–5]. Almost 90% of amputees report "phantom sensations," which are described as a vague feeling that the missing upper or lower extremity is still present; some amputees experience severe pain in what seems to be the missing limb [6–9]. Transcranial magnetic stimulation combined with EEG recordings has demonstrated enhanced responses, or neural plasticity, in both motor and somatosensory cortexes in amputees with phantom limb pain [2]. Further, resting-state functional magnetic resonance imaging (rs-fMRI) studies have shown that phantom limb pain is correlated with primary sensorimotor functional remapping after amputation, suggesting that this functional reorganization represents an inappropriate adjustment to deafferentation.

Maladaptive plasticity in sensorimotor networks after nerve deafferentation [10, 11] is one hypothesis to explain the phenomenon of phantom pain. Reorganization of the somatotopic body map in the cortex seems to be an important element in distinguishing painful from nonpainful phantom sensations [10]. However, the widely accepted theory that maladaptive plasticity is the cause of phantom pain has been challenged recently. Rather than plasticity, unusually elevated neural activity in the affected sensorimotor regions of the amputated upper extremity may be responsible for phantom pain [12, 13]. These results may indicate that a more complex and multifactorial cause may underlie phantom pain. Accordingly, studies have also investigated cortical plasticity in amputee patients without phantom pain [5, 14, 15] and found that the alteration in the primary somatosensory cortex is not consistently related to pain symptoms [1].

In the last few decades, neuroimaging techniques like fMRI have been routinely used to detect and analyze functional and anatomical changes in the brain [16, 17], essentially probing the functional architecture of the brain. rs-fMRI is a type of fMRI that provides an estimate of the blood-oxygen-level dependent (BOLD) signal in the brain while subjects are awake, quiet, and not performing any task, and rs-fMRI can provide anatomical specificity of sensorimotor cortex subregional somatotopy [18, 19]. The BOLD signals represent the hemodynamic response to neural activity [20]. The amplitude of low-frequency fluctuations (ALFFs) of the BOLD signal is thought to reflect the magnitude of intrinsic neural activity (local activity of individual regions or voxels) and can provide information about interregional functional connectivity. Thus, rs-fMRI research can reveal neurological processes that occur without external stimulation, and analysis of rs-fMRI signals can reveal information about resting-state connectivity of networks. Only a few studies have analyzed rs-fMRI connectivity and its other metrics such as ALFF to determine whole-brain changes after a traumatic event or in neurological pathology like Parkinson's disease.

In the present study, we used rs-fMRI to investigate local and global brain plasticity in patients with upper-limb amputations. Our aim in this study was to map out how local and global structural and functional connectivity in sensorymotor cortical networks and other brain regions change temporally and spatially after upper-limb amputation. We used two reliable and effective measures of rs-MRI: (1) the ALFF and (2) the degree of centrality (DC), the latter of which reflects the number of instantaneous functional connections between one region and the rest of the brain and thus how much a node influences entire brain areas. These parameters were used to indicate the intensity of spontaneous fluctuations in the BOLD signal at 2, 6, and 12 months after traumatic amputation.

## 2. Methods

*2.1. Participants.* Eight healthy limb-intact man and woman volunteers (control group) were recruited, along with 16 traumatic upper-limb amputees, between the ages of 24 years and 55 years (Table 1). The convenience sample of control subjects was recruited to be balanced by age and sex with the amputee group. A detailed medical history, together with careful examination of head CT scans, confirmed that neither amputees nor controls showed evidence of brain lesions, and their medical history showed no evidence of neurological or psychiatric illness.

All procedures used in this study were approved by the Committee for Medical Ethics of Shanghai Jiao Tong University, Affiliated Sixth People's Hospital, and followed the Ethical Principles for Medical Research Involving Human Subjects (WMA-Declaration of Helsinki). Written informed consent was obtained from all study participants.

*2.2. Data Acquisition and Scanning Procedures.* Scans were acquired on a SIEMENS TRIO 3-Tesla scanner in the Shanghai Sixth People's Hospital, Shanghai Jiao Tong University (SJTU). Anatomical data was acquired using a T1-weighted magnetization prepared rapid acquisition gradient echo sequence with the following parameters: TR = 1900 ms, TE = 2.52 ms, flip angle = 9°, and voxel size = 1m misotropic resolution. Functional data based on the BOLD signal were acquired using a multiple gradient echo planar T2*-weighted pulse sequence, with the following parameters: TR = 3000 ms, TE = 21 ms, flip angle = 90°, imaging matrix = 96 × 96, and FOV = 210 mm axial slices. 40 slices with slice thickness of 2.7 mm and no gap were oriented in the oblique axial plane, covering the whole cortex, with partial coverage of the cerebellum. A total of 240 volumes were collected, during which participants were asked to lie still in a dimmed room with their eyes open. They were explicitly asked not to move any body parts.

*2.3. rs-fMRI Data Preprocessing.* rs-fMRI data of each subject were preprocessed with the software Data Processing Assistant for Resting-State fMRI (DPARSF) [21], which is based on Statistical Parametric Mapping software, SPM8 (Wellcome Trust Centre for Neuroimaging, London, UK; http://www.fil.ion.ucl.ac.uk/spm) and the rs-fMRI Data Analysis Toolkit [22]. Functional image preprocessing was executed according to the following steps: (1) the first 10 volumes were discarded from analysis, since the subjects were adapting to the noise of the scanner and the test situation; this

Table 1: Demographic and clinical characteristics of patients with upper-limb amputation ($n = 16$).

| No. | Sex | Age (yr) | Amputated side (dominant side) | | Amputation level (% limb remaining) | | Elapsed time after amputation (mo.) for rs-fMRI scans | | |
|---|---|---|---|---|---|---|---|---|---|
| 1 | M | 35 | R | (R) | P | (16) | 2 | 6 | 12 |
| 2 | M | 33 | L | (R) | P | (25) | 2 | 6 | 12 |
| 3 | M | 49 | L | (R) | P | (20) | 2 | 6 | 12 |
| 4 | F | 45 | R | (R) | P | (30) | 2 | 6 | 12 |
| 5 | F | 47 | R | (R) | D | (45) | 2 | 6 | 12 |
| 6 | F | 46 | R | (R) | D | (72) | 2 | 6 | 12 |
| 7 | M | 24 | R | (R) | P | (28) | 2 | 6 | 12 |
| 8 | M | 40 | R | (R) | D | (66) | 2 | 6 | 12 |
| 9 | M | 29 | R | (R) | D | (58) | 2 | 6 | 12 |
| 10 | F | 55 | L | (R) | D | (50) | 2 | 6 | 12 |
| 11 | F | 49 | R | (R) | P | (18) | 2 | 6 | 12 |
| 12 | M | 48 | L | (R) | D | (65) | 2 | 6 | 12 |
| 13 | M | 35 | R | (R) | D | (44) | 2 | 6 | 12 |
| 14 | M | 30 | L | (R) | D | (40) | 2 | 6 | 12 |
| 15 | M | 50 | L | (R) | D | (34) | 2 | 6 | 12 |
| 16 | M | 44 | L | (R) | P | (12) | 2 | 6 | 12 |

M: male; F: female; L: left; R: right; D: distal; P: proximal.

Table 2: Relative regional changes in ALFFs at 2 months* in upper-limb amputees ($n = 16$) compared to normal control subjects ($n = 8$).

| Direction of change | Brain region | Voxels* | $t$-value | MNI coordinates | | |
|---|---|---|---|---|---|---|
| | | | | $x$ | $y$ | $z$ |
| Positive ALFF | Hippocampus_L | 189 | 4.257 | -21 | -27 | -12 |
| | ParaHippocampal_L | 189 | 3.452 | -21 | -9 | -30 |
| | Cingulate_Ant_R | 100 | 3.295 | 3 | 27 | 0 |
| | ParaHippocampal_R | 49 | 4.258 | 18 | 0 | -21 |
| | Putamen_L | 34 | 3.489 | -27 | -15 | 3 |
| | Insula_R | 19 | 3.583 | 42 | -9 | -9 |
| | Putamen_R | 16 | 3.334 | 27 | 3 | -3 |
| | Postcentral_L | 11 | 3.414 | -63 | -21 | 18 |
| | Supp_Motor_Area_L | 8 | 3.729 | -3 | 21 | 54 |
| Negative ALFF | Precentral_R | 97 | -4.332 | 42 | -12 | 57 |
| | Precuneus_R | 51 | -4.492 | 6 | -66 | 54 |
| | Precentral_L | 51 | -4.128 | -27 | 0 | 60 |
| | Postcentral_R | 44 | -3.836 | 27 | -42 | 63 |
| | Supp_Motor_Area_R | 42 | -3.705 | 3 | -15 | 72 |
| | Postcentral_L | 19 | -3.758 | -21 | -45 | 69 |

*rs-fMRI scan done 2-month postamputation; MNI: Montreal Neurological Institute; *number of voxels exceeding threshold (cluster size).

preacquisition period also allowed the scanner to stabilize. The number of time points for this period was not less than 230; (2) slice scan time corrections were made; (3) head movement corrections were made; (4) spatial normalization was done, in which the corrected images were then registered to the T1 structural image, and spatially normalized into the standard Montreal Neurological Institute template (resampled into $3 \times 3 \times 3\,\text{mm}^3$); (5) nuisance variables, including white matter signals and head motions, were measured using the Friston-24 model, and cerebrospinal fluid signals were removed by regression; (6) spatial smoothing using a 6 mm FWHM Gaussian kernel was performed; (7) finally, linear trends in the time series were removed.

*2.4. ALFF Calculations.* To study the relationship between functional plasticity after upper extremity deafferentation and resting-state brain functions, we employed ALFF analysis to explore which resting-state networks might be

Table 3: Relative regional changes in ALFFs at 6 months*.

| Direction of change | Brain region | Voxels | $t$-value | MNI coordinates | | |
|---|---|---|---|---|---|---|
| | | | | $x$ | $y$ | $z$ |
| Positive ALFF | Putamen_L | 88 | 4.993 | -21 | -3 | 3 |
| | Hippocampus_L | 36 | 3.804 | -30 | -21 | -21 |
| | Caudate_R | 17 | 3.924 | 15 | 15 | 3 |
| | Putamen_R | 11 | 3.386 | 24 | 6 | -6 |
| | Supp_Motor_Area_L | 10 | 3.521 | -3 | 24 | 54 |
| Negative ALFF | Paracentral_Lobule_L | 903 | -6.797 | -15 | -36 | 63 |
| | Supp_Motor_Area_R | 903 | -5.979 | 6 | -6 | 60 |
| | Lingual_R | 428 | -5.184 | 6 | -72 | -9 |
| | Cuneus_R | 428 | -4.449 | 9 | -81 | 24 |
| | Precuneus_R | 86 | -5.02 | 15 | -66 | 39 |
| | Fusiform_R | 47 | -3.948 | 24 | 9 | -45 |
| | Precentral_R | 30 | -5.233 | 48 | -3 | 42 |
| | Temporal_Inf_R | 27 | -3.21 | 42 | -57 | -9 |

*rs-fMRI scan done 6-month postamputation.

Table 4: Relative regional changes in ALFFs at 12 months.

| Direction of change | Brain region | Voxels | $t$-value | MNI coordinates | | |
|---|---|---|---|---|---|---|
| | | | | $x$ | $y$ | $z$ |
| Positive ALFF | Caudate_R | 202 | 3.91 | 15 | 12 | 3 |
| | Rectus_L | 202 | 3.835 | 3 | 30 | -18 |
| | Cingulate_Mid_L | 95 | 4.198 | -12 | -42 | 42 |
| | Cingulate_Ant_R | 69 | 3.1 | 3 | 18 | 21 |
| | Frontal_Sup_Medial_R | 41 | 3.936 | 6 | 57 | 27 |
| | ParaHippocampal_L | 32 | 3.362 | -27 | -39 | -12 |
| | Cingulate_Mid_R | 30 | 6.424 | 12 | -33 | 42 |
| | Thalamus_R | 30 | 3.805 | 15 | -9 | -3 |
| | Precuneus_L | 28 | 4.674 | -9 | -69 | 60 |
| | Pallidum_L | 25 | 4.531 | -21 | -3 | 0 |
| | Occipital_Mid_R | 24 | 3.614 | 51 | -66 | 24 |
| | Caudate_R | 18 | 5.593 | 21 | -3 | 18 |
| | Supp_Motor_Area_L | 16 | 4.509 | -3 | 21 | 54 |
| | Hippocampus_R | 14 | 4.155 | 36 | -30 | -6 |
| | Putamen_L | 12 | 3.368 | -27 | -15 | 3 |
| | Insula_R | 10 | 3.873 | 39 | -18 | 0 |
| Negative ALFF | Lingual_R | 476 | -6.267 | 18 | -63 | -6 |
| | Fusiform_R | 102 | -5.381 | 24 | 3 | -45 |
| | Lingual_L | 67 | -3.192 | -12 | -75 | -6 |
| | Precuneus_R | 55 | -4.646 | 24 | -45 | 6 |
| | Postcentral_R | 41 | -6.032 | 27 | -42 | 63 |
| | Precentral_R | 29 | -6.454 | 30 | -21 | 63 |
| | Precentral_L | 26 | -4.588 | -21 | -18 | 63 |
| | Supp_Motor_Area_R | 25 | -5.477 | 3 | -9 | 57 |
| | Paracentral_Lobule_L | 13 | -3.299 | -18 | -30 | 66 |

*rs-fMRI scan done 12-month postamputation.

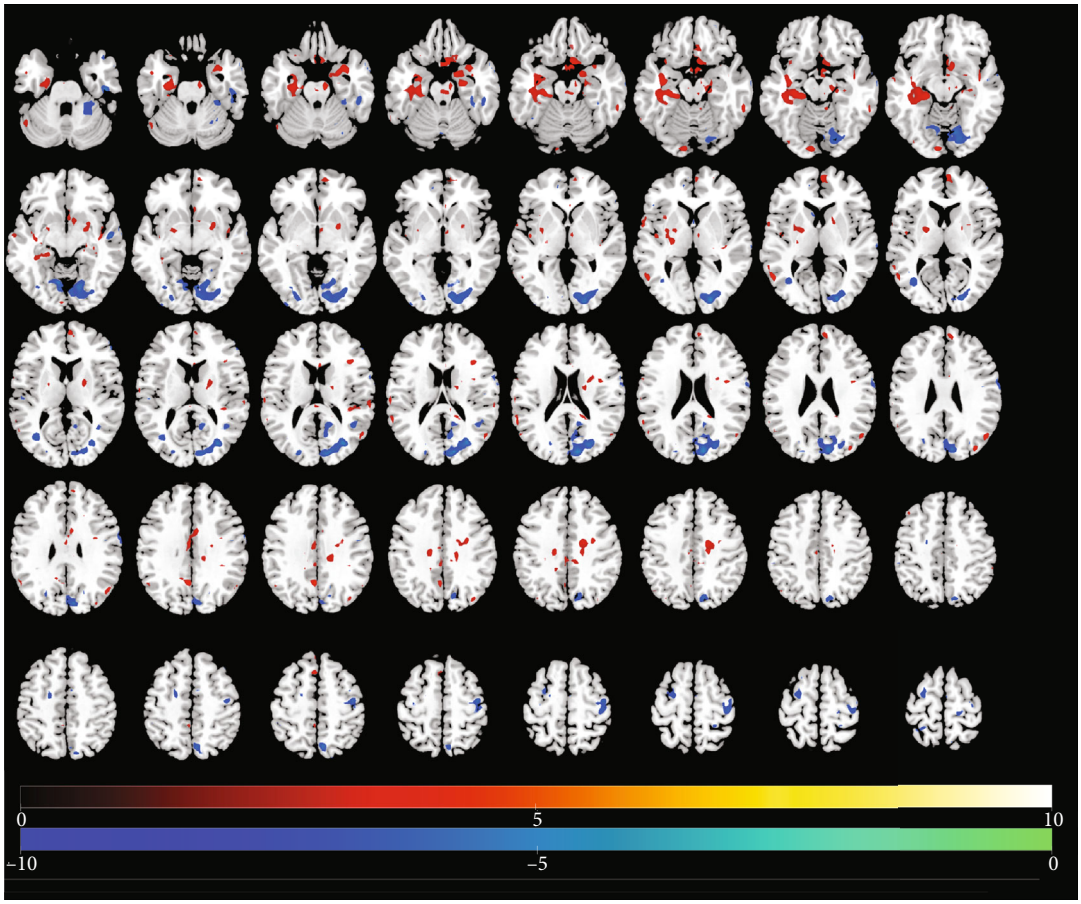


Figure 1: Identification of changed regional brain activity 2 months after traumatic amputation by using rs-fMRI. Relative magnitude of ALFF between upper-limb amputee patients ($n = 16$) and normal control subjects ($n = 8$) is plotted in axial images (top to bottom, inferior to superior). Colors toward red indicate increases in ALFF (significant $t$-values), and colors toward blue indicate significant decreases in ALFF relative to controls (cf. Table 2).

differentially activated in amputees compared to healthy control subjects. ALFF is calculated from the BOLD time course at each voxel [23]. The ALFF calculation was performed identically to that described in the studies of Zang et al. [24, 25]. ALFF was calculated for the traditional low-frequency band (0.01-0.08 Hz).

*2.5. DC Calculations.* DC reflects the strength of connections for a given voxel with all other voxels in the brain and can thus capture its relationship with the whole brain network at the voxel level; it represents a node characteristic of large-scale brain intrinsic connectivity networks [26]. Compared to a binary version of DC, weighted DC provides a more precise centrality characterization of functional brain networks [27]. Therefore, we used weighted DC. Pearson's correlations were calculated between the time courses of each voxel with that of every other voxel in the entire brain. Correlation coefficients with $r > 0.2$ were summed for each voxel, and then, a weighted DC was obtained for each voxel. The threshold of 0.2 was used to eliminate counting voxels that had low temporal correlation. It has been shown that different threshold selections do not qualitatively change the results [28]. Spatial smoothing (FWHM = 6 mm) was carried out after DC calculations, since lack of spatial smoothing may lead to artificial local correlations. We used the following formula for this DC calculation:

$$D = \sum aij, \quad j = 1, \cdots, N, i \neq j, aij = \begin{cases} 0, & aij < 0.2, \\ aij, & aij \geq 0.2. \end{cases} \tag{1}$$

In line with previous rs-fMRI studies, we removed negative correlations [29]. Since the physiological basis of negative correlations is uncertain, it was not calculated [30–32].

*2.6. Statistical Analysis.* Two-sample $t$-tests were used on the two indices of the BOLD signal (ALFF and DC) separately. The results were corrected for multiple comparisons with a combined threshold of a single voxel ($P < 0.05$) with Gaussian random field (GRF) correction.

## 3. Results

*3.1. Demographic and Clinical Characteristics of Subjects.* Table 1 shows basic demographic and clinical characteristics

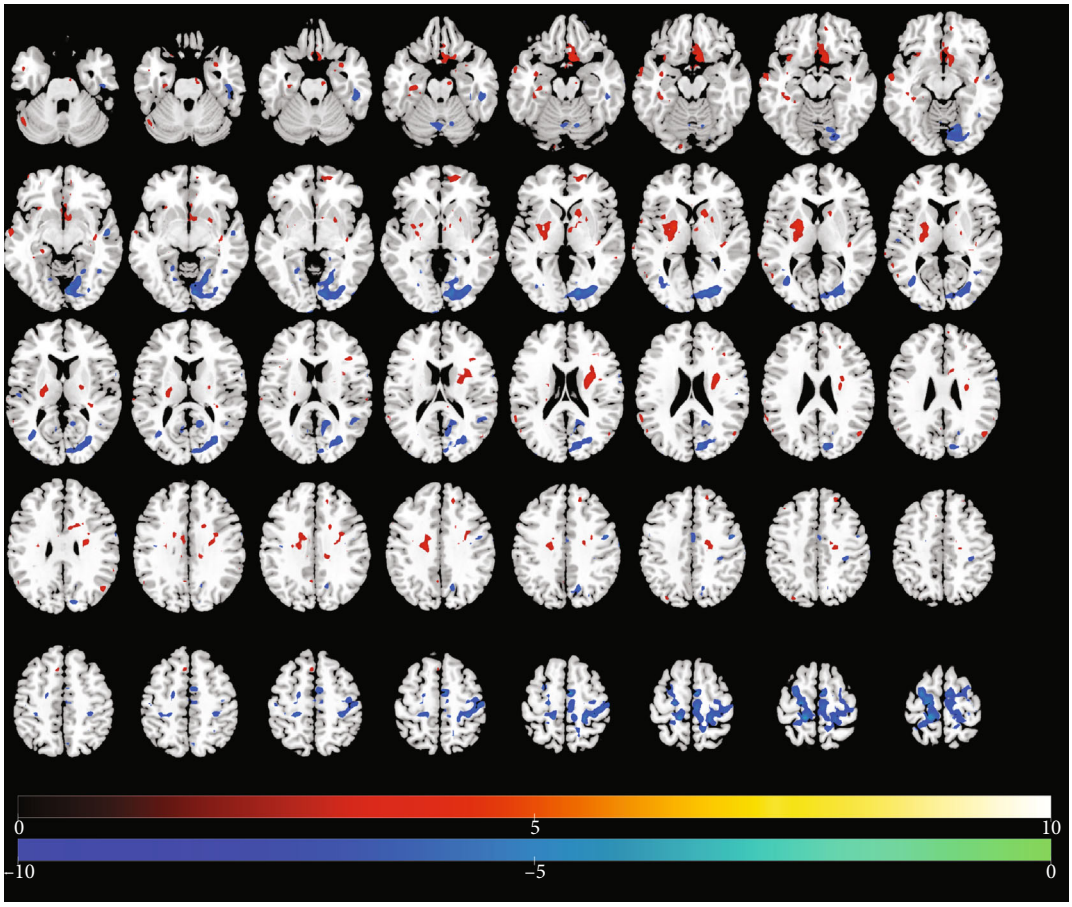


Figure 2: Changes in regional brain activity 6 months after traumatic amputation by using rs-fMRI. Differences in the magnitude of ALFF between the same upper-limb amputee patients and control subjects. Same conventions as in Figure 1.

of the amputees contributing data for this study. The mean age of the 8 healthy control subjects and 16 upper-limb amputees was statistically indistinguishable (37.9 years vs. 41.2 years, $P = 0.07 > 0.05$). Also, the two groups were reasonably well balanced by sex, with 3 females and 5 males in the control group and 5 females and 11 males in the amputee group.

*3.2. Changes in ALFF Over Time.* Tables 2–4 present results of significant regional brain changes in ALFFs at 2-, 6-, and 12-month postamputation, respectively. Figures 1–3 are the corresponding axial images of rs-fMRIs showing relative changes in ALFFs of amputees compared to control subjects.

*3.2.1. Two-Month Postamputation.* In rs-fMRIs, we observed the largest positive ALFFs in the temporal lobe, cingulate gyrus, pre- and post-central gyri, and precuneus (Table 2, Figure 1). Compared to normal controls at 2-month post-traumatic amputation, in upper-limb amputee patients, we detected significant positive ALFFs in the right side of the brain in the anterior cingulate, parahippocampal gyrus, insula, and putamen, while in the left side at this time point, significant positive ALFFs were detected in the hippocampus, parahippocampal gyrus, putamen, postcentral gyrus, and supplementary motor area. Significant negative ALFFs at 2 months were detected in the right side of the brain in the precentral gyrus, precuneus, and supplementary motor area, while in the left side at this time point, significant negative ALFFs were detected in the precentral gyrus and postcentral gyrus.

*3.2.2. Six-Month Postamputation.* Six months after the first rs-fMRI scans, a different pattern of regional ALFF changes emerged. In general, the large positive ALFFs we observed in the temporal lobe regions at 2 months were no longer detectable at 6 months or were much reduced in voxel extent (e.g., left hippocampus). One exception was a large relative increase in a negative ALFF in the right supplementary motor area from 42 voxels at 2 months to 903 voxels at 6 months (Table 3, Figure 2). At the 6-month time point, the largest changes were significant negative ALFFs in the paracentral lobule, supplementary motor area, lingual area, and cuneus. Other notable significant positive changes in ALFFs were in the left putamen, right caudate, and negative ALFFs in the fusiform gyrus and inferior temporal lobe.

*3.2.3. Twelve-Month Postamputation.* In general, at 12-month postamputation, more significant positive and negative changes in ALFFs were detected, but the voxel extents tended to be smaller, and some previously undetected regions

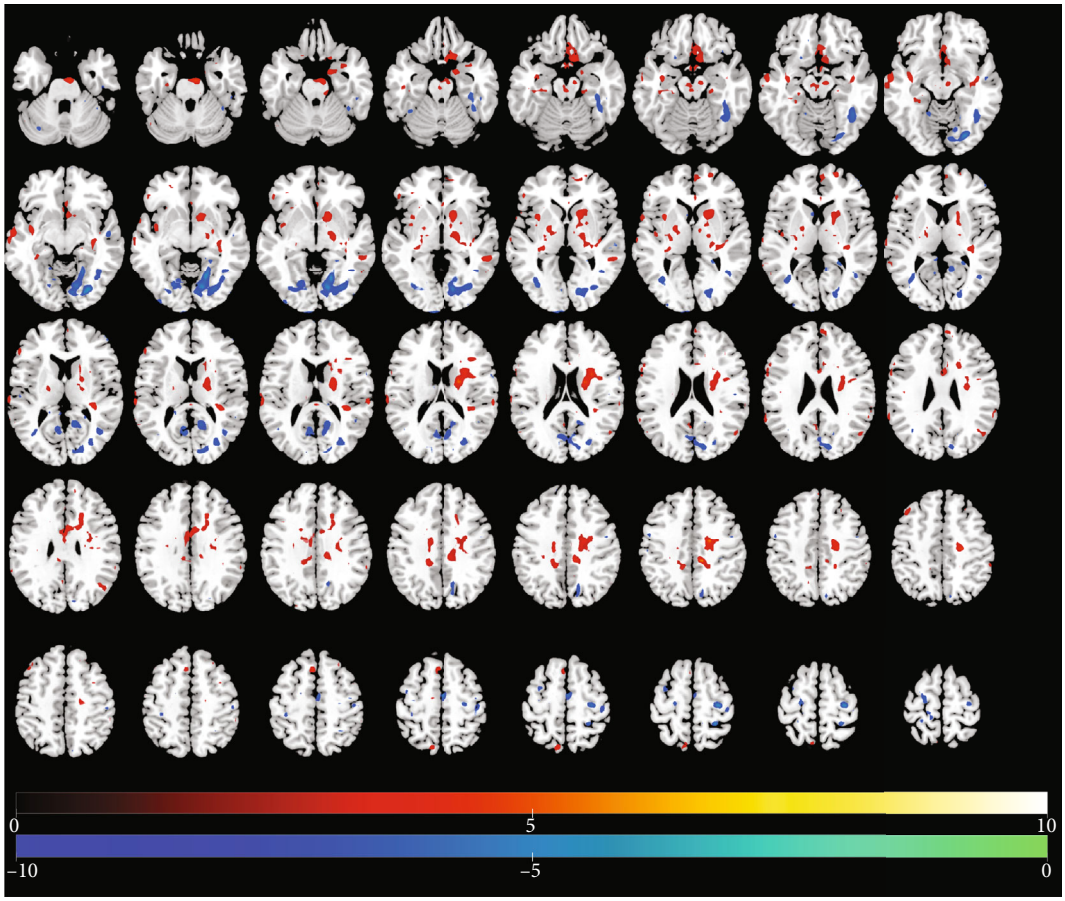


Figure 3: Changes in regional brain activity 12 months after traumatic amputation by using rs-fMRI. Differences in the magnitude of ALFF between the same upper-limb amputee patients and control subjects. Same conventions as in Figure 1.

Table 5: Relative regional changes in DC at 2 months.

| Direction of change | Brain region | Voxels | *t*-value | MNI coordinates | | |
|---|---|---|---|---|---|---|
| | | | | *x* | *y* | *z* |
| Positive DC | Cingulate_Mid_L | 27 | 3.373 | -6 | 12 | 39 |
| | Frontal_Med_Orb_R | 12 | 3.29 | 9 | 42 | -12 |
| | Rolandic_Oper_L | 11 | 4.459 | -63 | -3 | 12 |
| | Postcentral_L | 10 | 3.603 | -63 | -21 | 27 |
| Negative DC | Precuneus_R | 105 | -4.736 | 15 | -48 | 21 |
| | ParaHippocampal_R | 105 | -3.788 | 18 | -39 | -6 |
| | Caudate_R | 23 | -4.711 | 21 | 24 | -6 |
| | Precuneus_L | 23 | -3.808 | -9 | -60 | 15 |
| | Occipital_Mid_L | 18 | -4.159 | -27 | -78 | 0 |
| | Frontal_Inf_Tri_R | 10 | -3.876 | 51 | 24 | 6 |
| | Precentral_R | 10 | -3.426 | 60 | 9 | 15 |

emerged at this 12-month scan (Table 4, Figure 3). Exceptions are large positive ALFF changes in the right caudate and left rectus gyrus of the frontal lobe, and large negative ALFF changes in the right lingual area and fusiform gyrus. Interestingly, while the function of the rectus gyrus is unclear, it may be involved in higher cognitive function. We observed the largest positive ALFFs in the cingulate gyrus, pre- and post-central gyri, and precuneus. Persistent significant relative changes in ALFFs were detected in the sensorimotor cortex and some temporal lobe regions (Table 4, Figure 3) across the 2-, 6-, and 12-month scans.

*3.3. Changes in DC Over Time.* Tables 4–6 present results of significant regional brain changes in DCs at 2-, 6-, and 12-

Table 6: Relative regional changes in DC at 6 months.

| Direction of change | Brain region | Voxels | $t$-value | MNI coordinates | | |
|---|---|---|---|---|---|---|
| | | | | $x$ | $y$ | $z$ |
| Positive DC | Calcarine_R | 103 | 5.182 | 18 | -99 | 0 |
| | Cuneus_L | 19 | 6.229 | 0 | -90 | 33 |
| | ParaHippocampal_L | 14 | 3.29 | -18 | 3 | -33 |
| | Postcentral_L | 9 | 4.074 | -63 | -21 | 24 |
| | Postcentral_R | 6 | 3.138 | 45 | -42 | 63 |
| Negative DC | Precuneus_R | 31 | -4.937 | 21 | -51 | 18 |
| | ParaHippocampal_R | 27 | -4.193 | 21 | -39 | -6 |
| | Hippocampus_R | 15 | -4.685 | 27 | -21 | -15 |
| | Precuneus_L | 15 | -4.31 | -3 | -54 | 69 |
| | Cingulate_Mid_R | 14 | -5.296 | 12 | -6 | 39 |
| | Cingulate_Mid_L | 11 | -3.602 | -12 | -33 | 42 |
| | Postcentral_L | 6 | -3.025 | -30 | -33 | 54 |
| | Caudate_R | 5 | -4.04 | 21 | 24 | -6 |

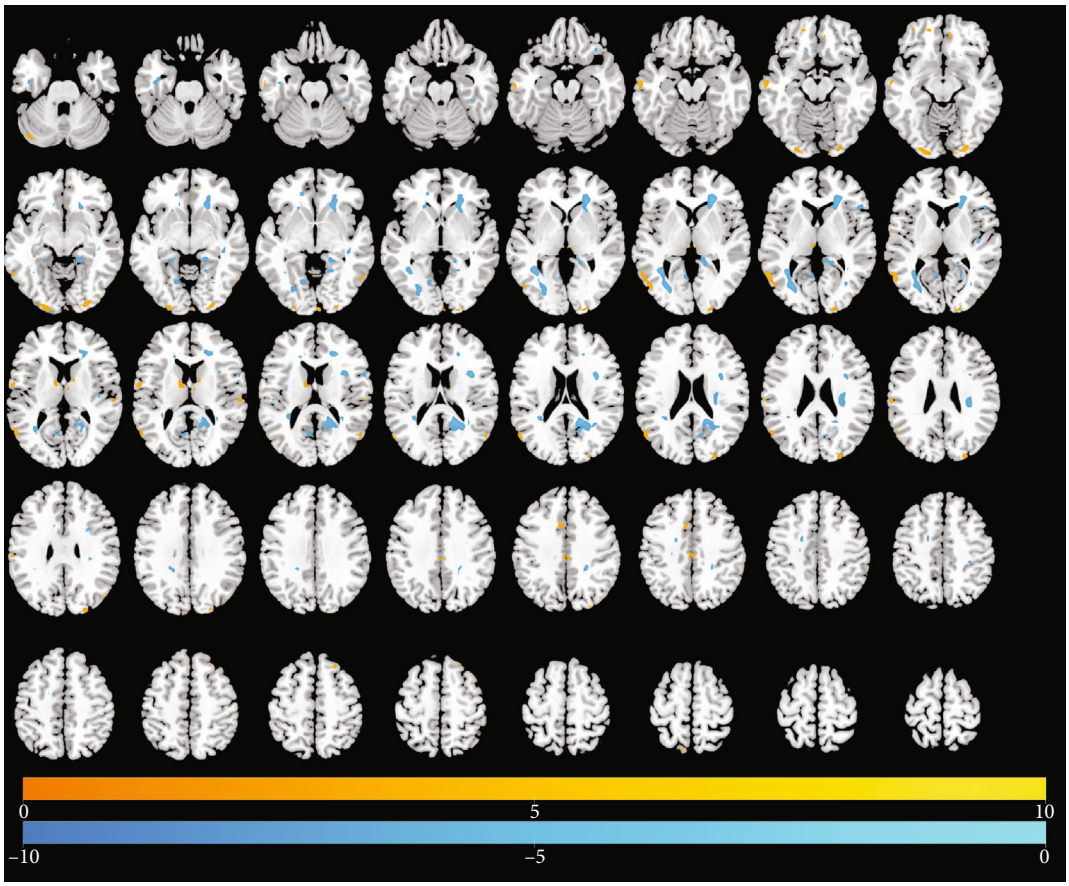


Figure 4: Differences in the magnitude of DC between the same upper-limb amputee patients and control subjects at 2 months of rs-fMRI scan. Same conventions as in Figure 1.

month postamputation, respectively. Figures 4–6 are the corresponding axial images of rs-fMRIs showing relative changes in DCs of amputees compared to control subjects.

*3.3.1. Two-Month Postamputation.* In rs-fMRIs, we observed the largest positive changes in DC in the left midcingulate gyrus and the largest negative changes in the right precuneus and right parahippocampal gyri (Table 5, Figure 4). In general, the spatial extent of DC changes at 2-month postamputation was much smaller than the corresponding ALFFs at 2 months (cf. Figures 1 and 4). Smaller significant positive or negative changes in DCs were detected in the rolandic

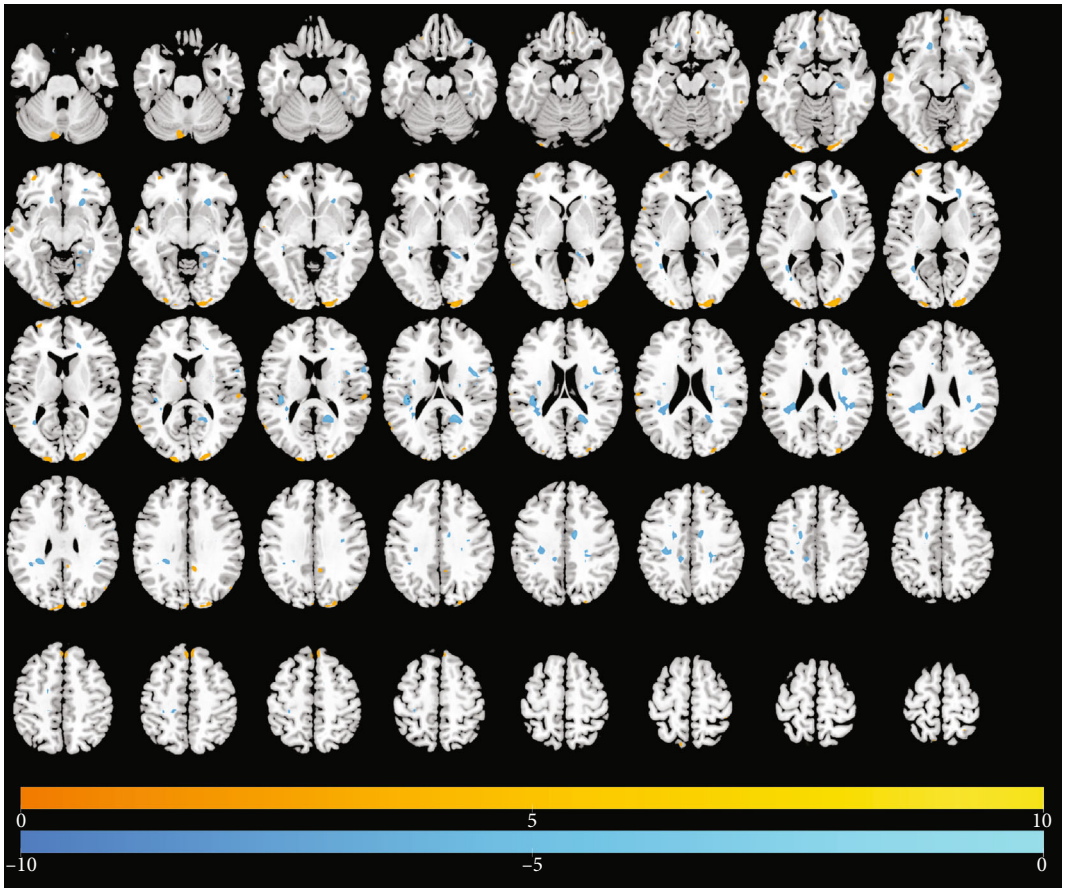


Figure 5: Differences in the magnitude of DC between the same upper-limb amputee patients and control subjects at 6 months of rs-fMRI scan. Same conventions as in Figure 1.

operculum, frontal medial orbital cortex, precuneus, parahippocampal gyrus, caudate, midoccipital cortex, and right parts of the triangularis of the inferior frontal gyrus.

*3.3.2. Six-Month Postamputation.* Six months after the first rs-fMRI scans, a different pattern of regional functional connectivity emerged. At this time point, we detected a new large positive DC in the right calcarine, and other positive and negative DCs were on the same order of magnitude as those observed at 2 months (Table 6, Figure 5).

*3.3.3. Twelve-Month Postamputation.* At the final scan at 12 months, we detected large positive changes in DC in the right lingual and cuneus and large negative changes in the parahippocampal gyrus and precuneus (Table 7, Figure 6). These changes in functional connectivity either were absent in earlier scans or were much smaller in magnitude.

## 4. Discussion

The temporal and spatial extents of cortical somatotopic reorganization after upper-limb amputation are unclear. In the present study, we described changes in spatial patterns of intrinsic brain activity (ALFFs) and functional connectivity (DC) by measuring rs-fMRI in traumatic upper-limb amputees at 2 months, 6 months, and 12 months. Relative to ALFFs and DC in normal controls, selective increases occurred in the sensory and motor cortex, as expected, but also increases and decreases occurred in related brain regions involved in functional plasticity after upper extremity deafferentation. The regional distribution of increases/decreases in ALFFs and DC documented at 2-month postamputation was very different from those at 6 and 12 months.

The sensory and motor brain networks of the human brain are somatotopically organized. A drastic upper extremity injury in humans, like traumatic amputation, may change the somatotopy of the primary motor cortex and primary sensory cortex of the deafferented hemisphere. Denervation due to amputation or nerve injury disrupts normal sensorimotor function. It is reported that cortical reorganization in the sensorimotor cortex, where cortical maps of intact body parts "expand" into areas associated previously with afferents of the missing limb, also has been reported in numerous animal studies of experimental amputation [33–35].

Sensorimotor reorganization is also observed in some transcranial magnetic stimulation studies in amputees. In these studies, increased excitability in motor areas contralateral to the amputated limb occurs. Remaining stump muscles have higher response amplitudes that can be evoked by transcranial magnetic stimulation applied in a larger area on the scalp than those responses in the intact arm [36, 37]. In addition, a shift in the somatotopy of the lip [38], chin [39], and

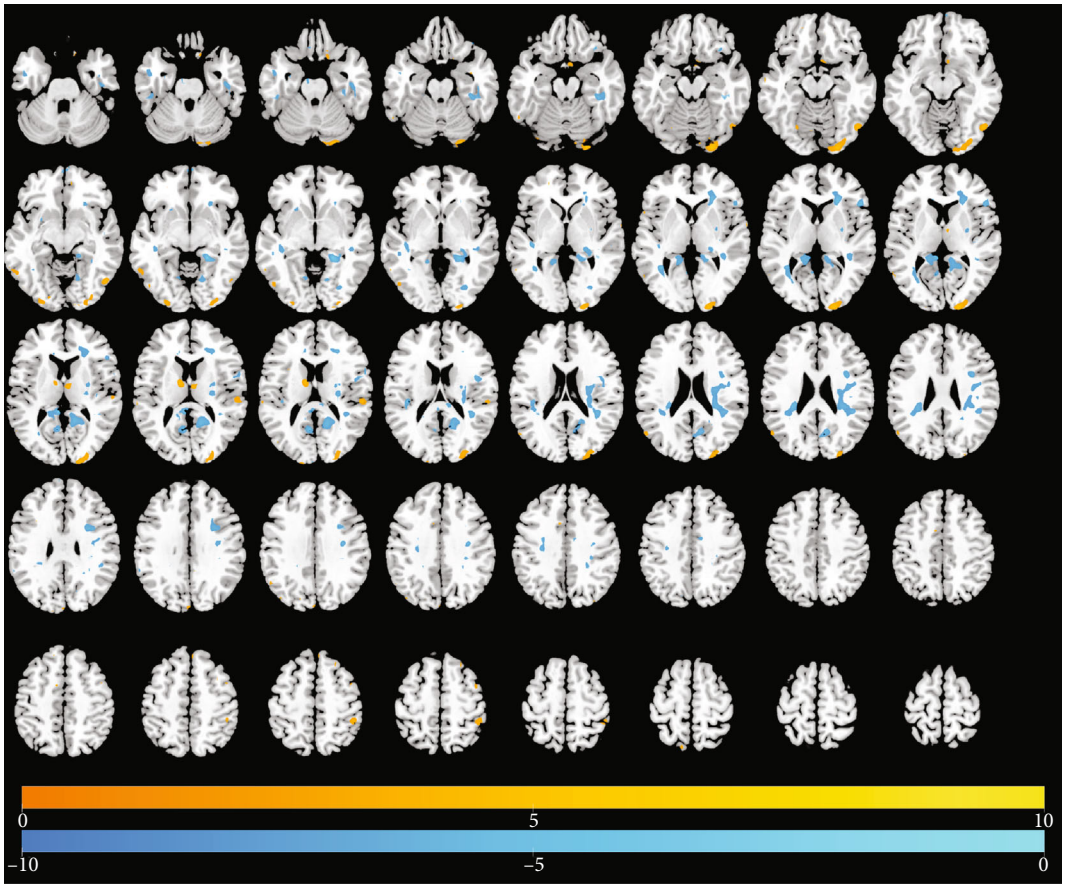


Figure 6: Differences in the magnitude of DC between the same upper-limb amputee patients and control subjects at 12 months of rs-fMRI scan. Same conventions as in Figure 1.

Table 7: Relative regional changes in DC at 12 months.

| Direction of change | Brain region | Voxels | *t*-value | MNI coordinates | | |
|---|---|---|---|---|---|---|
| | | | | *x* | *y* | *z* |
| Positive DC | Lingual_R | 188 | 6.163 | 24 | -93 | -15 |
| | Cuneus_R | 188 | 5.813 | 18 | -99 | 9 |
| | Fusiform_L | 23 | 4.308 | -21 | 3 | -45 |
| | Parietal_Inf_R | 21 | 3.916 | 45 | -39 | 54 |
| | Caudate_L | 12 | 4.725 | -12 | -3 | 15 |
| | Postcentral_L | 10 | 4.03 | -21 | -30 | 78 |
| Negative DC | ParaHippocampal_R | 162 | -8.29 | 21 | -39 | -6 |
| | Precuneus_R | 162 | -4.969 | 12 | -63 | 24 |
| | Cingulate_Post_L | 56 | -6.593 | -6 | -39 | 12 |
| | Fusiform_R | 47 | -4.827 | 39 | -33 | -18 |
| | Precuneus_L | 25 | -5.595 | -6 | -60 | 15 |
| | Frontal_Inf_Oper_R | 20 | -4.427 | 36 | 6 | 27 |
| | Frontal_Inf_Tri_R | 16 | -5.115 | 51 | 24 | 6 |
| | Putamen_R | 12 | -3.446 | 30 | -6 | 6 |

shoulder [40] representation into the deafferented cortical hand area of upper-limb amputees has been reported using magnetoencephalography (MEG) and fMRI.

Denervation does not lead to a complete loss of the affected limb cortical representation, since the sensorimotor cortex still seems to be working with so-called "attempted

movement" by the amputee. When an amputee tries to "move" their phantom limb, activation in the corresponding sensorimotor areas appears in fMRI, and this activation is similar to real executed movements in able-bodied subjects [38, 41, 42].

It has been shown that the persistent cortical representation of upper-limb amputees is relatively detailed for the postcentral gyrus and parietal cortex. For example, in a tetraplegic patient, movement trajectories and movement goals have been successfully decoded from electrophysiological activity in the posterior parietal cortex using intracranial recordings [43]. A persistent hand representation in S1 was also reported in a long-term spinal cord injury patient as measured by microstimulation [44]. Also, the topography of a persistent individual finger representation of a phantom hand has been shown in the somatosensory cortex of amputees [45].

ALFF measures the amplitude of time series fluctuations at each voxel, and DC represents the large-scale intrinsic connectivity of the brain at the voxel level. These measures of rs-fMRI probe brain activity from different perspectives. In our investigation, we found that the ALFF and DC overlap spatially, which mainly occurred in the left superior frontal gyrus (Frontal_Sup_L). This result may suggest that changes in cognition may occur in amputation patient, and may have an extended impact on the brain plasticity.

We also found that the ALFFs in the primary motor cortex and primary sensory cortex decreased at 2, 6, and 12 months after the amputation. The brain regions involved with sensorimotor integration increased, specifically in the putamen, caudate, and precuneus. We speculate that this could represent a compensatory pattern after amputation. The deactivation of sensorimotor cortex may influence the associate cortex of sensory feedback. Since DC values decreased in the precuneus, caudate, and postcentral gyrus, this may indicate that sensorimotor integration is also impaired after limb amputation. It is expected that the primary motor cortex and the primary sensory cortex were silent after the deafferentation of the injured limb. Afterwards, the connection in the sensorimotor network at the affected hemisphere was diminished. In general, we found that amputation patients had significant brain function alterations in local regions and extensive alterations in widespread brain regions, such as corpus striatum and cognition-emotion cortex.

This study had several limitations. First, the sample size of the normal controls and amputation patients was relatively small, which may reduce confidence in the results. Therefore, more subjects would be recruited in future research to definitively evaluate these findings. Second, we chose ALFF and DC as the indices to detect the fluctuations in regional spontaneous activity strength. According to these two measures, the brain of amputation patients showed large-scale changes over 12 months. To clarify the underlying neural mechanisms related to amputation-related brain changes, future studies should examine alterations at the brain network level. Finally, clinical assessment with validated neuropsychological instruments should be performed in future studies, which could uncover a more interesting relationship between amputation and the changed BOLD signals.

## 5. Conclusion

Our findings show that local and extensive temporal and spatial changes occur in intrinsic cortical activity and functional connectivity in the sensorimotor and cognitive-related brain regions after limb amputation. With future confirmatory research, this plasticity may imply that dysfunction occurs not only in sensory and motor regions but also in areas responsible for sensorimotor integration and motor planning. Regardless, these results and others' on how ALFF and DC are plastic after traumatic limb amputation highlight how analyzing intrinsic brain activity in the absence of any task-related sensory or cognitive stimulus (rs-fMRI) may be a fruitful approach for analyzing plasticity after "natural deafferentation" that occurs in Alzheimer's disease or Parkinson's disease.

## Data Availability

The present study includes 8 healthy volunteers of 5 men and 3 women (mean age: 37.9 years old) and 16 patients with amputation (11 men and 5 women; mean age: 41.2 years old). All procedures used in this study were approved by the Committee for Medical Ethics of Shanghai Jiao Tong University Affiliated Sixth People's Hospital. Written informed consent was obtained from all study participants.

## Disclosure

This article has been accepted for publication in Preprint by Research Square. Bingbo Bao is the first author. Lei Duan is the co-first author. Haifeng Wei, Pengbo Luo, Hongyi Zhu, Tao Gao, Xiaoer Wei, Jing Li, Yuehua Li, Yimin Chai, and Changqing Zhang are the joint co-authors.

## Conflicts of Interest

All authors declare no competing interests.

## Authors' Contributions

Bingbo Bao and Lei Duan contributed equally to this work. Xianyou Zheng was responsible for the study design and manuscript writing. Bingbo Bao and Lei Duan were responsible for the data collection and analysis. Bingbo Bao was responsible for the revision of the manuscript. All the authors critically reviewed the content of the manuscript. All authors read and approved the final manuscript.

## Acknowledgments

This study was supported by the Shanghai Municipal Education Commission-Gaofeng Clinical Medicine Grant (grant number 20161429) and the National Natural Science Foundation of China (grant number 81371965).

## References


[1] S. M. Grüsser, C. Winter, W. Mühlnickel et al., "The relationship of perceptual phenomena and cortical reorganization in upper extremity amputees," *Neuroscience*, vol. 102, no. 2, pp. 263–272, 2001.

[2] A. Karl, N. Birbaumer, W. Lutzenberger, L. G. Cohen, and H. Flor, "Reorganization of motor and somatosensory cortex in upper extremity amputees with phantom limb pain," *The Journal of Neuroscience*, vol. 21, no. 10, pp. 3609–3618, 2001.

[3] L. G. Cohen, B. J. Roth, E. M. Wassermann et al., "Magnetic stimulation of the human cerebral cortex, an indicator of reorganization in motor pathways in certain pathological conditions," *Journal of Clinical Neurophysiology*, vol. 8, no. 1, pp. 56–65, 1991.

[4] H. Flor, T. Elbert, S. Knecht et al., "Phantom-limb pain as a perceptual correlate of cortical reorganization following arm amputation," *Nature*, vol. 375, no. 6531, pp. 482–484, 1995.

[5] P. Giraux, A. Sirigu, F. Schneider, and J. M. Dubernard, "Cortical reorganization in motor cortex after graft of both hands," *Nature Neuroscience*, vol. 4, no. 7, pp. 691-692, 2001.

[6] J. I. Romero-Romo, C. C. C. Bauer, E. H. Pasaye, R. A. Gutiérrez, R. Favila, and F. A. Barrios, "Abnormal functioning of the thalamocortical system underlies the conscious awareness of the phantom limb phenomenon," *The Neuroradiology Journal*, vol. 23, no. 6, pp. 671–679, 2010.

[7] E. H. Pasaye, R. A. Gutiérrez, S. Alcauter et al., "Event-related functional magnetic resonance images during the perception of phantom limb. A brushing task," *The Neuroradiology Journal*, vol. 23, no. 6, pp. 665–670, 2010.

[8] V. S. Ramachandran, M. Stewart, and D. C. Rogers-Ramachandran, "Perceptual correlates of massive cortical reorganization," *Neuroreport*, vol. 3, no. 7, pp. 583–586, 1992.

[9] V. S. Ramachandran and W. Hirstein, "The perception of phantom limbs. The D. O. Hebb lecture," *Brain*, vol. 121, no. 9, pp. 1603–1630, 1998.

[10] H. Flor, L. Nikolajsen, and T. Staehelin Jensen, "Phantom limb pain: a case of maladaptive CNS plasticity?," *Nature Reviews Neuroscience*, vol. 7, no. 11, pp. 873–881, 2006.

[11] T. R. Makin, N. Filippini, E. P. Duff, D. Henderson Slater, I. Tracey, and H. Johansen-Berg, "Network-level reorganisation of functional connectivity following arm amputation," *NeuroImage*, vol. 114, pp. 217–225, 2015.

[12] T. R. Makin, J. Scholz, N. Filippini, D. Henderson Slater, I. Tracey, and H. Johansen-Berg, "Phantom pain is associated with preserved structure and function in the former hand area," *Nature Communications*, vol. 4, no. 1, article 1570, 2013.

[13] T. R. Makin, A. O. Cramer, J. Scholz et al., "Deprivation-related and use-dependent plasticity go hand in hand," *eLife*, vol. 2, article e01273, 2013.

[14] C. D. Vargas, A. Aballéa, E. C. Rodrigues et al., "Re-emergence of hand-muscle representations in human motor cortex after hand allograft," *Proceedings of the National Academy of Sciences of the United States of America*, vol. 106, no. 17, pp. 7197–7202, 2009.

[15] E. L. Simões, I. Bramati, E. Rodrigues et al., "Functional expansion of sensorimotor representation and structural reorganization of callosal connections in lower limb amputees," *The Journal of Neuroscience*, vol. 32, no. 9, pp. 3211–3220, 2012.

[16] B. Biswal, F. Zerrin Yetkin, V. M. Haughton, and J. S. Hyde, "Functional connectivity in the motor cortex of resting human brain using echo-planar MRI," *Magnetic Resonance in Medicine*, vol. 34, no. 4, pp. 537–541, 1995.

[17] R. van Veen, V. Gurvits, R. V. Kogan et al., "An application of generalized matrix learning vector quantization in neuroimaging," *Computer Methods and Programs in Biomedicine*, vol. 197, p. 105708, 2020.

[18] S. Ogawa, R. S. Menon, D. W. Tank et al., "Functional brain mapping by blood oxygenation level-dependent contrast magnetic resonance imaging. A comparison of signal characteristics with a biophysical model," *Biophysical Journal*, vol. 64, no. 3, pp. 803–812, 1993.

[19] S. Ogawa, T. M. Lee, A. R. Kay, and D. W. Tank, "Brain magnetic resonance imaging with contrast dependent on blood oxygenation," *Proceedings of the National Academy of Sciences of the United States of America*, vol. 87, no. 24, pp. 9868–9872, 1990.

[20] T. T. Liu, "Neurovascular factors in resting-state functional MRI," *NeuroImage*, vol. 80, pp. 339–348, 2013.

[21] Y. Chao-Gan and Z. Yu-Feng, "DPARSF: a MATLAB toolbox for "pipeline" data analysis of resting-state fMRI," *Frontiers in Systems Neuroscience*, vol. 4, p. 13, 2010.

[22] X. W. Song, Z. Y. Dong, X. Y. Long et al., "REST: a toolkit for resting-state functional magnetic resonance imaging data processing," *PLoS One*, vol. 6, no. 9, article e25031, 2011.

[23] X. N. Zuo, A. Di Martino, C. Kelly et al., "The oscillating brain: complex and reliable," *NeuroImage*, vol. 49, no. 2, pp. 1432–1445, 2010.

[24] Z. Yu-Feng, H. Yong, Z. Chao-Zhe et al., "Altered baseline brain activity in children with ADHD revealed by resting- state functional MRI," *Brain & Development*, vol. 29, no. 2, pp. 83–91, 2007.

[25] Y. Zang, T. Jiang, Y. Lu, Y. He, and L. Tian, "Regional homogeneity approach to fMRI data analysis," *NeuroImage*, vol. 22, no. 1, pp. 394–400, 2004.

[26] X. N. Zuo, R. Ehmke, M. Mennes et al., "Network centrality in the human functional connectome," *Cerebral Cortex*, vol. 22, no. 8, pp. 1862–1875, 2012.

[27] M. W. Cole, S. Pathak, and W. Schneider, "Identifying the brain's most globally connected regions," *NeuroImage*, vol. 49, no. 4, pp. 3132–3148, 2010.

[28] R. L. Buckner, J. Sepulcre, T. Talukdar et al., "Cortical hubs revealed by intrinsic functional connectivity: mapping, assessment of stability, and relation to Alzheimer's disease," *The Journal of Neuroscience*, vol. 29, no. 6, pp. 1860–1873, 2009.

[29] S. Li, X. Ma, R. Huang et al., "Abnormal degree centrality in neurologically asymptomatic patients with end- stage renal disease: a resting-state fMRI study," *Clinical Neurophysiology*, vol. 127, no. 1, pp. 602–609, 2016.

[30] M. D. Fox, D. Zhang, A. Z. Snyder, and M. E. Raichle, "The global signal and observed anticorrelated resting state brain networks," *Journal of Neurophysiology*, vol. 101, no. 6, pp. 3270–3283, 2009.

[31] K. Murphy, R. M. Birn, D. A. Handwerker, T. B. Jones, and P. A. Bandettini, "The impact of global signal regression on resting state correlations: are anti-correlated networks introduced?," *NeuroImage*, vol. 44, no. 3, pp. 893–905, 2009.

[32] X. N. Zuo, C. Kelly, A. Di Martino et al., "Growing together and growing apart: regional and sex differences in the lifespan developmental trajectories of functional homotopy," *The Journal of Neuroscience*, vol. 30, no. 45, pp. 15034–15043, 2010.

[33] M. M. Merzenich, R. J. Nelson, M. P. Stryker, M. S. Cynader, A. Schoppmann, and J. M. Zook, "Somatosensory cortical map changes following digit amputation in adult monkeys," *The Journal of Comparative Neurology*, vol. 224, no. 4, pp. 591–605, 1984.

[34] J. P. Donoghue and J. N. Sanes, "Peripheral nerve injury in developing rats reorganizes representation pattern in motor cortex," *Proceedings of the National Academy of Sciences of the United States of America*, vol. 84, no. 4, pp. 1123–1126, 1987.

[35] C. W. H. Wu and J. H. Kaas, "Reorganization in primary motor cortex of primates with long-standing therapeutic amputations," *The Journal of Neuroscience*, vol. 19, no. 17, pp. 7679–7697, 1999.

[36] L. G. Cohen, S. Bandinelli, T. W. Findley, and M. Hallett, "Motor reorganization after upper limb amputation in man," *Brain*, vol. 114, no. 1, pp. 615–627, 1991.

[37] S. Roricht, B. U. Meyer, L. Niehaus, and S. A. Brandt, "Long-term reorganization of motor cortex outputs after arm amputation," *Neurology*, vol. 53, no. 1, pp. 106–111, 1999.

[38] M. Lotze, H. Flor, W. Grodd, W. Larbig, and N. Birbaumer, "Phantom movements and pain an fMRI study in upper limb amputees," *Brain*, vol. 124, no. 11, pp. 2268–2277, 2001.

[39] T. Elbert, H. Flor, N. Birbaumer et al., "Extensive reorganization of the somatosensory cortex in adult humans after nervous system injury," *NeuroReport*, vol. 5, no. 18, pp. 2593–2597, 1994.

[40] C. Dettmers, T. Adler, R. Rzanny et al., "Increased excitability in the primary motor cortex and supplementary motor area in patients with phantom limb pain after upper limb amputation," *Neuroscience Letters*, vol. 307, no. 2, pp. 109–112, 2001.

[41] J. A. Turner, J. S. Lee, O. Martinez, A. L. Medlin, S. L. Schandler, and M. J. Cohen, "Somatotopy of the motor cortex after long-term spinal cord injury or amputation," *IEEE Transactions on Neural Systems and Rehabilitation Engineering*, vol. 9, no. 2, pp. 154–160, 2001.

[42] F. E. Roux, J. A. Lotterie, E. Cassol, Y. Lazorthes, J. C. Sol, and I. Berry, "Cortical areas involved in virtual movement of phantom limbs: comparison with normal subjects," *Neurosurgery*, vol. 53, no. 6, pp. 1342–1353, 2003.

[43] T. Aflalo, S. Kellis, C. Klaes et al., "Neurophysiology. Decoding motor imagery from the posterior parietal cortex of a tetraplegic human," *Science*, vol. 348, no. 6237, pp. 906–910, 2015.

[44] S. N. Flesher, J. L. Collinger, S. T. Foldes et al., "Intracortical microstimulation of human somatosensory cortex," *Science Translational Medicine*, vol. 8, no. 361, article 361ra141, 2016.

[45] S. Kikkert, J. Kolasinski, S. Jbabdi et al., "Revealing the neural fingerprints of a missing hand," *eLife*, vol. 5, article e15292, 2016.

Hindawi
Neural Plasticity
Volume 2021, Article ID 8819169, 5 pages
https://doi.org/10.1155/2021/8819169

*Research Article*

# Focal Vibration Alters Human Digital Sensory Nerve Action Potentials: A Pilot Study

**Dong Qing Zhu,[1] Fang Liu,[2] Yu Zhu,[3] Duan Lei,[4] Xiang Jin,[5] Lan Xu,[1] Chao Jun Zheng,[5] Robert Weber,[3] and Xiang Jun Chen[1]**

[1]*Department of Neurology, Huashan Hospital, Fudan University, Shanghai, China*
[2]*Department of Rehabilitation Medicine, The Second Affiliated Hospital of Jiaxing University, Jiaxing, China*
[3]*Department of Physical Medicine and Rehabilitation, Upstate Medical University Hospital, Syracuse, USA*
[4]*Department of Traumatology and Orthopedics, Yueyang Hospital, Shanghai University of Traditional Chinese Medicine, Shanghai, China*
[5]*Department of Orthopedic Surgery, Huashan Hospital, Fudan University, Shanghai, China*

Correspondence should be addressed to Xiang Jun Chen; xiangjchen@fudan.edu.cn

Received 31 August 2020; Revised 17 December 2020; Accepted 5 February 2021; Published 3 March 2021

Academic Editor: Jia-Jia Wu



*Introduction*. We studied the impact of vibratory stimulation on the electrophysiological features of digital sensory nerve action potential (SNAP). *Methods*. The antidromic digit 3 SNAP was recorded in 19 healthy adults before, during, and after applying a vibration to either 3rd or 5th metacarpal phalangeal joint (MCPJ) at 60 Hz and amplitude of 2 mm. 100% supramaximal stimulus intensity was performed in 5 subjects (randomly selected from the 19 subjects) where the SNAP sizes were recorded. *Results*. The amplitude of digit 3 SNAP declined to $58.9 \pm 8.6\%$ when a vibration was applied to MCPJ digit 3. These impacts did not change by increasing the electrical stimulus intensity. The SNAP regained its baseline value immediately after the cessation of vibration stimulation. The magnitude of size reduction of digit 3 SNAP was less when vibration was moved to from MCPJ of digit 3 to MCPJ of digit 5. *Discussion*. The marked drop of the SNAP size during vibratory stimulation reflects the decreased responsiveness of A$\beta$ afferents to electrical stimulation, which deserve further investigation in the study of focal vibration in neurorehabilitation.

## 1. Introduction

Vibration exerts powerful stimulation on neuromuscular system. Numerous studies have confirmed the effects of focal vibratory stimuli at various levels of the nervous system and the therapeutic effects of focal vibration in neurorehabilitation for patients with motor and sensory impairment conditions such as stroke, spinal cord injury, multiple sclerosis, Parkinson's disease and dystonia [1–3]. When applied to the human hands, vibration activates the cutaneous mechanoreceptors, including Merkel disk for low frequencies (5–15 Hz), Meissner's corpuscles for midrange (20-50 Hz) in the superficial layers of the skin, and Pacinian corpuscles for high frequencies (60-400 Hz) in deeper layers of the skin and periosteum [4–6]. These receptors are innervated by A$\beta$-type myelinated fibers.

The main component of the digital sensory nerve action potential (SNAP) is produced by the summation of action potentials of large, myelinated A$\beta$ fibers. The size of SNAP is proportional to the number of nerve axons depolarized by the testing electrical stimulation. Both the function of skin mechanoreceptors and A$\beta$ fibers during vibration could affect the measures of digital 3 SNAP. Our study was designed to examine the electrophysiological features of digital SNAP during acute and transient exposure to vibratory stimulation.

## 2. Methods

*2.1. Subjects.* Nineteen healthy subjects (10 men), aged 23-50 (mean, 32) years, with no known neuromuscular or musculoskeletal disorders participated in this study. They were recruited from the university research center population.

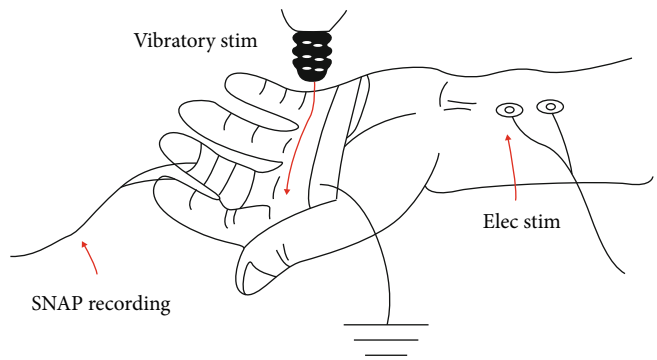


Figure 1: Schematic diagrams illustrating the settings of the experiment with conditioning stimulation of vibration.

The Human Ethics Committee of Huashan Hospital, Fudan University, China, granted the ethical committee approval, and each subject gave his/her informed consent prior to the study. Each subject was seated comfortably on a chair, with the left forearm and hand supinated on a solid wooden table with the fingers relaxed and unsupported (Figure 1).

Only minimal discomfort was caused by the brief application of vibration to the palm either at metacarpophalangeal joint (MCPJ) of digit 3 or MCPJ of digit 5. No visible venous stasis or color changes on the fingers were observed on any subject.

*2.2. Stimuli.* The median nerve was stimulated with a bar electrode at the midwrist 13 cm proximal to the active recording electrode. The electrical stimulation consisted of a square wave, 0.1 ms in duration, and was delivered at a rate of 2/s. The stimulus intensity started at a level below the threshold of the action potential and was incrementally increased until the maximal response was reached. The intensity was then increased by an additional 20% to ensure the supramaximal activation of SNAP.

With five subjects, we used 100% supramaximal stimulus to test the effects of an additional 100% increase in intensity for a maximal achievable activation of the sensory axons.

*2.3. Recording.* The antidromic median nerve SNAPs were recorded from the left hand with a self-adhesive ring electrode (Nihon Kohden, MEB-9400, Japan) placed 1 cm distal to the metacarpophalangeal joint (MCPJ) of the digit 3 with the reference electrode 4 cm further distally. A surface ground was adhered to the skin between the stimulating and recording electrodes. The impedance was maintained below 5 k ohm.

*2.4. Palm Vibration.* We utilized a hand-held massage vibrator (YH-3U, Yihe Electronic, China) with the vibration frequency at 60 Hz and a displacement of 2 mm. The vibration was applied to the palm at the MCPJ of digit 3. A constant force was applied to the MCPJ by using the own weight of the vibrator (0.9 kg). The diameter of the circular contact area between the skin and the vibrator was 2.5 cm. The vibrator was secured manually rather than being strapped to the palm. This method worked better in keeping the vibrator in place and ensuring the constant force of application during the experiment.

Table 1: Measurements of digit 3 SNAP.

| $N = 19$ | Amplitude ($\mu$V) Mean | Reduction (%) | $P$ |
|---|---|---|---|
| Baseline | 54.5 ± 6.9 | | |
| Vib MCPJ 3 | 22.3 ± 5.1 | 58.9 ± 8.6 | <0.05 |
| Vib MCPJ 5 ($N = 7$) | 40.0 ± 3.3 | 27.5 ± 3.2 | <0.05 |
| After vibration | 54.3 ± 6.7 | | |

Vib MCPJ 3: vibration at MCPJ3; Vib MCPJ 5: vibration at MCPJ 5.

In addition, the digit 3 SNAP was recorded with the vibrator applied to the palm at MCPJ of digit 5 for seven subjects.

*2.5. SNAPs Were Recorded in the following Steps*

(1) Before the start of vibration—as the baseline

(2) During continuous vibration—register 20 SNAPs

(3) After the cessation of the vibratory stimuli

Measurements of SNAPs included (1) amplitudes from the baseline to the negative peak and (2) onset latencies. The digital skin temperature was maintained at 32 ± 0.5°C.

*2.6. Statistical Analysis.* Statistical evaluation was performed by Student's $t$-test for paired data. Values, given as mean ± SD, were considered significant at $P < 0.05$.

## 3. Results

The traces of SNAP recorded before, during, and after vibration showed a satisfactory signal to noise ratio, without increased noise from muscle activity or electromagnetic interferences during vibration.

*3.1. Vibration Stimulation at MCPJ 3.* The amplitude of digit 3 SNAP showed a significant decrease ($P < 0.05$) from the baseline value during vibration (Table 1, Supplementary Figure 1, Supplementary Table 1). The use of 100% supramaximal intensity did not produce a regaining of the amplitude of SNAP. The amplitude of the SNAP reverted back to the baseline level immediately when the vibration stimulation

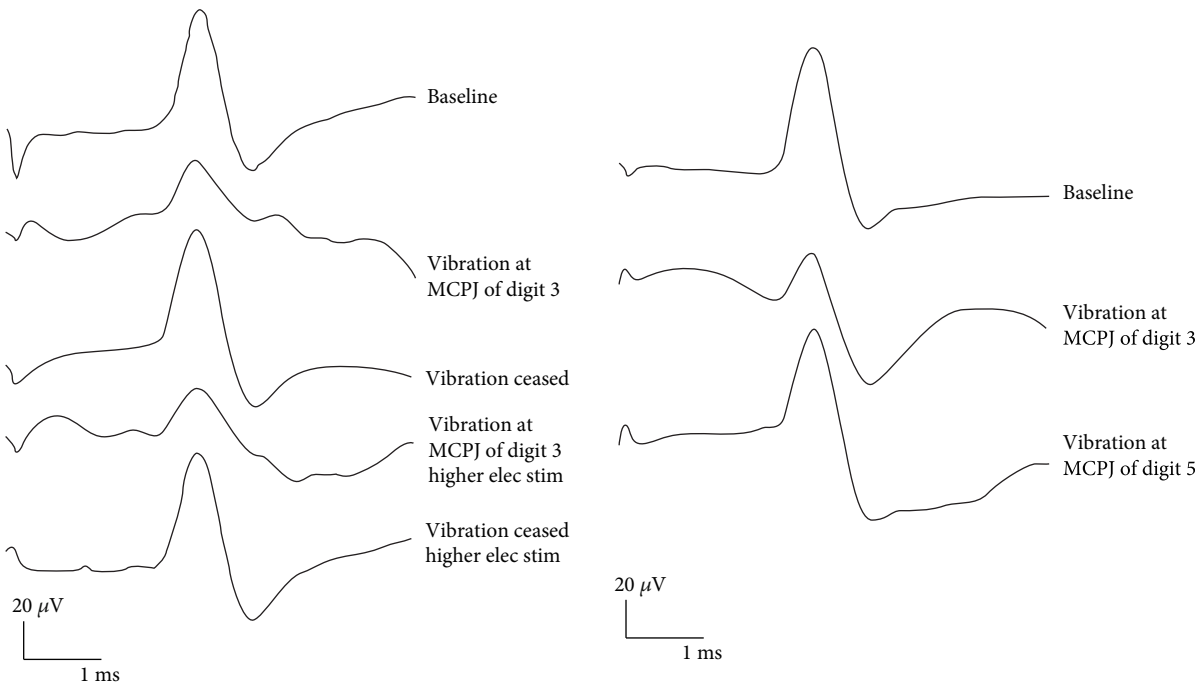


Figure 2: Digit 3 SNAP. (a) Recordings from subject 14, the amplitude of SNAP reduces with the similar extent (52.4.0% vs. 54.1%) at the two different stimulation intensities. The SNAP amplitude regains its baseline value after vibration. (b) Recordings from subject 3, illustrating a smaller reduction of digit 3 SNAP amplitude when vibration applied to the MCPJ of digit 5 (62.9%) in comparison with the greater reduction when vibration to the MCPJ of digit 3 (31.5%). No notable changes of the onset latencies during or after vibration.

ceased in both cases. The mean onset latency remained unchanged before, during, and after vibration.

*3.2. Vibration Relocated to the MCPJ Digit 5.* In seven subjects, when the vibration was moved to MCPJ of digit 5, the reduction of the amplitude of digit 3 SNAP was significantly smaller than when the vibration was applied to the MCPJ of digit 3 ($P < 0.05$ (Table 1). The SNAP amplitude again regained its baseline value after vibration ceased. There was no notable change in the onset latency of the SNAP throughout the experiments (Figure 2).

## 4. Discussion

We found that the mechanical vibration applied to the palm remarkably reduces the size of the digital SNAP. In addition, the SNAP amplitude returned to the baseline level immediately after the cessation of the vibration.

The fact that the digit 3 SNAP reduction was smaller when the vibration was moved from MCPJ of digit 3 to digit 5 suggests a position specific effect caused by the vibration stimulation.

Our experimental setup was carefully designed to minimize the impact of other possible factors for this phenomenon such as a change in intensity of the electrical stimulus or displacement of the recording electrodes.

*4.1. Possible Mechanisms for Vibration-Induced Reduction of Digital SNAP*

*4.1.1. Hyperpolarization.* A prolonged high-frequency impulse train may hyperpolarize the afferent axons, thereby inhibiting the impulse propagation, which in turn may cause SNAP reduction [7]. This seems unlikely considering an approximately 40% increase in threshold attributable to this phenomenon. With the use of 100% supramaximal intensity, vibration-induced SNAP reduction remained the same, which, otherwise, would have activated the hyperpolarized axons. Second, hyperpolarization that is sufficient to produce a significant SNAP depression would have increased its onset latency, a finding not seen in our experiments [8]. Third, hyperpolarization develops slowly after the application of stimulation and wears off gradually over many minutes after its cessation [9, 10]. This stands in contrast to the present findings, where vibration caused immediate suppression of SNAPs, which then recovered to the baseline level as soon as the stimulation ceased.

*4.1.2. Collision and "Line Busy" Phenomenon.* The magnitude of the size reduction of digital SNAP shown in the present study implies that vibration should have activated mechanoreceptors wildly, and the vibration-induced afferent volley should have come from multiple types of sensitive mechanoreceptors. It is likely that the reduction in the amplitude of the SNAP reflects spike collision between the vibratory evoked depolarization and the electrically evoked spike. The "line busy" hypothesis implies the occurrence of an afferent spikes and associated after potential followed by the absolutely refractory, which prevents generation of action potentials, as suggested by Hagbarth [11]. Consistent with single nerve fiber studies in animals [12], microneurographic recordings in humans demonstrated the absolute refractory periods of the distal median nerve sensory axons to range

from 0.7 to 4.5 ms (mean: 2.1 ± 0.9 ms) for all the afferent fibers with no difference between the rapid and slow adapting afferents [4, 13]. Paired stimulus technique [14] also yielded the absolute refractory period of 0.7 ms for the human digital nerveSNAPs [15]. Maintaining the absolute refractory periods for all afferents would require the different types of A$\beta$ fibers to discharge at approximately 222 to 1,428 Hz or above.

It has been well established that in studies such as by Muniak et al. [16] that low-frequency vibratory stimuli (e.g., 20 Hz at amplitude of 50 $\mu$m) activate all types of hand mechanoreceptors and evoke multiple spikes per cycle. Nevertheless, there are no studies which provide direct evidences of the very-high-frequency tonic discharges of A$\beta$ afferents during vibration to corroborate the hypotheses of "line busy" effects.

Focal vibratory stimuli have been used in neurorehabilitation including the neurological diseases or disorders like stroke, spinal cord injury, multiple sclerosis, Parkinson's disease, and dystonia. Focal vibration stimulated the proprioceptive system to obtain an efficient motor control in functional activities [2]. Our study demonstrated in vivo that the A$\beta$ afferent fibers (proprioceptive system) were stimulated by vibratory stimulation and coursed the reduction of the responsiveness of A$\beta$ afferent fibers to the electrical stimulation.

In conclusion, the remarkable drop of the SNAP size during acute exposure to vibratory stimulation reflects the significant reduction of the responsiveness of A$\beta$ afferents to electrical stimulation. These changes of electrophysiological features of SNAP deserve further investigation in the study of the effects of focal vibration in neurorehabilitation.

## Data Availability

Datasets analyzed during the current study are available from the corresponding author on reasonable request.

## Conflicts of Interest

The authors declare that they have no conflicts of interest.

## Authors' Contributions

Dong QingZhu and FangLiu contributed equally to this work and should be considered co-first authors.

## Supplementary Materials

*Supplementary 1*. Supplementary Figure 1 Baseline: the amplitude of recording of Sensory Nerve Action Potential (SNAP) of digit 3before vibration with electrical stimulation of the median nerve of the wrist. Vib MCPJ 3: the amplitude of recording of SNAP of digit 3 DURING vibration at 3rd metacarpal phalangeal joint (MCPJ) with electrical stimulation of the median nerve of the wrist. Vib MCPJ 5: the amplitude of recording of SNAP of digit 3 DURING vibration at 5th MCPJ with electrical stimulation of the median nerve of the wrist. Vib ceased: the amplitude of recording of SNAP of digit 3 after vibration ceased immediately with electrical stimulation of the median nerve of the wrist. There are significant statistical differences of digit 3 SNAP between vibration at MCPJ 3 and baseline (**, $P < 0.05$), vibration at MCPJ 5 and baseline (##, $P < 0.05$), vibration at MCPJ 3, and vibration at MCPJ 5 (***, $P < 0.05$). There are no significant statistical differences of digit 3 SNAP between baseline and vibration ceased (*, $P > 0.05$).

*Supplementary 2*. Supplementary Table 1 Digit 3 SNAP amplitude ($\mu$V) before, during, and after vibration of MCPJ 3 and MCPJ 5.

## References

[1] K. Rosenkranz and J. C. Rothwell, "The effect of sensory input and attention on the sensorimotor organization of the hand area of the human motor cortex," *The Journal of Physiology*, vol. 561, no. 1, pp. 307–320, 2004.

[2] N. Murillo, J. Valls-Sole, J. Vidal, E. Opisso, J. Medina, and H. Kumru, "Focal vibration in neurorehabilitation," *European Journal of Physical and Rehabilitation Medicine*, vol. 50, no. 2, pp. 231–242, 2014.

[3] R. Saggini, R. G. Bellomo, and L. Cosenza, "Vibration in neurorehabilitation: a narrative review," *Medical Research Archives*, vol. 5, p. 11, 2017.

[4] R. Mackel, "Conduction of neural impulses in human mechanoreceptive cutaneous afferents," *The Journal of Physiology*, vol. 401, no. 1, pp. 597–615, 1988.

[5] E. P. Gardner, J. H. Martin, and T. M. Jessell, "The bodily senses," in *Principles of Neural Science*, E. R. Kandel, J. H. Schwatz, and T. M. Jessell, Eds., pp. 430–450, McGraw-Hill, NewYork, 2000.

[6] S. Gilman, "Joint position sense and vibration sense: anatomical organisation and assessment," *Journal of Neurology, Neurosurgery & Psychiatry*, vol. 73, no. 5, pp. 473–477, 2002.

[7] H. Bostock and P. Grafe, "Activity-dependent excitability changes in normal and demyelinated rat spinal root axons," *The Journal of Physiology*, vol. 365, no. 1, pp. 239–257, 1985.

[8] D. Burke, "Effects of activity on axonal excitability: implications for motor control studies," *Advances in Experimental Medicine and Biology*, vol. 508, pp. 33–37, 2002.

[9] R. Vagg, I. Mogyoros, M. C. Kiernan, and D. Burke, "Activity-dependent hyperpolarization of human motor axons produced by natural activity," *The Journal of Physiology*, vol. 507, no. 3, pp. 919–925, 1998.

[10] M. C. Kiernan, C. S. Lin, and D. Burke, "Differences in activity-dependent hyperpolarization in human sensory and motor axons," *The Journal of Physiology*, vol. 558, no. 1, pp. 341–349, 2004.

[11] K.-E. Hagbarth, "The effect of muscle vibration in normal man and inpatients with motor disorders," in *New Development in Electromyography and Clinical Neurophysiology*, J. E. Demedt, Ed., vol. 3, pp. 428–443, Karger, Bassel, 1973.

[12] I. Tasaki, "Conduction of the nerve impulse," in *Handbook of Physiology*, J. Field, H. W. Magoun, and V. E. Hall, Eds., pp. 75–121, American Physiological Society, Washington, 1959.

[13] E. E. Brink and R. G. Mackel, "Time course of action potentials recorded from single human afferents," *Brain*, vol. 116, no. 2, pp. 415–432, 1993.

[14] W. Tackmann and H. J. Lehmann, "Refractory period in human sensory nerve fibres," *European Neurology*, vol. 12, pp. 277–292, 2004.

[15] F. Buchthal and A. Rosenfalck, "Evoked action potentials and conduction velocity in human sensory nerves," *Brain Research*, vol. 3, no. 1, pp. v–122, 1966.

[16] M. A. Muniak, S. Ray, S. S. Hsiao, J. F. Dammann, and S. J. Bensmaia, "The Neural Coding of Stimulus Intensity: Linking the Population Response of Mechanoreceptive Afferents with Psychophysical Behavior," *The Journal of Neuroscience*, vol. 27, no. 43, pp. 11687–11699, 2007.

Hindawi
Neural Plasticity
Volume 2021, Article ID 8854461, 13 pages
https://doi.org/10.1155/2021/8854461

*Research Article*

# Impact of Hepatoma-Derived Growth Factor Blockade on Resiniferatoxin-Induced Neuropathy

**Chieh-Hsin Wu,[1,2] Ming-Kung Wu,[3] Chun-Ching Lu,[4,5] Hung-Pei Tsai,[1] Ying-Yi Lu,[6,7,8] and Chih-Lung Lin[1,2]**

[1]*Division of Neurosurgery, Department of Surgery, Kaohsiung Medical University Hospital, Kaohsiung 807, Taiwan*
[2]*Department of Surgery, School of Medicine, College of Medicine, Kaohsiung Medical University, Kaohsiung 807, Taiwan*
[3]*Department of Psychiatry, Kaohsiung Chang Gung Memorial Hospital and Chang Gung University College of Medicine, Kaohsiung 833, Taiwan*
[4]*Department of Orthopaedics and Traumatology, Taipei Veterans General Hospital, Taipei 112, Taiwan*
[5]*Faculty of Medicine, National Yang Ming Chiao Tung University, Taipei 112, Taiwan*
[6]*Department of Dermatology, Kaohsiung Veterans General Hospital, Kaohsiung 813, Taiwan*
[7]*Graduate Institute of Medicine, College of Medicine, Kaohsiung Medical University, Kaohsiung 807, Taiwan*
[8]*Shu-Zen Junior College of Medicine and Management, Kaohsiung 821, Taiwan*

Correspondence should be addressed to Ying-Yi Lu; u103800011@cc.kmu.edu.tw and Chih-Lung Lin; chihlung1@yahoo.com

Received 30 September 2020; Revised 5 January 2021; Accepted 8 February 2021; Published 28 February 2021

Academic Editor: Xu-Yun Hua



Resiniferatoxin is an ultrapotent capsaicin analog that mediates nociceptive processing; treatment with resiniferatoxin can cause an inflammatory response and, ultimately, neuropathic pain. Hepatoma-derived growth factor, a growth factor related to normal development, is associated with neurotransmitters surrounding neurons and glial cells. Therefore, the study aims to investigate how blocking hepatoma-derived growth factor affects the inflammatory response in neuropathic pain. Serum hepatoma-derived growth factor protein expression was measured via ELISA. Resiniferatoxin was administrated intraperitoneally to induce neuropathic pain in 36 male Sprague-Dawley rats which were divided into three groups (resiniferatoxin+recombinant hepatoma-derived growth factor antibody group, resiniferatoxin group, and control group) ($n = 12$/group). The mechanical threshold response was tested with calibration forceps. Cell apoptosis was measured by TUNEL assay. Immunofluorescence staining was performed to detect apoptosis of neuron cells and proliferation of astrocytes in the spinal cord dorsal horn. RT-PCR technique and western blot were used to measure detect inflammatory factors and protein expressions. Serum hepatoma-derived growth factor protein expression was higher in the patients with sciatica compared to controls. In resiniferatoxin-group rats, protein expression of hepatoma-derived growth factor was higher than controls. Blocking hepatoma-derived growth factor improved the mechanical threshold response in rats. In dorsal root ganglion, blocking hepatoma-derived growth factor inhibited inflammatory cytokines. In the spinal cord dorsal horn, blocking hepatoma-derived growth factor inhibited proliferation of astrocyte, apoptosis of neuron cells, and attenuated expressions of pain-associated proteins. The experiment showed that blocking hepatoma-derived growth factor can prevent neuropathic pain and may be a useful alternative to conventional analgesics.

## 1. Introduction

After peripheral nerve degeneration, nociceptive input was reduced and neuropathic pain was developed. Sciatica, which is characterized by radicular leg pain radiating along the sciatic distribution, is an exemplary cause of neuropathic pain [1, 2]. Sensory nerve fibers in the peripheral nerves are axonal processes of dorsal root ganglion (DRG) neurons composed of large- and small-size neurons with corresponding diameters of nerve fibers. By affecting nociceptive nerves with small-diameter, some patients with peripheral nerve diseases have paradoxical symptoms such as neuropathic pain combined with skin denervation that reduces sensitivity to noxious stimuli [3, 4]. Similar phenomena may result from

capsaicin-induced skin denervation [5, 6]. However, it is unclear whether injury to only small neurons can cause this paradoxical combination of reduced neuropathic pain and nociception. Therefore, this study used a rat model of neuropathic pain to investigate whether treatment with the ultrapotent capsaicin analog resiniferatoxin (RTX) induces paradoxical changes in mechanical sensitivities [7, 8]. Unmyelinated nerves degeneration together with denervation of skin is the main feature of RTX-induced neuropathy [9], which is a precursor of pure small-fiber neuropathy and a good model of neuropathic pain. Studies show RTX can induce neuropathic pain through interaction with and upregulation of tumor necrosis factor $\alpha$ (TNF-$\alpha$) [10], which then induces cell apoptosis through an inflammatory response [11, 12]. After nerve injury and inflammation, activated glial cells in the central nervous system express TNF-$\alpha$, which then induces the release of proapoptotic factors [11, 12]. In a previous study, a global analysis that integrated proteome analysis revealed that a lack of hepatoma-derived growth factor (HDGF) genes can limit apoptosis induced by TNF-$\alpha$ [11].

The HDGF is a 240 amino-acid protein isolated from human hepatoma cells [13]. Surface expressed nucleoli have recently been identified as HDGF receptors [14]. During cell development, HDGF stimulates cell proliferation in fibroblasts, endothelial cells, and hepatoma cells [15]. The HDGF contributes to the normal development and regeneration of the liver [16–18] and to the development of the lungs [19, 20], vascular system [21–23], and heart [24]. This multifunctional protein also has important roles in cancer development due to its participation in various cellular events such as processing of RNA, ribosome biogenesis, transcriptional regulation, and damage repair of DNA [25]. Many studies have also documented the role of HDGF as a mitogen with extracellular proliferative effects on hepatoma cells, fibroblasts, vascular smooth muscle cells, and endothelial cells [19]. Additionally, HDGF is reportedly synthesized and localized mainly in brain neurons, which is retained in nucleus and released under necrotic status. It also upregulated in astrocytes exposed to neural cell adhesion molecules and has mitogenic and/or inflammatory effects on glial cells. Since glial cells express HDGF when activated and/or stimulated by certain signals, HDGF may function as a mitogenic factor in glial cells or an autocrine neurotrophic factor in neighboring neurons [26].

We hypothesized that transduction of pain signals to activated glial cells in the spinal cord produces an abundance of TNF-$\alpha$, which then causes RTX-induced neuropathic pain. A rat model was used to investigate the role of recombinant HDGF antibody (rHDGF antibody) in attenuating pain behaviors.

## 2. Materials and Methods

*2.1. Patient Serum Collection.* Patients with sciatica secondary to disc herniation were recruited from our hospital. The inclusion criteria were age more than 20 years, lumbar disc herniation verified by magnetic resonance imaging, and a dermatomal distribution of pain in a lower limb. Exclusion criteria were any history of spinal infections, spinal tumor, or other refractory neuropathic pain. The inclusion criteria for the control group were age more than 20 years and no sciatic pain. All participants signed informed consent forms. Serum was collected, centrifuged at 3,000 × rpm for 10 minutes at 4°C, and stored at -80°C until analysis. The study design was evaluated and approved by the Institutional Review of Board of Kaohsiung Medical University Hospital (KMUHIRB-20140262).

*2.2. Preparation of rHDGF Antibody.* The rHDGF antibody was customized by Leadgene Biomedical Inc. (Tainan, Taiwan). 50 $\mu$g recombinant rat HDGF (rrHDGF) protein in complete Freund's adjuvant were injected by intraperitoneal (i.p.) route to 6- to 8-week-old BALB/c mice each for priming. Two weeks after the first injection, the mice were injected with another 25 $\mu$g of rrHDGF protein in PBS. The procedures were repeated twice on week 4 and 5 after antigen priming. The sera were collected and stored at -20°C until use. The capability of rHDGF antibody from mice has a blocking effect that can inhibit the activity of HDGF.

*2.3. Cell Culture.* The PC-12 cells (BCRC 60048) were cultured in RPMI-1640 medium (Gibco) supplemented with 10% horse serum (Gibco) and 5% fetal bovine serum (Gibco) maintained in a humidified atmosphere containing 5% $CO_2$ at 37°C.

*2.4. MTT Assay.* Treatment of PC12 cells for 14 days with 50 ng/ml nerve growth factor induction of the neuronal phenotype when plated on Collagen IV coated culture flask. These PC-12 cells ($1 \times 10^4$ cells/well in 24-well plates) were incubated with different concentrations of rHDGF antibody (0, 10, 20, 50, and 100 ng/ml) for 24 hours, and the medium was removed afterwards. Furthermore, the cells were treated with 500 $\mu$M $H_2O_2$ for 24 hours. At the end of the treatment, 3-(4, 5-dimethylthiazol-2-yl)-2, 5-diphenyltetrazolium bromide (MTT) were added to each well at a final concentration of 0.5 mg/ml, and these cells were then incubated for another 90 minutes. The medium was then removed, and the purple formazan crystals were dissolved in DMSO (200 $\mu$/well). Absorbance was determined with a Multiskan FC microplate photometer reader (Thermo Scientific) with a test wavelength of 570 nm and a reference wavelength of 620 nm to obtain the sample signal (OD570–OD620).

*2.5. Animal Model.* Thirty-six male Sprague-Dawley rats weighing 300-350 g were purchased from the National Animal Center (Taiwan). From the time of their arrival at the laboratory until completion of the experiment, the rats were housed in plastic cages with a temperature of 22 + 1°C, a relative humidity of 70%, a 12-hr light/12-hr dark cycle, and ad libitum access to normal food and water.

The rats were divided into three groups ($n = 12$/group). In the RTX group, neuropathy was induced by intraperitoneal administration of a single dose of RTX (50 $\mu$g/kg, Sigma, St. Louis, MO) as described in the literature [9, 27, 28]. In the RTX+rHDGF antibody group, 100 $\mu$g/kg rHDGF antibody was administered and applied 24 hours before RTX injection.

The control group received no rHDGF antibody pretreatment and no RTX injection.

All procedures were performed according to ethical guidelines for the care and use of laboratory animals [29], and the protocol for use of the experimental animals in this study was approved by the Institutional Animal Care and Use Committee of Kaohsiung Medical University. All experimental procedures were carefully performed to minimize the suffering of the laboratory animals.

*2.6. Calibrated Forceps Testing.* Calibrated forceps (Rodent Pincher-Analgesia Meter; Bioseb In Vivo Research Instruments, Vitrolles, France) were used to apply mechanical stimulation in the experimental animals, and the mechanical threshold response was measured with an algometer and quantified on a linear scale. The maximum force (g) applied to the paw at the time of withdrawal was recorded with a dynamometer. For sensitive and reliable measurements, mechanical threshold was measured three times in each hindpaw as previously described by Luis-Delgado et al. [30]. All measurements were obtained by a single trained technician who was blinded to the experiment group.

*2.7. Immunofluorescence Staining.* Transversal frozen sections (8 $\mu$m) of spinal cord (L3-L5) were dried and incubated in a blocking buffer containing 1.5% normal goat serum and 0.2% Triton X-100 in PBS. The sections were washed with PBS twice, incubated overnight with the primary antibodies [GFAP (1 : 1000; BD Pharmingen™; 55639), Neu-N (1 : 1000; Millipore; MAB377)] at 4°C, washed repeatedly with PBS, and finally replaced in secondary antibodies conjugated with Alexa 488 (1 : 1000; Millipore) or Cy3 (1 : 1000; Millipore) for 3 h at room temperature. Each image from 3 to 5 sections stained at least from 6 rats for each group was photographed under a confocal microscope. The total numbers of apoptotic neuron cells were obtained manually from 5 tissue sections. The mean intensity of GFAP were determined from 5-randomly selected fields of each tissue section (laminae I-II of spinal cord dorsal horn) through Image J.

*2.8. Terminal Deoxynucleotidyl Transferase- (TdT-) Mediated dUTP Nick End Labeling (TUNEL) Assay.* Cell death was assessed by TUNEL assay (Millipore; S7110). A mixture of 1 $\mu$l TdT enzyme, 45 $\mu$l equilibrium buffer, and 5 $\mu$l nucleotide mix was prepared in the dark, added onto each slide, and incubated at 37°C for 1-2 hours in the dark. The enzymatic reaction was stopped by adding 4 $\mu$l of SSC (2X) onto each slide and then incubating for another 15 minutes at room temperature. Unbound fluorescent-12-dUTP was removed by washing with PBS. The cells were stained by immersing the slides in propidium iodide for 15 minutes in the dark. The slides were dried after rinsing with deionized water and then overlaid with cover slips. The TUNEL positive cells were observed under a fluorescence microscope (Olympus, U-RFL-T).

*2.9. Western Blot.* For protein extraction, the spinal cord dorsal horn tissues (L3-L5) were homogenized in protein lysis buffer in the presence of protease inhibitors (Sigma) and incubated at room temperature for 30 minutes. Samples were centrifuged at 13,000 × rpm for 30 minutes at 4°C. Protein concentrations in the supernatants were determined with a Bio-Rad DC Protein Assay Kit. For Western blot analysis, an equal amount of total proteins was separated by 12% sodium dodecyl-sulfate polyacrylamide gel electrophoresis and transferred onto polyvinylidene fluoride membranes. After blocking in Tris-buffered saline containing 0.05% Tween-20 and 5% nonfat milk for 1 hour at room temperature, the membranes were incubated overnight at 4°C with various primary antibodies [iNOS (1 : 500; BD; 610328), TrkB (1 : 500; ABGENT; AN1211), PI3K (1 : 500; ABGENT; AP52796), Akt (1 : 500; Cell Signaling; #9272), p-Akt (1 : 500; Cell Signaling; #9271), substance P (1 : 500; Abcam; ab10353), HDGF (1 : 500; proteintech; 60064-1-lg), and $\beta$-actin (1 : 20000; Sigma; A5441)] directed against the protein of interest. After several washes, an appropriate HRP-conjugated secondary antibody (1 : 5000; Millipore; P36599A) was applied for 1 hour at room temperature. Peroxidase activity was visualized with an ECL Western Blotting Detection kit and a Mini Chemi professional machine (Sage Creation Science, Co., Ltd., Beijing, China).

*2.10. Enzyme-Linked Immunosorbent Assay (ELISA).* High sensitivity ELISA was performed to assess HDGF levels in serum (Elabscience; E-EL-H5651). A 96-well plate was coated overnight in carbonate coating buffer, blocked in the provided sample buffer for 2 hours at room temperature, and treated with human HDGF antibody for 2 hours at room temperature. Acid-treated samples and provided standards were added to the plate in duplicate. Wells were then treated with anti-IgY conjugated to HRP for 1 hour at room temperature, and color was developed with provided tetrametylbenzidine dihydrochloride solution for 10 mins and stopped with 1 N HCl. The absorbance of wells was measured at 450 nm. The HDGF concentration was determined by comparing mean absorbance between duplicate samples and standards. The HDGF concentration was then normalized to total protein content and expressed as ng/$\mu$l total protein.

*2.11. Reverse Transcription-Polymerase Chain Reaction (RT-PCR).* Total RNA from DRG was isolated with an SV Total RNA Isolation System (Promega, Madison, WI). The integrity of the isolated RNA was confirmed by agarose gel electrophoresis. The RNA concentration was determined by spectrophotometry. For RT, 1-$\mu$g samples of total RNA were reverse transcribed into cDNA in 20 $\mu$l of reaction mixture containing 200 units of Superscript II (Gibco BRL, Rockville, MD), 0.5 $\mu$g oligo(dT)12-18, 200 pmol dithiothreitol, 10 pmol dNTP, and 40 units of ribonuclease inhibitor (Gibco BRL, Life Technologies) in a buffer supplied with the enzymes. The RT procedure was performed according to the protocol suggested by the manufacturer (Superscript II; Gibco BRL). The resulting cDNA was frozen at -20°C for mRNA detection. Target genes were amplified by PCR performed with a Taq DNA polymerase kit (Fast Start Taq DNA polymerase; Roche Diagnostics GmbH, Mannheim, Germany). Next, 1.5 $\mu$l cDNA from RT was replicated in PCR reactions in

a total volume of 25 $\mu$l containing Taq DNA polymerase (0.63 units), buffer supplied with enzymes, $MgCl_2$ (50 pmol), dNTP (200 $\mu$mol), and primers (20 pmol). The PCR conditions were 1 cycle of 95°C for 20 seconds followed by 40 cycles of 95°C for 3 seconds and 60°C for 30 seconds. After completion of PCR, a final melting curve was performed by denaturation at 95°C for 15 seconds and then recorded by cooling to 60°C and then heating slowing until 95°C for 15 seconds. All primers were manufactured by Fisher Scientific. Primer of GAPDH (glyceraldehydes-3-phosphate dehydrogenase): forward sequence: 5′-AGAC AGCCGCATCTTCTTGT-3′ and reverse sequence: 5′ -CTTGCCGTGGGTAGAGTCAT-3′. Primers of TNF-$\alpha$: forward sequence: 5′-GCCCAGACCCTCACACTC-3′ and reverse sequence: 5′-CACTCCAGCTGCTCCTCT-3′. Primer of IL-1$\beta$: forward sequence: 5′-CACCTTCTTTT CCTTCATCTTTG-3′ and reverse sequence: 5′-GTCGTT GCTTGT CTCTCCTTGTA-3′. The RT-PCR was performed on a Step One Plus Real-Time PCR system using the Step One software V2.3 (Applied Biosystems).

*2.12. Data Analyses.* All data from this study were expressed as mean + standard error of the mean (SEM). Differences between multiple groups were analyzed by analysis of variance (ANOVA) with two-tailed probabilities; multiple comparisons were performed by Tukey post hoc test. A $P$ value less than 0.05 was considered statistically significant. Representative results for a least three independent experiments were recorded. All of the above analyses were performed with the SPSS statistical software (V24.0) (SPSS, IBM, New York) and GraphPad Prism 6.0 (GraphPad Software., CA, USA).

## 3. Results

*3.1. HDGF Protein Expression in Sciatica.* To evaluate HDGF protein expression in patients with sciatica, serum samples were collected from 6 normal controls and from 31 patients with sciatica. The ELISA results showed that serum HDGF protein expression was significantly higher in the sciatica group (1.2725 + 0.79225 ng/$\mu$l) compared to the control group (0.1664 + 0.32404 ng/$\mu$l) ($P < 0.01$) (Figure 1(a)). This difference suggested that HDGF may have a crucial role in sciatica.

*3.2. Blocking HDGF Had Protective Effects on Neuron Cells.* To decide the concentration of rHDGF antibody with protective effect, we used PC-12 cells as neuron cells and MTT assay to detect the cell viability. In this study, we compared the different concentrations of 0, 10, 20, 50, and 100 nM rHDGF antibody with 500 $\mu$M $H_2O_2$. The MTT assay results showed that the cell viability of control group treated with 500 $\mu$M $H_2O_2$ was significantly lower that control group (without rHDGF antibody and $H_2O_2$) ($P < 0.001$). Treatment with 100 nM rHDGF antibody significantly protected the cell viability with 500 $\mu$M $H_2O_2$ ($P < 0.01$) (Figure 1(b)). These data indicate that $H_2O_2$ decreased the viability of neuron cells whereas blocking HDGF protected neuron cell viability.

*3.3. rHDGF Antibody Attenuated RTX-Induced Neuropathic Pain.* The rat model was used to investigate how blocking HDGF affects neuropathic pain induced by intraperitoneally injection with RTX. Calibrated forceps test was performed to detect the mechanical threshold. The RTX group showed significant decreases in paw withdrawal thresholds from day 1 after RTX injection as compared with the control in the same group ($P < 0.01$). Moreover, the RTX+rHDGF antibody group showed significant increases in paw withdrawal thresholds ($P < 0.01$) as compared with RTX group (Figure 1(c)). That is, pretreatment with rHDGF antibody improved the mechanical threshold for neuropathic pain induced by RTX injection.

*3.4. rHDGF Antibody Inhibited Astrocyte Reactions.* Nerve injury from sciatic nerve ligation is known to activate glial reactions [31, 32]. Astrocyte reaction (GFAP upregulation and astrogliosis) has also been observed in various injury conditions associated with enhanced pain states [33]. Immunofluorescence staining for GFAP staining was used to detect reactive astrocytes. The staining results showed that RTX induced significant increases in the proliferation of astrocytes on day 3 and day 7 ($P < 0.001$). As well, the astrocytes became swollen after exposed to RTX (Figure 2(a)). Pretreatment with rHDGF antibody significantly inhibited proliferation of astrocytes as well as morphology on day 3 after RTX injection ($P < 0.01$) but not on day 7 after RTX injection (Figures 2(a) and 2(b)).

*3.5. rHDGF Antibody Decreased Inflammatory Cytokines.* Activated inflammatory mediators that develop after peripheral nerve injury may cause a series of cellular and molecular events [34, 35]. Inflammatory responses induced by RTX in DRG and the spinal cord dorsal horn were investigated by performing RT-PCR and western blot analysis. Compared to the control group, the RTX group had significantly higher mRNA expressions of TNF-$\alpha$ (Figure 3(a)) and IL-1$\beta$ (Figure 3(b)) in DRG on day 3 ($P < 0.05$) and day 7 after RTX injection. In the RTX+rHDGF antibody group, pretreatment with rHDGF antibody significantly inhibited mRNA expression of TNF-$\alpha$ and IL-1$\beta$ on day 3 ($P < 0.05$) after RTX injection but not on day 7 after RTX injection (Figures 3(a) and 3(b)). Western blot analysis of the spinal cord dorsal horn showed that protein expression of iNOS was significantly higher in the RTX group compared to the control group on day 3 after RTX injection ($P < 0.05$) and on day 7 after RTX injection (Figure 3(c)). Pretreatment with rHDGF antibody significantly inhibited the iNOS protein expression on day 3 ($P < 0.05$) but not on day 7 (Figure 3(c)).

*3.6. rHDGF Antibody Inhibited Neuron Cells Apoptosis.* Peripheral or central nerve injuries result in Wallerian degeneration of axons at a lesion site [35–37]. Double immunofluorescence staining for TUNEL assay and neuron cell marker (Neu-N) showed increased apoptotic neurons in the spinal cord dorsal horn in rats treated with RTX. In the spinal cord dorsal horn, RTX induced neuron cell apoptosis on day 3 ($P < 0.001$) and day 7 after RTX injection (Figure 4). Pretreatment with rHDGF antibody decreased the number of

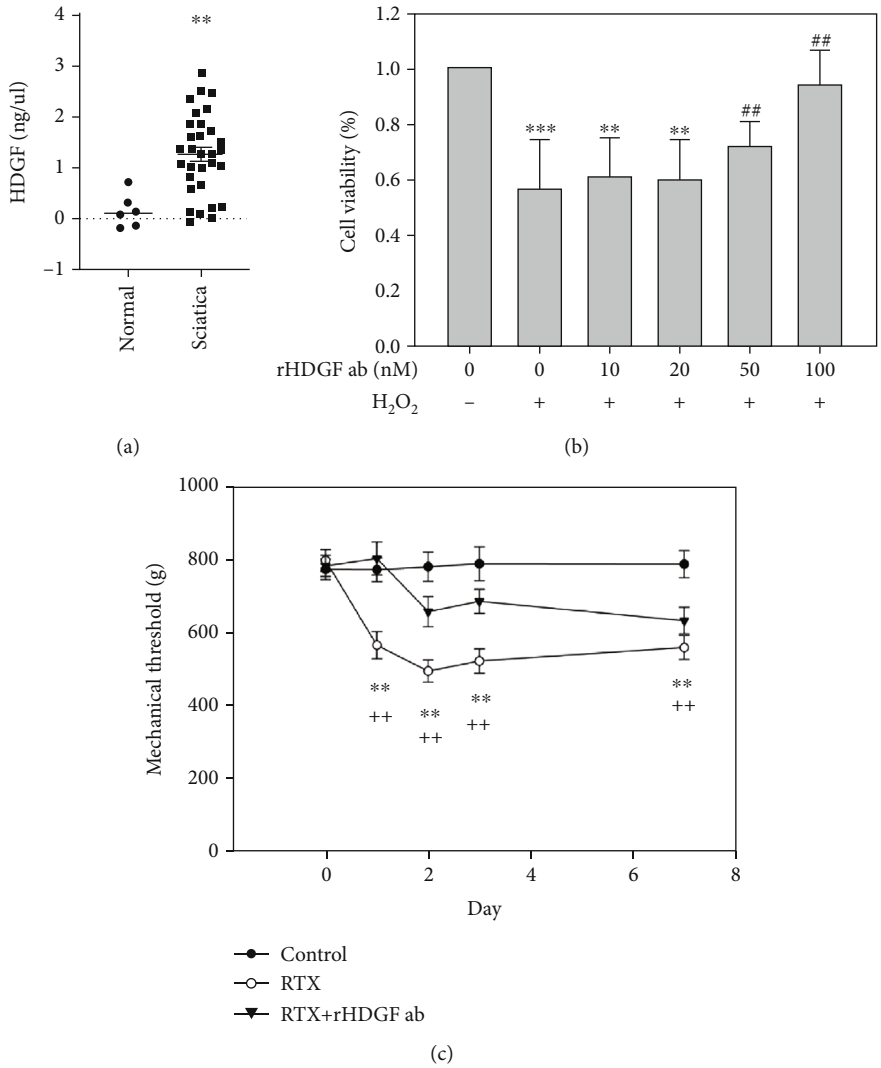


Figure 1: Serum HDGF is expressed higher in sciatica patients and rHDGF antibody increases pain threshold in RTX-treated rats. (a) Comparison of serum HDGF protein expression between sciatica patients and normal controls after ELISA analysis. The values detected from individuals were drawn as dots. The expression levels were shown as scattered plots; the middle line demonstrated the mean value. $^{**}P < 0.01$ compared with normal controls. (b) The PC-12 cells were incubated with different concentrations of rHDGF antibody (0, 10, 20, 50, and 100 nM) and 500 $\mu$M $H_2O_2$. Values are expressed as percentages of viable cells. $^{**}P < 0.01$, $^{***}P < 0.001$ compared with control group (without rHDGF antibody and $H_2O_2$). $^{\#\#}P < 0.01$ compared with the control group treated with 500 $\mu$M $H_2O_2$. Data are expressed as the mean + SEM ($n = 6$). (c) After the rats were divided into three groups, neuropathy was induced by intraperitoneally administration of a single dose of RTX (50 $\mu$g/kg). In the RTX+rHDGF antibody group, 100 $\mu$g/kg rHDGF antibody was administered and applied 24 hours before RTX injection. The control group received no rHDGF antibody pretreatment and no RTX injection. Calibrated forceps test was used to test the mechanical threshold for pain before and 1, 2, 3, and 7 days after RTX injection. $^{**}P < 0.01$, compared with control group. $^{++}P < 0.01$ compared with RTX+rHDGF antibody group. Data are expressed as the mean + SEM ($n = 6$ per group).

the apoptotic neuron cells in the spinal cord dorsal horn on day 3 ($P < 0.001$), but not on day 7 after RTX injection (Figure 4). These data indicate that blocking HDGF prevented neuron cell apoptosis induced by RTX in the spinal cord dorsal horn.

*3.7. Effect of rHDGF Antibody on Protein Expressions Associated with Pain.* The effects of blocking HDGF on RTX-induced neuropathic pain in the spinal cord dorsal horn were investigated by western blot analysis of expressions of proteins associated with pain, including HDGF, p-Akt/Akt, PI3K, substance P, and TrkB. Figure 5 shows that, compared to the control group, the RTX group had significantly higher expressions of HDGF ($P < 0.01$), p-Akt/Akt ($P < 0.01$), PI3K ($P < 0.05$), substance P ($P < 0.05$), and TrkB ($P < 0.01$) on day 3 after RTX injection and significantly higher expressions of HDGF, p-Akt/Akt, PI3K, substance P, and TrkB on day 7 after RTX injection. In contrast, compared to the RTX group, the RTX+rHDGF antibody group had significantly lower expressions of HDGF ($P < 0.01$), p-Akt/Akt ($P < 0.01$), PI3K ($P < 0.05$), substance P ($P < 0.05$), and TrkB ($P < 0.01$) on day 3. On day 7 after RTX injection,

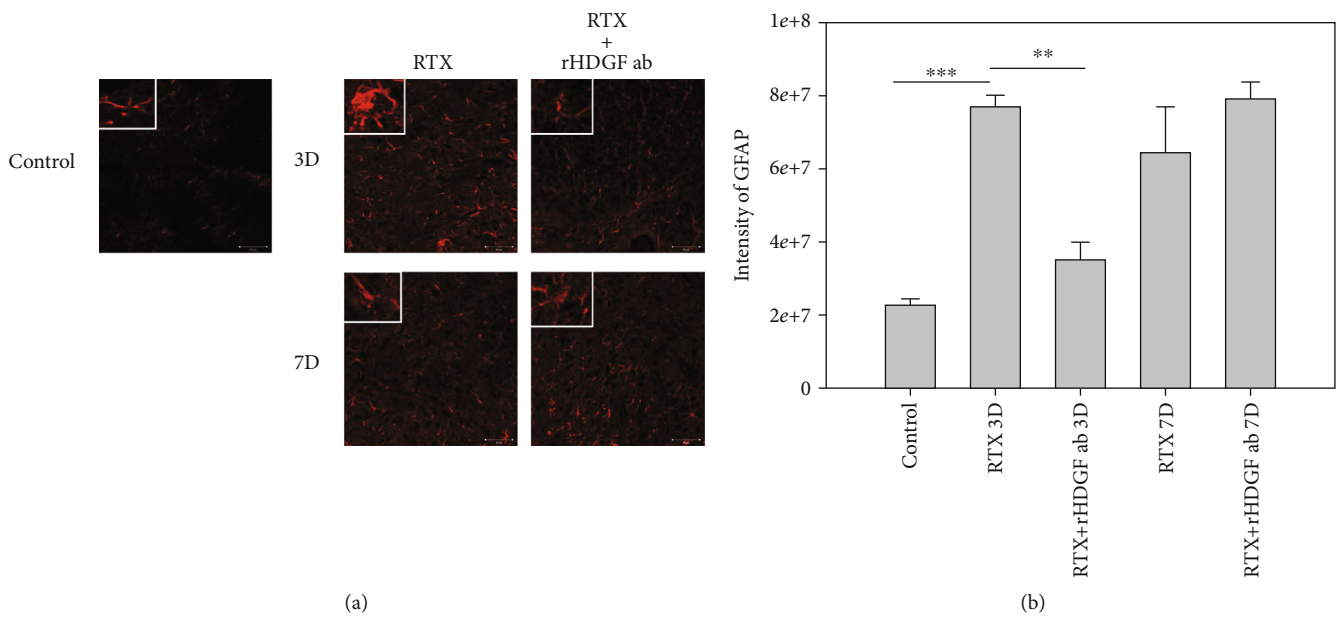


Figure 2: Effect of rHDGF antibody on astrocytes in the L3/L5 spinal cord dorsal horn (laminae I-II) of RTX-treated rats. After the rats were divided into three groups, neuropathy was induced by intraperitoneally administration of a single dose of RTX (50 $\mu$g/kg). In the RTX +rHDGF antibody group, 100 $\mu$g/kg rHDGF antibody was administered and applied 24 hours before RTX injection. The control group received no rHDGF antibody pretreatment and no RTX injection. At 3 or 7 days after RTX injection and/or pretreated with rHDGF antibody, L3-L5 spinal cord dorsal horn were harvested, and the proliferation of astrocytes (GFAP) was detected through immunofluorescence staining (200x magnification). (a) Representative immunofluorescence staining image shown are from 3 to 5 sections stained at least from 6 rats for each group. White rectangle in (a) indicates the astrocyte morphology for high magnifications. (b) Changes in intensity. $^{**}P < 0.01$, $^{***}P < 0.001$. Data are expressed as the mean + SEM ($n = 6$ per group).

however, the RTX+rHDGF antibody group did not reveal significantly lower expressions of HDGF, p-Akt/Akt, PI3K, substance P, or TrkB.

## 4. Discussion

The comparisons in this study revealed significantly higher levels of serum HDGF in the sciatica patients compared to normal controls. The rat model of neuropathy used in this study showed that RTX injections decreased the mechanical threshold for pain, upregulated TNF-$\alpha$ inflammation in the DRG, and upregulated expressions of HDGF, PI3K, p-Akt/Akt, TrkB, iNOS, and substance P in the spinal cord. The model obtained structural evidence of the role of central nervous system sensitization in the development of neuropathic pain after RTX injection. The HDGF is a growth factor and a mitogen with proliferative effect in various cells. The experiments demonstrated that blocking HDGF can reverse molecular events associated with the perception of pain induced by TNF-$\alpha$-mediated inflammation.

Glial alteration is a unifying mechanism of persistent hypersensitivity in chronic pain [38–40]. Many models agree that changes in glial phenotype mainly occur in the spinal cord, higher brain regions [41], and the peripheral nervous system [12, 42]. In the spinal cord, glial cells are responsible for functional and structural modifications. Activation of astrocytes may be responsible for long term maintenance of chronic pain [43]. Glial cells produce and release the proinflammatory cytokines, which can directly act on their receptors expressed on superficial dorsal horn neurons through synaptic mechanisms such as neural-glial interaction. Therefore, they sensitize the nociceptive pathway by enhancing excitatory synaptic transmission and by reducing inhibitory synaptic transmission [44, 45]. Inflammatory responses in the peripheral and central nervous systems are known to play crucial roles in the development and persistence of pathological pain states [46]. The proinflammatory cytokine TNF-$\alpha$ is expressed in various cell types, including neuronal and immune cells. Following nerve injury, TNF-$\alpha$ is synthesized by glial cells in the central nervous system and by Schwann cells in the peripheral nervous system [12]. Additionally, TNF-$\alpha$ is expressed in DRG neurons and is upregulated after peripheral nerve injury [47, 48]. Many studies suggest that TNF-$\alpha$ initiates and modulates neuronal activity in various classes of neurons and peripheral axons [48, 49]. Furthermore, TNF-$\alpha$ modulates nociceptive stimuli by enhancing downstream N-Methyl-D-aspartate (NMDA) currents [44]. Intraganglional application of TNF-$\alpha$ induces thermal hyperalgesia and sustained mechanical allodynia in rats [50, 51]. The increased expression of TNF-$\alpha$ induced by pain stimuli in nervous tissue indicates its essential role in the sensation of pain. Production of TNF-$\alpha$ starts as soon as 1 hour after injury and can continue for up to 2 weeks before decreasing. Fluctuation in TNF-$\alpha$ levels tends to increase or decrease with states of mechanical allodynia and thermal hyperalgesia [52]. Our rat model revealed that RTX induced proliferation of astrocytes and inflammatory cytokines on day 3 and day 7 after injection, and the proliferating effects were consistent

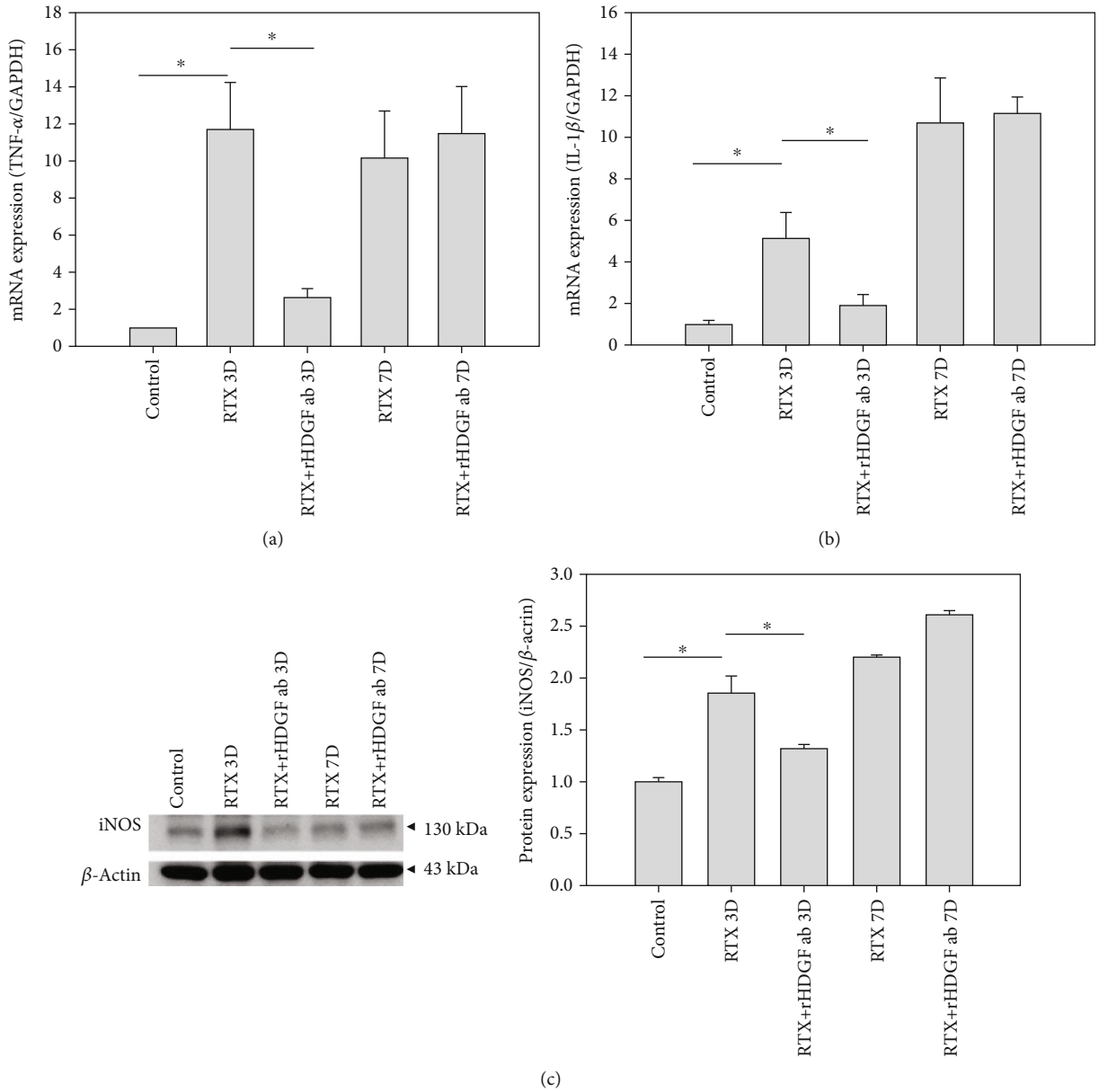


Figure 3: Effect of rHDGF antibody on inflammatory cytokines in RTX-treated rats. After the rats were divided into three groups, neuropathy was induced by intraperitoneally administration of a single dose of RTX (50 $\mu$g/kg). In the RTX+rHDGF antibody group, 100 $\mu$g/kg rHDGF antibody was administered and applied 24 hours before RTX injection. The control group received no rHDGF antibody pretreatment and no RTX injection. At 3 or 7 days after RTX injection and/or pretreated with rHDGF antibody, L3-L5 dorsal root ganglion and spinal cord dorsal horn were harvested. Inflammatory cytokines were examined through RT-PCR or western blot analysis. (a) Gene expression of TNF-$\alpha$ and (b) IL-1$\beta$ in dorsal root ganglion of rats. Gene expressions are ratios relative to GAPDH. $^*P < 0.05$. (c) iNOS expression in the spinal cord dorsal horn of rats. Representative Western blot results was shown. Expression levels were normalized to $\beta$-actin. $^*P < 0.05$. Data are expressed as the mean + SEM ($n = 6$ per group).

with changes in pain behavior. In the spinal cord dorsal horn, blocking HDGF inhibited the proliferation of glial cells and inhibited the release of inflammatory factors.

The important role of apoptosis in neuropathic pain is well established. Peripheral nerve injury causes neuronal apoptosis in the spinal cord dorsal horn [53, 54], which was consistent with our study shown on day 3 and day 7 after injection of RTX. The mechanical threshold of neuropathic pain significantly decreased with changes in apoptosis beginning on day 1 after RTX injection and continued until day 7. This suggests that neuron cell apoptosis has an important contributing role in persistent neuropathic pain. Binding between TNF-$\alpha$ and TNF receptors causes recruitment of TNFR1-associated protein and release of Smac/Diablo from mitochondria and is a hypothesized cause of neuronal cell death [52, 55]. Studies show that silencing HDGF prevents TNF-$\alpha$-induced release of proapoptotic factors from mitochondria [11]. However, other studies have reported that an HDGF knockdown can induce apoptosis [56] and cell cycle arrest in several human cancers. A HDGF knockdown can

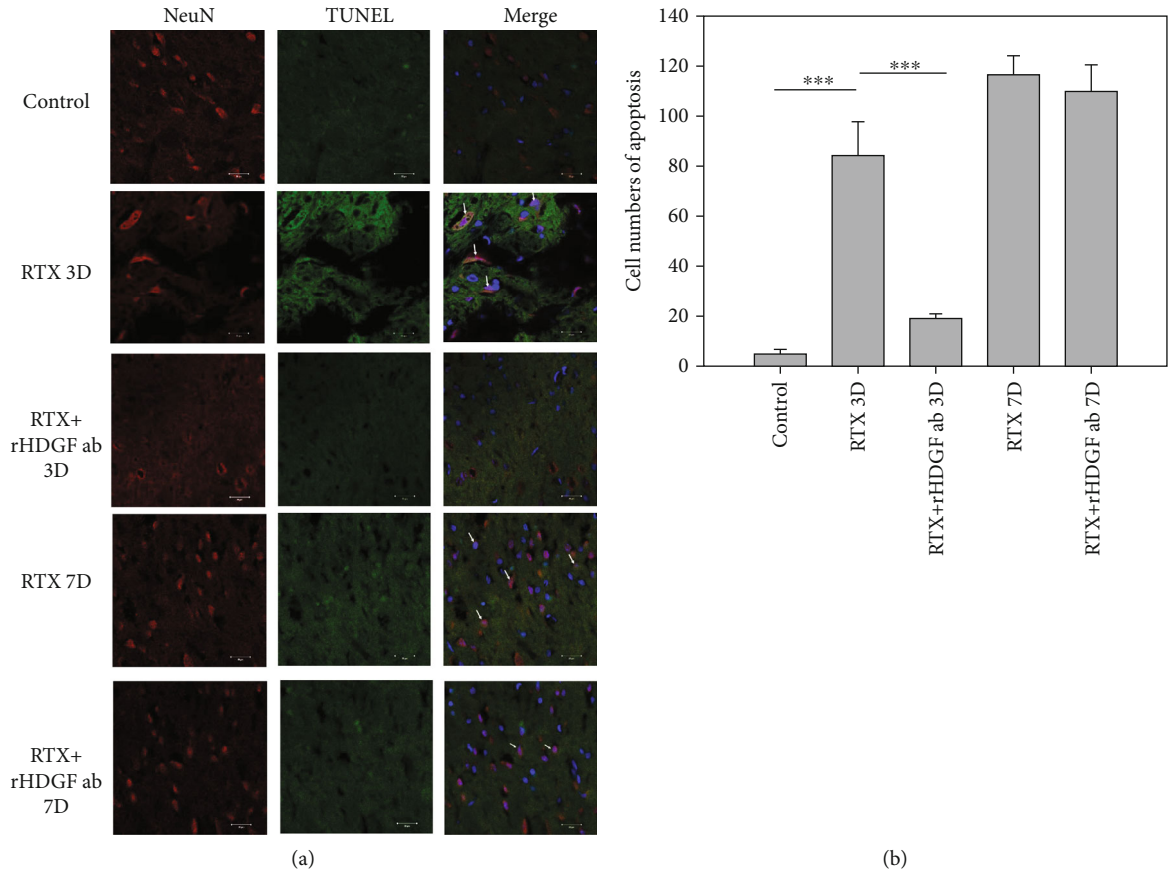


Figure 4: Effect of rHDGF antibody on neuron cells in the L3/L5 spinal cord dorsal horn of RTX-treated rats. After the rats were divided into three groups, neuropathy was induced by intraperitoneally administration of a single dose of RTX (50 $\mu$g/kg). In the RTX+rHDGF antibody group, 100 $\mu$g/kg rHDGF antibody was administered and applied 24 hours before RTX injection. The control group received no rHDGF antibody pretreatment and no RTX injection. At 3 or 7 days after RTX injection and/or pretreated with rHDGF antibody, L3-L5 spinal cord dorsal horn were harvested, and the expression of apoptotic neurons were evaluated through immunofluorescence staining by TUNEL assay (green), neuron cell marker (Neu-N) (Red), and DAPI (blue) (400x magnification). (a) Representative immunofluorescence staining image shown are from 3 to 5 sections stained at least from 6 rats for each group. Apoptotic neurons visualized (indicated by arrows) in the dorsal horn of the L3/L5 spinal cord are also shown. (b) The numbers of apoptotic neurons per animal were shown. $^{***}P < 0.001$. Data are expressed as the mean + SEM ($n = 6$ per group).

also induce apoptosis through a Fas-mediated extrinsic apoptotic pathway and can induce apoptosis through a Bad-mediated intrinsic apoptotic pathway when ERK and Akt are inactivated [57, 58]. Our study showed that pretreatment with rHDGF antibody decreased the number of the apoptotic neuron cells in the spinal cord dorsal horn on day 3 after neuropathic pain was experimentally induced by injection of RTX.

Neuropathic pain induced by peripheral or central nerve injury evokes various changes in biological and biochemical markers [59–61]. Central and peripheral sensitization ensue after many inflammatory processes [62]. The PI3K signal transducer enzyme is involved in various physiological and pathological functions. It activates plasma membrane localized protein kinase (Akt) and is a key mediator of central sensitization of spinal cord neurons associated with persistent afferent inputs. This enzyme also contributes to chronic pain and has been implicated in NMDA receptors and wind-up of dorsal horn nociceptive neurons [63–65]. Production of NO is triggered by calcium influx into neurons after NMDA receptors are opened [64]. The PI3K/Akt signaling reportedly participates in activation of NOS [66–69]. Of all isoforms, iNOS has the most important roles in inflammation and pain. In high concentrations, iNOS is neurotoxic and can trigger Wallerian degeneration [70]. Damage to peripheral sensory neurons then affect the central nervous system through release of neurotransmitters, including glutamate, substance P, and brain-derived neuropathic factor (BDNF), from the central terminals in the primary nociceptor afferents [71–73]. Binding of BDNF to tyrosine kinase receptor in the post synaptic membrane in turn mediates phosphorylation of NMDA receptors, which is associated with onset and maintenance of neuropathic pain [74, 75]. Substance P coexists with glutamate and plays a crucial role in pain perception. Since a release of substance P induced by noxious simulation can modulate NMDA receptors, substance P promotes central hyperexcitability and increases pain sensitivity [62, 72, 76]. Our study showed that expressions of proteins PI3K, p-Akt/Akt, TrkB, iNOS, and substance P were significantly higher in the RTX group compared to the control

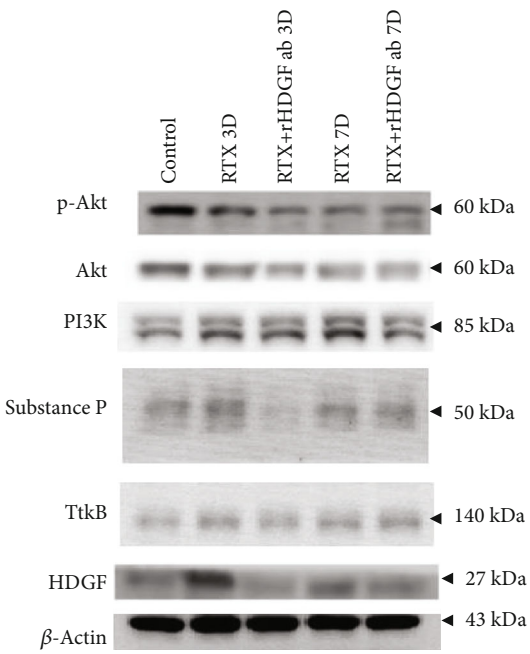


(a)

Figure 5: Continued.

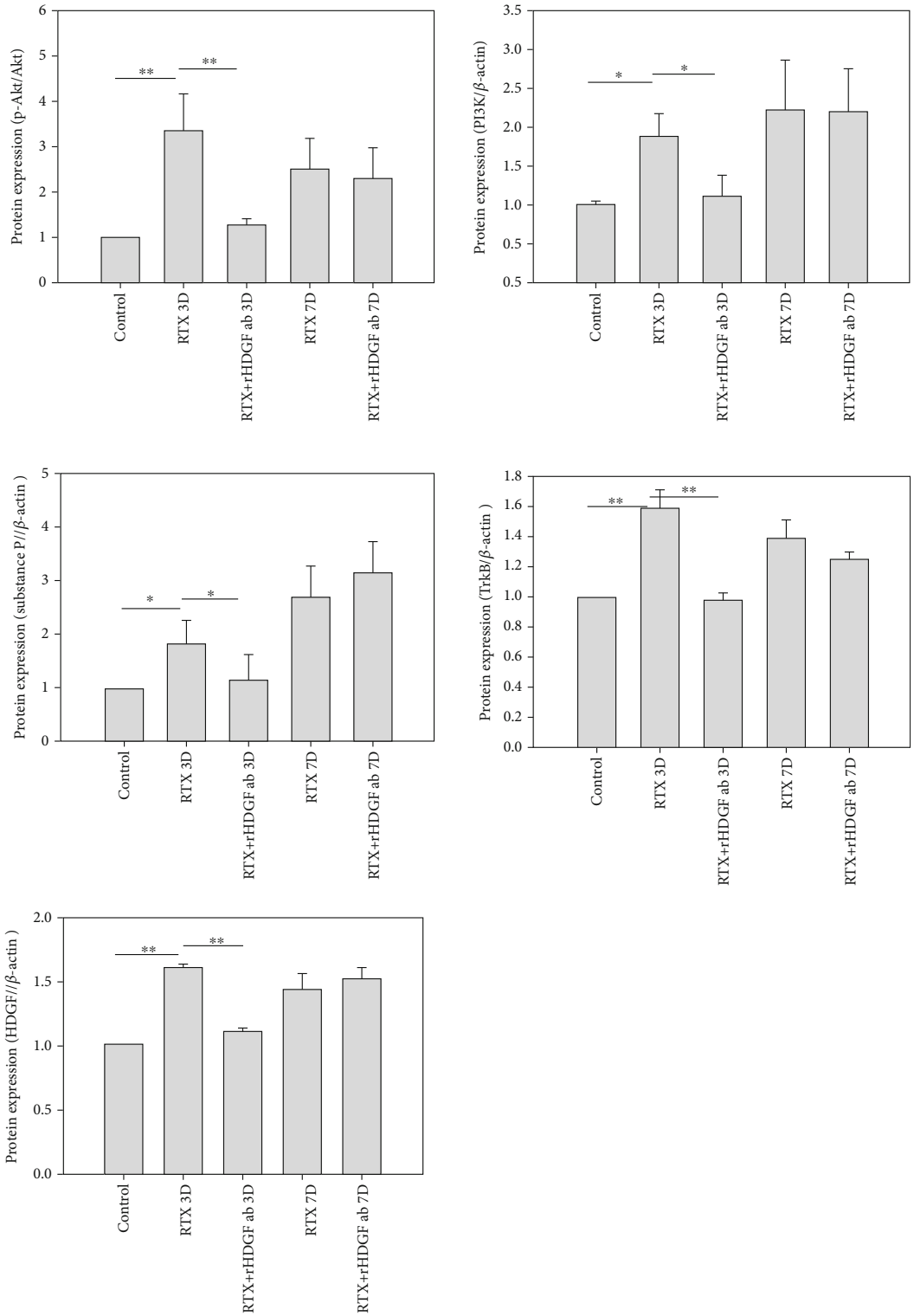


(b)

Figure 5: Effect of rHDGF antibody on expressions of HDGF, p-Akt/Akt, PI3K, substance P, and TrkB in the L3/L5 spinal cord dorsal horn of RTX-rats. After the rats were divided into three groups, neuropathy was induced by intraperitoneally administration of a single dose of RTX (50 $\mu$g/kg). In the RTX+rHDGF antibody group, 100 $\mu$g/kg rHDGF antibody was administered and applied 24 hours before RTX injection. The control group received no rHDGF antibody pretreatment and no RTX injection. At 3 or 7 days after RTX injection and/or pretreated with rHDGF antibody, L3-L5 spinal cord dorsal horn were harvested and protein expressions were measured through western blot analysis. (a) Representative Western blot results. (b) Expression levels were normalized to $\beta$-actin. $^{*}P < 0.05$, $^{**}P < 0.01$. Data are expressed as the mean + SEM ($n = 6$ per group).

group. Pretreatment with rHDGF antibody significantly decreased expressions of proteins PI3K, p-Akt/Akt, TrkB, iNOS, and substance P on day 3 after RTX injection.

## 5. Conclusions

Our results suggest that rHDGF antibody protects against RTX-induced neuropathic pain mediating inflammation induced by proinflammatory cytokines. The serum level of HDGF was higher in sciatica patients compared to normal controls. Our animal model of RTX-induced neuropathic pain revealed that higher protein expression of HDGF in spinal cord and blocking HDGF improved the mechanical threshold response. In DRG, blocking HDGF inhibited inflammatory cytokines. In the spinal cord dorsal horn, blocking HDGF inhibited proliferation of astrocytes and inhibited apoptosis of neuronal cells. Additionally, blocking HDGF attenuated expressions of proteins associated with pain (iNOS, TrkB, substance P, PI3K, and p-Akt/Akt). Taken together, the experimental results indicate that inhibiting HDGF can reduce neuropathic pain caused by an inflammatory response.

## Data Availability

The data used to support the findings of this study are included within the article.

## Conflicts of Interest

All the authors declare they have no conflicts of interest.

## Authors' Contributions

Ying-Yi Lu and Chih-Lung Lin contributed equally to this work.

## Acknowledgments

This work was supported by grants NSYSUKMU-104-P10 from NSYSU-KMU Joint Research Project and KMUH105-5M17, KMUH106-6T09, KMUH108-8M23, and KMU-Q108029 from Kaohsiung Medical University Hospital. The funders had no role in the design of the study, in the collection, analyses, or interpretation of data, in the writing of the manuscript, or in the decision to publish the results.

## References

[1] R. A. Lewis, N. H. Williams, A. J. Sutton et al., "Comparative clinical effectiveness of management strategies for sciatica: systematic review and network meta-analyses," *The Spine Journal*, vol. 15, no. 6, pp. 1461–1477, 2015.

[2] F. Tubach, J. Beaute, and A. Leclerc, "Natural history and prognostic indicators of sciatica," *Journal of Clinical Epidemiology*, vol. 57, no. 2, pp. 174–179, 2004.

[3] R. Baron, "Mechanisms of disease: neuropathic pain–a clinical perspective," *Nature Clinical Practice. Neurology*, vol. 2, no. 2, pp. 95–106, 2006.

[4] H. T. Cheng, J. R. Dauch, J. M. Hayes, Y. Hong, and E. L. Feldman, "Nerve growth factor mediates mechanical allodynia in a mouse model of type 2 diabetes," *Journal of Neuropathology and Experimental Neurology*, vol. 68, no. 11, pp. 1229–1243, 2009.

[5] M. Ragé, N. Van Acker, P. Facer et al., "The time course of $CO_2$ laser-evoked responses and of skin nerve fibre markers after topical capsaicin in human volunteers," *Clinical Neurophysiology*, vol. 121, no. 8, pp. 1256–1266, 2010.

[6] C. H. Gibbons, N. Wang, and R. Freeman, "Capsaicin induces degeneration of cutaneous autonomic nerve fibers," *Annals of Neurology*, vol. 68, no. 6, pp. 888–898, 2010.

[7] H. L. Pan, G. M. Khan, K. D. Alloway, and S. R. Chen, "Resiniferatoxin induces paradoxical changes in thermal and mechanical sensitivities in rats: mechanism of action," *The Journal of Neuroscience*, vol. 23, no. 7, pp. 2911–2919, 2003.

[8] N. Tanaka, M. Yamaga, S. Tateyama, T. Uno, I. Tsuneyoshi, and M. Takasaki, "The effect of pulsed radiofrequency current on mechanical allodynia induced with resiniferatoxin in rats," *Anesthesia and Analgesia*, vol. 111, no. 3, pp. 784–790, 2010.

[9] Y. L. Hsieh, H. Chiang, T. J. Tseng, and S. T. Hsieh, "Enhancement of cutaneous nerve regeneration by 4-methylcatechol in resiniferatoxin-induced neuropathy," *Journal of Neuropathology and Experimental Neurology*, vol. 67, no. 2, pp. 93–104, 2008.

[10] S.-C. Lu, Y.-S. Chang, H.-W. Kan, and Y.-L. Hsieh, "Tumor necrosis factor-alpha mediated pain hypersensitivity through Ret receptor in resiniferatoxin neuropathy," *The Kaohsiung Journal of Medical Sciences*, vol. 34, no. 9, pp. 494–502, 2018.

[11] N. Machuy, B. Thiede, K. Rajalingam et al., "A global approach combining proteome analysis and phenotypic screening with RNA interference yields novel apoptosis regulators," *Molecular & Cellular Proteomics*, vol. 4, no. 1, pp. 44–55, 2005.

[12] S. Ohtori, K. Takahashi, H. Moriya, and R. R. Myers, "TNF-alpha and TNF-alpha receptor type 1 upregulation in glia and neurons after peripheral nerve injury: studies in murine DRG and spinal cord," *Spine (Phila Pa 1976)*, vol. 29, no. 10, pp. 1082–1088, 2004.

[13] H. Nakamura, Y. Izumoto, H. Kambe et al., "Molecular cloning of complementary DNA for a novel human hepatoma-derived growth factor. Its homology with high mobility group-1 protein," *The Journal of Biological Chemistry*, vol. 269, no. 40, pp. 25143–25149, 1994.

[14] S. Bremer, K. Klein, A. Sedlmaier, M. Abouzied, V. Gieselmann, and S. Franken, "Hepatoma-derived growth factor and nucleolin exist in the same ribonucleoprotein complex," *BMC Biochemistry*, vol. 14, no. 1, p. 2, 2013.

[15] Y. Kishima, K. Yoshida, H. Enomoto et al., "Antisense oligonucleotides of hepatoma-derived growth factor (HDGF) suppress the proliferation of hepatoma cells," *Hepato-Gastroenterology*, vol. 49, no. 48, pp. 1639–1644, 2002.

[16] H. Enomoto, K. Yoshida, Y. Kishima, Y. Okuda, and H. Nakamura, "Participation of hepatoma-derived growth factor in the regulation of fetal hepatocyte proliferation," *Journal of Gastroenterology*, vol. 37, Supplement 14, pp. 158–161, 2002.

[17] H. Enomoto, K. Yoshida, Y. Kishima et al., "Hepatoma-derived growth factor is highly expressed in developing liver and promotes fetal hepatocyte proliferation," *Hepatology*, vol. 36, no. 6, pp. 1519–1527, 2002.

[18] H. Enomoto, H. Nakamura, W. Liu et al., "Hepatoma-derived growth factor is induced in liver regeneration," *Hepatology Research*, vol. 39, no. 10, pp. 988–997, 2009.

[19] R. E. Cilley, S. E. Zgleszewski, and M. R. Chinoy, "Fetal lung development: airway pressure enhances the expression of developmental genes," *Journal of Pediatric Surgery*, vol. 35, no. 1, pp. 113–119, 2000, discussion 9.

[20] A. D. Everett, J. V. Narron, T. Stoops, H. Nakamura, and A. Tucker, "Hepatoma-derived growth factor is a pulmonary endothelial cell-expressed angiogenic factor," *American Journal of Physiology. Lung Cellular and Molecular Physiology*, vol. 286, no. 6, pp. L1194–L1201, 2004.

[21] J. V. Narron, T. D. Stoops, K. Barringhaus, M. Matsumura, and A. D. Everett, "Hepatoma-derived growth factor is expressed after vascular injury in the rat and stimulates smooth muscle cell migration," *Pediatric Research*, vol. 59, no. 6, pp. 778–783, 2006.

[22] A. D. Everett, T. Stoops, and C. A. McNamara, "Nuclear targeting is required for hepatoma-derived growth factor-stimulated mitogenesis in vascular smooth muscle cells," *The Journal of Biological Chemistry*, vol. 276, no. 40, pp. 37564–37568, 2001.

[23] A. D. Everett, D. R. Lobe, M. E. Matsumura, H. Nakamura, and C. A. McNamara, "Hepatoma-derived growth factor stimulates smooth muscle cell growth and is expressed in vascular development," *The Journal of Clinical Investigation*, vol. 105, no. 5, pp. 567–575, 2000.

[24] A. D. Everett, "Identification, cloning, and developmental expression of hepatoma-derived growth factor in the developing rat heart," *Developmental Dynamics*, vol. 222, no. 3, pp. 450–458, 2001.

[25] J. A. Oliver and Q. Al-Awqati, "An endothelial growth factor involved in rat renal development," *The Journal of Clinical Investigation*, vol. 102, no. 6, pp. 1208–1219, 1998.

[26] Z. Zhou, Y. Yamamoto, F. Sugai et al., "Hepatoma-derived growth factor is a neurotrophic factor harbored in the nucleus," *The Journal of Biological Chemistry*, vol. 279, no. 26, pp. 27320–27326, 2004.

[27] Y. L. Hsieh, H. Chiang, J. H. Lue, and S. T. Hsieh, "P2X3-mediated peripheral sensitization of neuropathic pain in resiniferatoxin-induced neuropathy," *Experimental Neurology*, vol. 235, no. 1, pp. 316–325, 2012.

[28] C. L. Lin, Y. S. Fu, T. H. Hsiao, and Y. L. Hsieh, "Enhancement of purinergic signalling by excessive endogenous ATP in resiniferatoxin (RTX) neuropathy," *Purinergic Signal*, vol. 9, no. 2, pp. 249–257, 2013.

[29] M. Zimmermann, "Ethical guidelines for investigations of experimental pain in conscious animals," *Pain*, vol. 16, no. 2, pp. 109-110, 1983.

[30] O. E. Luis-Delgado, M. Barrot, J. L. Rodeau et al., "Calibrated forceps: a sensitive and reliable tool for pain and analgesia studies," *The Journal of Pain*, vol. 7, no. 1, pp. 32–39, 2006.

[31] Z. Y. Zhuang, P. Gerner, C. J. Woolf, and R. R. Ji, "ERK is sequentially activated in neurons, microglia, and astrocytes by spinal nerve ligation and contributes to mechanical allodynia in this neuropathic pain model," *Pain*, vol. 114, no. 1, pp. 149–159, 2005.

[32] S. X. Jin, Z. Y. Zhuang, C. J. Woolf, and R. R. Ji, "p38 mitogen-activated protein kinase is activated after a spinal nerve ligation in spinal cord microglia and dorsal root ganglion neurons and contributes to the generation of neuropathic pain," *The Journal of Neuroscience*, vol. 23, no. 10, pp. 4017–4022, 2003.

[33] Y. J. Gao and R. R. Ji, "Targeting astrocyte signaling for chronic pain," *Neurotherapeutics*, vol. 7, no. 4, pp. 482–493, 2010.

[34] F. Fregnan, L. Muratori, A. R. Simoes, M. G. Giacobini-Robecchi, and S. Raimondo, "Role of inflammatory cytokines in peripheral nerve injury," *Neural Regeneration Research*, vol. 7, no. 29, pp. 2259–2266, 2012.

[35] V. H. Perry, M. C. Brown, and S. Gordon, "The macrophage response to central and peripheral nerve injury. A possible role for macrophages in regeneration," *The Journal of Experimental Medicine*, vol. 165, no. 4, pp. 1218–1223, 1987.

[36] R. Wagner, H. M. Heckman, and R. R. Myers, "Wallerian degeneration and hyperalgesia after peripheral nerve injury are glutathione-dependent," *Pain*, vol. 77, no. 2, pp. 173–179, 1998.

[37] E. R. Lunn, V. H. Perry, M. C. Brown, H. Rosen, and S. Gordon, "Absence of Wallerian degeneration does not hinder regeneration in peripheral nerve," *The European Journal of Neuroscience*, vol. 1, no. 1, pp. 27–33, 1989.

[38] M. Tsuda, A. Mizokoshi, Y. Shigemoto-Mogami, S. Koizumi, and K. Inoue, "Activation of p38 mitogen-activated protein kinase in spinal hyperactive microglia contributes to pain hypersensitivity following peripheral nerve injury," *Glia*, vol. 45, no. 1, pp. 89–95, 2004.

[39] R. R. Ji, Y. Kawasaki, Z. Y. Zhuang, Y. R. Wen, and I. Decosterd, "Possible role of spinal astrocytes in maintaining chronic pain sensitization: review of current evidence with focus on bFGF/JNK pathway," *Neuron Glia Biology*, vol. 2, no. 4, pp. 259–269, 2006.

[40] E. D. Milligan and L. R. Watkins, "Pathological and protective roles of glia in chronic pain," *Nature Reviews. Neuroscience*, vol. 10, no. 1, pp. 23–36, 2009.

[41] B. C. Hains and S. G. Waxman, "Activated microglia contribute to the maintenance of chronic pain after spinal cord injury," *The Journal of Neuroscience*, vol. 26, no. 16, pp. 4308–4317, 2006.

[42] C. M. Peters, J. M. Jimenez-Andrade, B. M. Jonas et al., "Intravenous paclitaxel administration in the rat induces a peripheral sensory neuropathy characterized by macrophage infiltration and injury to sensory neurons and their supporting cells," *Experimental Neurology*, vol. 203, no. 1, pp. 42–54, 2007.

[43] R. D. Gosselin, M. R. Suter, R. R. Ji, and I. Decosterd, "Glial cells and chronic pain," *The Neuroscientist*, vol. 16, no. 5, pp. 519–531, 2010.

[44] Y. Kawasaki, L. Zhang, J. K. Cheng, and R. R. Ji, "Cytokine mechanisms of central sensitization: distinct and overlapping role of interleukin-1beta, interleukin-6, and tumor necrosis factor-alpha in regulating synaptic and neuronal activity in the superficial spinal cord," *The Journal of Neuroscience*, vol. 28, no. 20, pp. 5189–5194, 2008.

[45] Y. J. Gao and R. R. Ji, "Chemokines, neuronal-glial interactions, and central processing of neuropathic pain," *Pharmacology & Therapeutics*, vol. 126, no. 1, pp. 56–68, 2010.

[46] J. M. Zhang and J. An, "Cytokines, inflammation, and pain," *International Anesthesiology Clinics*, vol. 45, no. 2, pp. 27–37, 2007.

[47] G. M. Murphy, Y. L. I. Lee, X.-C. Jia et al., "Tumor necrosis factor-alpha and basic fibroblast growth factor decrease glial fibrillary acidic protein and its encoding mRNA in astrocyte

cultures and glioblastoma cells," *Journal of Neurochemistry*, vol. 65, no. 6, pp. 2716–2724, 1995.

[48] M. Schafers, D. H. Lee, D. Brors, T. L. Yaksh, and L. S. Sorkin, "Increased sensitivity of injured and adjacent uninjured rat primary sensory neurons to exogenous tumor necrosis factor-alpha after spinal nerve ligation," *The Journal of Neuroscience*, vol. 23, no. 7, pp. 3028–3038, 2003.

[49] L. S. Sorkin and C. M. Doom, "Epineurial application of TNF elicits an acute mechanical hyperalgesia in the awake rat," *Journal of the Peripheral Nervous System*, vol. 5, no. 2, pp. 96–100, 2000.

[50] M. Schafers, L. S. Sorkin, C. Geis, and V. I. Shubayev, "Spinal nerve ligation induces transient upregulation of tumor necrosis factor receptors 1 and 2 in injured and adjacent uninjured dorsal root ganglia in the rat," *Neuroscience Letters*, vol. 347, no. 3, pp. 179–182, 2003.

[51] Y. Homma, S. J. Brull, and J. M. Zhang, "A comparison of chronic pain behavior following local application of tumor necrosis factor alpha to the normal and mechanically compressed lumbar ganglia in the rat," *Pain*, vol. 95, no. 3, pp. 239–246, 2002.

[52] P. Andrade, V. Visser-Vandewalle, C. Hoffmann, H. W. Steinbusch, M. A. Daemen, and G. Hoogland, "Role of TNF-alpha during central sensitization in preclinical studies," *Neurological Sciences*, vol. 32, no. 5, pp. 757–771, 2011.

[53] M. Sekiguchi, H. Kobayashi, Y. Sekiguchi, S. Konno, and S. Kikuchi, "Sympathectomy reduces mechanical allodynia, tumor necrosis factor-alpha expression, and dorsal root ganglion apoptosis following nerve root crush injury," *Spine (Phila Pa 1976)*, vol. 33, pp. 1163–1169, 2008.

[54] W. M. Campana and R. R. Myers, "Exogenous erythropoietin protects against dorsal root ganglion apoptosis and pain following peripheral nerve injury," *The European Journal of Neuroscience*, vol. 18, no. 6, pp. 1497–1506, 2003.

[55] L. Leung and C. M. Cahill, "TNF-$\alpha$ and neuropathic pain-a review," *Journal of Neuroinflammation*, vol. 7, no. 1, p. 27, 2010.

[56] Y. Yu, H. Shen, H. Yu et al., "Systematic proteomic analysis of human hepotacellular carcinoma cells reveals molecular pathways and networks involved in metastasis," *Molecular BioSystems*, vol. 7, no. 6, pp. 1908–1916, 2011.

[57] T. Y. Tsang, W. Y. Tang, W. P. Tsang, N. N. Co, S. K. Kong, and T. T. Kwok, "Mechanistic study on growth suppression and apoptosis induction by targeting hepatoma-derived growth factor in human hepatocellular carcinoma HepG2 cells," *Cellular Physiology and Biochemistry*, vol. 24, no. 3-4, pp. 253–262, 2009.

[58] T. Y. Tsang, W. Y. Tang, W. P. Tsang, N. N. Co, S. K. Kong, and T. T. Kwok, "Downregulation of hepatoma-derived growth factor activates the Bad-mediated apoptotic pathway in human cancer cells," *Apoptosis*, vol. 13, no. 9, pp. 1135–1147, 2008.

[59] R. W. Colburn, A. J. Rickman, and J. A. DeLeo, "The effect of site and type of nerve injury on spinal glial activation and neuropathic pain behavior," *Experimental Neurology*, vol. 157, no. 2, pp. 289–304, 1999.

[60] D. Bridges, S. W. Thompson, and A. S. Rice, "Mechanisms of neuropathic pain," *British Journal of Anaesthesia*, vol. 87, no. 1, pp. 12–26, 2001.

[61] C. J. Woolf and R. J. Mannion, "Neuropathic pain: aetiology, symptoms, mechanisms, and management," *The Lancet*, vol. 353, no. 9168, pp. 1959–1964, 1999.

[62] S. P. Cohen and J. Mao, "Neuropathic pain: mechanisms and their clinical implications," *BMJ*, vol. 348, no. feb05 6, p. f7656, 2014.

[63] S. Pezet, F. Marchand, R. D'Mello et al., "Phosphatidylinositol 3-kinase is a key mediator of central sensitization in painful inflammatory conditions," *The Journal of Neuroscience*, vol. 28, no. 16, pp. 4261–4270, 2008.

[64] S. Begon, G. Pickering, A. Eschalier, A. Mazur, Y. Rayssiguier, and C. Dubray, "Role of spinal NMDA receptors, protein kinase C and nitric oxide synthase in the hyperalgesia induced by magnesium deficiency in rats," *British Journal of Pharmacology*, vol. 134, no. 6, pp. 1227–1236, 2001.

[65] W. Liu, Y. Lv, and F. Ren, "PI3K/Akt pathway is required for spinal central sensitization in neuropathic pain," *Cellular and Molecular Neurobiology*, vol. 38, no. 3, pp. 747–755, 2018.

[66] N. A. Umoh, R. K. Walker, R. M. Millis, M. Al-Rubaiee, P. R. Gangula, and G. E. Haddad, "Calcitonin gene-related peptide regulates cardiomyocyte survival through regulation of oxidative stress by PI3K/Akt and MAPK signaling pathways," *Annals of Clinical and Experimental Hypertension*, vol. 2, p. 1007, 2014.

[67] S. Dimmeler, I. Fleming, B. Fisslthaler, C. Hermann, R. Busse, and A. M. Zeiher, "Activation of nitric oxide synthase in endothelial cells by Akt-dependent phosphorylation," *Nature*, vol. 399, no. 6736, pp. 601–605, 1999.

[68] D. Fulton, J.-P. Gratton, T. J. McCabe et al., "Regulation of endothelium-derived nitric oxide production by the protein kinase Akt," *Nature*, vol. 399, no. 6736, pp. 597–601, 1999.

[69] Z. H. Ouyang, W. J. Wang, Y. G. Yan, B. Wang, and G. H. Lv, "The PI3K/Akt pathway: a critical player in intervertebral disc degeneration," *Oncotarget*, vol. 8, no. 34, pp. 57870–57881, 2017.

[70] A. Ahlawat and S. Sharma, "A new promising simultaneous approach for attenuating type II diabetes mellitus induced neuropathic pain in rats: iNOS inhibition and neuroregeneration," *European Journal of Pharmacology*, vol. 818, pp. 419–428, 2018.

[71] M. Tomiyama, K. Furusawa, M. Kamijo, T. Kimura, M. Matsunaga, and M. Baba, "Upregulation of mRNAs coding for AMPA and NMDA receptor subunits and metabotropic glutamate receptors in the dorsal horn of the spinal cord in a rat model of diabetes mellitus," *Brain Research. Molecular Brain Research*, vol. 136, no. 1-2, pp. 275–281, 2005.

[72] C. De Felipe, J. F. Herrero, J. A. O'Brien et al., "Altered nociception, analgesia and aggression in mice lacking the receptor for substance P," *Nature*, vol. 392, no. 6674, pp. 394–397, 1998.

[73] Y. Q. Cao, P. W. Mantyh, E. J. Carlson, A. M. Gillespie, C. J. Epstein, and A. I. Basbaum, "Primary afferent tachykinins are required to experience moderate to intense pain," *Nature*, vol. 392, no. 6674, pp. 390–394, 1998.

[74] D. V. Tillu, O. K. Melemedjian, M. N. Asiedu et al., "Resveratrol engages AMPK to attenuate ERK and mTOR signaling in sensory neurons and inhibits incision-induced acute and chronic pain," *Molecular Pain*, vol. 8, pp. 1744–8069, 2012.

[75] N. Khan and M. T. Smith, "Neurotrophins and neuropathic pain: role in pathobiology," *Molecules*, vol. 20, no. 6, pp. 10657–10688, 2015.

[76] Y. De Koninck and J. L. Henry, "Substance P-mediated slow excitatory postsynaptic potential elicited in dorsal horn neurons in vivo by noxious stimulation," *Proceedings of the National Academy of Sciences*, vol. 88, pp. 11344–11348, 1991.

Hindawi
Neural Plasticity
Volume 2021, Article ID 6684176, 8 pages
https://doi.org/10.1155/2021/6684176

*Research Article*

# Celecoxib-Loaded Electrospun Fibrous Antiadhesion Membranes Reduce COX-2/$PGE_2$ Induced Inflammation and Epidural Fibrosis in a Rat Failed Back Surgery Syndrome Model

**Wei Wang,[1] Yunhao Wang,[2] Tengfei Lou,[1] Mingqian Ding,[3] Juehong Li,[1] Hao Xiong,[1] Zhixiao Yao,[1] Yingying Ma,[4] Huajiang Chen,[2] and Shenghe Liu[1]**

[1]*Department of Orthopaedics, Shanghai Jiao Tong University Affiliated Sixth People's Hospital, 600 Yishan Road, Shanghai, China*
[2]*Department of Spinal Surgery, Changzheng Hospital Affiliated to Second Military Medical University, 415 Fengyang Road, Shanghai 200003, China*
[3]*Taian TSCM Hospital, No. 265 Lingshan Street, Taian, Shandong 271000, China*
[4]*Department of Medical Engineering, Shandong Provincial Hospital Affiliated to Shandong University, 423 5th Longitude Crossing 7th Latitude Road, Shandong 250021, China*

Correspondence should be addressed to Huajiang Chen; spine.chen@163.com and Shenghe Liu; liush82@163.com

Received 12 November 2020; Revised 4 January 2021; Accepted 1 February 2021; Published 23 February 2021

Academic Editor: Mou-Xiong Zheng



To date, failed back surgery syndrome (FBSS) remains a therapy-refractory clinical condition after spinal surgery. The antiadhesion membrane is applied to prevent FBSS by isolating fibrosis; however, the inflammation stimulated by the foreign body and surgical trauma needs to be further resolved simultaneously. Therefore, we developed new electrospun polycaprolactone (PCL) fibrous membranes loaded with celecoxib (CEL) to prevent fibrosis and inflammation associated with FBSS. The CEL-loaded PCL fibers were randomly distributed, and the drug was released over two weeks. Fluorescence micrographs revealed that the fibroblasts proliferated less on the PCL-CEL fibrous membranes than in the PCL group and the blank control. In the rat laminectomy model after 4 weeks, magnetic resonance imaging of epidural fibrosis was least in the PCL-CEL group. Expression of COX-2 and $PGE_2$ was lower in the PCL-CEL group. It concluded that the CEL-loaded PCL membrane could reduce fibrosis and inflammation in a rat model of FBSS via COX-2/$PGE_2$ signaling pathways.

## 1. Introduction

Until now, failed back surgery syndrome (FBSS) remains a therapy-refractory clinical complication after spinal surgery [1–3]. A characteristic manifestation of FBSS is persistent low back pain, leading to disability, low quality of life, and unemployment [4, 5]. It is estimated to occur in 13–61% of all postoperative patients [6, 7]. Considering the increased incidence of spinal surgeries, the high associated costs, and the increasing prevalence of FBSS, the cost burden of this disease is a significant problem [3].

Epidural fibrosis caused by migrated paravertebral fibroblasts is generally accepted as the pathologic mechanism of FBSS. However, the degree of compression of the epidural scar revealed by imaging analysis shows an ambiguous relationship with the severity of clinical symptoms of FBSS [8, 9]. Inspired by clinical findings, scientists found that inflammation-related arachnoiditis was a potential pathologic mechanism of FBSS rather than mechanical compression [10, 11]. Although an antifibrotic membrane was used to prevent FBSS by isolating the immigration of fibrotic factors [12, 13], the inflammation stimulated by foreign bodies and biodegradation products [14, 15] overwhelms the advantage of a physical barrier. To date, the pathophysiological mechanism in the development of FBSS is under investigation.

It is well known that inflammation is involved in arachidonic acid metabolism, in which cyclooxygenase-2 (COX-2) and prostaglandin E2 ($PGE_2$) signaling plays key roles in the migration and proliferation of fibroblasts [16–18].

Meanwhile, a selected cyclooxygenase-2 inhibitor (celecoxib (CEL)) was found to downregulate ERK1/2 and SMAD2/3 phosphorylation, leading to reduced collagen I and collagen III expression, inflammatory reactions, and fibroblast proliferation [19]. A recent study found that macrophages and COX-2 can be triggered by fibrous membranes and may lead to subsequent inflammation and granuloma formation [14, 15]. Thus, the downregulation of COX-2 expression might reduce the adhesion induced by trauma (surgery) and foreign bodies in the pathophysiological processes of FBSS.

$PGE_2$ is a crucial mediator of inflammatory pain sensitization [20, 21]. Furthermore, prostaglandin-mediated modulation of serotonergic transmission controls the affective component of inflammatory pain [22], making $PGE_2$ more potent in the pain mechanism of inflammation. Furthermore, a study has shown that $PGE_2$ may facilitate the transmission of nociceptive input through the spinal cord dorsal horn to higher brain areas where pain becomes conscious [23]. These findings suggest that $PGE_2$ could play an essential role in the pain mechanism of inflammation-related arachnoiditis in FBSS. However, few studies have revealed the relationship between PGE and FBSS.

Selective nonsteroidal anti-inflammatory agents (such as CEL) are highly selective against COX-2. They are widely used in clinics with acceptable safety profiles [24]. Consequently, selective nonsteroidal anti-inflammatory agents would be an ideal drug for reducing adhesion formation and inflammation to prevent FBSS induced by fibrous biomaterials. In this study, we developed new electrospun polycaprolactone (PCL) fibrous membranes loaded with CEL. To investigate its antiadhesion, anti-inflammation, and pain relief functions via the COX-2/$PGE_2$ signaling pathways, *in vitro* cell experiments and rat laminectomy models were performed.

## 2. Materials and Methods

*2.1. Preparation of CEL-Loaded Electrospun Fibrous Membranes.* PCL (Mw = 80 kDa) and CEL were analytical reagents acquired from Sigma-Aldrich (Saint Louis, MO, USA). The electrospun techniques were performed according to our previous study [12]. Briefly, PCL-CEL fibrous membranes (CEL-loaded PCL) were produced by completely dissolving 1 g of PCL and 20 mg (0.2% wt/v) or 60 mg CEL (0.6% wt/v) in 10 mL 1,1,1,3,3,3-hexafluoro-2-propanol (HFIP, Shanghai Darui Fine Chemical Co., Ltd.). The solution was then fed at 2 mL/h by a syringe pump, electrospun at 15 kV, and collected by a slowly rotating mandrel. The obtained fibrous membranes were dried at room temperature under vacuum for at least one week to remove residual solvent.

*2.2. SEM Characterizations of PCL Electrospun Membranes.* Scanning electron microscopy (SEM, FEI Quanta 200, Netherlands) was used to detect the morphological characteristics of the PCL electrospun membranes loaded or unloaded with CEL. At least five images of each sample were investigated (10,000x magnification).

*2.3. CEL Release Characteristics of Fibrous Membranes.* Exactly 100 mg of each fibrous membrane sample was immersed in 20 mL of phosphate-buffered saline (PBS, pH 7.4) with lipase (0.05 mg/mL). The release kinetics of CEL were investigated in a thermostatic shaking water bath (37°C, Taichang Medical Apparatus Co., Jiangsu, China) at a frequency of 100 cycles per minute. Equal portions of the release buffer (5.0 mL each) were collected and refreshed with 5.0 mL PBS at scheduled time points. The release of CEL was determined by spectrophotometry (Shimadzu, Japan) at UV-2550.

*2.4. In Vitro Cell Culture.* Chicken embryonic fibroblasts (UMNSAH/DF-1) were used to evaluate the adhesion and proliferation on the surfaces of CEL-loaded and non-CEL-loaded fibrous membranes. The cells were cultured in Dulbecco's modified Eagle's medium (supplemented with 10% fetal bovine serum, 100 U/mL penicillin, and 100 mg/mL streptomycin) at 37°C with 5% $CO_2$ atmosphere with culture medium replaced three times per week. For timely collection, cells were digested with 0.25% trypsin and washed with PBS for 90 min. Finally, a 24-well plate held 100 mL per well of transferred samples with a density of $1 \times 10^5$ cells/mL.

*2.5. Cell Proliferation and Viability Assay.* 100 $\mu$L of the cell suspension ($1 \times 10^5$ cells/mL) was seeded into each well of 96-well plates, and the plates were incubated for 1, 3, or 5 days (37°C, 5% $CO_2$) to allow the cells to adhere to the wall. At each time point, cells were incubated in the medium at 10% volume (10 $\mu$L) mixed with Cell Counting Kit-8 (CCK-8, Dojindo, Japan). The absorbance was measured at 450 nm with a microplate reader (Multiskan Mk3, Thermo Fisher Scientific, USA). The cell number was calculated based on the CCK-8 standard curve.

The influence of the surface of different materials on cell viability was assessed using a live/dead staining kit (Invitrogen, Eugene, OR). In the 24-well plates, cells were cultured in each well with a density of $4 \times 10^4/cm^2$ for 24 h. The cells were collected, washed twice with PBS, and then resuspended in 2 mM calcein-AM and 10 mM EthD-1 staining solution, then incubated at 4°C in the dark for 30 min. Finally, under a confocal laser scanning microscope (Leica TCS SP2, Heidelberg, Germany), the stained cells were observed. The membranes of living cells were stained bright green, while the dead cell membranes were red; thus, the dead/live cell ratio was obtained. All experiments were repeated three times.

*2.6. Animal Model.* The ethics and safety of the animal experiments were ensured following the guidelines of Shanghai Jiao Tong University. Male Sprague-Dawley rats (provided by Shanghai SLAC Laboratory Co., Ltd.) (300 ± 20 g) were divided into three groups. Electrospun fibrous membranes were prepared with dimensions of 4 mm × 6 mm. Anesthesia was performed using intramuscular ketamine injected at a dose of 20 mg/kg. After sterilization, the second through fifth lumbar vertebral spinous processes were excised under surgical microscopy through

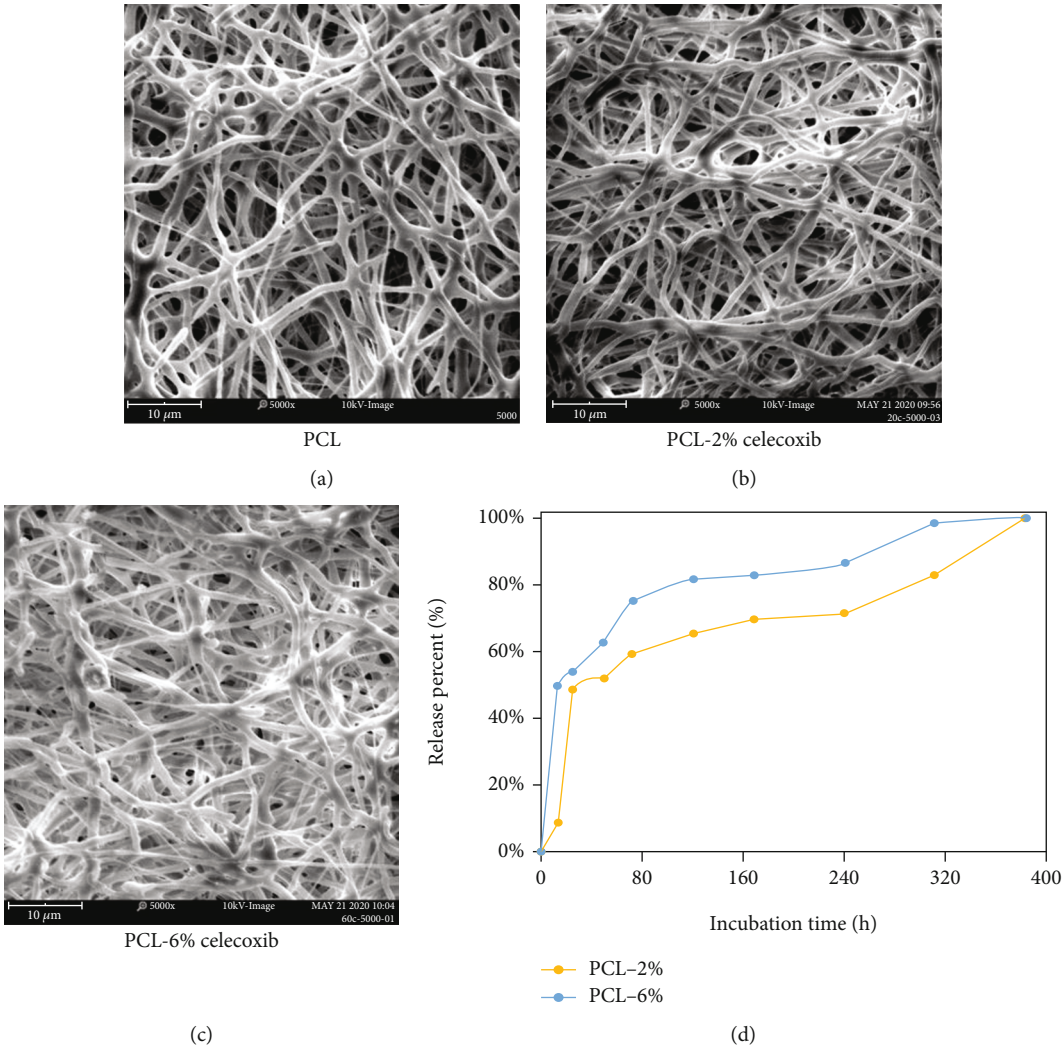


Figure 1: SEM observation of PCL fibrous membranes (a), PCL-2%-CEL fibrous membrane (b), and PCL-6%-CEL fibrous membrane (c). The cumulative release profiles of CEL-loaded PCL fibrous membranes (d).

the dorsal approach [25, 26]. The dura mater was protected while exposing the spinal cord. The blank group (without membranes), the control group (non-CEL-loaded membranes), and the experimental groups (CEL-loaded membranes) were defined after placing fibrous membranes on the dura mater. Finally, the incision was closed. The exclusion criteria of animal models included dura mater lesions during surgery, postoperative infection, and neurological defects. The procedures were performed by trained surgeons. Rats were sacrificed with a lethal dose of anesthetic after 4 weeks of feeding. Before intact vertebral columns were harvested for histological and molecular biological assays, animals underwent magnetic resonance imaging to evaluate epidural fibrosis.

*2.7. MRI Assessment of Epidural Fibrosis.* After 4 weeks, the animals underwent magnetic resonance imaging (MRI) analysis to investigate epidural fibrosis. All animals were imaged on a Siemens Magnetom Verio 3.0 T MRI system (Siemens, Germany), with a 19-layer cross-section of the spine. Following localization images, the TRA MRI sequence was used (repetition time/time to echo 4970/114 ms, with a field-of-view of 66 × 96 mm, and a 282 × 512 matrix). The range of epidural fibrosis was evaluated according to the following criteria: Grade 0, no epidural fibrosis; Grade 1, only thin adhesive bands were observed on the dura and scar tissue; Grade 2, epidural fibrosis observed in <2/3 of the laminectomy site; and Grade 3, large scar tissue affecting >2/3 of the laminectomy site, or the adherence extends to the nerve roots [27, 28]. Two investigators who were blinded to the treatment performed this evaluation independently.

*2.8. Inflammation Assessment.* The expression of COX-2 and $PGE_2$ was investigated using immunohistochemical staining to detect inflammation in epidural fibrosis tissue. First, the dewaxed and dehydrated parts of xylene were carried out in a continuous gradient concentration of ethanol. Then, they

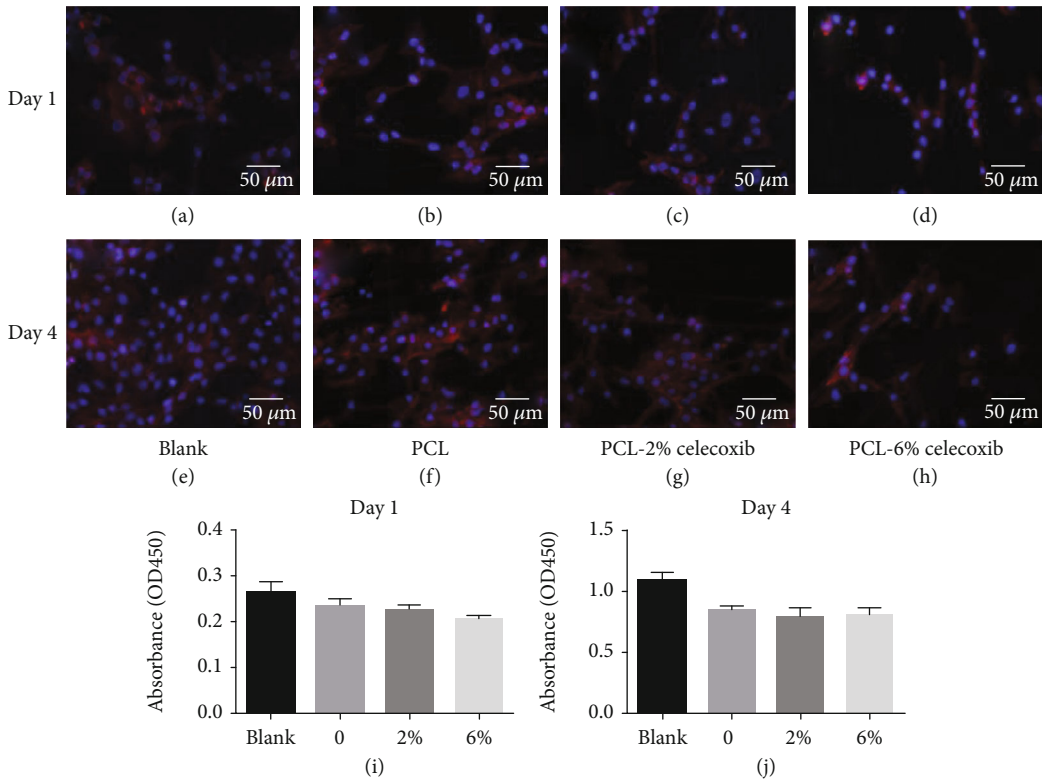


Figure 2: Fluorescence micrographs of chicken embryonic fibroblasts (UMNSAH/DF-1) after 24 h and 4 days of incubation. The cytoskeleton was stained red, and the nuclei were stained blue on the surfaces of the fibrous membranes. The fibroblast proliferation on the sample surfaces ($n = 3$), blank (a, e), PCL fibrous membranes (b, f), PCL-20%-CEL fibrous membranes (c, g), and PCL-60%-CEL fibrous membranes (d, h).

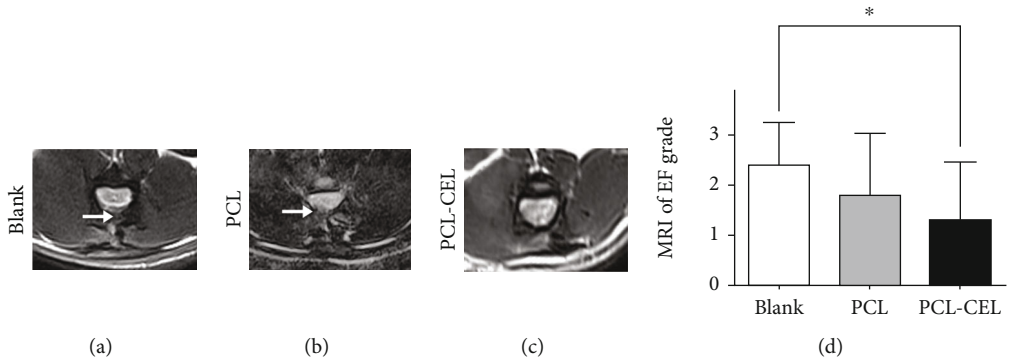


Figure 3: Magnetic resonance imaging (MRI) of the spine. MRI images of epidural fibrosis in the control group (a), the PCL group (b), and the PCL-CEL group. Epidural fibrosis grades based on MRI images (d). White arrows indicate epidural fibrosis. $^{*}P < 0.05$. EF: epidural fibrosis.

were treated in methanol with 3% hydrogen peroxide for 10 min. To extract the antigen, histologic sections were soaked in 100°C 10 mM citrate buffer (pH = 6.0) for 10 min, then diluted in PBS (pH = 7.4) to 1 : 200 of COX-2 (Abcam) and $PGE_2$ (Abcam) primary antibodies for incubation, and stored overnight at 4°C. The samples were incubated with rabbit anti-COX-2 and anti-$PGE_2$ antibodies at 37°C for 1 h after washing with PBS. The peroxide reaction was performed as a chromogenic agent, and DAPI was used to counterstain the slides. To quantify, we investigated COX-2 and $PGE_2$ in a physical barrier plantation. The tissue area normalization of each sample ($n = 10$) was used to detect the degree of inflammation in each area.

*2.9. Statistical Analysis.* In general, the results are presented as the means ± standard deviation (SD) values. One-way analysis of variance (ANOVA) was used to analyze the data among each group. A $P$ value < 0.05 was considered statistically significant. SPSS 10.0 (Chicago, IL, USA) was used for the data analysis of this study.

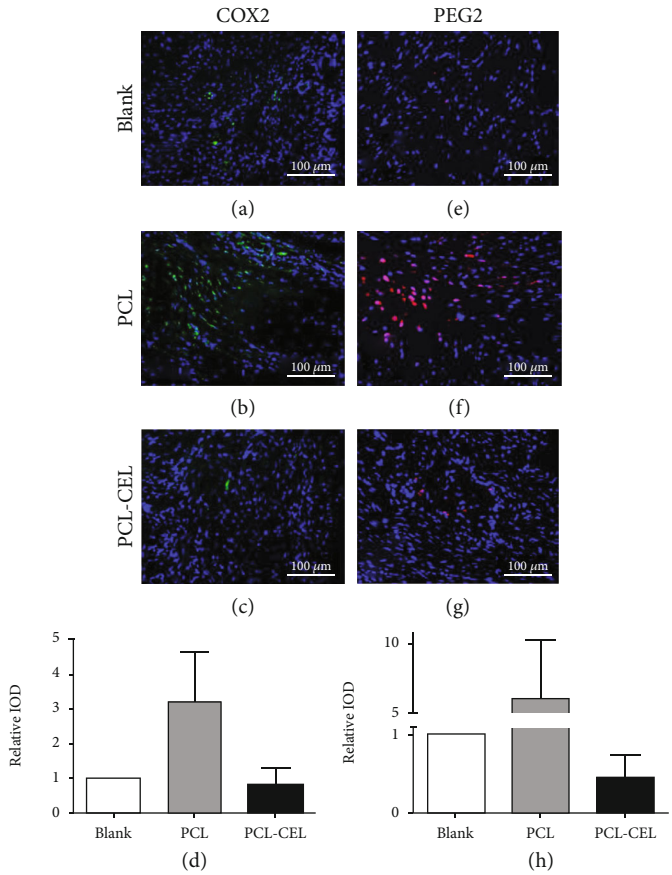


Figure 4: Immunofluorescence of tissue around epidural fibrosis. (a–d) Expression of COX-2; (e–h) expression of $PGE_2$.

## 3. Results

*3.1. SEM Appearance and Drug Release Characteristics of Fibrous Membranes.* SEM images of electrospun fibrous membranes (Figures 1(a)–1(c)) showed that the fibers were randomly distributed in a well-distributed manner. All the microfibers were round, continuous, and bead-free. The surface of the CEL-loaded fibers was smooth with no drug crystallization. The surface structures were not significantly different among 2%- and 6%-CEL-loaded fibers and control fibers. The porosity of CEL-loaded PCL fibrous scaffolds was 58.9%, 61.2%, and 63.8% for PCL, PCL-2%, and PCL-6%, respectively, and the porosity was not significantly affected by the drug incorporation. The release profiles of CEL are shown in Figure 2. It took nearly one week (2% CEL) and two weeks (6% CEL) for the PCL-CEL electrospun fibrous membrane to release approximately 80% of the loaded drug with a burst release of about 50% of the drug in the first 2 days (Figure 1(d)). Meanwhile, the PCL-2%-CEL electrospun fibrous membrane presented a longer release duration than that of the PCL-6%-CEL.

*3.2. Cell Proliferation and Viability.* Figure 2 shows fibroblast proliferation on the PCL-CEL and PCL-control fibrous membranes one and four days after culture. Fluorescence micrographs showed that the adherence of fibroblasts was less on the PCL-CEL fibrous membranes than on the PCL membranes and in the blank controls (Figures 2(a)–2(j)).

*3.3. In Vivo Magnetic Resonance Imaging of the Extent of Fibrosis.* Four weeks after laminectomies, dense epidural fibrosis tissues with widespread adhesions to the dura mater were detected by MRI examination at the caudal surgical sites in the control group (Figure 3(a)). More adhesion tissues were found in the laminectomy site of the PCL group than in that of the PCL-CEL group in the cross-sectional MRI images (Figure 3(b)), and few epidural adhesion tissues with well-defined dura were seen after 4 weeks in the PCL-CEL group (Figure 3(c)). According to the grading of extent of epidural fibrosis, the score of the control group was larger than that of the PCL-CEL group with significant difference at 4 weeks and also larger than that of the PCL group with significant difference (Figure 3(d)).

*3.4. In Vivo Evaluation of Inflammation.* Immunofluorescence staining at 4 weeks showed that the amount of COX-2 and $PGE_2$ in the PCL group was significantly higher than that in the PCL-CEL and control groups, whereas it was lowest in the PCL-CEL group (Figure 4).

## 4. Discussion

In this study, we investigated the effect of CEL-loaded PCL antiadhesion membranes in preventing FBSS, and its related mechanism. The drug release characteristics of this novel biomaterial ensured sufficient working time for surgical trauma and secondary inflammatory responses. *In vivo*, the density of epidural fibrosis was lower in the laminectomy site in the CEL-loaded PCL group compared to the control group based on the MRI assessment. Meanwhile, the nerve function of the CEL-loaded PCL group was significantly better than that of the control group. Furthermore, immunofluorescence staining indicated that the expression of COX-2 and $PGE_2$ was lower in the CEL-loaded PCL group.

The pathophysiological bases of FBSS are epidural fibrosis and inflammation-related arachnoiditis [10, 11]. Studies have shown that the severity of clinical symptoms of FBSS could not be confirmed by imaging analysis of the epidural fibrosis clinically [8, 9]; however, in an endoscopic study in patients with persistent pain after extensive back surgery, 91.1% had severe epidural fibrosis, of which 84.3% of patients presented with concordant pain [29]. Many studies have revealed a positive correlation between inflammation and fibrosis or adhesion formation [25, 30, 31]. Overall, this suggests that inflammation is one of the most critical pathophysiological mechanisms in the development of FBSS.

Recent studies have found that the expression of COX-2 is upregulated in the fibrosis of diseases such as cirrhosis, chronic obstructive pulmonary disease, chronic kidney disease, cardiac hypertrophy, and tendon adhesion [32–36]. The extracellular signal-regulated kinase 2 and SMAD signaling pathways are the most likely mechanisms in COX-2-related fibrosis. Jiang et al. reported that a selective cyclooxygenase-2 inhibitor (CEL) inhibited ERK1/2 and SMAD2/3 phosphorylation, and as a result, the expression of collagen I/III and the proliferation of fibroblasts were reduced [19]. Meanwhile, it was found that the macrophage/COX-2 pathway can be triggered by antiadhesion fibrous membranes, leading to subsequent granuloma formation [14, 15]. Thus, downregulation of COX-2 expression might reduce the adhesion formation induced by trauma (surgery) and foreign bodies in the pathophysiological process of FBSS. In this study, the expression of COX-2 was significantly lower in the PCL-CEL group, and the extent of adhesion to the dura mater was lower in the MRI assessment.

It is well known that inflammation is based on arachidonic acid metabolism, in which the COX-2/$PGE_2$ pathway plays a key role [16–18]. $PGE_2$ is a crucial mediator of inflammatory pain sensitization [20–22], which can further facilitate the transmission of nociceptive input through the spinal cord dorsal horn to higher brain areas where pain reaches consciousness [23]. In addition, foreign bodies such as fibrous membranes could trigger macrophages and COX-2, which would lead to subsequent inflammation [14, 15]. In the three groups of this study, the expression of COX-2 and $PGE_2$ at four weeks postoperatively was highest in the PCL group (higher than in the control group), whereas it was lowest in the PCL-CEL group. Considering the similar relative pain analysis trends in the nerve function assessment, these findings suggested that fibrous biomaterial served as an antiadhesion barrier that could trigger inflammation.

Meanwhile, the CEL-loaded fibrous PCL membranes reversed the COX-2-based inflammation and reduced pain by downregulating $PGE_2$ expression. To our knowledge, this is the first study to reveal the role of PGE in the process of FBSS. Based on the crosslinking of adhesion and inflammation, selected cyclooxygenase-2 inhibitors could be ideal agents for preventing the epidural fibrosis and inflammation associated with FBSS. Further in-depth studies are required to understand the mechanism fully before clinical application. For example, there are four known $PGE_2$ receptors: EP1, EP2, EP3, and EP4. Of these, EP4 expression in tenocytes was much higher than any other $PGE_2$ receptor type [37]. The influence of CEL-loaded fibrous membranes on these receptors in surgical sites should be further investigated.

There are some shortcomings in this study. First, the observation time of the animal model was not very long. However, the levels of inflammation factors and extent of fibrosis were similar between 4 weeks and longer time points [26]. Second, a selective antagonist of $PGE_2$ receptor 4 (EP4) was not detected, and further research should be performed to clarify the relevant mechanisms. Finally, the sample size needs to be expanded in subsequent studies.

## 5. Conclusions

In a rat laminectomy model, CEL-loaded PCL membranes could reduce fibrosis and inflammation associated with FBSS via the COX-2/$PGE_2$ signaling pathways. Further evidence is needed for clinical application of these findings.

## Data Availability

All data used to support the findings of this study are available from the corresponding authors upon request.

## Conflicts of Interest

The authors declare that they have no competing interests.

## Authors' Contributions

Wei Wang, Yunhao Wang, Tengfei Lou, and Mingqian Ding are co-first authors.

## Acknowledgments

This work was supported by the Shanghai Sailing Program (Grant no. 19YF1437700) and the Science Foundation of Shanghai Health and Family Planning Commission (Grant no. 20174Y0225). We would like to thank Dr. Shen Liu for his excellent technical assistance. We would like to thank Editage (http://www.editage.cn) for English language editing.

## References


[1] M. de Jaeger, L. Goudman, S. Eldabe, R. van Dongen, A. de Smedt, and M. Moens, "The association between pain intensity and disability in patients with failed back surgery syndrome, treated with spinal cord stimulation," *Disability and Rehabilitation*, vol. 1, pp. 1–7, 2019.

[2] S. de Groote, L. Goudman, R. Peeters et al., "The influence of high dose spinal cord stimulation on the descending pain modulatory system in patients with failed back surgery syndrome," *NeuroImage: Clinical*, vol. 24, article 102087, 2019.

[3] M. Müller, A. Limacher, C. A. Agten et al., "Can quantitative sensory tests predict failed back surgery?: a prospective cohort study," *European Journal of Anaesthesiology*, vol. 36, no. 9, pp. 695–704, 2019.

[4] C. W. Chan and P. Peng, "Failed back surgery syndrome," *Pain Medicine*, vol. 12, no. 4, pp. 577–606, 2011.

[5] A. Manca, S. Eldabe, E. Buchser, K. Kumar, and R. S. Taylor, "Relationship between health-related quality of life, pain, and functional disability in neuropathic pain patients with failed back surgery syndrome," *Value in Health*, vol. 13, no. 1, pp. 95–102, 2010.

[6] D. Fiume, S. Sherkat, G. M. Callovini, G. Parziale, and G. Gazzeri, "Treatment of the failed back surgery syndrome due to lumbo-sacral epidural fibrosis," *Acta Neurochirurgica Supplementum*, vol. 64, pp. 116–118, 1995.

[7] H. P. Richter, E. Kast, R. Tomczak, W. Besenfelder, and W. Gaus, "Results of applying ADCON-L gel after lumbar discectomy: the German ADCON-L study," *Journal of Neurosurgery*, vol. 95, 2 Supplement, pp. 179–189, 2001.

[8] J. G. Lee, S. C. Lee, Y. C. Kim et al., "Effects of low and high molecular weight hyaluronic acids on peridural fibrosis and inflammation in lumbar laminectomized rats," *The Korean Journal of Pain*, vol. 24, no. 4, pp. 191–198, 2011.

[9] J. Yang, B. Ni, J. Liu, L. Zhu, and W. Zhou, "Application of liposome-encapsulated hydroxycamptothecin in the prevention of epidural scar formation in New Zealand white rabbits," *The Spine Journal*, vol. 11, no. 3, pp. 218–223, 2011.

[10] E. Coskun, T. Süzer, O. Topuz, M. Zencir, E. Pakdemirli, and K. Tahta, "Relationships between epidural fibrosis, pain, disability, and psychological factors after lumbar disc surgery," *European Spine Journal*, vol. 9, no. 3, pp. 218–223, 2000.

[11] J. Liu, B. Ni, L. Zhu, J. Yang, X. Cao, and W. Zhou, "Mitomycin C-polyethylene glycol controlled-release film inhibits collagen secretion and induces apoptosis of fibroblasts in the early wound of a postlaminectomy rat model," *The Spine Journal*, vol. 10, no. 5, pp. 441–447, 2010.

[12] S. Liu, C. Hu, F. Li, X. J. Li, W. Cui, and C. Fan, "Prevention of peritendinous adhesions with electrospun ibuprofen-loaded poly(L-lactic acid)-polyethylene glycol fibrous membranes," *Tissue Engineering Part A*, vol. 19, no. 3-4, pp. 529–537, 2013.

[13] C. Y. Lin, H. H. Peng, M. H. Chen, J. S. Sun, T. Y. Liu, and M. H. Chen, "In situ forming hydrogel composed of hyaluronate and polygalacturonic acid for prevention of peridural fibrosis," *Journal of Materials Science. Materials in Medicine*, vol. 26, no. 4, p. 168, 2015.

[14] S. Liu, H. Chen, T. Wu et al., "Macrophage infiltration of electrospun polyester fibers," *Biomaterials Science*, vol. 5, no. 8, pp. 1579–1587, 2017.

[15] Y. Hui, E. Ricciotti, I. Crichton et al., "Targeted deletions of cyclooxygenase-2 and atherogenesis in mice," *Circulation*, vol. 121, no. 24, pp. 2654–2660, 2010.

[16] N. Muraoka, K. Nara, F. Tamura et al., "Role of cyclooxygenase-2-mediated prostaglandin E2-prostaglandin E receptor 4 signaling in cardiac reprogramming," *Nature Communications*, vol. 10, no. 1, p. 674, 2019.

[17] C. N. Serhan and J. Savill, "Resolution of inflammation: the beginning programs the end," *Nature Immunology*, vol. 6, no. 12, pp. 1191–1197, 2005.

[18] G. Kwapiszewska, A. Gungl, J. Wilhelm et al., "Transcriptome profiling reveals the complexity of pirfenidone effects in idiopathic pulmonary fibrosis," *The European Respiratory Journal*, vol. 52, no. 5, article 1800564, 2018.

[19] S. Jiang, X. Zhao, S. Chen et al., "Down-regulating ERK1/2 and SMAD2/3 phosphorylation by physical barrier of celecoxib-loaded electrospun fibrous membranes prevents tendon adhesions," *Biomaterials*, vol. 35, no. 37, pp. 9920–9929, 2014.

[20] R. J. Harvey, U. B. Depner, H. Wässle et al., "GlyR alpha3: an essential target for spinal $PGE_2$-mediated inflammatory pain sensitization," *Science*, vol. 304, no. 5672, pp. 884–887, 2004.

[21] S. Chopra, P. Giovanelli, P. A. Alvarado-Vazquez et al., "IRE1$\alpha$-XBP1 signaling in leukocytes controls prostaglandin biosynthesis and pain," *Science*, vol. 365, no. 6450, article eaau6499, 2019.

[22] A. K. Singh, J. Zajdel, E. Mirrasekhian et al., "Prostaglandin-mediated inhibition of serotonin signaling controls the affective component of inflammatory pain," *The Journal of Clinical Investigation*, vol. 127, no. 4, pp. 1370–1374, 2017.

[23] S. Ahmadi, S. Lippross, W. L. Neuhuber, and H. U. Zeilhofer, "$PGE_2$ selectively blocks inhibitory glycinergic neurotransmission onto rat superficial dorsal horn neurons," *Nature Neuroscience*, vol. 5, no. 1, pp. 34–40, 2002.

[24] C.-C. Szeto, K. Sugano, J.-G. Wang et al., "Non-steroidal anti-inflammatory drug (NSAID) therapy in patients with hypertension, cardiovascular, renal or gastrointestinal comorbidities: joint APAGE/APLAR/APSDE/APSH/APSN/-PoA recommendations," *Gut*, vol. 69, no. 4, pp. 617–629, 2020.

[25] C.-L. Lin, I.-M. Jou, C.-Y. Wu et al., "Topically applied cross-linked hyaluronan attenuates the formation of spinal epidural fibrosis in a swine model of laminectomy," *Scientific Reports*, vol. 9, no. 1, p. 14613, 2019.

[26] S. Liu, G. Pan, G. Liu et al., "Electrospun fibrous membranes featuring sustained release of ibuprofen reduce adhesion and improve neurological function following lumbar laminectomy," *Journal of Controlled Release*, vol. 264, pp. 1–13, 2017.

[27] C. Zhang, X. Kong, H. Zhou et al., "An experimental novel study: angelica sinensis prevents epidural fibrosis in laminectomy rats via downregulation of hydroxyproline, IL-6, and TGF-$\beta$1," *Evidence-based Complementary and Alternative Medicine*, vol. 2013, Article ID 291814, 7 pages, 2013.

[28] Y. Y. Tseng, J. Y. Liao, W. A. Chen, Y. C. Kao, and S. J. Liu, "Biodegradable poly([D,L]-lactide-co-glycolide) nanofibers for the sustainable delivery of lidocaine into the epidural space after laminectomy," *Nanomedicine (London)*, vol. 9, no. 1, pp. 77–87, 2014.

[29] H. A. Bosscher and J. E. Heavner, "Incidence and severity of epidural fibrosis after back surgery: an endoscopic study," *Pain Practice*, vol. 10, no. 1, pp. 18–24, 2010.

[30] B. W. J. Hellebrekers and T. Kooistra, "Pathogenesis of postoperative adhesion formation," *The British Journal of Surgery*, vol. 98, no. 11, pp. 1503–1516, 2011.

[31] C. Zhang, X. Kong, C. Liu et al., "ERK2 small interfering RNAs prevent epidural fibrosis via the efficient inhibition of collagen expression and inflammation in laminectomy rats," *Biochemical and Biophysical Research Communications*, vol. 444, no. 3, pp. 395–400, 2014.

[32] J. Alcaraz-Quiles, M. Casulleras, K. Oettl et al., "Oxidized albumin triggers a cytokine storm in leukocytes through P38 mitogen-activated protein kinase: role in systemic inflammation in decompensated cirrhosis," *Hepatology*, vol. 68, no. 5, pp. 1937–1952, 2018.

[33] T. Wang, F. Dai, G.-H. Li et al., "*Trans*-4,4′-dihydroxystilbene ameliorates cigarette smoke-induced progression of chronic obstructive pulmonary disease via inhibiting oxidative stress and inflammatory response," *Free Radical Biology & Medicine*, vol. 152, pp. 525–539, 2020.

[34] N. Perretta-Tejedor, J. M. Muñoz-Félix, A. Düwel et al., "Cardiotrophin-1 opposes renal fibrosis in mice: potential prevention of chronic kidney disease," *Acta Physiologica*, vol. 226, no. 2, article e13247, 2019.

[35] Y. L. Zhou, Q. Q. Yang, Y. Y. Yan, C. Zhu, L. Zhang, and J. B. Tang, "Localized delivery of miRNAs targets cyclooxygenases and reduces flexor tendon adhesions," *Acta Biomaterialia*, vol. 70, pp. 237–248, 2018.

[36] R. A. Eladwy, E. M. Mantawy, W. M. el-Bakly, M. Fares, L. A. Ramadan, and S. S. Azab, "Mechanistic insights to the cardioprotective effect of blueberry nutraceutical extract in isoprenaline-induced cardiac hypertrophy," *Phytomedicine*, vol. 51, pp. 84–93, 2018.

[37] O. Dolkart, T. Liron, O. Chechik et al., "Statins enhance rotator cuff healing by stimulating the COX2/$PGE_2$/EP4 pathway: an in vivo and in vitro study," *The American Journal of Sports Medicine*, vol. 42, no. 12, pp. 2869–2876, 2014.

Hindawi
Neural Plasticity
Volume 2021, Article ID 6649135, 10 pages
https://doi.org/10.1155/2021/6649135

*Research Article*

# Predicting Upcoming Events Occurring in the Space Surrounding the Hand

**Maria L. Rangel**,[1,2,3] **Lidiane Souza**,[1,2] **Erika C. Rodrigues**,[4,5] **José M. Oliveira**,[1] **Michelle F. Miranda**,[6] **Antonio Galves**,[7] **and Claudia D. Vargas**[1,2]

[1]*Laboratório de Neurobiologia do Movimento, Instituto Biofísica Carlos Chagas Filho, Universidade Federal do Rio de Janeiro, Rio de Janeiro, Brazil 21941 900*
[2]*Núcleo de Pesquisa em Neurociências e Reabilitação, Instituto de Neurologia Deolindo Couto, Universidade Federal do Rio de Janeiro, Rio de Janeiro, Brazil 22290 140*
[3]*Universidade Estácio de Sá, Rio de Janeiro, Brazil 26220-099*
[4]*Programa de Pós-graduação em Ciências da Reabilitação, Centro Universitário Augusto Motta-UNISUAM, Rio de Janeiro, Brazil 21041 020*
[5]*Instituto D'Or de Pesquisa e Ensino IDOR, Rio de Janeiro, Brazil 22281 100*
[6]*Instituto de Matemática e Estatística, Universidade de São Paulo, São Paulo, Brazil 05508-090*
[7]*Department of Mathematics and Statistics, University of Victoria, Canada*

Correspondence should be addressed to Claudia D. Vargas; claudiadvargas@gmail.com

Received 12 October 2020; Revised 21 January 2021; Accepted 6 February 2021; Published 20 February 2021

Academic Editor: Zhongyu Li



Predicting upcoming sensorimotor events means creating forward estimates of the body and the surrounding world. This ability is a fundamental aspect of skilled motor behavior and requires an accurate and constantly updated representation of the body and the environment. To test whether these prediction mechanisms could be affected by a peripheral injury, we employed an action observation and electroencephalogram (EEG) paradigm to assess the occurrence of prediction markers in anticipation of observed sensorimotor events in healthy and brachial plexus injury (BPI) participants. Nine healthy subjects and six BPI patients watched a series of video clips showing an actor's hand and a colored ball in an egocentric perspective. The color of the ball indicated whether the hand would grasp it (hand movement), or the ball would roll toward the hand and touch it (ball movement), or no event would occur (no movement). In healthy participants, we expected to find distinct electroencephalographic activation patterns (EEG signatures) specific to the prediction of the occurrence of each of these situations. Cluster analysis from EEG signals recorded from electrodes placed over the sensorimotor cortex of control participants showed that predicting either an upcoming hand movement or the occurrence of a tactile event yielded specific neural signatures. In BPI participants, the EEG signals from the sensorimotor cortex contralateral to the dominant hand in the hand movement condition were different compared to the other conditions. Furthermore, there were no differences between ball movement and no movement conditions in the sensorimotor cortex contralateral to the dominant hand, suggesting that BPI blurred specifically the ability to predict upcoming tactile events for the dominant hand. These results highlight the role of the sensorimotor cortex in creating estimates of both actions and tactile interactions in the space around the body and suggest plastic effects on prediction coding following peripheral sensorimotor loss.

## 1. Introduction

Predicting upcoming movements in a variable environment is a fundamental aspect of skilled motor behavior [1–5]. This prediction ability demands an accurate and constantly updated representation of the body and its surrounding space [6, 7] and can be critical for survival [8, 9]. Interestingly, the mere knowledge of a coming action performed by others has been shown to automatically trigger the motor system [8, 10, 11]. Furthermore, the integrity of

the parietal cortex has been proven to be important in relation to the capacity to predict upcoming actions [11].

Action observation paradigms have shown that the capacity to estimate the consequences of others' actions seems to be bonded to our own sensorimotor representations [12]. Early seminal work showed the existence of bimodal neurons that were both responsive to tactile stimuli applied to a given body part and to the sight of objects moving towards the same body part in the premotor area F4 of macaque monkeys [13, 14] as well as in the posterior parietal cortex [15, 16]. Such neurons form a network devoted to the representation of peripersonal space, defined as the space directly surrounding different parts of the body [17].

In another series of studies, it was shown that observing other peoples' skin being touched or tickled activated the observer's somatosensory representation in the brain [18–20]. Thus, anticipating the occurrence of a tactile event in the peripersonal body space might trigger specific responses in those brain regions [21, 22]. Furthermore, as suggested by recent behavioral studies, the networks in the brain coding for the space of action ("arm reaching space") and the peripersonal space could be at least partially segregated. An important finding is that the space within arms' reach is not body part centered, while the peripersonal space is [23]. As a consequence, the predictive coding signatures associated with each of these two networks might also differ.

There is mounting evidence indicating that modifications in the body can alter peripersonal space [24–28]. Among the different types of peripheral injury, brachial plexus injury (BPI) has been seen as a challenging model for the study of brain plasticity [29–35]. Although the upper limb is still connected to the body/trunk, its sensory and motor functions can be deeply impaired due to nerve damage [34]. BPI patients present structural brain change, as well as grey matter atrophy in multiple cortical areas mostly related with motor function [36]. Furthermore, both behavioral [37] and neurophysiological [38] effects have been reported after peripheral lesions affecting the dominant versus nondominant limb. Thus, one could expect that predictive coding aspects that are associated with the peripersonal space might be altered after a BPI in the dominant hand.

The aim of this study was to investigate in healthy participants whether prediction of movement and tactile events occurring in the space surrounding the hand trigger specific electroencephalographic signatures in the sensorimotor cortex. We employed a modified version of the action observation paradigm originally devised by Kilner et al. [10], in which a prediction marker was retrieved from the EEG signals collected over the sensorimotor cortex region when the participants expected to observe a hand moving towards an object. In addition, we introduced a new condition associated specifically with the prediction of an upcoming tactile event, a ball moving towards a hand at rest. We hypothesized that distinct EEG signatures would be associated with the prediction of these upcoming events. If this was the case, then distinct neural networks might be enrolled in coding peripersonal and motor prediction events. Furthermore, in BPI participants, we expected that these EEG signatures would be affected as a function of sensorimotor loss.

## 2. Materials and Methods

*2.1. Participants.* Two groups of right-handed participants were tested: (i) nine neurologically healthy subjects (two women and seven men; mean age 30 years, range 21–49) and (ii) six participants suffering from traumatic unilateral brachial plexus injury (BPI; all males, mean age 28.67 years, range 20–40, see Table 1 for the patients' demographic and clinical data). Handedness was evaluated considering their laterality before the BPI occurrence using the Edinburgh Inventory [39]. All subjects gave informed consent prior to testing. The experiment was approved by the local ethics committee (process number: 298.925, Instituto de Neurologia Deolindo Couto of the Federal University of Rio de Janeiro).

Each patient underwent a neurological evaluation comprising sensory tests using Semmes-Weinstein microfilaments over hand points of exclusive innervation [35]. Muscular manual testing was based on the classification proposed by the Medical Research Council (see Table S1 in the supplementary materials for detailed functional evaluation of BPI participants). The myotomes corresponding to the roots that form the brachial plexus (C5–T1) were assessed [40]. Presence of pain during the experiment was assessed through a numerical verbal scale (0: no pain to 100: acute/sharp pain).

The ability to perform a reaching and grasping movement similar to those observed in the videoclips was tested after the experimental session. All the BPI participants with upper trunk (superior and middle branch) injury were able to reach the ball with their impaired hand, although with compensatory strategies (the quality of movement was not considered, only their ability to perform the movement, see Table S1 in the supplementary material for participant evaluation information). Overall, four participants were diagnosed with a superior trunk BPI on the right side and two participants were diagnosed with complete BPI on the left side (Table 1). One participant reported mild pain during the experimental session.

*2.2. Experimental Protocol.* The experimental protocol was modified from Kilner et al. [10]. Participants sat comfortably in front of a 17-inch LCD monitor at 60 cm from the screen. EEG signals were recorded while the subjects watched passively a series of video clips presenting an actor's hand and a ball, whose color determined the experimental conditions. Videos were displayed with the software Presentation, version 16.5 (Neurobehavioral Systems, Inc.). All videos started with both the actor's hand and ball halted. In the videos with a yellow ball, 2.5 seconds after the start, the hand moved and grasped the ball (hand movement condition); in the videos with a blue ball, 2.5 seconds after the start, the ball moved toward the actor's hand and touched it (ball movement condition); in videos with a white ball, both the actor's hand and ball remained immobile (no movement condition) (Figure 1 and supplementary 2.). The color rule was explained in advance to the participants by means of verbal instruction. Thus, upcoming events were entirely predictable by the color of the ball at the beginning of each video clip presentation. In

Table 1: Characteristics of participants with BPI.

| ID | Age | Handedness | Injury side | Lesion | Time since injury (months) |
|---|---|---|---|---|---|
| BPI1 | 30 | R | R | S, M | 15 |
| BPI2 | 20 | R | R | S, M | 8 |
| BPI3 | 24 | R | R | S, M | 7 |
| BPI4 | 32 | R | R | S, M | 8 |
| BPI5 | 26 | R | L | S, M, I | 24 |
| BPI6 | 40 | R | L | S, M, I | 6 |

Anatomical localization of BPI: S: superior trunk; M: middle trunk; I: inferior trunk; R: right; L: left.

order to maintain the participants' attention, one out of eight video clips recorded for each condition contained small changes in hand position and were randomly selected for presentation. In addition, participants were asked to answer a few questions about the videos at the end of the experiment.

Each video clip lasted 3 seconds and was presented 20 times in randomized order, interspersed with a fixation cross on a black screen presented for 1 s (Figure 1(a)). Three blocks of 60 video clips showing the right hand and three blocks of 60 video clips showing the left hand were presented, totaling 60 videos per condition and per hand. Each experimental block lasted about 6 min. There was a rest interval of about 4 min between blocks. The order of presentation of videoclips and blocks was randomized.

During the presentation of the experimental blocks, participants were required to rest their hands in their lap. EMG signals from the first digital interosseous and from the biceps brachialis muscles were monitored bilaterally to detect any hand movement during the task for further trial exclusion upon detection of any hand movement (Figure 1(b)).

*2.3. Data Acquisition.* The EEG signal was acquired with a 128-channel Geodesic Sensor Net coupled with high input impedance amplifier (200 MΩ, Net Amps, Electrical Geodesics INC., Eugene, OR, USA), sampled at 500 Hz, and filtered (bandpass filter of 0.3 to 50 Hz). Each electrode impedance was kept below 50 kΩ. Electromyographic signals were recorded (MP 100, BIOPAC System) from the first dorsal interosseous (FDI) and biceps brachii (BB) muscles bilaterally, sampled at 1 kHz, amplified (gain: 1000), and filtered (bandpass filter: 10-500 Hz).

*2.4. Data Analysis.* MATLAB 6.5 (Mathworks, USA) was used for the EEG data analysis. The signal was filtered (bandpass filter: 0.3 to 30 Hz) and rereferenced to average auricular electrodes. The signal was presegmented into 60 epochs per experimental condition (hand movement, ball movement, and no movement). A time window of 500 ms (between 2500 and 3000 ms after the start of each video clip) was then selected for analysis. This corresponds to the negative slope time window occurring prior to the movement start [10]. Eye movement and blink artifacts were removed considering a signal amplitude threshold of ±50 mV in the three frontal electrodes (9, 14, and 22 corresponding to Fp2, FpZ, and Fp1 in the 10-10 electrode international positioning system, respectively) and through visual inspection before averaging. EEG was acquired from two sets of electrodes: 8 electrodes in the sensorimotor cortex (36, 42, 41, 47, 104, 93, 103, and 98, corresponding to C3, Cp3, C5, Cp5, C4, Cp4, C6, and Cp6, respectively, using the 10-10 electrode International System, Figure 1(c) in red), and 8 control electrodes in the temporal lobes (48, 43, 44 (corresponding to T9), 49, 113, 114 (corresponding to T10), 119, 129, Figure 1(c) in blue).

*2.5. Statistical Analysis.* The hypothesis that the sensorimotor cortex engages in distinct neural signatures depending on the prediction context was tested. If confirmed, we would be able to distinguish the specific signatures corresponding to each of the three experimental conditions in the EEG segments recorded from the sensorimotor cortex electrodes. To test this hypothesis, we employed a hierarchical approach as follows:

(1) For each electrode of interest, we computed the average signal across epochs for each experimental condition (example in Figure 1(d))

(2) Next, we considered four sensorimotor cortex electrodes and their corresponding averaged signals from three experimental conditions, and a group of four control electrodes in the temporal cortex and their corresponding averaged signals from three experimental conditions. The electrodes are represented in Figure 1(c), with the control electrodes in blue. For each set of four electrodes and three experimental conditions, the data looks like the example in Figure 1(e)

(3) For each subject and each set of electrodes, the 12 averaged signals were submitted to a hierarchical analysis

(4) In a first stage, a $k$-means cluster analysis ($k = 3$) for each subject was performed. For each set of electrodes, the goal was to group the 12 averaged signals into three possible clusters: A, B, or C. If the signal in the sensorimotor cortex is different between conditions, the signals from the same condition should belong to the same cluster, with a high separation between the clusters. If the signals in two different conditions belong to the same cluster, there is an indication that this brain region is not recognizing the conditions as distinct from each other

(5) In a second stage, the null hypothesis that "the cluster label is independent of the experimental condition" was tested by Fisher's exact test, comparing each pair of conditions for both sets of electrodes. The Fisher exact test is suitable for small sample sizes, and the $p$ values of the test can be calculated exactly, rather than relying on an asymptotic approximation of the test statistics. The null hypothesis stated that the cluster label was independent of the experimental condition, while the alternative hypothesis stated that the cluster label was not independent of the experimental condition. Thus, rejection of the null hypothesis

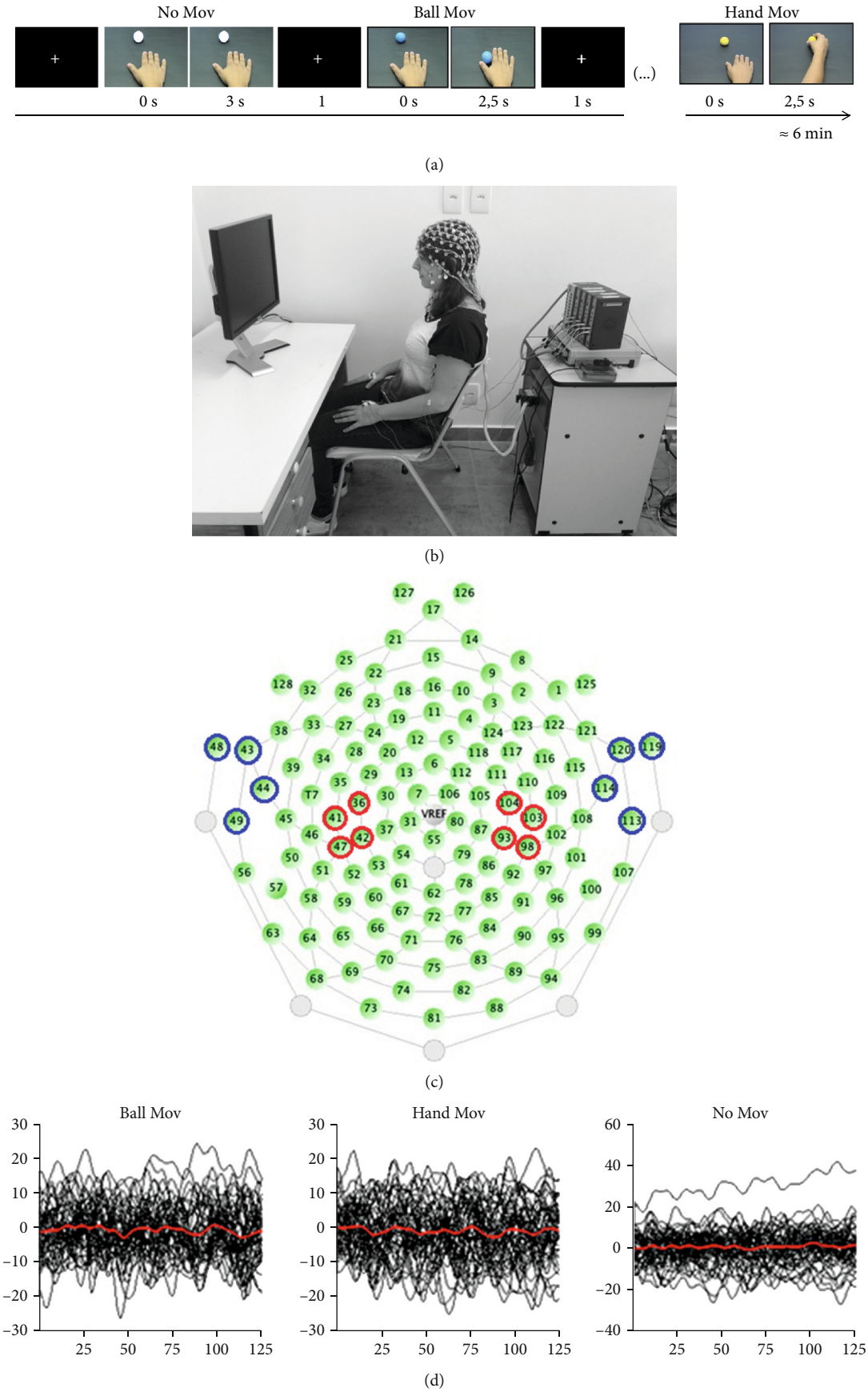


Figure 1: Continued.

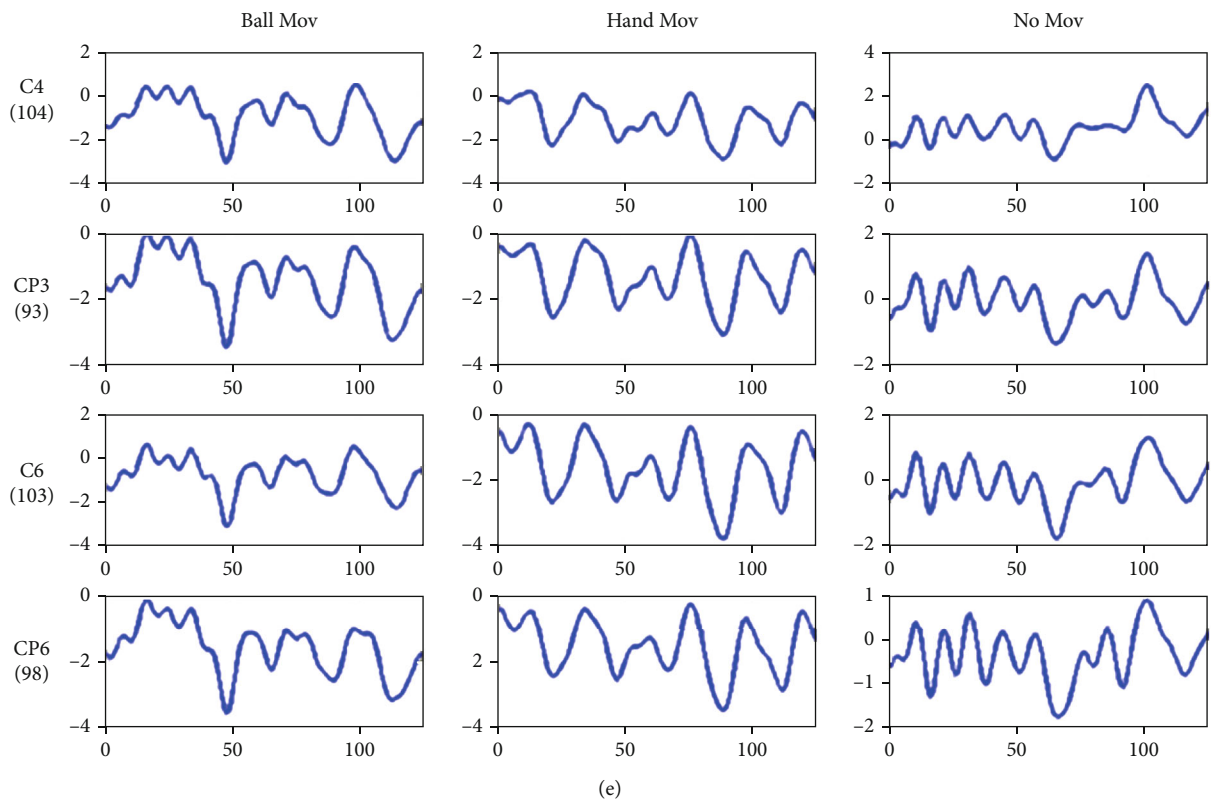


Figure 1: Experimental procedures. (a) The three experimental conditions (no movement (No Mov), ball movement (Ball Mov), and hand movement (Hand Mov)) were presented randomly (total of 60 trials per condition) in a computer screen positioned in front of the participant (b). (c) A dense array geodesic EEG cap depicting in red the target electrodes over the sensorimotor cortex (36, 42, 41, 47, 104, 93, 103, and 98 corresponding to C3, Cp3, C5, Cp5, C4, Cp4, C6, and Cp6, respectively, in 10-10 electrode International System). Control electrodes in the temporal region (48, 43, 44 (corresponding to T9), 49, 113, 114 (corresponding to T10), 119, and 129) are depicted in blue. (d) For each subject and electrode, EEG segments were averaged per condition (signals are represented in millivolts ($y$ axis) vs. 125 data points corresponding to 500 ms ($x$ axis). (e) These averaged EEG signals were then classified using $k$-means clustering, and Fisher exact-test was performed to test the dependence between condition and cluster label.

meant that it was possible to distinguish between the experimental conditions

(6) In the last stage of the hierarchical approach, the Benjamini–Hochberg [41] procedure was used to control the false positive rate in multiple comparisons. Since Fisher's exact test was performed individually within each group of subjects, there is a need to adjust the $p$ value accordingly. The adjustment was performed in the statistical software R using the function p.adjust [42].

## 3. Results

The results from the nine controls and the six right-handed BPI participants are presented as contingency tables (Tables 2 and 3). The tables are depicted as a function of the dominance of the hand presented in the videoclip and considering the hemispheres contralateral and ipsilateral to the viewed hand. For most control participants the null hypothesis was rejected for the electrodes over the sensorimotor cortex, indicating that EEG signals coming from the electrodes in the sensorimotor cortex display specific signatures for each of the tested conditions (Table 2). The cluster distinction found between hand movement versus ball movement suggests that at least partially independent neuronal networks code in anticipation of a hand movement versus an object movement directed towards the hand. Finally, no distinction between EEG clusters was found for the electrodes over the temporal cortex.

Table 2: Contingency table showing the number of rejections of H0 for control participants' hypotheses tests (see also Tables S2, S3, S4 and S5 for individual results).

| Condition comparison | Control ($n = 9$) | | | |
|---|---|---|---|---|
| | Dominant hand view | | Nondominant hand view | |
| | C. H. | I. H. | C. H. | I. H. |
| Ball Mov x No Mov | 7 | 9 | 9 | 9 |
| Hand Mov x No Mov | 8 | 8 | 9 | 8 |
| Hand Mov x Ball Mov | 8 | 7 | 9 | 6 |

C.H.: hemisphere contralateral to the observed hand; I.H.: hemisphere ipsilateral to the observed hand.

Table 3: Contingency table showing the number of rejections of H0 for BPI participants' hypotheses tests (see also Tables S6, S7, S8 and S9 for individual results).

| *Condition Comparison* | BPI patients (n =6) Dominant* hand view | | Nondominant* hand view | |
|---|---|---|---|---|
| | C. H. | I. H. | C. H. | I. H. |
| Ball Mov x No Mov | 0 | 4 | 4 | 5 |
| Hand Mov x No Mov | 4 | 0 | 0 | 0 |
| Hand Mov x Ball Mov | 5 | 0 | 0 | 0 |

C.H.: hemisphere contralateral to the observed hand; I.H.: hemisphere ipsilateral to the observed hand. *All the participants were right-handed before the BPI injury.

No cluster difference between the ball movement and no movement conditions was found for any BPI participant in the sensorimotor cortex contralateral to the videos depicting the dominant hand (Table 3). This result indicates that the ability to predict an incoming tactile event in the space surrounding the dominant limb was blurred in these participants.

Cluster analysis further revealed that the contrast between the ball movement and no movement conditions was absent in four of the six tested BPI participants in the hemisphere ipsilateral to the dominant hand. Finally, the difference between ball movement and no movement conditions was preserved in at least four BPI participants, both for the contralateral and the ipsilateral hemispheres in the nondominant hand block. Taken together, these results indicate BPI affected only the ability to estimate upcoming events for the dominant hand.

The comparison between hand movement and no movement conditions when observing the dominant hand showed that the null hypothesis was rejected for the electrodes over the contralateral sensorimotor cortex in four out of six participants. This indicates that the ability to predict an incoming dominant hand movement was preserved in these subjects. However, contrarily to the control subjects, no other difference was found for this comparison condition in the BPI group (Table 3). Likewise, in five of the six BPI participants, the contrast between hand movement and ball movement conditions revealed a difference only for the contralateral sensorimotor cortex during the observation of the dominant hand. The latter result indicates that, in contrast to control participants, the hand movement versus ball movement conditions were indistinguishable in the remaining comparisons (see supplementary tables S6, S7, S8 and S9 for individual results on hypothesis tests). As found in control participants, no distinction between EEG clusters was found for the electrodes over the temporal cortex in BPI participants.

## 4. Discussion

In this study, we investigated the specificity of EEG signatures recorded in anticipation of observing a hand grasping a ball (hand movement), observing a ball touching a hand (ball movement), or observing a stationary hand (no movement) in healthy and in brachial plexus injury (BPI) participants. In healthy participants, the sensorimotor cortex showed a strong dependence between the condition and cluster label irrespective of the observed hand. These results indicate that predicting an upcoming hand movement or predicting the occurrence of a tactile event yields specific neural signatures in the sensorimotor cortex.

In the BPI participants, the hand movement condition differed from the other conditions only for the EEG signals collected in the sensorimotor cortex contralateral to the dominant hand, which, in most cases, was also the affected limb. This result is indicative of a preserved ability to predict others' hand actions. However, no distinction between ball movement and no movement was found in the sensorimotor cortex contralateral to the dominant hand, suggesting that BPI blurred specifically the ability to predict upcoming tactile events for the dominant hand. Interestingly, distinct neural signatures were found for ball movement x no movement conditions for the remaining comparisons, indicating a preserved ability to estimate upcoming tactile events occurring around the nondominant hand.

In contrast with the control group, in the BPI participants, the hand movement condition was not different to the ball movement and no movement conditions for both hemispheres when observing the nondominant hand, as well as for the ipsilateral sensorimotor cortex when observing the dominant hand. Thus, for all these conditions, the neural signatures associated with upcoming hand movements and body envelope events seemed intermingled in the sensorimotor cortex after a BPI.

As expected, both for the control group and the BPI patients, the EEG activity collected in the temporal electrodes did not yield distinct signatures between conditions. Taken together, these results highlight the role of the sensorimotor cortex in creating estimates of both actions and tactile events in the space around the body and suggest plastic effects on this predicting ability following brachial plexus injury.

*4.1. Estimating Sensorimotor Events.* Contemporary neuroscience has consistently shown that predicting other agents' sensorimotor behavior from observation leads to the recruitment of neural circuits similar to those enrolled in their implementation [8]. Kilner et al. [10] investigated whether the readiness potential, traditionally described as an electrophysiological marker of motor preparation, could also be detected whenever an observer expected an upcoming action to occur in a visual display. Results showed the occurrence of a readiness potential when both the nature and onset time of the upcoming action was predictable [10]. Fontana et al. [11] examined whether a readiness potential was generated in chronic stroke patients with focal lesions in the parietal or the premotor cortex when they expected to observe an upcoming movement in a visual display. They found that this prediction marker was preserved in the patients with premotor lesions but abolished in those with parietal lesions, suggesting that the integrity of the parietal cortex is important in relation to the capacity to estimate the occurrence of upcoming actions performed by others.

In the present study, we have shown that the EEG activity associated with the estimation of upcoming hand movements is different from that related to estimating upcoming tactile events in the hand in healthy participants. Both conditions, in turn, were different from the control (no movement) condition. These results indicate that there are specific neural signatures in the sensorimotor cortex for predicting other's touch events. These results are in accordance with the existence of a network devoted specifically to the representation of peripersonal space [13, 16, 17, 43].

The peripersonal space has been proposed to define a safety boundary around the body [44] and a space mediating goal-directed actions [45]. Our results suggest that at least partially separate parietofrontal networks could be at play in anticipating motor or tactile events experienced by others. In a similar manner, employing a set of psychophysical tasks, Zanini et al. [23] argued that the peripersonal space and the within arms' reach space representations are not superimposable. Studies using EEG [46], TMS [47], and fMRI [6, 43, 48] have confirmed that a multisensory representation of peripersonal space takes place in both the parietal and prefrontal areas. As a matter of fact, multisensory integration of both dynamic auditory and looming visual stimuli in the peripersonal space are especially efficient in terms of enhancing an observer's responses to tactile stimulation presented to the body surface [21, 22, 49]. Furthermore, early P100 responses are evoked in the primary somatosensory cortex upon visuotactile synchronic stimulation, irrespectively of whether or not the subject is paying attention to the tactile stimuli, suggesting a preattentive stage of processing [46].

Interestingly, tactile awareness occurs even in the absence of tactile stimulation. Actually, an experience of touch entirely triggered by a visual stimulus can be a relatively common phenomenon, with the predictive processes having a key role in the subjective experience of touch [24]. Since biological systems must face the uncertainty of the environment, the most adaptive responses are those which succeed in minimizing the cost of the surprise effect. The best way to achieve this is to develop a system capable of anticipating, through preattentive processes, the most probable events in a certain context [1, 35, 50, 51]. The neural signatures described herein for upcoming tactile events in others' hands may be a physiological correlate of a predictive mechanism specifically devoted to body envelope events.

*4.2. Plastic Changes after BPI Affects Predictive Coding.* It has been widely demonstrated that lesions in the body are capable of promoting structural and functional modifications in the sensory (S1) and motor (M1) primary cortices [52]. Likewise, long-lasting changes in the body envelope caused by traumatic BPI should be expected to lead to modifications in the brain. Mano et al. [53] and Malessy et al. [31] were pioneers in investigating cortical plasticity in BPI. Later on, employing resting-state fMRI, Fraiman et al. [33] found evidence that these modifications encompass the M1 trunk/lower limb representation, suggesting that BPI might imply a bodily extended motor dysfunction. Accordingly, it was found that BPI affects body balance [54]. Ramalho et al. [35] showed that a unilateral BPI impairs bilateral touch threshold, suggesting that higher order mechanisms of plasticity are at play after a BPI. Moreover, plasticity after BPI does not seem to be restricted to the sensorimotor cortex, involving regions such as the precuneus, the lateral aspect of the posterior parietal cortex, the superior parietal lobe, and the intraparietal sulcus [37]. Thus, we expected that traumatic BPI would also lead to changes in the brain signatures associated with the detection of upcoming motor and tactile events.

In a small sample of six BPI participants, we found evidence of preserved capacity to predict upcoming movements of the dominant hand. Four of them had an upper trunk BPI in the dominant hand. The remaining two participants had complete BPI in the nondominant hand. Rodrigues et al. (2008) reported the loss of a prediction marker associated with upcoming movements in the hemisphere contralateral to the injured limb in unilateral amputees [55]. Thus, a parsimonious explanation could be that the predictive coding associated specifically with the goal of the task (grasping the ball) was preserved in BPI patients as a consequence of a "motorically" preserved hand, even though the arm was rendered immobile by the BPI. There were no further differences between hand movement, ball movement, or no movement conditions in any of the remaining comparisons and for none of the tested BPI participants. Although limited by the reduced number of BPI participants, these results suggest that the plastic reorganization after BPI is associated with modifications in motor planning at a higher level. As a matter of fact, a resting-state FMRi connectivity study showed that the dominant hand disability seems to trigger changes not only in sensorimotor but also in higher order areas [56]. In BPI participants, the default mode and executive control networks functional connectivity were abnormally synchronized, possibly resulting in inefficient performance. Thus, a cascade functional remodeling might have occurred after severe peripheral nerve injury [56].

Compelling evidence points to plastic changes in both hemispheres after a unilateral BPI [33, 35, 57]. Interestingly, a study found that slower reaction times and reduced accuracy in mental imagery tasks are associated with amputation of the dominant limb compared to amputation of the nondominant limb. The authors suggested that the loss of a dominant upper limb might degrade the efficiency of both dominant and nondominant limb motor behaviors and imagery at the motor preparation level [37]. Event-related potentials measured in long-standing right hand amputees while they performed a mental rotation task revealed a bilateral decrease in N200 during the categorization phase whose magnitude was correlated with the time of amputation [58]. Furthermore, amputees displayed an increase in P300 in the hemisphere contralateral to the intact limb during the mental rotation phase that was interpreted as resulting from a change in hand dominance [58]. In our sample, BPI had occurred relatively recently at the time of testing (up to two years). Patients with right side injury were still able to use their dominant/right hand, which may have contributed to the maintenance of a vivid motoric representation of the hand in the left (dominant) sensorimotor cortex.

Accordingly, our results show that four of the six tested BPI participants did present a neural signature associated with predictive coding of movements of the dominant hand. Further studies are necessary to understand the role of hand dominance in the predictive coding of hand movements after a peripheral lesion.

BPI also specifically blurred the prediction marker associated with an incoming tactile event in the hemisphere contralateral to the dominant hand. The difference between ball movement and no movement conditions was, however, preserved for the remaining comparisons. Traumatic BPI often leads to severe impairment of tactile threshold detection throughout the affected limb [35]. Moreover, the peripersonal space representation was shown to be body centered [6, 17, 22], continuously recalibrating upon receiving updated environmental information [59]. By impairing this sensory updating, BPI would blur the predictive mechanisms relating to upcoming tactile events in the space surrounding the hand.

The shape and size of peripersonal space are not fixed, but instead adapt as a function of interaction with the environment. In a seminal work, Iriki et al. [15] have shown in monkeys that the active reach for a piece of food with a tool expands the visual receptive field of neurons in the intraparietal sulcus. In humans, the peripersonal space extends in space after using a tool to reach far locations [60]. Previous research has shown that voluntary object-oriented actions induce an online, continuous remapping of the peripersonal space of the hand, evidence that supports a role for this space in the guidance of actions [43, 61]. On the other hand, the mere immobilization of the upper limb has been shown to shrink the boundaries of peripersonal space, suggesting a fundamental role of physical constraint over space representation [25]. Thus, peripersonal space representations seem to be highly dependent on ongoing behavior.

In BPI, the physical presence of the injured limb attached to the body may play an important role in modifying peripersonal space representation. Indeed, it has been shown that traumatic upper limb amputation leads to an asymmetry in the upper limb space of action, expressed by a distortion in the visuospatial perception of the affected limb [27]. Interestingly, the implicit perception of limb size and the peripersonal space representation surrounding the amputated limb are restored by the use of a prosthesis [62]. Further research might shed light on higher order peripersonal modifications induced by peripheral lesions.

## 5. Conclusions

Cluster analysis from EEG signals recorded from the sensorimotor cortex of control participants indicates that specific neural signatures are associated with the prediction of an upcoming hand action or the occurrence of a tactile event. For BPI participants, predicting actions for the dominant hand yielded distinct activity in the contralateral sensorimotor cortex, an indication of preserved ability to predict others' hand actions. Conversely, the ability to code for an upcoming tactile event was abolished for this hand, suggesting a dependency of the online sensory information to estimate events in the hand space. Despite the small sample size, our results draw attention to the role of the sensorimotor cortex in creating estimates of both actions and tactile interactions in the space around the body and suggest plastic effects on predicting ability following peripheral sensorimotor loss.

## Data Availability

The EEG data used to support the findings of this study are available on request. Please contact the corresponding author for more information.

## Conflicts of Interest

The authors declare that there is no conflict of interest regarding the publication of this paper.

## Acknowledgments

The authors would like to thank José Fernando Guedes Correa, Paulo Leonardo Tavares, José Vicente Martins and Bia Ramalho for their contribution to this work. This work is part of FAPESP project "Research, Innovation and Dissemination Center for Neuromathematics" (FAPESP grant 2013/07699-0), University of São Paulo project Mathematics, computation, language and the brain", the project 'Plasticity in the brain after a brachial plexus lesion' (FAPERJ grant E26/010002474/2016), and the project 'PROINFRA HOSPITALAR' (FINEP grant 18.569-8). AG and CDV are partially supported by CNPq fellowships (grants 311 719/2016-3 and 309560/2017-9, respectively). CDV is also partially supported by a FAPERJ fellowship (CNE grant E-26/202.785/2018). MFM is supported by the Natural Sciences and Engineering Research Council of Canada (NSERC).

## Supplementary Materials

*Supplementary 1.* Table S1: BPI functional evaluation of BPI participants. Table S2: contingency table showing the $p$ values of Fisher's exact tests for control participants in the dominant hand observation. Table S3: contingency table showing the adjusted $p$ values of the Fisher's exact tests for control participants in the dominant hand observation. Table S4: Contingency table showing the $p$ values of Fisher's exact tests for each control participant in the nondominant hand observation. Table S5: contingency table showing the adjusted $p$ values of Fisher's exact tests for each control participant in the nondominant hand observation. Table S6: contingency table showing the $p$ values of Fisher's exact tests for each BPI participant in the dominant hand observation. Table S7: contingency table showing the adjusted $p$ values of Fisher's exact tests for each BPI participant in the dominant hand observation. Table S8: contingency table showing the $p$ values of Fisher's exact tests for each BPI patient in the nondominant hand observation. Table S9: contingency table showing the adjusted $p$ values of Fisher's exact tests for each BPI patient in the nondominant hand observation.

*Supplementary 2*. Supplementary video 1 Hand movement, ball movement, and no movement conditions employed in the experiment: https://drive.google.com/file/d/1IZgeVNrckUPtCAUS5ks8QqMwRvZtJHLG/view?usp=drivesdk.

## References


[1] S. J. Blakemore and A. Sirigu, "Action prediction in the cerebellum and in the parietal lobe," *Experimental Brain Research*, vol. 153, no. 2, pp. 239–245, 2003.

[2] M. Kawato, K. Furukawa, and R. Suzuki, "A hierarchical neural-network model for control and learning of voluntary movement," *Biological Cybernetics*, vol. 57, no. 3, pp. 169–185, 1987.

[3] R. C. Miall and D. M. Wolpert, "Forward models for physiological motor control," *Neural Networks*, vol. 9, no. 8, pp. 1265–1279, 1996.

[4] D. M. Wolpert, Z. Ghahramani, and J. R. Flanagan, "Perspectives and problems in motor learning," *Trends in Cognitive Sciences*, vol. 5, no. 11, pp. 487–494, 2001.

[5] R. R. Flanagan, P. Vetter, R. S. Johansson, and D. M. Wolpert, "Prediction precedes control in motor learning," *Current Biology*, vol. 13, no. 2, pp. 146–150, 2003.

[6] C. Brozzoli, G. Gentile, L. Bergouignan, and H. H. Ehrsson, "A shared representation of the space near oneself and others in the human premotor cortex," *Current Biology*, vol. 23, no. 18, pp. 1764–1768, 2013.

[7] N. P. Holmes and C. Spence, "The body schema and the multisensory representation (s) of peripersonal space," *Cognitive Processing*, vol. 5, no. 2, pp. 94–105, 2006.

[8] S. M. Aglioti, P. Cesari, M. Romani, and C. Urgesi, "Action anticipation and motor resonance in elite basketball players," *Nature Neuroscience*, vol. 11, no. 9, pp. 1109–1116, 2008.

[9] C. D. Vargas, M. L. Rangel, and A. Galves, "Predicting upcoming actions by observation: some facts, models and challenges," pp. 1–14, 2014, http://arxiv.org/abs/1409.6744.

[10] J. M. Kilner, C. D. Vargas, S. Duval, S. J. Blakemore, and A. Sirigu, "Motor activation prior to observation of a predicted movement," *Nature Neuroscience*, vol. 7, no. 12, pp. 1299–1301, 2004.

[11] A. P. Fontana, J. M. Kilner, E. C. Rodrigues, M. Joffily, and N. Nighoghossian, "Role of the parietal cortex in predicting incoming actions," *NeuroImage*, vol. 59, no. 1, pp. 556–564, 2012.

[12] L. Bonini and P. F. Ferrari, "Evolution of mirror systems: a simple mechanism for complex cognitive functions," *Annals of the New York Academy of Sciences*, vol. 1225, no. 1, pp. 166–175, 2011.

[13] L. Fogassi, V. Gallese, L. Fadiga, G. Luppino, M. Matelli, and G. Rizzolatti, "Coding of peripersonal space in inferior premotor cortex (area F4)," *Journal of Neurophysiology*, vol. 76, no. 1, pp. 141–157, 1996.

[14] MSA Graziano and CG, "Gross Visual responses with and without fixation: neurons in premotor cortex encode spatial locations independently of eye position," *Experimental Brain Research*, vol. 118, no. 3, pp. 373–380, 1998.

[15] A. Iriki, M. Tanaka, and Y. Iwamura, "Coding of modified body schema during tool use by macaque postcentral neurones," *Neuroreport*, vol. 7, no. 14, pp. 2325–2330, 1996.

[16] J. R. Duhamel, C. L. Colby, and M. E. Goldberg, "Ventral intraparietal area of the macaque: congruent visual and somatic response properties," *Journal of Neurophysiology*, vol. 79, no. 1, pp. 126–136, 1998.

[17] G. Rizzolatti, F. L. Fogassi, and V. Gallese, "The space around us," *Science*, vol. 277, no. 5323, pp. 190-191, 1997.

[18] S. J. Blakemore, D. Bristow, G. Bird, C. Frith, and J. Ward, "Somatosensory activations during the observation of touch and a case of vision-touch synaesthesia," *Brain*, vol. 128, no. 7, pp. 1571–1583, 2005.

[19] C. Keysers, B. Wicker, V. Gazzola, J. L. Anton, L. Fogassi, and V. Gallese, "A touching sight: SII/PV activation during the observation and experience of touch," *Neuron*, vol. 42, no. 2, pp. 335–346, 2004.

[20] M. Costantini, G. Galati, G. L. Romani, and S. M. Aglioti, "Empathic neural reactivity to noxious stimuli delivered to body parts and non-corporeal objects," *The European Journal of Neuroscience*, vol. 28, no. 6, pp. 1222–1230, 2008.

[21] E. Canzoneri, E. Magosso, and A. Serino, "Dynamic sounds capture the boundaries of peripersonal space representation in humans," *PLoS One*, vol. 7, no. 9, pp. 3–10, 2012.

[22] T. R. Makin, N. P. Holmes, C. Brozzoli, Y. Rossetti, and A. Farnè, "Coding of visual space during motor preparation: approaching objects rapidly modulate corticospinal excitability in hand-centered coordinates," *The Journal of Neuroscience*, vol. 29, no. 38, pp. 11841–11851, 2009.

[23] A. Zanini, I. Patané, E. Blini, R. Salemme, E. Koun, and A. F. CB, "Patterns of multisensory facilitation distinguish peripersonal from reaching space," *Bio Rxiv preprint*1–36.

[24] J. Cléry and S. BenHamed, "Frontier of self and impact prediction," *Frontiers in Psychology*, vol. 9, p. 1073, 2018.

[25] M. Bassolino, A. Finisguerra, E. Canzoneri, A. Serino, and T. Pozzo, "Dissociating effect of upper limb non-use and overuse on space and body representations," *Neuropsychologia*, vol. 70, pp. 385–392, 2014.

[26] C. Teneggi, E. Canzoneri, G. Di Pellegrino, and A. Serino, "Social modulation of peripersonal space boundaries," *Current Biology*, vol. 5, no. 5, pp. 406–411, 2013.

[27] T. R. Makin, M. Wilf, I. Schwartz, and E. Zohary, "Amputees "neglect" the space near their missing hand," *Psychological Science*, vol. 21, no. 1, pp. 55–57, 2010.

[28] V. S. Ramachandran and D. Brang, "Sensations evoked in patients with amputation from watching an individual whose corresponding intact limb is being touched," *Archives of Neurology*, vol. 66, no. 10, pp. 1281–1284, 2009.

[29] D. J. Anastakis, M. J. A. Malessy, R. Chen, K. D. Davis, and D. Mikulis, "Cortical plasticity following nerve transfer in the upper extremity," *Hand Clinics*, vol. 24, no. 4, pp. 425–444, 2008.

[30] M. J. A. Malessy, D. Bakker, A. J. Dekker, J. G. Van Dijk, and R. T. W. M. Thomeer, "Functional magnetic resonance imaging and control over the biceps muscle after intercostal-musculocutaneous nerve transfer," *Journal of Neurosurgery*, vol. 98, no. 2, pp. 261–268, 2003.

[31] M. J. A. Malessy, R. T. W. M. Thomeer, and J. G. Van Dijk, "Changing central nervous system control following intercostal nerve transfer," *Journal of Neurosurgery*, vol. 89, no. 4, pp. 568–574, 1998.

[32] T. Yoshikawa, N. Hayashi, Y. Tajiri, Y. Satake, and K. Ohtomo, "Brain reorganization in patients with brachial plexus injury: a longitudinal functional MRI study," *The Scientific World Journal*, vol. 2012, 501711 pages, 2012.

[33] D. Fraiman, M. F. Miranda, F. Erthal et al., "Reduced functional connectivity within the primary motor cortex of patients

with brachial plexus injury," *NeuroImage Clin*, vol. 12, pp. 277–284, 2016.

[34] F. F. Torres, B. L. Ramalho, C. B. Patroclo et al., "Plasticity in the brain after a traumatic brachial plexus injury in adults," in *Treatment of Brachial Plexus Injury*, V. Vanaclocha, Ed., 2019.

[35] B. L. Ramalho, M. L. Rangel, A. C. Schmaedeke, F. S. Erthal, and C. D. Vargas, "Unilateral brachial plexus lesion impairs bilateral touch threshold," *Front Neurol*, vol. 10, pp. 1–11, 2019.

[36] Y. Lu, H. Liu, X. Hua, J. G. Xu, Y. D. Gu, and Y. L. Shen, "Attenuation of brain grey matter volume in brachial plexus injury patients," *Neurological Sciences*, vol. 37, no. 1, pp. 51–56, 2016.

[37] D. Nico, E. Daprati, F. Rigal, L. Parsons, and A. Sirigu, "Left and right hand recognition in upper limb amputees," *Brain*, vol. 127, no. 1, pp. 120–132, 2004.

[38] J. Feng, H. Liu, J. Xu, Y. Gu, and Y. Shen, "Differences in brain adaptive functional reorganization in right and left total brachial plexus injury patients," *World Neurosurgery*, vol. 84, no. 3, pp. 702–708, 2015.

[39] R. C. Oldfield, "The assessment and analysis of handedness: the Edinburgh inventory," *Neuropsychologia*, vol. 9, no. 1, pp. 97–113, 1971.

[40] F. M. Maynard Jr., M. B. Bracken, G. Creasey et al., "International standards for neurological and functional classification of spinal cord injury," *Spinal Cord*, vol. 35, no. 5, pp. 266–274, 1997.

[41] Y. Benjamini and Y. Hochberg, "Controlling the false discovery rate: a practical and powerful approach to multiple testing," *Journal of the Royal Statistical Society: Series B (Methodological)*, vol. 57, pp. 289–300, 1995.

[42] R Core Team, "R: a language and environment for statistical computing. R Foundation for Statistical Computing," 2020, https://www.R-project.org/.

[43] M. S. A. Graziano, X. I. N. T. H. CG, S. A. M. Gross, X. T. Hu, and C. G. Gross, "Visuo-spatial properties of ventral premotor cortex," *Journal of Neurophysiology*, vol. 77, no. 5, pp. 2268–2292, 1997.

[44] M. S. A. Graziano and D. F. Cooke, "Parieto-frontal interactions, personal space, and defensive behavior," *Neuropsychologia*, vol. 44, no. 6, pp. 845–859, 2006.

[45] C. Brozzoli, H. H. Ehrsson, and A. Farnè, "Multisensory representation of the space near the hand: from perception to action and interindividual interactions," *The Neuroscientist*, vol. 20, no. 2, pp. 122–135, 2014.

[46] C. F. Sambo and B. Forster, "An ERP investigation on visuotactile interactions in peripersonal and extrapersonal space: evidence for the spatial rule," *Journal of Cognitive Neuroscience*, vol. 21, no. 8, pp. 1550–1559, 2009.

[47] A. Serino, E. Canzoneri, and A. Avenanti, "Fronto-parietal areas necessary for a multisensory representation of peripersonal space in humans: an rTMS study," *Journal of Cognitive Neuroscience*, vol. 23, no. 10, pp. 2956–2967, 2011.

[48] T. R. Makin, N. P. Holmes, and E. Zohary, "Is that near my hand? Multisensory representation of peripersonal space in human intraparietal sulcus," *J Neurosci*, vol. 27, no. 4, pp. 731–740, 2007.

[49] J. Cléry, O. Guipponi, S. Odouard, S. Pinède, and C. Wardak, "The prediction of impact of a looming stimulus onto the body is subserved by multisensory integration mechanisms," *The Journal of Neuroscience*, vol. 37, no. 44, pp. 10656–10670, 2017.

[50] J. M. Kilner and C. D. Frith, "A possible role for primary motor cortex during action observation," *Proceedings of the National Academy of Sciences of the United States of America*, vol. 104, no. 21, pp. 8683-8684, 2007.

[51] G. Orbán and D. M. Wolpert, "Representations of uncertainty in sensorimotor control," *Current Opinion in Neurobiology*, vol. 21, no. 4, pp. 629–635, 2011.

[52] G. Lundborg, "Nerve injury and repair - a challenge to the plastic brain," *Journal of the Peripheral Nervous System*, vol. 8, no. 4, pp. 209–226, 2003.

[53] Y. Mano, T. Nakamuro, R. Tamural et al., "Central motor reorganization after anastomosis of the musculocutaneous and intercostal nerves following cervical root avulsion," *Annals of Neurology*, vol. 38, no. 1, pp. 15–20, 1995.

[54] L. Souza, T. Lemos, D. C. Silva et al., "Balance impairments after brachial plexus injury as assessed through clinical and posturographic evaluation," *Front Hum Neurosci*, vol. 9, pp. 1–7, 2016.

[55] E. C. Rodrigues, A. P. Fontana, M. Jofilly, J. M. Kilner, C. D. Vargas, and A. Sirigu, "Predicting an observed movement after unilateral upper-limb amputation," *Clinical Neurophysiology*, vol. 119, no. 9, p. e132, 2008.

[56] J.-T. Feng, H.-Q. Liu, X.-Y. Hua, Y.-D. Gu, J.-G. Xu, and W.-D. Xu, "Brain functional network abnormality extends beyond the sensorimotor network in brachial plexus injury patients," *Brain Imaging and Behavior*, vol. 10, no. 4, pp. 1198–1205, 2016.

[57] B. Liu, T. Li, W. J. Tang et al., "Changes of inter-hemispheric functional connectivity between motor cortices after brachial plexuses injury: a resting-state fMRI study," *Neuroscience*, vol. 243, pp. 33–39, 2013.

[58] Y. Lyu, X. Guo, R. Bekrater-Bodmann, H. Flor, and S. Tong, "An event-related potential study on the time course of mental rotation in upper-limb amputees," *Clinical Neurophysiology*, vol. 128, no. 5, pp. 744–750, 2017.

[59] J. P. Noel, T. Bertoni, E. Terrebonne et al., "Rapid recalibration of peri-personal space: psychophysical, electrophysiological, and neural network modeling evidence," *Cerebral Cortex*, vol. 30, no. 9, pp. 5088–5106, 2020.

[60] E. Làdavas and A. Serino, "Action-dependent plasticity in peripersonal space representations," *Cognitive Neuropsychology*, vol. 25, no. 7-8, pp. 1099–1113, 2008.

[61] I. Patané, L. Cardinali, R. Salemme, F. Pavani, A. Farnè, and C. Brozzol, "Action planning modulates peripersonal space," *Journal of Cognitive Neuroscience*, vol. 31, no. 8, pp. 1141–1154, 2019.

[62] E. Canzoneri, M. Marzolla, A. Amoresano, G. Verni, and A. Serino, "Amputation and prosthesis implantation shape body and peripersonal space representations," *Scientific Reports*, vol. 3, no. 1, p. 2844, 2013.

Hindawi
Neural Plasticity
Volume 2021, Article ID 6689476, 8 pages
https://doi.org/10.1155/2021/6689476

*Research Article*

# Impaired Limb Functional Outcome of Peripheral Nerve Regeneration Is Marked by Incomplete Recovery of Paw Muscle Atrophy and Brain Functional Connectivity in a Rat Forearm Nerve Repair Model

**Qiyuan Bao,[1] Qi Liu,[1] Jun Wang,[2] Yuhui Shen ,[1] and Weibin Zhang [1]**

[1]*Department of Orthopaedics, Shanghai Ruijin Hospital, Shanghai Jiao Tong University School of Medicine, Shanghai, China*
[2]*Department of Orthopaedics, Shanghai Institute of Traumatology and Orthopaedics, Shanghai, China*

Correspondence should be addressed to Yuhui Shen; yuhuiss@163.com and Weibin Zhang; zhangweibin10368@163.com

Received 4 December 2020; Revised 22 January 2021; Accepted 1 February 2021; Published 11 February 2021

Academic Editor: Zhongyu Li



Skilled sensorimotor deficit is an unsolved problem of peripheral nerve injury (PNI) led by limb trauma or malignancies, despite the improvements in surgical techniques of peripheral nerve anastomosis. It is now accepted that successful functional recovery of PNI relies tremendously on the multilevel neural plasticity from the muscle to the brain. However, animal models that recapitulate these processes are still lacking. In this report, we developed a rat model of PNI to longitudinally assess peripheral muscle reinnervation and brain functional reorganization using noninvasive imaging technology. Based on such model, we compared the longitudinal changes of the rat forepaw intrinsic muscle volume and the seed-based functional connectivity of the sensorimotor cortex after nerve repair. We found that the improvement of skilled limb function and the recovery of paw intrinsic muscle following nerve regeneration are incomplete, which correlated with the functional connectivity between the primary motor cortex and dorsal striatum. Our results were highly relevant to the clinical observations and provided a framework for future investigations that aim to study the peripheral central sensorimotor circuitry underlying skilled limb function recovery after PNI.

## 1. Introduction

Skilled sensorimotor deficit is a common yet unsolved clinical problem of peripheral nerve injury (PNI) [1–4] and surgical repair (PNR) [1, 5, 6] due to limb trauma or extremity malignancy. Despite improvements in surgical techniques to foster peripheral nerve regeneration, PNI still leads to long-lasting disabilities in terms of lost fine sensorimotor function [6, 7]. Previous human studies suggest that the brain undergoes a sensorimotor relearning process after peripheral nerve regeneration, and such misorganization and reorganization process could significantly impact the outcome of nerve regeneration [8, 9]. It is now increasingly accepted that successful peripheral nerve rehabilitation is, rather than simply a matter of surgical reconstruction, a combinatorial effort of the integrated treatment strategies targeting the plasticity from the muscle to the brain [10, 11]. However, the animal models that recapitulate these processes are still lacking. To date, the mechanistic details of the coordination and reorganization of the peripheral reinnervation and central plasticity after PNI are still poorly understood.

In this report, we developed a rat model of PNI to assess the peripheral muscle reinnervation and brain functional reorganization process longitudinally using noninvasive imaging technology, with the skilled forelimb function recovery monitored using ladder rung walking task [12]. Using such model, we analyzed the longitudinal changes of the rat forepaw intrinsic muscle and the functional connectivity of

the primary motor cortex after PNI and PNR, to interrogate the potential neural mechanism of the sensorimotor circuitry underlying the limb functional recovery.

## 2. Methods

*2.1. Animals.* For both limb muscle reinnervation model and the paw intrinsic muscle reinnervation model, 15 adult male Sprague-Dawley rats weighing 200–250 grams were randomly assigned to the control ($n = 5$), nerve injury ($n = 5$), and nerve repair ($n = 5$) groups. Experiment animals were given access to food and water ad libitum and housed with soft bedding on a 12 h light/dark cycle in a temperature-controlled environment (21 ± 2°C). Rats were handled regularly before any surgical procedures, MR imaging, and behavioral testing, and were sacrificed at week 10 following the behavioral assessment.

*2.2. Limb Muscle Reinnervation Model.* To investigate the skilled functional outcome, limb muscle reinnervation model was designed (Figures 1(a) and 1(b)). Briefly, all rats were anesthetized with isoflurane (1.5–2%) and a mixture of 30% $N_2O$ and 70% $O_2$. With the longitudinal incision at the right proximal upper limb, the musculocutaneous nerve (MCN) and the radial nerve were exposed before their innervation of the biceps muscle and the triceps muscle, respectively. For the nerve injury group, both nerves were transected and tightly ligated to prevent the nerve stump regeneration. For the nerve repair group, both nerves were exposed in the same fashion. Then, the stumps of both nerves were immediately anastomosed through a 10-0 monofilament epineurial microstitch (Ethicon, USA) following the nerve transection. For the control group, sham operations were performed, where MCN and radial nerve were exposed as in the injury group, but received no further manipulations.

*2.3. Paw Intrinsic Muscle Model.* The paw intrinsic muscle reinnervation model was established to investigate its impact on the skilled functional outcome after PNI (Figures 1(a) and 1(c)). Under anesthesia, a longitudinal incision was placed at the right distal forearm of the rat. The medial and ulnar nerves were explored at the wrist level. Both of the nerves were transected and ligated in the nerve injury group, or transected and then repaired through a 10-0 monofilament epineurial microstitch (Ethicon, USA) in the repair group. In contrast, the nerves were only exposed without any further procedure in the control (sham) group.

*2.4. Ladder Rung Skilled Walking Task.* Prior to the behavioral testing, rats were handled and trained to acclimate the ladder for 7 consecutive days in the ladder rung apparatus, which was made according to the original report [13]. The apparatus was composed of self-made horizontal ladder rungs between the transparent sidewalls. 51 ladder rungs in 2 cm intervals (a total length of 1 m) were presented to the rat toward the home cage. During the walking of the rats, we performed video recording for each walking trial of the animal to capture the foot errors, including slight slip, deep slip, and total miss of the step. Skilled limb sensorimotor function was measured as the number of errors divided by the number of total steps for the affected limb, averaged for five consecutive trials. The foot fault rate between groups was compared using Student's $t$-test, with a $p$ value $< 0.05$ considered statistically significant.

*2.5. MR Scanning Parameters of the Rat Brain.* MR imaging of the rat forepaw and brain was carried out with a Bruker 7 T/40 cm horizontal magnet (ClinScan, Bruker BioSpin, Germany). The functional changes of the rat brain were studied using parameters as previously reported [14]. Briefly, anesthesia was given to the rats during the experiments with isoflurane (1.75–2.5%) mixed with air. The respiratory rate and heart rate were monitored and recorded during scans. The rat body temperature was maintained and surveilled at about 37°C during the imaging session. MRI scans were started when physiological parameters stabilized for at least 10 minutes. Blood oxygen level-dependent (BOLD) contrast-sensitive T2∗-weighted gradient-echo echo-planar images were acquired for resting-state fMRI scans. Each scan consisted of 300 volumes of 14 slice acquisitions (repetition time (TR) of 1.3 seconds, echo time (TE) of 25 milliseconds, flip angle = 60°, 1.0 mm slice thickness, and $0.5 \times 0.5\,mm^2$ in-plane resolution). A high-resolution T2-weighted RARE anatomical reference was acquired for each animal (1.0 mm slice thickness and $0.273 \times 0.273\,mm^2$ in-plane resolution). An additional T2-weighted RARE anatomical scan with the same geometry as the functional image (1 mm slice thickness and $0.5 \times 0.5\,mm^2$ in-plane resolution) was also acquired and used as a low-resolution anatomical reference.

*2.6. MR Scanning Parameters of the Rat Forepaw.* After the MRI scan of the rat brain, imaging of the rat forepaw was immediately conducted. A total of four sequencing protocols were tested and compared in the preliminary study: (1) the turbo spin echo (TSE) sequence (parameter 1) with an in-plane resolution of $0.27 \times 0.27\,mm^2$, (2) gradient echo (GRE) sequence with an in-plane resolution of $0.99 \times 0.5\,mm^2$, (3) GRE sequence with an in-plane resolution of $0.5 \times 0.5\,mm^2$, and (4) GRE sequence with an in-plane resolution of $0.15 \times 0.15\,mm^2$ (Table 1). MR images of the rat forepaw were given to four independent readers, who were asked to report their confidence in the manual segmentation of the intrinsic muscle with a ranking of 1 (worst) to 4 (best) assigned to the four scanning parameters. The scanning parameter with the highest ranking was chosen for the formal study, where rat brain functional imaging and rat forepaw muscle volumetry imaging were acquired for each of the rats.

*2.7. Image Preprocessing.* Resting-state fMRI data were preprocessed with FSL 5.1 (https://www.fmrib.ox.ac.uk/fsl) [15]. The fMRI was skull stripped and preprocessed with signal despiking, removal of physiological artifacts from respiration and heartbeat, and correction for slice timing. Preprocessed images were then corrected for motion, followed by spatially smoothing with a Gaussian kernel of 0.8 mm FWHM and high-pass filtering with a cutoff of 100 seconds. Volumes from functional images were registered to a standard space with a three-step process. Images were first aligned with the individual's low-resolution anatomical image, followed by alignment with the

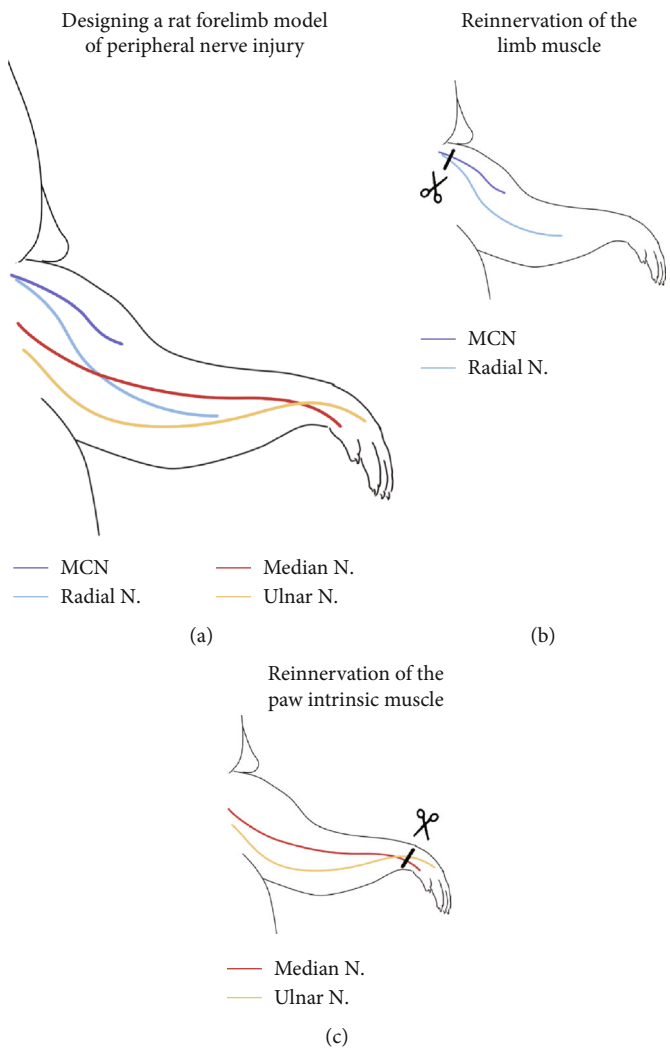


Figure 1: The surgical procedure of the raw forepaw. (a) To assess the skilled functional recovery outcome after peripheral neural repair, we designed a nerve anastomosis model using rat forelimb. (b) The musculocutaneous nerve (MCN) and radial nerve of the rat forelimb were resected with or without nerve repair, to investigate the impact of limb muscle denervation and reinnervation on the skilled limb function. (c) Similarly, the median nerve and the ulnar nerve were manipulated to study the denervation and reinnervation of the paw intrinsic muscle.

Table 1: Establishing the optimal sequencing parameter for measuring the forepaw intrinsic muscle volume.

| Parameter | Sequence | Resolution (mm) | FoV read (mm) | FoV phase (%) | Slice thickness (mm) | SNR | TR (ms) | TE (ms) | Confidence of the segmentation | | | | | Total time (mm:ss) |
|---|---|---|---|---|---|---|---|---|---|---|---|---|---|---|
| | | | | | | | | | Rater 1 | Rater 2 | Rater 3 | Rater 4 | Average score | |
| 1 | TSE* | 0.27 × 0.27 | 35.00 | 79.70 | 1.20 | 1.00 | 2000 | 24 | 1 | 2 | 2 | 1 | 1.5 | 28:18 |
| 2 | GRE | 0.99 × 0.50 | 130.00 | 100.00 | 1.00 | 5.25 | 28 | 4 | 2 | 1 | 1 | 2 | 1.5 | 13:18 |
| 3 | GRE | 0.50 × 0.50 | 129.00 | 40.00 | 0.50 | 4.64 | 28 | 4 | 3 | 3 | 3 | 3 | 3.0 | 11:35 |
| 4 | GRE | 0.15 × 0.15 | 40.00 | 53.10 | 0.15 | 1.22 | 28 | 4 | 4 | 4 | 4 | 4 | 4.0 | 17:23 |

*We did not further increase the resolution of the TSE scanning sequence, due to the tremendous amount of imaging time (>28 min) at this parameter.

individual's high-resolution anatomical image, and then coregistered to a standard space. Average time courses from all of the voxels inside white matter (WM) and cerebrospinal fluid (CSF) were extracted. Confounding regressors that modeled WM and CSF signals and six motion parameters, including translations and rotations, were removed from the images through linear regression.

*2.8. Seed-Based Resting-State Functional Connectivity (FC) Analysis.* Whole-brain resting-state connectivity of the region

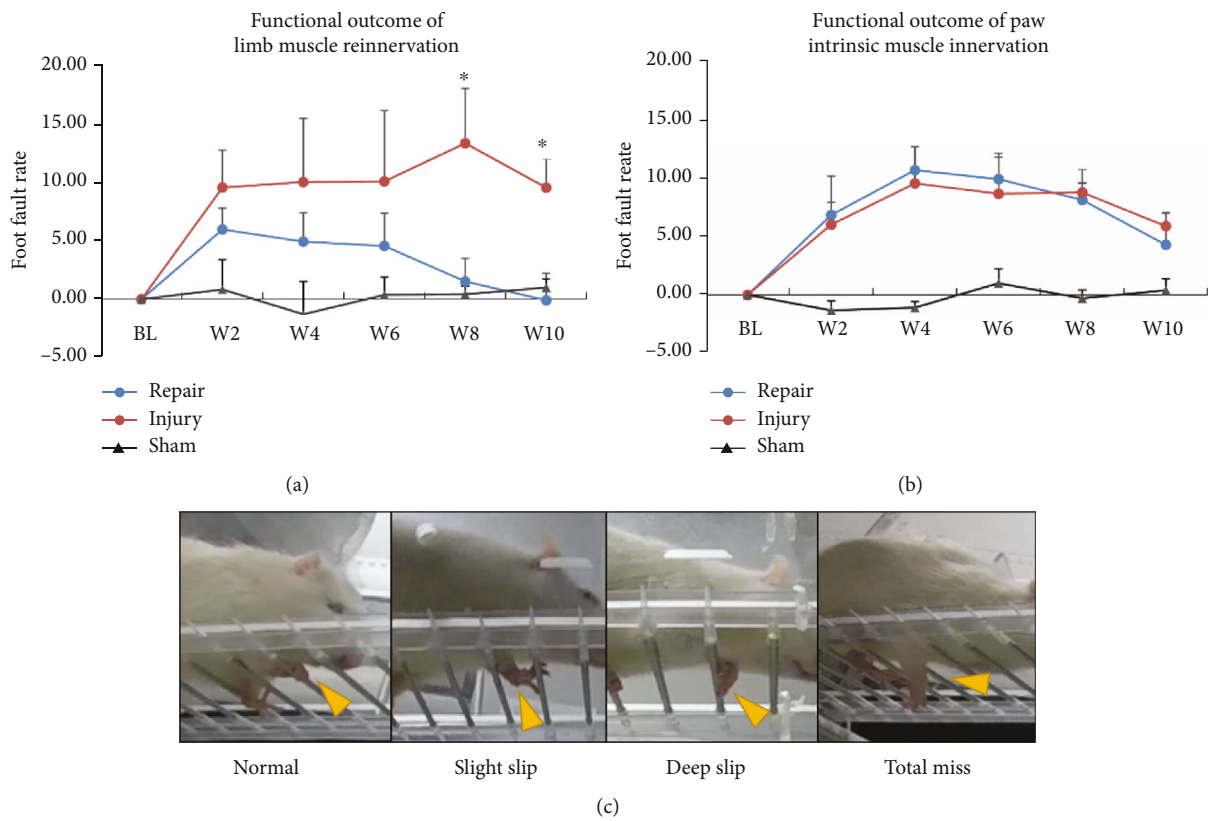


Figure 2: The functional outcome of the skilled limb movement after peripheral nerve injury. (a) In the limb muscle reinnervation design, the foot fault rate of the nerve repair group was observed to be indifferent from the sham group at W8 and W10, but significantly lower than that of the injury group. (b) In the intrinsic muscle reinnervation design, we found no recovery of the skilled foot function in the repair group compared to the injury group, resulting in a significantly higher foot fault rate than the sham group. (c) Exemplary patterns of various degrees of foot fault (yellow arrow) in rat forelimb during skill walking. $^*p < 0.050$. ns: nonsignificant.

of interest (ROI) was constructed as described in [14, 16]. Briefly, a standard rat atlas [17] comprising 96 anatomical ROIs (48 regions in each hemisphere) was used as the reference. The contralateral (left) primary motor cortex was chosen as the seed for analyzing the whole-brain FC. We then extracted the time course of BOLD signal across all voxels within a given ROI and generated the mean time course for each ROI. The functional correlation was computed using the Pearson correlation coefficient between the time courses of the seed with every other ROI. Correlation coefficients were transformed to $z$-scores using Fisher's $z$ transformation as the final FC value for each subject. The FC strength was compared between the corresponding connections using FSL FEAT analysis to find significant brain regions. The FC with a $p$ value $< 0.05$ after multiple comparison correction was considered statistically significant.

## 3. Results

*3.1. The Recovery of Skilled Forelimb Function following Muscle Denervation and Reinnervation.* We first compared the effect of limb muscle (large muscle) reinnervation versus paw intrinsic muscle (small muscle) reinnervation on the functional recovery of the skilled forelimb performance. In both large muscle model and small muscle model, the nerve injury group exhibited an increased foot fault rate compared to the baseline ($p < 0.05$) postsurgery. In contrast, the skilled forelimb functional recovery demonstrated a highly different pattern between the two model designs. In the large muscle model, we observed a gradual recovery of the foot fault rate in the repair group after surgery. The foot fault rate of the repair group was significantly lower than that of the injury group at week 8 ($p = 0.049$) and week 10 ($p = 0.038$) (Figure 2(a)). However, the similar trend was not seen in the repair group of the small muscle model. Various degrees of impaired forepaw positioning (slight and deep slip) and compensatory adjustment ability (total miss) were observed (Figure 2(c)). The foot fault rates of the injury and the repair groups were not significantly different postoperatively from week 2 to week 10 ($p > 0.05$) (Figure 2(b)), suggesting a defective functional recovery of the intrinsic muscle compared to the large muscle following PNI.

*3.2. Establishing the MR Imaging Paradigm for Noninvasive Assessment of the Paw Intrinsic Muscle Volume.* Since there were no established MR parameters for imaging rat paw intrinsic muscle, we prioritized the optimal sequencing parameters from a total of four potential settings (Table 1 and Figure 3(a)) based on the imaging quality and time consumption. Due to the fact that rat forepaw intrinsic muscle is contoured by the metacarpal bone and the flexor/extensor tendons (Figure 3(b)), we then asked four independent

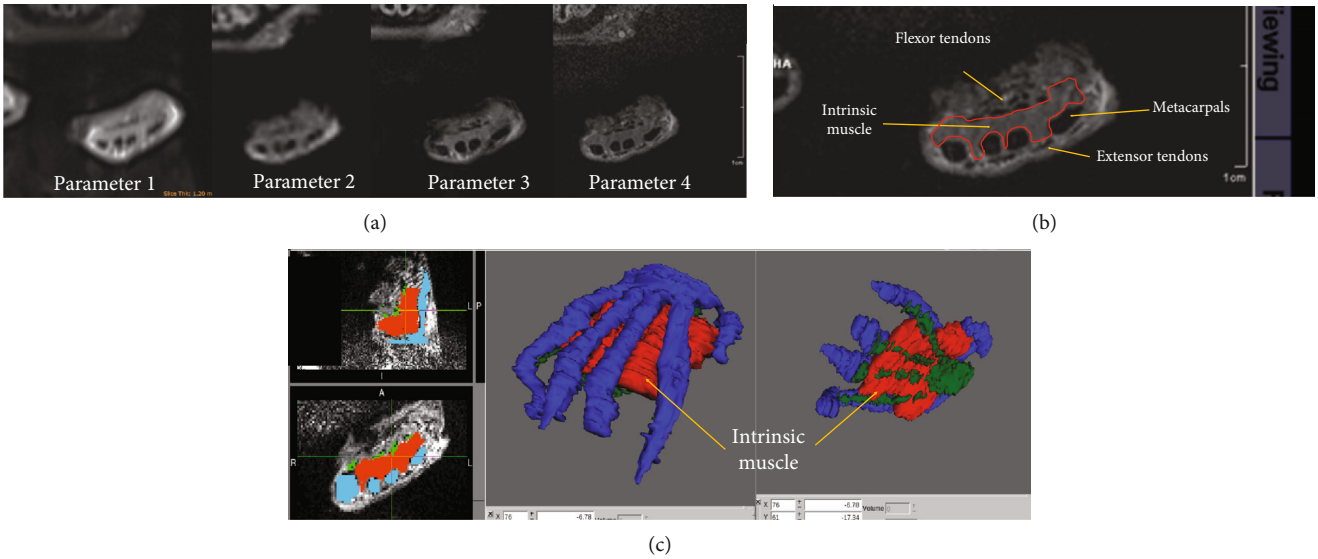


Figure 3: Establishing the MR imaging paradigm to assess the paw intrinsic muscle volume. (a) To determine the best imaging protocol, we compare the imaging quality of the four parameters specified in Table 1. Readers were asked to report their confidence in the manual segmentation of the intrinsic muscle, which was contoured by the metacarpal bone and the flexor/extensor tendons (b). (c) Finally, manual segmentation of the intrinsic muscle (red voxels) based on parameter 4 was taken as the final setup for muscle volumetry of the subsequent study.

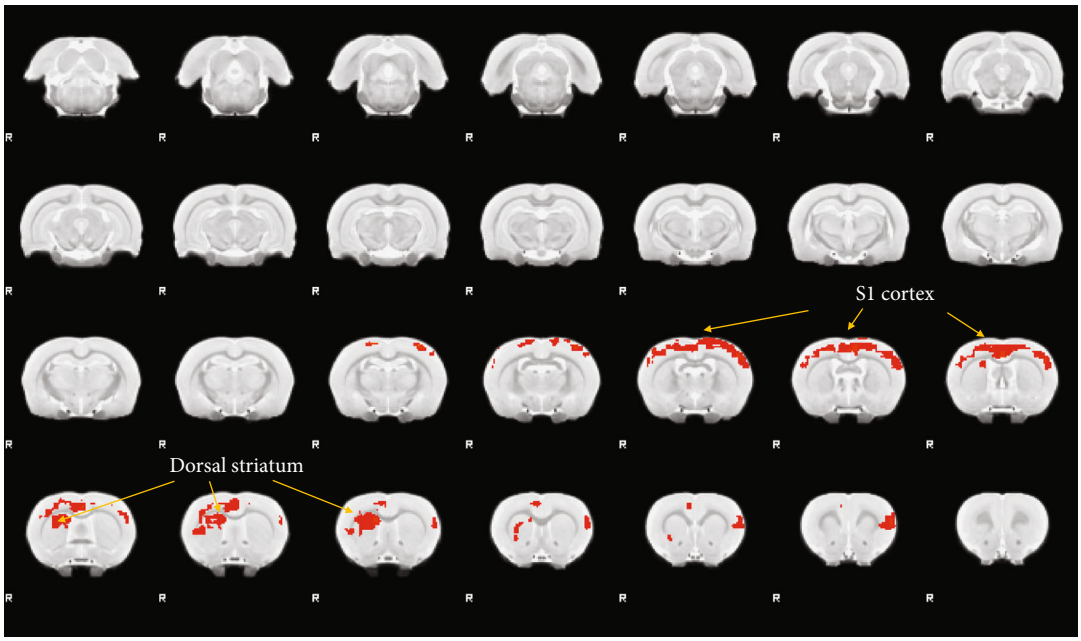


Figure 4: Brain functional reorganization analysis of the primary motor cortex (M1) after nerve repair. We performed a seed-based whole-brain functional connectivity (FC) analysis of the contralateral primary motor cortex (M1) between the nerve repair and the nerve injury groups (repair-injury). The rat contralateral M1 cortex (left) demonstrated an extensive FC reorganization (marked in red) with bilateral sensory cortex (S1) as well as right dorsal striatum (dS) at week 8.

readers to report their confidence in the manual segmentation of the intrinsic muscle contour based on the MR imaging with the aforementioned four parameters. The turbo spin echo (TSE) sequence (parameter 1) achieved an acceptable imaging quality, yet at the expense of an extremely prolonged acquisition time (>28 min). Therefore, further optimization based on TSE sequence was not attempted. Then, gradient echo (GRE) sequence was performed with three sets of parameters, at the resolution of 0.99 mm × 0.5 mm, 0.5 mm × 0.5 mm, and 0.15 mm × 0.15 mm, respectively. Interestingly, all four readers assigned parameter 4 as the highest quality one (parameter 4 versus the other, $p = 0.025$) (Table 1). Therefore, we chose parameter 4 with manual segmentation of the muscle contour (Figure 3(c)) as the final setup for volumetry of paw intrinsic muscle in the subsequent study.

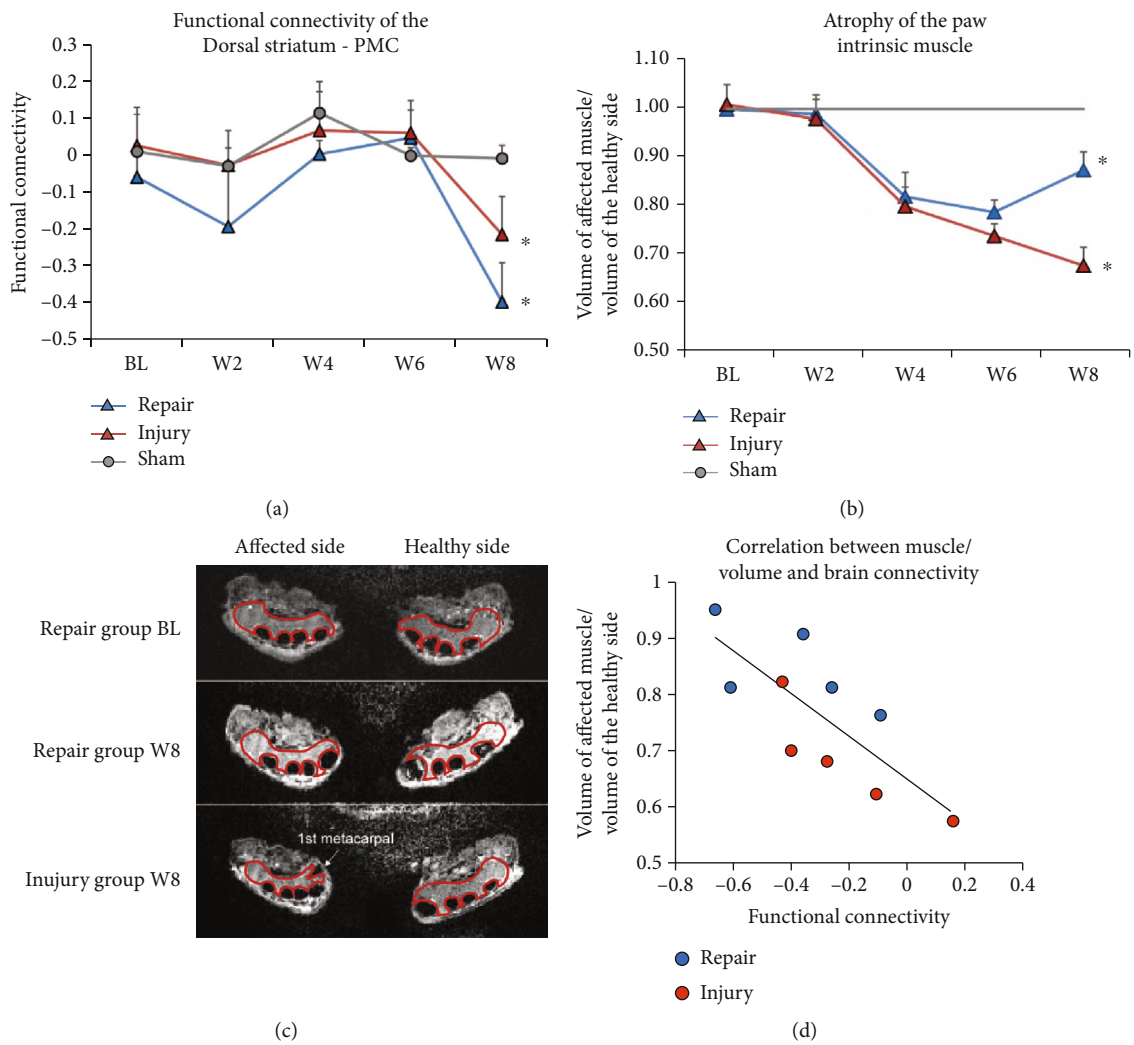


Figure 5: The change of dS-M1 connectivity and paw muscle atrophy following PNR. (a) The FC of the dS-M1 remains similar among the three groups until week 8, when the FC of the nerve injury and the repair group was statistically different from that of the sham group. (b) The degree of muscle atrophy was gradually aggravated from week 2 postsurgery in the nerve injury and repair groups. However, the nerve repair group demonstrated only partial recovery of muscle volume at week 8. (c) The muscle atrophy of the repair and the injury groups was shown in an exemplary graph. Note that remarkable muscle atrophy of the injured side was observed at week 8 in the injury group, but not in the repair group. The adduction of the 1st metacarpal was also observed due to the thenar atrophy of the paw. (d) We observed a significant correlation between the dS-M1 FC and the degree of muscle atrophy in rats with nerve injury and repair at week 8. $^{*}p < 0.05$ compared to the control.

*3.3. Brain Functional Reorganization Analysis of the Primary Motor Cortex (M1).* To investigate the brain functional reorganization process following peripheral reinnervation of the paw intrinsic muscle, we performed a seed-based whole-brain functional connectivity (FC) analysis of the contralateral primary motor cortex (M1) between the nerve injury and the nerve repair groups. There was no significant difference of connections involving the M1 cortex at week 6. Interestingly, the rat contralateral M1 cortex (left) demonstrated an extensive FC reorganization with the left sensory cortex (S1), the right sensorimotor cortex (S1M1), and the right dorsal striatum (dS) (Figure 4) at week 8. Remarkably, the dorsal striatum has been reported as a principal structure facilitating the neural plasticity underlying the locomotion function [18–20], supporting our hypothesis that dS-M1 connectivity change might be a critical central reorganization process of peripheral reinnervation following PNI.

*3.4. Tracing the Dynamics of dS-M1 Connectivity and Paw Reinnervation following PNI.* We then asked whether the dS-M1 functional reorganization was in parallel with peripheral reinnervation of the rat forelimb intrinsic muscle. The degree of muscle atrophy was gradually aggravated from week 2 postsurgery. However, the muscle atrophy of the nerve repair group demonstrated a partial recovery at week 8 (Figure 5(b)), which was significantly higher than that of the nerve injury group ($p = 0.020$). In contrast, the atrophy of the affected intrinsic muscle in the injury group was further exacerbated at week 8 (Figure 5(c)). Accordantly, we observed a highly similar trend of dS-M1 plasticity dynamics.

The FC change of the nerve repair group was indifferent from either the nerve repair or the sham group before week 6. However, dS-M1 FC of the repair group and the injury group was statistically different from that of the sham group at week 8 ($p < 0.05$) (Figure 5(a)). Interestingly, we observed a significant correlation between the dS-M1 FC and the degree of muscle atrophy ($r = 0.601$, $p = 0.011$) (Figure 5(d)), suggesting potential neural feedback and functional circuitry of the peripheral reinnervation with central plasticity.

## 4. Discussion

Numerous animal models have been established in the previous literature for assessing the loss and recovery of limb skilled locomotion function after brain [21] or spinal cord injury [22]. However, rodent studies regarding central plasticity following PNR are surprisingly lacking, which is in sharp contrast with the unmet need for surgical repair and rehabilitative interventions for PNI [23]. In the last decades, a plethora of emerging treatment modalities that target central plasticity has been investigated, such as activity-based sensory reeducation, selective deafferentation, crossmodal sensory substitution, and mental motor imagery [23, 24]. While the importance of strengthening the central relearning process during the sensorimotor reinnervation and skilled function recovery has been increasingly recognized, novel animal models were needed to unravel these mechanisms. Our study, for the first time, proposed a paradigm using non-invasive MR imaging to monitor the peripheral reinnervation and central functional reorganization in a longitudinal manner. Our finding also demonstrated that the ladder rung walking task, which was originally designed for brain or spinal cord injury measurement [12], can be implemented to faithfully capture the skilled limb function following PNI and regeneration.

Unlike previous models of sciatic nerve regeneration, our findings highlighted the incomplete recovery of the intrinsic muscle atrophy and skilled sensorimotor deficit. Interestingly, reinnervation of the large limb muscle caused by the MCN and radial nerve repair also failed to capture such suboptimal neurorehabilitation outcomes. Hypothetically, this discrepancy is likely due to a higher degree of loss or misdirected sensory input following axonal regrowth, resulting in a heavier mismatch of the cortical representation of the reinnervated forepaw [24]. Furthermore, the cortical representation of the paw sensorimotor function was much larger than that of the limb, which enables a greater encroachment of the adjacent intact cortical areas into the nerve-injured cortex [25]. It is reported that such extensive maladaptive plasticity has a limited role in and might even jeopardize the process of the sensorimotor function outcome [24]. Additionally, our model emphasized on skilled locomotion, rather than gross muscle function following PNR. Such a recovery process demands more complex and extensive central plasticity in the nervous system, which is reinforced by our findings that the FC changes of M1 with dS and S1M1 regions occur at a later stage and correlate with the temporal dynamics of muscle atrophy recovery. Finally, the denervation atrophy was hypothesized to be more irreversible for the paw intrinsic muscle, compared to that for the large muscle [26] after neural regeneration.

To our knowledge, this is the first report examining the dynamics of paw intrinsic muscle reinnervation and central reorganization in parallel using the rat peripheral nerve model. Our results were highly relevant to clinical observations of the suboptimal outcome of skilled hand functional recovery [27, 28]. Further studies are warranted at the cellular and neural circuit levels to determine the peripheral central feedback mechanisms, as well as the potential therapeutic targets underlying the functional rehabilitation after peripheral nerve reinnervation.

## Data Availability

The data used to support the findings of this study are available from the corresponding author upon request.

## Conflicts of Interest

The authors declare that they have no conflicts of interest.

## Authors' Contributions

Yuhui Shen and Weibin Zhang are co-corresponding authors.

## Acknowledgments

This study is supported by the National Natural Science Foundation of China (Grant no. 81600953) and the Shanghai Science and Technology Committee (Grant no. 20164Y0143).

## References

[1] W. C. Pederson, "Median nerve injury and repair," *The Journal of Hand Surgery*, vol. 39, no. 6, pp. 1216–1222, 2014.

[2] H. R. Park, G. S. Lee, I. S. Kim, and J. C. Chang, "Brachial plexus injury in adults," *Nerve*, vol. 3, no. 1, pp. 1–11, 2017.

[3] J. K. Terzis and V. K. Kostopoulos, "The surgical treatment of brachial plexus injuries in adults," *Plastic and Reconstructive Surgery*, vol. 119, no. 4, pp. 73e–92e, 2007.

[4] G. Lundborg, "Richard P. Bunge memorial lecture. Nerve injury and repair–a challenge to the plastic brain," *Journal of the Peripheral Nervous System*, vol. 8, no. 4, pp. 209–226, 2003.

[5] V. Decrouy-Duruz, T. Christen, and W. Raffoul, "Evaluation of surgical treatment for neuropathic pain from neuroma in patients with injured peripheral nerves," *Journal of Neurosurgery*, vol. 128, no. 4, pp. 1235–1240, 2018.

[6] S. Polatkan, E. Orhun, O. Polatkan, E. Nuzumlali, and O. Bayri, "Evaluation of the improvement of sensibility after primary median nerve repair at the wrist," *Microsurgery*, vol. 18, no. 3, pp. 192–196, 1998.

[7] G. Lundborg and B. Rosen, "Hand function after nerve repair," *Acta Physiologica (Oxford, England)*, vol. 189, no. 2, pp. 207–217, 2007.

[8] G. Lundborg and B. Rosen, "Sensory relearning after nerve repair," *The Lancet*, vol. 358, no. 9284, pp. 809-810, 2001.

[9] M. X. Zheng, Y. D. Shen, X. Y. Hua, A. L. Hou, Y. Zhu, and W. D. Xu, "Cortical reorganization in dual innervation by single peripheral nerve," *Neurosurgery*, vol. 83, no. 4, pp. 819–826, 2018.

[10] E. C. Meyers, N. Kasliwal, B. R. Solorzano et al., "Enhancing plasticity in central networks improves motor and sensory recovery after nerve damage," *Nature Communications*, vol. 10, no. 1, p. 5782, 2019.

[11] M. P. Willand, C. D. Chiang, J. J. Zhang, S. W. P. Kemp, G. H. Borschel, and T. Gordon, "Daily electrical muscle stimulation enhances functional recovery following nerve transection and repair in rats," *Neurorehabilitation and Neural Repair*, vol. 29, pp. 690–700, 2014.

[12] G. A. Metz and I. Q. Whishaw, "The ladder rung walking task: a scoring system and its practical application," *Journal of Visualized Experiments*, no. 28, pp. 319–327, 2009.

[13] G. A. Metz and I. Q. Whishaw, "Cortical and subcortical lesions impair skilled walking in the ladder rung walking test: a new task to evaluate fore- and hindlimb stepping, placing, and coordination," *Journal of Neuroscience Methods*, vol. 115, no. 2, pp. 169–179, 2002.

[14] P. C. Chang, S. L. Pollema-Mays, M. V. Centeno et al., "Role of nucleus accumbens in neuropathic pain: linked multi-scale evidence in the rat transitioning to neuropathic pain," *Pain*, vol. 155, no. 6, pp. 1128–1139, 2014.

[15] S. M. Smith, M. Jenkinson, M. W. Woolrich et al., "Advances in functional and structural MR image analysis and implementation as FSL," *NeuroImage*, vol. 23, pp. S208–S219, 2004.

[16] Z. Liang, J. King, and N. Zhang, "Intrinsic organization of the anesthetized brain," *The Journal of Neuroscience*, vol. 32, no. 30, pp. 10183–10191, 2012.

[17] A. J. Schwarz, A. Danckaert, T. Reese et al., "A stereotaxic MRI template set for the rat brain with tissue class distribution maps and co-registered anatomical atlas: application to pharmacological MRI," *NeuroImage*, vol. 32, no. 2, pp. 538–550, 2006.

[18] K. Kobayashi, R. Fukabori, and K. Nishizawa, "Chapter seven - neural circuit mechanism for learning dependent on dopamine transmission: roles of striatal direct and indirect pathways in sensory discrimination," in *Advances in Pharmacology*, L. E. Eiden, Ed., pp. 143–153, Academic Press, 2013.

[19] D. M. Lovinger and B. N. Mathur, "Chapter 10 - endocannabinoid signaling in the striatum," in *Handbook of Behavioral Neuroscience*, H. Steiner and K. Y. Tseng, Eds., pp. 197–215, Elsevier, 2016.

[20] S. L. Hawes, R. C. Evans, B. A. Unruh et al., "Multimodal plasticity in dorsal striatum while learning a lateralized navigation task," *The Journal of Neuroscience*, vol. 35, no. 29, pp. 10535–10549, 2015.

[21] M. X. Zheng, X. Y. Hua, S. Jiang, Y. Q. Qiu, Y. D. Shen, and W. D. Xu, "Contralateral peripheral neurotization for a hemiplegic hindlimb after central neurological injury," *Journal of Neurosurgery*, vol. 128, no. 1, pp. 304–311, 2018.

[22] G. Muir, *Locomotion in the Behavior of the Laboratory Rat*, I. Q. Whishaw and B. Kolb, Eds., Oxford University Press, Oxford, 2005.

[23] P. J. Zink and B. A. Philip, "Cortical plasticity in rehabilitation for upper extremity peripheral nerve injury: a scoping review," *American Journal of Occupational Therapy*, vol. 74, pp. 7401205030p1–7401205030p15, 2020.

[24] C. B. Mohanty, D. Bhat, and B. I. Devi, "Role of central plasticity in the outcome of peripheral nerve regeneration," *Neurosurgery*, vol. 77, no. 3, pp. 418–423, 2015.

[25] J. Xu and J. T. Wall, "Rapid changes in brainstem maps of adult primates after peripheral injury," *Brain Research*, vol. 774, no. 1-2, pp. 211–215, 1997.

[26] J.-X. Wu, L. Chen, F. Ding, L.-Z. Chen, and Y.-D. Gu, "mRNA expression characteristics are different in irreversibly atrophic intrinsic muscles of the forepaw compared with reversibly atrophic biceps in a rat model of obstetric brachial plexus palsy (OBPP)," *Journal of Muscle Research and Cell Motility*, vol. 37, no. 1-2, pp. 17–25, 2016.

[27] C. Kachramanoglou, T. Carlstedt, M. Koltzenburg, and D. Choi, "Long-term outcome of brachial plexus reimplantation after complete brachial plexus avulsion injury," *World Neurosurgery*, vol. 103, pp. 28–36, 2017.

[28] M. Htut, P. Misra, P. Anand, R. Birch, and T. Carlstedt, "Pain phenomena and sensory recovery following brachial plexus avulsion injury and surgical repairs," *Journal of Hand Surgery*, vol. 31, no. 6, pp. 596–605, 2006.

Hindawi
Neural Plasticity
Volume 2021, Article ID 8815144, 11 pages
https://doi.org/10.1155/2021/8815144

*Research Article*

# Altered Topological Properties of Grey Matter Structural Covariance Networks in Complete Thoracic Spinal Cord Injury Patients: A Graph Theoretical Network Analysis

**Wen-Li Wang,[1] Yu-Lin Li,[2] Mou-Xiong Zheng,[3] Xu-Yun Hua,[3] Jia-Jia Wu,[4] Fei-Fei Yang,[5] Nan Yang,[5] Xia He,[1] Li-Juan Ao,[1] and Jian-Guang Xu[2,4]**

[1]*School of Rehabilitation, Kunming Medical University, Yunnan, China*
[2]*Department of Rehabilitation Medicine Science, Shanghai University of Traditional Chinese Medicine, Shanghai, China*
[3]*Department of Traumatology and Orthopedics, Yueyang Hospital of Integrated Traditional Chinese and Western Medicine, Shanghai University of Traditional Chinese Medicine, Shanghai, China*
[4]*Department of Rehabilitation Medicine, Yueyang Hospital of Integrated Traditional Chinese and Western Medicine, Shanghai University of Traditional Chinese Medicine, Shanghai, China*
[5]*The Second Affiliated Hospital of Kunming Medical University, Yunnan, China*

Correspondence should be addressed to Li-Juan Ao; aolijuan@kmmu.edu.cn and Jian-Guang Xu; xjg@shutcm.edu.cn

Received 5 August 2020; Revised 12 January 2021; Accepted 16 January 2021; Published 2 February 2021

Academic Editor: Feng Liu



*Purpose*. This study is aimed at investigating brain structural changes and structural network properties in complete spinal cord injury (SCI) patients, as well as their relationship with clinical variables. *Materials and Methods*. Structural MRI of brain was acquired in 24 complete thoracic SCI patients (38.50 ± 11.19 years, 22 males) within the first postinjury year, while 26 age- and gender-matched healthy participants (38.38 ± 10.63 years, 24 males) were enrolled as control. The voxel-based morphometry (VBM) approach and graph theoretical network analysis based on cross-subject grey matter volume- (GMV-) based structural covariance networks (SCNs) were conducted to investigate the impact of SCI on brain structure. Partial correlation analysis was performed to explore the relationship between the GMV of structurally changed brain regions and SCI patients' clinical variables, including injury duration, injury level, Visual Analog Scale (VAS), American Spinal Injury Association Impairment Scale (AIS), International Classification of Functioning, Disability and Health (ICF) scale, Self-rating Depression Scale (SDS), and Self-rating Anxiety Scale (SAS), after removing the effects of age and gender. *Results*. Compared with healthy controls, SCI patients showed higher SDS score ($t = 4.392$ and $p < 0.001$). In the VBM analysis, significant GMV reduction was found in the left middle frontal cortex, right superior orbital frontal cortex (OFC), and left inferior OFC. No significant difference was found in global network properties between SCI patients and healthy controls. In the regional network properties, significantly higher betweenness centrality (*BC*) was noted in the right anterior cingulum cortex (ACC) and left inferior OFC and higher nodal degree and efficiency in bilateral middle OFCs, while decreased *BC* was noted in the right putamen in SCI patients. Only negative correlation was found between GMV of right middle OFC and SDS score in SCI patients ($r = -0.503$ and $p = 0.017$), while no significant correlation between other abnormal brain regions and any of the clinical variables (all $p > 0.05$). *Conclusions*. SCI patients would experience depressive and/or anxious feelings at the early stage. Their GMV reduction mainly involved psychology-cognition related rather than sensorimotor brain regions. The efficiency of regional information transmission in psychology-cognition regions increased. Greater GMV reduction in psychology region was related with more severe depressive feelings. Therefore, early neuropsychological intervention is suggested to prevent psychological and cognitive dysfunction as well as irreversible brain structure damage.

## 1. Introduction

The global incidence of spinal cord injury (SCI) is 250,000 to 500,000 every year, and the major etiology is trauma, including road traffic injuries, falls, and violence, which mostly occurs in males [1, 2]. SCI is a kind of permanent neurological disorders characterized by a wide range of dysfunctions in motor, sensory, and autonomic nervous systems below the level of injury. It not only reduces patients' self-efficacy and the quality of life (QoL), but also leads to structural and functional brain reorganization.

The underlying pathophysiological process of SCI consists of primary and secondary phases [3]. The primary phase is the initial injury suffered upon impact, leading the direct mechanical injury for some neurons [4]. Because most of the posttraumatic neurochemical mediators of secondary injury may act as neurodestructive compounds, the secondary phase mainly referred to the progressive neurodegeneration, including autophagy and apoptosis at sites that are distant to the vicinity of primary injury [5–8]. These morphological changes may play an important role in the pathophysiology of the brain cortex and could be directly examined by immunohistochemical techniques [9]. However, it is impossible to apply immunohistochemical techniques in human beings, which makes it difficult to evaluate structural changes in human's brain following SCI.

Structural magnetic resonance imaging (MRI) is a noninvasive technique that allows direct access to the structural changes of the human brain. Voxel-based morphometry (VBM) analysis is a valid and spatially unbiased automated method that quantifies structural changes in white and gray matter volume (WMV and GMV) in living human brain [10]. Both adaptive and maladaptive reorganization may occur following SCI [11]. Previous studies revealed that SCI reduced the GMV in multiple brain regions, including the primary motor cortex (M1) [12, 13], primary sensory cortex (S1) [14, 15], supplemental motor area (SMA) [16], inferior frontal cortex [17], bilateral orbital frontal cortices (OFCs), dorsal anterior cingulate cortex (ACC), bilateral anterior insular cortices, and right superior temporal gyrus [14, 18]. But mere morphometric analysis may be inadequate to uncover the structural reorganization mechanisms [19]. In the present study, we reported a covariant change of structural network in a group of subjects, which may provide a new perspective for this issue.

Structural covariance network (SCN) constructed from cross-subject morphometric correlations is another useful method to explore the structural reorganization mechanisms in living human brain. Structural covariances are defined as the interindividual differences in the morphology of one brain region covary with other brain regions. SCNs are constructed generally with one of three experimental approaches including seed-based analysis, principal component analysis, and graph theoretical network analysis [20]. Graph theoretical network analysis is a useful analytic tool in studying brain structural network [21]. The topological properties of SCNs including global and regional covariance parameters could be explored accordingly [22]. The graph theoretical network analysis of SCNs has been widely used in neurodegenerative diseases (e.g., Parkinson disease [23, 24] and Alzheimer disease [25]) and psychological diseases (e.g., obsessive-compulsive disorder [26, 27], schizophrenia [28] and major depression [29]). The brain morphometric and topological properties in these diseases were found rearranged, providing a fundamental for further improvement of clinical diagnose and specific treatments. How the human brain reacts to the disconnection of motor efferent and sensory afferent after SCI has been attracting more and more attention. Graph theoretical network analysis has been applied in resting-state functional MRI (rs-fMRI) [26, 27] and electroencephalography (EEG) studies [30] in SCI patients. However, to our knowledge, previous studies more focused on functional network changes [31–33]. The alterations of the topological properties of SCNs in brain at the early stage following SCI are largely unknown.

In the present study, we aimed to investigate the GMV changes with VBM analysis and to estimate topological properties of GMV-based SCNs using graph theoretical network analysis by characterizing and comparing the graph theoretical metrics between SCI patients and healthy controls. The potential correlation between GMV of structurally changed brain regions and clinical variables will also be explored. Combination of structural and structural covariance network information may provide more comprehensive knowledge about how brain reorganized after SCI. It may also be helpful to modify current strategy of rehabilitation sessions by providing more accurate and specific trainings for SCI patients at early stage to prevent irreversible brain structural changes.

## 2. Materials and Methods

*2.1. Participants.* From November 2018 to December 2019, we recruited 24 patients with complete thoracic SCI ($38.50 \pm 11.19$ years, 22 males) from the Department of Rehabilitation, the Second Affiliated Hospital of Kunming Medical University. And 26 healthy controls ($38.38 \pm 10.63$ years, 24 males) were enrolled in this study. SCI patients underwent cross-sectional evaluation of clinical assessments and MR scanning. Age- and sex-matched healthy controls were recruited from the community. Inclusion criteria of SCI patients are as follows: (1) age between 20 and 60 years old, no gender limitation; (2) complete SCI (AIS score = A); (3) traumatic SCI at thoracic level; (4) with a duration of less than 1 year from injury. Participants who had a history of traumatic brain injury, brain deformity, mental illness, epilepsy, cognitive impairment, or contraindications of MR scanning were excluded.

The study protocol was approved by the Ethics Committee of the Second Affiliated Hospital of Kunming Medical University, Yunnan, China (No.: FEY-BG-39-2.0). The purposes and procedures of this study were explained to all of the participants at recruitment. All participants provided written informed consent before enrolment.

*2.2. Clinical Assessments*

*2.2.1. American Spinal Injury Association Impairment Scale (AIS).* AIS (https://asia-spinalinjury.org/) is usually used to

define severity of SCI injury and the level of neurological impairment. It contains three components including myotomal-based motor assessment, dermatomal-based sensory assessment, and anorectal assessment [34].

*2.2.2. Psychological Impact.* Self-rating Depression Scale (SDS) and Self-rating Anxiety Scale (SAS) were used for quantifying depressive and anxious status, respectively [35, 36]. Both scales are 20-item scales associated with affective and somatic symptoms (10 negative and 10 positive experience items in SDS; 15 negative and 5 positive experience items in SAS), with a normalized total score ranged from 25 to 100. The score of SDS/SAS ranges 50-59, 60-69, and ≥70 indicated mild-moderate, moderate-severe, and severe depression/anxiety, respectively [37, 38].

*2.2.3. Pain.* Visual analog scale (VAS) is a 10 cm line with the endpoints labeled "no pain" (score of 0) and "worst possible pain" (score of 10), with a higher score of VAS indicates greater pain [39]. All of SCI patients were asked to mark the VAS according to their pain intensity, and the score was recorded by measuring the distance from 0 to the mark (cm).

*2.2.4. Functional Impairment.* International Classification of Functioning, Disability and Health (ICF) is a framework for the description, assessment, and classification of ability and disability in the areas of *body functions* and *body structures*, *activities*, *participation*, *personal factors*, and *environmental factors* [40]. The "Spinal Cord Injury Long-Term Brief Cord Set" was used to describe most relevant functionality in SCI patients. It includes 33 items, and each item has 7 categories. A higher score indicates greater impairment of functionality [41].

*2.3. MRI Acquisition.* The MR images were collected by a 3T Philips MRI system with an 8-channel phase-array head coil. A three-dimensional magnetization-prepared rapid gradient echo sequence (MPRAGE) was applied to obtain high-resolution 3D structural T1-weighted images in sagittal orientation. The imaging parameters were as follows: repetition time (TR) = 7.87 ms, echo time (TE) = 3.83 ms, flip angle (FA) = 15°, field of view (FOV) = $256 \times 256\,\text{mm}^2$, matrix size = $256 \times 256$, and slice thickness = 1 mm, resulting an isotropic voxel size of $1 \times 1 \times 1\,\text{mm}^3$.

*2.4. Structural Data Preprocessing and Whole-Brain VBM Analysis.* The VBM analysis was performed using the VBM8 toolbox in the Statistical Parametric Mapping software (SPM8, Wellcome Department of Cognitive Neurology, UCL, http://www.fil.ion.ucl.ac.uk/spm/) implemented in the Matlab environment (2014a, The MathWorks Inc.). After converting DICOM files into NIfTI images, all T1-weighted images were visually checked and poor-quality images with apparent artifacts would be excluded if any. And then, the anatomic image of each participant was reoriented so that the origin approximated the anterior commissure and the orientation approximated Montreal Neurological Institute (MNI) space. The T1-weighted structural images were segmented into grey matter (GM), white matter (WM), and cerebrospinal fluid (CSF) components. The GM images were spatially normalized into the standard MNI space by applying the Diffeomorphic Anatomical Registration using Exponentiated Lie (DARTEL) algorithm. The normalized GM component was modulated by nonlinear transform only and then smoothed with Gaussian kernel of full width at half-maximum (FWHM) (8 mm). The GM, WM, and CSF volumes were obtained separately, based on the segmented images. The total intracranial volume (TIV) was calculated as the sum of all the GM, WM, and CSF volumes.

*2.5. Structural Covariance Network Construction.* Pearson correlation was used to compute structural covariance based on GMV. SCN construction and network property analysis were processed with Brain Connectivity Toolbox (BCT, version 2017-15-01, http://www.brain-connectivity-toolbox.net/). The process of SCN construction is shown in Figure 1.

Regional parcels for GMV were extracted based on the Automatic Anatomic Labeling (AAL) atlas, including 90 region of interests (ROIs) [42]. Each of all the 90 AAL brain regions was considered as a node of a network. The effects of age and gender were regressed out using generalized linear model before network construction. The edge of the network was defined as the Pearson correlation coefficient of the normalized GMV between all pairs of the 90 regions across the participants in the same group [43]. Thus, a single network was generated for each group. To ensure that all the resultant networks had the same number of edges, the range of sparsity was set for each correlation matrix, which allowed prominent small-world properties in brain networks to be observed. According to the literature, we restricted each absolute correlation matrix to a specific range of sparsity (0.05-0.5) at an interval of 0.01 [44, 45]. Through this thresholding procedure, we obtained a set of undirected and unweighted binarized networks. Graph theoretical network analysis was then used to investigate the topological properties of whole-brain structural networks in SCI patients and healthy controls.

*2.5.1. Global Network Analysis.* Topological properties of global network including clustering coefficient, characteristic path length, small-worldness index, global efficiency and local efficiency were used to characterize the global topological organization of SCNs (Details in the Supplemental Materials).

*2.5.2. Regional Network Analysis.* Three topological properties of regional network including degree ($D$), nodal efficiency ($E_{\text{nod}}$), and betweenness centrality ($BC$) were used to demonstrate the nodal characteristics of the SCNs [46]. Nodal degree $D$ is defined as the sum of all direct connections between a given node and other nodes, and the index $D$ is used to measure the importance of a node. Nodal efficiency ($E_{\text{nod}}$) is the mean reciprocal of the shortest path length between a given node and all the others, and $E_{\text{nod}}$ is an evaluation for regional connectivity. The $BC$ is defined as the fraction of all shortest paths in the network that passed through a given node, and $BC$ is used to find important anatomical or functional connections.

*2.6. Statistical Analysis*

*2.6.1. Baseline Characteristics and Clinical Assessment.* The baseline characteristics and clinical assessment data were

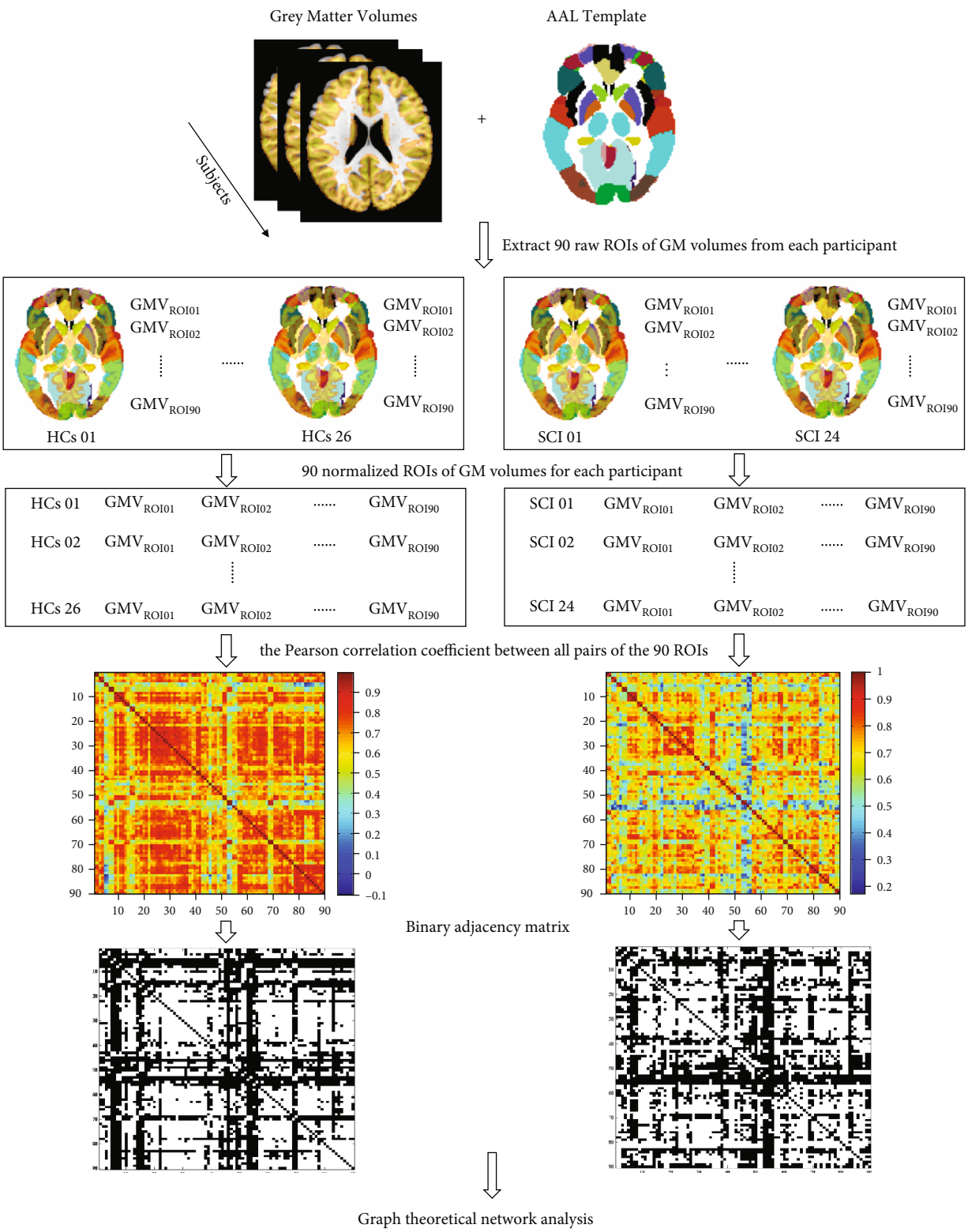


Figure 1: The diagram of structural covariance network construction and analysis. AAL: anatomical automatic labeling; GMV: grey matter volume: ROI: region of interest; HCs: healthy controls; SCI: spinal cord injury.

analyzed using the statistical package IBM SPSS Statistics V21 (SPSS Inc., Chicago, IL, USA). Data were assessed for normality using the Kolmogorov-Smirnov test. Mean (SD, standard deviation) was used to describe normally distributed data, and intergroup differences were analyzed using two-sample $t$-test.

*2.6.2. Voxel-Based Morphometry Analysis.* GMV differences between SCI patients and healthy controls were compared using voxel-wise two-sample $t$-test with the function of "second level model" in SPM8. The multiple comparison was corrected by voxel-wise family-wise error (FWE) method with significance level of $p < 0.05$. The results of VBM statistical analysis were visualized using the MRIcroGL (Version 11, https://www.mccauslandcenter.sc.edu/mricrogl/) and GraphPad (Inc. Prism Version 7, US, https://www.graphpad.com/).

*2.6.3. Graph Theoretical Network Analysis.* Intergroup difference of structural covariance network topological properties was analyzed by using nonparametric permutation test with 5000 repetitions. In each permutation cycle, the GMV of ROI for each participant was randomly assigned to either SCI or healthy control group to form two new groups with the same size in each group as the original ones. Then, the randomized, undirected, and unweighted binarized network of each group was constructed based on the new dataset. The network properties in each permutation cycle were calculated across all sparsity thresholds, resulting a corresponding area under the curve (AUC) over the sparsity range of both groups. Intergroup differences of 5000 AUCs constituted permutation distribution under null hypothesis; the $p$ value was obtained according to the position of the actual intergroup difference of AUC of network properties at the permutation distribution. The significance level for global network analysis was set at $p < 0.05$. And the significance level for regional network analysis was set at $p < 0.05$ after FDR correction for multiple comparisons.

*2.7. Partial Correlation Analysis.* Partial correlation analysis using the statistical package IBM SPSS Statistics V21 (SPSS Inc., Chicago, IL, USA) was conducted at ROI-wise to explore potential correlation between the GMV and injury duration, injury level, VAS, AIS, ICF scale, SDS, and SAS, respectively, after removing the effects of age and gender. The selection of ROIs was based on the brain regions presented intergroup differences both in VBM and network analyses. The results of partial correlation analysis were also visualized using the statistical package IBM SPSS Statistics V21 (SPSS Inc., Chicago, IL, USA).

## 3. Results

*3.1. Demographic Characteristics and Clinical Details.* The interval from injury to administration to our clinic was 5.58 ± 3.15 (mean ± SD) months (ranged from 1 to 11 months). The motor and sensory score were 50.46 ± 4.80 and 126.19 ± 23.38, respectively. The VAS score of SCI patients was 3.96 ± 2.46 (mean ± SD). Detailed information of demographic characteristics and clinical variables of SCI patients are listed in Table 1. The intergroup differences of demographic characteristics and clinical variables are listed in Table 2. There was no intergroup difference regarding age ($t = 0.037$ and $p = 0.970$) or gender ($\chi^2 = 0.007$ and $p = 0.933$) or SAS score ($t = 0.988$ and $p = 0.328$). The SDS score of SCI patients was higher than healthy controls ($t = 4.392$ and $p < 0.001$). In the preprocessing procedure, all the MR images were qualified and no participant was excluded from subsequent analysis.

*3.2. Reduction of GMV in SCI Patients.* Voxel-wise two-sample $t$-test was thresholded at voxel-wise FWE correction with $p < 0.05$. The results of VBM analysis revealed that compared with healthy controls, SCI patients showed significant GMV decrease in the left middle frontal cortex, right superior orbital frontal cortex (OFC), and left inferior OFC (Figure 2). No brain region showed greater GMV in SCI patients than the healthy controls. The cluster size, peak $T$ value, and peak MNI coordinates of regions with decreased GMV are listed in Table 3.

*3.3. Differences of Topological Properties of SCNs between SCI Patients and Healthy Controls.* There was no significant difference in topological properties of global network between SCI patients and healthy controls (all $p > 0.05$) (Supplementary Materials, Table S1, Figure S1).

Intergroup differences of the regional network parameters are listed in Table 4. Compared with healthy controls, SCI patients showed significantly higher *BC* in the right ACC and left inferior OFC and higher degree and efficiency in bilateral middle OFCs. *BC* in the right putamen in SCI patients was significantly lower than that in healthy controls.

*3.4. Relationship between GMV and SDS Score.* Partial correlation analysis only showed negative correlation between GMV in the right middle OFC and the SDS score in SCI patients ($r = -0.503$ and $p = 0.017$, Figure 3). However, no significant correlation was found between GMV of the rest ROIs (i.e., left middle frontal cortex, left inferior OFC, right superior OFC, right ACC, left inferior OFC, left middle OFC, and right putamen) and either of the injury duration, injury level, VAS, AIS, ICF scale, SDS score, or SAS score in SCI patients (all $p > 0.05$).

## 4. Discussion

In this study, the VBM and graph theoretical network analyses were used to demonstrate the alterations of GMV and GMV-based SCNs in complete thoracic SCI patients within one postinjury year, and partial correlation analysis was used to explore the association between GMV of structurally changed brain regions and clinical variables. In these patients, we only found GMV reduction in the left middle frontal cortex, left inferior OFC, and right superior OFC, which play an important role in the regulation of psychological or cognitive functions [47–49]. Compared with healthy controls, the GMV-based SCNs in SCI patients showed significant changes of topological properties in regional network evidenced by increased *BC* in the right ACC and left inferior OFC and nodal degree and efficiency in bilateral middle OFCs, as well as decreased *BC* in the right putamen. In addition, the GMV of right middle OFC was negatively associated with score of SDS. These findings may provide new insights into the structural reorganization of brain after SCI at the early stage.

In the present study, the GMV in psychology-cognition-related brain regions including frontal cortex and OFC significantly decreased in SCI patients compared with healthy

Table 1: Demographic characteristics and clinical variables of the spinal cord injury patients.

| No. | Age (years) | Gender | Etiology | Duration (month) | Injury level | AIS | Motor (0-100) | Sensory (0-224) | VAS | ICF scale |
|---|---|---|---|---|---|---|---|---|---|---|
| 1 | 41 | M | Fall injury | 6 | T8 | A | 50 | 125 | 5 | 120 |
| 2 | 46 | F | Crushing injury | 9 | T7 | A | 50 | 123 | 5 | 138 |
| 3 | 40 | M | Fall injury | 9 | T10 | A | 53 | 141 | 6 | 112 |
| 4 | 52 | M | Vehicle accident | 5 | T10 | A | 50 | 140 | 7 | 121 |
| 5 | 19 | M | Crushing injury | 10 | T11 | A | 56 | 82 | 6 | 121 |
| 6 | 43 | M | Crushing injury | 3 | T12 | A | 50 | 156 | 3 | 78 |
| 7 | 23 | M | Fall injury | 6 | T10 | A | 52 | 136 | 4 | 100 |
| 8 | 28 | M | Fall injury | 9 | T11 | A | 53 | 148 | 5 | 105 |
| 9 | 53 | M | Fall injury | 1 | T11 | A | 50 | 146 | 4 | 100 |
| 10 | 23 | M | Crushing injury | 10 | T9 | A | 50 | 132 | 6 | 125 |
| 11 | 32 | M | Fall injury | 3 | T10 | A | 52 | 141 | 0 | 120 |
| 12 | 43 | M | Fall injury | 6 | T11 | A | 54 | 148 | 2 | 107 |
| 13 | 33 | M | Fall injury | 3 | T11 | A | 52 | 148 | 10 | 124 |
| 14 | 39 | M | Fall injury | 4 | T3 | A | 50 | 86 | 3 | 140 |
| 15 | 29 | M | Fall injury | 6 | T11 | A | 52 | 149 | 3 | 142 |
| 16 | 61 | F | Fall injury | 1 | T7 | A | 42 | 112 | 2 | 145 |
| 17 | 44 | M | Vehicle accident | 2 | T3 | A | 50 | 88 | 2 | 129 |
| 18 | 49 | M | Fall injury | 7 | T11 | A | 50 | 148 | 6 | 76 |
| 19 | 33 | M | Vehicle accident | 2 | T11 | A | 60 | 78 | 3 | 126 |
| 20 | 50 | M | Fall injury | 11 | T10 | A | 60 | 143 | 8 | 136 |
| 21 | 34 | M | Fall injury | 3 | T9 | A | 50 | 132 | 3 | 125 |
| 22 | 43 | M | Vehicle accident | 10 | T6 | A | 42 | 108 | 3 | 122 |
| 23 | 46 | M | Fall injury | 4 | T10 | A | 52 | 136 | 0 | 124 |
| 24 | 20 | M | Fall injury | 4 | T6 | A | 40 | 100 | 0 | 129 |

Duration refers to the interval between injury and entry to this study. Injury level refers to the neurological level of spinal cord injury. AIS scale rates the severity of spinal cord injury: A, complete—no sensory or motor function is preserved in sacral segments S4–S5; B, incomplete—sensory but not motor function is preserved below the neurological level and extends through sacral segments S4–S5; C, incomplete—motor function is preserved below the neurological level, and more than half of the key muscles below the neurological level have a muscle grade of <3; D, incomplete—motor function is preserved below the neurological level, and at least half of the key muscles below the neurological level have a muscle grade of >3. M: male; F: female; AIS: American Spinal Injury Association Impairment Scale; VAS: visual analog scale; SDS: Self-rating Depression Scale (SDS); SAS: Self-rating Anxiety Scale; ICF: International Classification of Functioning, Disability and Health.

Table 2: Intergroup differences of demographic characteristics and clinical variables.

| | SCI patients ($n = 24$) | Healthy controls ($n = 26$) | $t$ / $\chi^2$ | $p$ value |
|---|---|---|---|---|
| Age (years), mean (SD) | 38.50 (11.19) | 38.38 (10.63) | 0.037 | 0.970 |
| SDS, mean (SD) | 55.65 (8.74) | 47.47 (3.87) | 4.392 | <0.001 |
| SAS, mean (SD) | 48.02 (7.14) | 46.41 (4.65) | 0.988 | 0.328 |
| Gender, male no. (%) | 22 (92%) | 24 (92%) | 0.007 | 0.933 |

SCI: spinal cord injury; SD: standard deviation; SDS: Self-rating Depression Scale; SAS: Self-rating Anxiety Scale.

controls. But majority of previous studies found structural changes in sensorimotor brain regions (M1 [12], S1 [14, 15], and SMA [16]), promoting the development and application of rehabilitation sessions including sensory and motor trainings. The sensory and motor trainings can provide repetitive stimulations to corresponding brain regions, which may potentially prevent or postpone irreversible structural changes in these patients. However, there are also studies [18, 50] reported GMV changes in nonsensorimotor brain regions after SCI, including frontal cortex and OFC, which was consistent with our findings. Frontal cortex plays a critical role in regulation of cognition [49], and structural abnormalities in OFC have also been found in psychological diseases including depression and anxiety [47, 48]. Furthermore, there is close relationship between psychological and cognitive functions [51]. Psychological and cognitive interventions were inadequate or even neglected in many SCI patients. According to the theory of activity-dependent brain reorganization [52], the potential reason why GMV reduction after SCI mainly involved psychology-cognition related rather than sensorimotor brain

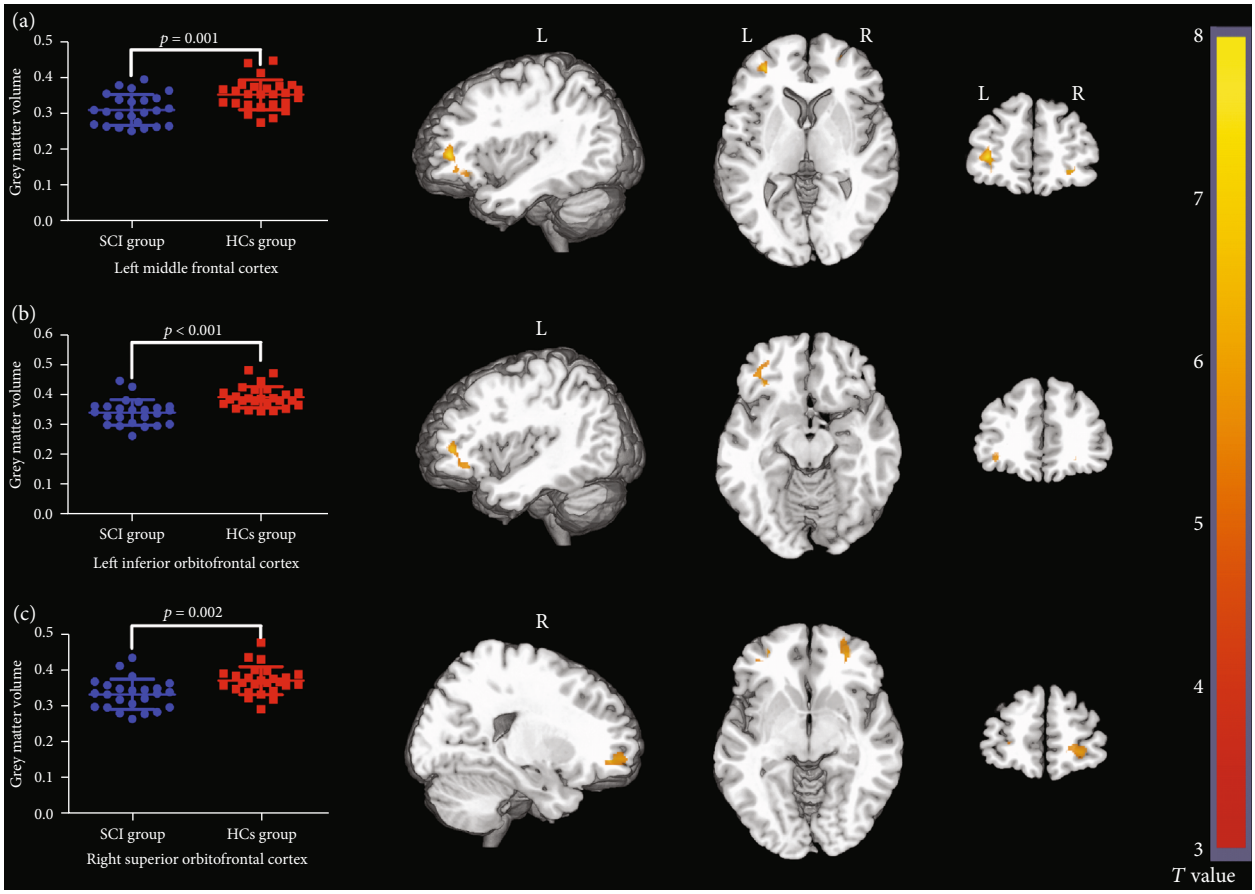


Figure 2: The results of voxel-based morphometry (VBM) analysis. Regions in (a) left middle frontal cortex, (b) left inferior orbitofrontal cortex, and (c) right superior orbitofrontal cortex showed significantly lower grey matter volume (GMV) in spinal cord injury (SCI) patients compared with healthy controls (HCs) (voxel-wise FWE correction with $p < 0.05$). SCI: spinal cord injury; HCs: healthy controls; L: left; R: right.

regions might be that physicians focused more on sensory and motor trainings, and psychological and/or cognitive interventions might be relatively insufficient.

This study also investigated SCI-related alteration of topological properties of global network. The results indicated that structural network segregation and integration in brain were not changed in SCI patient in the first postinjury year. Similar to GMV, the results of regional network analysis showed that SCI also led to significant changes of topological properties of regional structural network in nonsensorimotor brain regions. Nodes with high structural nodal degree and *BC* indicate that nodes are highly interactive with the other nodes in the regional structural network [46]. The present findings indicated that the information transfer through bilateral middle OFCs, right ACC, and left inferior OFC were more efficient in SCI patients than healthy controls, but less efficient in the right putamen. Structural alterations in psychology-related brain region of present study were consistent with clinical findings that almost all of the SCI patients in the present study experienced mild-to-severe depressive feelings. And we did find that greater GMV reduction in psychology-related brain region was related with more severe depressive feelings. Plenty of studies have focused on the alterations of functional network in brain after SCI, instead of structural network [31–33]. However, SCNs were more commonly applied in psychological diseases, and higher *BC* was also noted in the OFC in depression [53]. It is a common knowledge that ACC is activated in pain [54], which was consistent with the present results that almost all of SCI patients experienced mild-to-severe neuropathic pain. Furthermore, the presence and severity of pain may also be related with depressive and anxious feelings [55]. Putamen is one of the important components of the striatum, which is known for motor coordination [56]. The lacking of functional walking and running in complete thoracic SCI patients may have reduced the demand of coordination functions in bilateral lower extremities or between upper and lower extremities.

According to above findings, SCI patients had impairments both in psychological status and alterations in psychology-related brain region. It involves a complex issue that how a nonbrain disease (e.g., SCI) impacts the brain structure. It may potentially be summed up in two aspects. Firstly, the development of psychoneuroimmunology demonstrates that there is a bilateral connection between depression and inflammation [57]. The inflammation associated with depression does not involve a major destruction of the blood-brain barrier (BBB) but primarily activates localized immune mechanisms inducing the activation of central sympathetic nervous

Table 3: Regions showing significantly decreased grey matter volume (GMV) in spinal cord injury (SCI) patients.

| Regions of decreased GMV | Hemisphere side | Cluster size (voxels) | Peak $T$ value | Peak MNI coordinate (mm) | | |
|---|---|---|---|---|---|---|
| | | | | $x$ | $y$ | $z$ |
| Middle frontal cortex | L | 296 | 7.762 | -33 | 47 | 3 |
| Inferior OFC | L | 200 | 5.898 | -35 | 30 | -11 |
| Superior OFC | R | 126 | 6.474 | 30 | 48 | -6 |

GMV: grey matter volume; OFC: orbitofrontal cortex; L: left; R: right.

Table 4: Brain regions are showing significant differences in any of the three nodal characteristics.

| Brain region | $p$ value | | |
|---|---|---|---|
| | BC | Degree | Efficiency |
| SCI patients>healthy controls | | | |
| Right ACC | 0.008 | - | - |
| Left inferior OFC | <0.001 | - | - |
| Left middle OFC | - | 0.002 | 0.006 |
| Right middle OFC | - | 0.002 | 0.008 |
| SCI patients<healthy controls | | | |
| Right putamen | 0.004 | - | - |

BC: betweenness centrality; SCI: spinal cord injury; ACC: anterior cingulum cortex; OFC: orbitofrontal cortex.

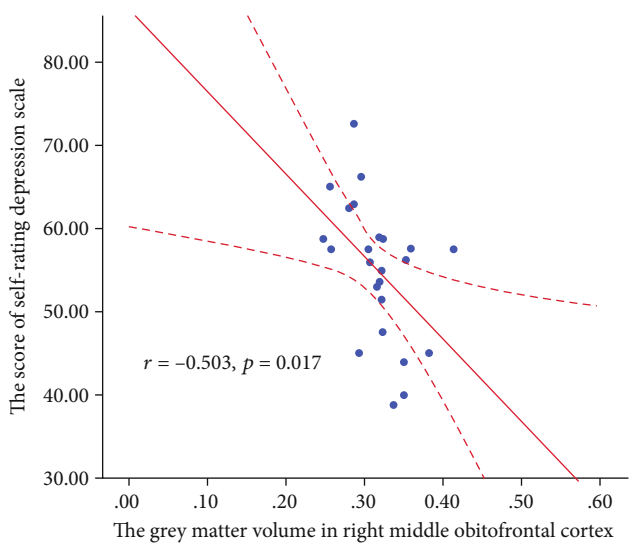


Figure 3: The correlation between grey matter volume (GMV) and clinical variables in spinal cord injury (SCI) patients. The partial correlation analysis revealed a negative correlation between GMV in the right middle orbitofrontal cortex (OFC) and the score of Self-rating Depression Scale (SDS) in SCI patients ($r = -0.503$ and $p = 0.017$).

system, the hypothalamic-pituitary-adrenal (HPA) axis, and proinflammatory mediators [58]. Secondly, brain-derived neurotrophic factor (BDNF) is a secretory protein in the neurotrophin family and is a crucial mediator of development of axon and pruning of dendrite [59]. It was proved that BDNF was involved in both depression and anxiety [60, 61]. The expression of BDNF was found decreased in dendrites, impairing structural integrity with retraction of distal dendrites of primary cortical neurons and decreased dendritic complexity [62]. Thus, the influence of psychological status on brain structure might be the potential way that SCI induced structural reorganization in brain.

Therefore, SCI not only impairs the physical functions, but also the psychological status in SCI patients. However, current rehabilitation strategies mainly focus on sensory and motor trainings, which might prevent irreversibly structural brain changes in sensorimotor brain regions. Previous studies more focused on functional alteration instead of structural reorganization after SCI, especially in psychology-cognition-related brain regions. However, SCI patients also have an increased risk of psychological problem that anxiety and depression are inevitable consequences after SCI [63–65]. The negative influence of depression and anxiety would not significantly diminish even over 2 years [66]. Furthermore, the cognitive impairment also exists and affects the QoL of SCI patients and their caregivers [51]. The present study emphasized the importance of psychological and cognitive evaluations for SCI patients and neuropsychological interventions including cognitive behavioral therapy (CBT), psychoeducation, motivational interviewing, and interpersonal therapy at the early stage following SCI.

## 5. Conclusion

In summary, SCI has profound effects on psychological status, as well as brain structures including GMV and SCNs within one postinjury year. GMV reduction after SCI mainly involved psychology-cognition-related brain regions rather than sensorimotor brain regions. The efficiency of regional information transmission in psychology-cognition brain regions increased after SCI. Patients may experience depressive and/or anxious feelings at the early stage, and greater GMV reduction in psychology-related brain region was related with more severe depressive feelings. The neuropsychological therapies are suggested to be taken account into the current rehabilitation sessions at the early stage to prevent psychological and cognitive dysfunction as well as irreversible brain structure damage.

## 6. Limitations

The sample size of the present study was relatively small. A cohort with larger samples may be helpful to obtain more information in the future study. The longitudinal comparison

of structural changes between pre- and posttherapies needs further investigation. Longer follow-up duration may be worthwhile to investigate time-dependent effects of SCI. The assessment of cognitive function following SCI is also worth exploring in the future.

## Data Availability

The data used to support the findings of present study are available from the corresponding authors upon request.

## Consent

The study protocol was approved by the Ethics Committee of the Second Affiliated Hospital of Kunming Medical University, Yunnan, China (No.: FEY-BG-39-2.0). All of participants provided written informed consent before enrolment.

## Conflicts of Interest

The authors declare that they have no conflict of interest.

## Authors' Contributions

Wen-Li Wang participated in the conceptualization; methodology was done by Wen-Li Wang; validation was done by Fei-Fei Yang, Nan Yang, and Xia He; formal analysis was performed by Yu-Lin Li, Wen-Li Wang, Jia-Jia Wu, Mou-Xiong Zheng, and Xu-Yun Hua; writing-original draft was done by Yu-Lin Li, Wen-Li Wang, Mou-Xiong Zheng, Xu-Yun Hua, and Jia-Jia Wu; Li-Juan Ao and Jian-Guang Xu contributed to the writing review and editing; all authors read and approved the final manuscript. Wen-Li Wang, Yu-Lin Li, and Mou-Xiong Zheng contributed equally to this work and co-first authors.

## Acknowledgments

This work was supported by the National Key R&D Program of China (Grant No.: 2018YFC2001600), Shanghai Commission of Science and Technology (Grant Nos.: 18511108300, 18441903900, 18441903800, and 19QA1409000), Shanghai "Rising Stars of Medical Talent" Youth Development Program (Grant No.: RY411.19.01.10), and Shanghai Municipal Health Commission (Grant No.: 2018YQ02).

## Supplementary Materials

Table S1: intergroup differences of topological properties of global network. Figure S1: changes in topological properties of global network of spinal cord injury patients and healthy controls as a function of increasing network density. *(Supplementary Materials)*

## References

[1] WHO-World Health Organization, *International Perspectives on Spinal Cord Injury*, WHO Press, Geneva, Switzerland, 2013.

[2] M. J. Devivo, "Epidemiology of traumatic spinal cord injury: trends and future implications," *Spinal Cord*, vol. 50, no. 5, pp. 365–372, 2012.

[3] C. H. Tator and M. G. Fehlings, "Review of the secondary injury theory of acute spinal cord trauma with emphasis on vascular mechanisms," *Journal of Neurosurgery*, vol. 75, no. 1, pp. 15–26, 1991.

[4] S. Quraishe, L. H. Forbes, and M. R. Andrews, "The extracellular environment of the CNS: influence on plasticity, sprouting, and axonal regeneration after spinal cord injury," *Neural Plasticity*, vol. 2018, 18 pages, 2018.

[5] S. K. Ray, C. E. Dixon, and N. L. Banik, "Molecular mechanisms in the pathogenesis of traumatic brain injury," *Histology and Histopathology*, vol. 17, no. 4, pp. 1137–1152, 2002.

[6] K. M. Schoch, S. K. Madathil, and K. E. Saatman, "Genetic manipulation of cell death and neuroplasticity pathways in traumatic brain injury," *Neurotherapeutics*, vol. 9, no. 2, pp. 323–337, 2012.

[7] C. Profyris, S. S. Cheema, D. W. Zang, M. F. Azari, K. Boyle, and S. Petratos, "Degenerative and regenerative mechanisms governing spinal cord injury," *Neurobiology of Disease*, vol. 15, no. 3, pp. 415–436, 2004.

[8] B. C. Hains, J. A. Black, and S. G. Waxman, "Primary cortical motor neurons undergo apoptosis after axotomizing spinal cord injury," *The Journal of Comparative Neurology*, vol. 462, no. 3, pp. 328–341, 2003.

[9] W. S. Ramadan, G. A. Abdel-Hamid, S. Al-Karim, and A. T. Abbas, "Histological, immunohistochemical and ultrastructural study of secondary compressed spinal cord injury in a rat model," *Folia Histochemica et Cytobiologica*, vol. 55, pp. 11–20, 2017.

[10] J. Ashburner and K. J. Friston, "Voxel-based morphometry-the methods," *NeuroImage*, vol. 11, no. 6, pp. 805–821, 2000.

[11] L. Solstrand Dahlberg, L. Becerra, D. Borsook, and C. Linnman, "Brain changes after spinal cord injury, a quantitative meta-analysis and review," *Neuroscience and Biobehavioral Reviews*, vol. 90, pp. 272–293, 2018.

[12] P. Freund, N. Weiskopf, J. Ashburner et al., "MRI investigation of the sensorimotor cortex and the corticospinal tract after acute spinal cord injury: a prospective longitudinal study," *Lancet Neurology*, vol. 12, no. 9, pp. 873–881, 2013.

[13] Y. Höller, A. Tadzic, A. C. Thomschewski et al., "Factors affecting volume changes of the somatosensory cortex in patients with spinal cord injury: to be considered for future neuroprosthetic design," *Frontiers in Neurology*, vol. 8, p. 662, 2017.

[14] R. Nardone, Y. Höller, L. Sebastianelli et al., "Cortical morphometric changes after spinal cord injury," *Brain Research Bulletin*, vol. 137, pp. 107–119, 2018.

[15] P. Freund, N. Weiskopf, N. S. Ward et al., "Disability, atrophy and cortical reorganization following spinal cord injury," *Brain*, vol. 134, no. 6, pp. 1610–1622, 2011.

[16] J. M. Hou, R. B. Yan, Z. M. Xiang et al., "Brain sensorimotor system atrophy during the early stage of spinal cord injury in humans," *Neuroscience*, vol. 266, pp. 208–215, 2014.

[17] K. D. Karunakaran, J. He, J. Zhao et al., "Differences in cortical gray matter atrophy of paraplegia and tetraplegia after complete spinal cord injury," *Journal of Neurotrauma*, vol. 36, no. 12, pp. 2045–2051, 2019.

[18] Q. Chen, W. Zheng, X. Chen et al., "Brain gray matter atrophy after spinal cord injury: a voxel-based morphometry study," *Frontiers in Human Neuroscience*, vol. 11, p. 211, 2017.

[19] V. D. Calhoun and J. Sui, "Multimodal fusion of brain imaging data: a key to finding the missing link(s) in complex mental illness," *Biological Psychiatry: Cognitive Neuroscience and Neuroimaging*, vol. 1, no. 3, pp. 230–244, 2016.

[20] A. Alexander-Bloch, J. N. Giedd, and E. Bullmore, "Imaging structural co-variance between human brain regions," *Nature Reviews. Neuroscience*, vol. 14, no. 5, pp. 322–336, 2013.

[21] O. Sporns, "The human connectome: a complex network," *Annals of the New York Academy of Sciences*, vol. 1224, no. 1, pp. 109–125, 2011.

[22] J. Wang, X. Zuo, and Y. He, "Graph-based network analysis of resting-state functional MRI," *Frontiers in Systems Neuroscience*, vol. 4, pp. 1–14, 2010.

[23] M. C. Wen, H. S. E. Heng, J. L. Hsu et al., "Structural connectome alterations in prodromal and de novo Parkinson's disease patients," *Parkinsonism & Related Disorders*, vol. 45, pp. 21–27, 2017.

[24] J. Fang, H. Chen, Z. Cao et al., "Impaired brain network architecture in newly diagnosed Parkinson's disease based on graph theoretical analysis," *Neuroscience Letters*, vol. 657, pp. 151–158, 2017.

[25] S. Y. Lin, C. P. Lin, T. J. Hsieh et al., "Multiparametric graph theoretical analysis reveals altered structural and functional network topology in Alzheimer's disease," *NeuroImage: Clinical*, vol. 22, article 101680, 2019.

[26] J. Y. Yun, B. PSW, C. Vriend et al., "Brain structural covariance networks in obsessive-compulsive disorder: a graph analysis from the ENIGMA consortium," *Brain*, vol. 143, pp. 684–700, 2020.

[27] T. J. Reess, O. G. Rus, D. A. Gürsel et al., "Network-based decoupling of local gyrification in obsessive-compulsive disorder," *Human Brain Mapping*, vol. 39, no. 8, pp. 3216–3226, 2018.

[28] S. Wang, G. Gong, S. Zhong et al., "Neurobiological commonalities and distinctions among 3 major psychiatric disorders: a graph theoretical analysis of the structural connectome," *Journal of Psychiatry & Neuroscience*, vol. 45, no. 1, pp. 15–22, 2020.

[29] T. Wang, K. Wang, H. Qu et al., "Disorganized cortical thickness covariance network in major depressive disorder implicated by aberrant hubs in large-scale networks," *Scientific Reports*, vol. 6, no. 1, p. 27964, 2016.

[30] V. Fallani Fde, F. Costa Lda, F. A. Rodriguez et al., "A graph-theoretical approach in brain functional networks. Possible implications in EEG studies," *Nonlinear Biomedical Physics*, vol. 4, no. S1, p. S8, 2010.

[31] Y.-S. Min, Y. Chang, J. W. Park et al., "Change of brain functional connectivity in patients with spinal cord injury: graph theory based approach," *Annals of Rehabilitation Medicine*, vol. 39, no. 3, pp. 374–383, 2015.

[32] A. H. Hawasli, J. Rutlin, J. L. Roland et al., "Spinal cord injury disrupts resting-state networks in the human brain," *Journal of Neurotrauma*, vol. 35, no. 6, pp. 864–873, 2018.

[33] M. Kaushal, A. Oni-Orisan, G. Chen et al., "Large-scale network analysis of whole-brain resting-state functional connectivity in spinal cord injury: a comparative study," *Brain Connectivity*, vol. 7, no. 7, pp. 413–423, 2017.

[34] S. Kirshblum and W. Waring, "Updates for the international standards for neurological classification of spinal cord injury," *Physical Medicine and Rehabilitation Clinics of North America*, vol. 25, no. 3, pp. 505–517, 2014.

[35] W. W. K. Zung, "A rating instrument for anxiety disorders," *Psychosomatics*, vol. 12, no. 6, pp. 371–379, 1971.

[36] W. W. K. Zung, "From art to science: the diagnosis and treatment of depression," *Archives of General Psychiatry*, vol. 29, no. 3, pp. 328–337, 1973.

[37] D. A. Dunstan and N. Scott, "Clarification of the cut-off score for Zung's Self-rating Depression Scale," *BMC Psychiatry*, vol. 19, pp. 1–7, 2019.

[38] D. A. Dunstan and N. Scott, "Norms for Zung's Self-rating Anxiety Scale," *BMC Psychiatry*, vol. 20, pp. 1–8, 2020.

[39] H. M. McCormack, D. J. Horne, and S. Sheather, "Clinical applications of visual analogue scales: a critical review," *Psychological Medicine*, vol. 18, no. 4, pp. 1007–1019, 1988.

[40] G. Stucki and G. Grimby, "Applying the ICF in medicine," *Journal of Rehabilitation Medicine. Supplement*, vol. 36, pp. 5-6, 2004.

[41] M. Selb, R. Escorpizo, N. Kostanjsek, G. Stucki, B. Üstün, and A. Cieza, "A guide on how to develop an International Classification of Functioning, Disability and Health Core Set," *European Journal of Physical and Rehabilitation Medicine*, vol. 51, no. 1, pp. 105–117, 2015.

[42] N. Tzourio-Mazoyer, B. Landeau, D. Papathanassiou et al., "Automated anatomical labeling of activations in SPM using a macroscopic anatomical parcellation of the MNI MRI single-subject brain," *NeuroImage*, vol. 15, no. 1, pp. 273–289, 2002.

[43] F. Liu, H. Tian, J. Li, S. Li, and C. Zhuo, "Altered voxel-wise gray matter structural brain networks in schizophrenia: association with brain genetic expression pattern," *Brain Imaging and Behavior*, vol. 13, no. 2, pp. 493–502, 2019.

[44] E. T. Bullmore and D. S. Bassett, "Brain graphs: graphical models of the human brain connectome," *Annual Review of Clinical Psychology*, vol. 7, no. 1, pp. 113–140, 2011.

[45] D. J. Watts and S. H. Strogatz, "Collective dynamics of 'small-world' networks," *Nature*, vol. 393, no. 6684, pp. 440–442, 1998.

[46] M. Rubinov and O. Sporns, "Complex network measures of brain connectivity: uses and interpretations," *NeuroImage*, vol. 52, no. 3, pp. 1059–1069, 2010.

[47] P. H. Rudebeck and E. L. Rich, "Orbitofrontal cortex," *Current Biology*, vol. 28, no. 18, pp. R1083–R1088, 2018.

[48] S. M. Grieve, M. S. Korgaonkar, S. H. Koslow, E. Gordon, and L. M. Williams, "Widespread reductions in gray matter volume in depression," *NeuroImage: Clinical*, vol. 3, pp. 332–339, 2013.

[49] M. J. Millan, J. M. Rivet, and A. Gobert, "The frontal cortex as a network hub controlling mood and cognition: probing its neurochemical substrates for improved therapy of psychiatric and neurological disorders," *Journal of Psychopharmacology*, vol. 30, no. 11, pp. 1099–1128, 2016.

[50] P. J. Wrigley, S. M. Gustin, P. M. Macey et al., "Anatomical changes in human motor cortex and motor pathways following complete thoracic spinal cord injury," *Cerebral Cortex*, vol. 19, pp. 224–232, 2008.

[51] R. Sachdeva, F. Gao, C. C. H. Chan, and A. V. Krassioukov, "Cognitive function after spinal cord injury: a systematic review," *Neurology*, vol. 91, no. 13, pp. 611–621, 2018.

[52] R. J. Zatorre, R. D. Fields, and H. Johansen-Berg, "Plasticity in gray and white: neuroimaging changes in brain structure during learning," *Nature Neuroscience*, vol. 15, no. 4, pp. 528–536, 2012.

[53] M. K. Singh, S. R. Kesler, S. M. Hadi Hosseini et al., "Anomalous gray matter structural networks in major depressive disorder," *Biological Psychiatry*, vol. 74, no. 10, pp. 777–785, 2013.

[54] T. V. P. Bliss, G. L. Collingridge, B. K. Kaang, and M. Zhuo, "Synaptic plasticity in the anterior cingulate cortex in acute and chronic pain," *Nature Reviews. Neuroscience*, vol. 17, no. 8, pp. 485–496, 2016.

[55] R. Shiao and C. A. Lee-Kubli, "Neuropathic pain after spinal cord injury: challenges and research perspectives," *Neurotherapeutics*, vol. 15, no. 3, pp. 635–653, 2018.

[56] S. N. Haber, "Corticostriatal circuitry," *Dialogues in Clinical Neuroscience*, vol. 18, no. 1, pp. 7–21, 2016.

[57] O. Kohler, J. Krogh, O. Mors, and M. E. Benros, "Inflammation in depression and the potential for anti-inflammatory treatment," *Current Neuropharmacology*, vol. 14, no. 7, pp. 732–742, 2016.

[58] B. E. Leonard, "Inflammation and depression a causal or coincidental link to the pathophysiology," *Acta Neuropsychiatrica*, vol. 30, no. 1, pp. 1–16, 2018.

[59] E. J. Huang and L. F. Reichardt, "Neurotrophins: roles in neuronal development and function," *Annual Review of Neuroscience*, vol. 24, no. 1, pp. 677–736, 2001.

[60] K. Martinowich, H. Manji, and B. Lu, "New insights into BDNF function in depression and anxiety," *Nature Neuroscience*, vol. 10, no. 9, pp. 1089–1093, 2007.

[61] R. S. Duman and L. M. Monteggia, "A neurotrophic model for stress-related mood disorders," *Biological Psychiatry*, vol. 59, no. 12, pp. 1116–1127, 2006.

[62] H. Oh, S. C. Piantadosi, B. R. Rocco, D. A. Lewis, S. C. Watkins, and E. Sibille, "The role of dendritic brain-derived neurotrophic factor transcripts on altered inhibitory circuitry in depression," *Biological Psychiatry*, vol. 85, no. 6, pp. 517–526, 2019.

[63] A. Craig, Y. Tran, and J. Middleton, "Psychological morbidity and spinal cord injury: a systematic review," *Spinal Cord*, vol. 47, no. 2, pp. 108–114, 2009.

[64] I. J. C. Orbaan, "Psychological adjustment problems in people with traumatic spinal cord lesions," *Acta Neurochirurgica*, vol. 79, no. 1, pp. 58–61, 1986.

[65] J. E. Salter, S. D. Smith, and K. D. Ethans, "Positive and negative affect in individuals with spinal cord injuries," *Spinal Cord*, vol. 51, no. 3, pp. 252–256, 2013.

[66] N. T. North, "The psychological effects of spinal cord injury: a review," *Spinal Cord*, vol. 37, no. 10, pp. 671–679, 1999.

Hindawi
Neural Plasticity
Volume 2021, Article ID 8819380, 12 pages
https://doi.org/10.1155/2021/8819380

*Research Article*

# Why It Is Necessary to Use the Entire Root rather than Partial Root When Doing Contralateral C7 Nerve Transfer: Cortical Plasticity Also Matters besides the Amount of Nerve Fibers

**Jinding Guo,[1,2,3] Xin Zhao,[1,2,3] Jie Lao,[1,2,3] and Kaiming Gao[1,2,3]**

[1]*Department of Hand Surgery, Huashan Hospital, Fudan University, Shanghai, China*
[2]*Key Laboratory of Hand Reconstruction, Ministry of Health, Shanghai, China*
[3]*Shanghai Key Laboratory of Peripheral Nerve and Microsurgery, Shanghai, China*

Correspondence should be addressed to Kaiming Gao; gaokaiming511@163.com

Received 6 August 2020; Revised 19 October 2020; Accepted 23 December 2020; Published 5 January 2021

Academic Editor: Clive Bramham



Previous studies suggested that the mode of donor transection is a critical factor affecting the efficacy of the contralateral C7 (CC7) nerve transfer. Nevertheless, the mechanism underlying this phenomenon remains elusive. The aim of this study was to investigate the relationship between the division modes of the CC7 nerve and cortical functional reorganization of Sprague-Dawley rats. We hypothesized that different methods of CC7 nerve transection might induce differences in cortical functional reorganization, thus resulting in differences in surgery efficacy. BDNF, TNF-$\alpha$/IL-6, and miR-132/134 were selected as indicators of cortical functional reorganization. No significant differences in all these indicators were noted between the entire group and the entire root+posterior division group ($P > 0.05$). BDNF and miR-132/134 levels in the entire group and the entire root+posterior division group were significantly increased compared with their levels in the posterior group and the blank control group ($P < 0.001$). In all groups, BDNF, TNF-$\alpha$/IL-6, and miR-132/134 levels in both hemispheres initially increased and subsequently decreased until week 40. In conclusion, this study provided the evidence of dynamic changes in BDNF, TNF-$\alpha$/IL-6, and miR-132/134 in the cortex of rats after CC7 nerve transfer using different transecting modes, demonstrating that different CC7 nerve divisions might result in different surgical effects through modulation of cortical reorganization.

## 1. Introduction

Total brachial plexus injury (TBPI) is a devastating peripheral nerve injury, which can cause paralysis of the entire upper arm. Contralateral C7 (CC7) nerve transfer is an effective neurotising procedure to restore the affected limb after TBPI [1].

The CC7 nerve root is a nerve donor with ample nerve fibers (27,000–41,000) that far exceeds its recipients, such as the median nerve and musculocutaneous nerve [2]. Thus, in recent years, partial CC7 nerve transfer, which refers to dividing a selective part of CC7 as the donor, has been applied in clinical practice. The efficacy of transferring the entire CC7 nerve root to repair the median nerve is better than that of transferring the hemi-CC7 nerve root [3–6]. The mechanism underlying this phenomenon involves transferring the whole CC7 nerve root to potentially provide more nerve fibers. However, it was also reported that the entire CC7 nerve root could be transferred to repair both median nerve and bicep branch with the satisfactory results [3, 7]. After comparing the above two situations, we found that the amount of nerve fibers received by the median nerve when transferring the entire CC7 nerve root to two recipients is similar to that of transferring the hemi-CC7 nerve root to the median nerve alone. However, the surgery results were quite different. These clinical studies inferred us that the amount of nerve fibers may not be the only factor affecting the nerve recovery.

Biologically, some rat experiments also mirrored the finding. Gao et al. have reported that electrophysiological examination including maximum amplitude, latency, and muscle tetanic contraction force showed no significant difference

between transferring the entire CC7 to repair the median nerve alone and transferring the entire CC7 to two recipient nerves, which were all better than partial CC7 transferring [8]. Similar results can also be obtained in terms of counts of myelinated axons in the median nerve.

Taking all the above clinical and experimental findings into consideration, we might draw the following hypothesis: the amount of nerve fibers may not be the only factor affecting the nerve recovery. In other words, harvesting the entire CC7 nerve root achieved significantly better recovery than partial harvesting for the same recipient, even if only part of the entire root was used as the donor nerve. Other mechanisms must exist besides the nerve fiber amounts underlying this phenomenon that different modes of donor transection lead to different surgery efficacies.

Recent studies have shown that CC7 nerve root transfer induces cortical functional reorganization, which has been proven to be a critical factor affecting the surgery efficacy [9–13]. Researchers compared the cerebral plasticity of intrinsic and extrinsic hand muscles both innervated by the median nerve, demonstrating that different target muscles correlated with different functional cortical reorganization [14]. Pan et al. conducted a research indicating that different recipient nerves also correlated with different functional cortical reorganization [15]. According to these studies, we hypothesized that the different modes of donor nerve transecting in addition to recipient nerves and target muscles might also influence cortical functional reorganization and eventually cause difference in surgery efficacy.

During cortical functional reorganization, many neurotrophins play a critical role. Recent studies show that brain-derived neurotrophic factor (BDNF) is much abundant during all neurotrophins and plays a well-established function in modulating cortical plasticity [16, 17]. BDNF is stored in dense-core synaptic vesicles and is overexpressed and released from neurons regulating the neural plasticity. Excreted BDNF promoted the activation of astrocytes and microglia to release some inflammatory cytokines [18]. Previous studies also demonstrated that tumor necrosis factor-$\alpha$ (TNF-$\alpha$), interleukin-6 (IL-6), and interleukin-1$\beta$ changed dynamically with the cortical reorganization after CC7 nerve root transfer [19, 20]. In addition, levels of BDNF also are regulated by microRNA. It has been reported that miR-132 and miR-134 can regulate levels of BDNF upon the nerve injury [21]. Studies also demonstrated that miR-132 and miR-134 expression might play a fundamental role in activity-dependent synaptic plasticity [22–25]. Above all, we chose the important neurotrophin BDNF, the downstream effectors TNF-$\alpha$ and IL-6, and the upstream regulator miR-132/134 as our biomarkers (Figure 1).

In the present study, we investigated dynamic changes in BDNF, miR-132/134, and TNF-$\alpha$/IL-6 in the motor cortex of Sprague-Dawley rats, which are critical biomarkers involved in the procedure of cortical reorganization. By comparing these critical biomarkers, we analyzed the relationship between different modes of donor nerve transection and cortical functional reorganization, thus elucidating the underlying mechanism of the different surgical outcomes.

## 2. Materials and Methods

*2.1. Animals.* Experiments were conducted on 168 adult male Sprague-Dawley (SD) rats provided by the Experiment Animal Center of Fudan University, China (license No. DF014) and weighed 200 g–250 g. The experimental procedures were performed in strict accordance with the United States National Institutes of Health Guide for the Care and Use of Laboratory Animals (NIH Publication No. 85–23, revised 1985). The Animal Ethics Committee of Fudan University of China (20150629A335) approved the study protocol. All experiments were designed to minimize the number of animals used and their suffering.

These 168 adult male SD rats all underwent root avulsion of the left brachial plexus. The rats were randomly distributed into four groups according to different division types. In the entire root group, the entire right CC7 nerve roots in 42 rats were transected to repair the left median nerve (Figure 2(a)). In the entire root+posterior division group, the entire right CC7 nerve roots in 42 rats were transected and only the posterior division was used to repair the left median nerve (Figure 2(b)). In the posterior division group, only the posterior divisions of the right CC7 nerve root in 42 rats were transected to repair the left median nerve (Figure 2(c)). In the blank control group, the total left brachial plexus was avulsed in 42 rats and the right brachial plexus was only exposed with no operation done (Figure 2(d)). In each group, we equally divided 42 rats into seven subgroups according to the time interval between the surgery and the test. These subgroups included rats tested at weeks 4 ($n = 6$), 8 ($n = 6$), 12 ($n = 6$), 16 ($n = 6$), 24 ($n = 6$), 32 ($n = 6$), and 40 ($n = 6$), respectively.

The rats were housed in plastic cages on clean sawdust, under a 12-hour light/dark cycle, with four animals per cage. The rats had free access to food and water. All rats were intraperitoneally injected preoperatively with 1% pentobarbital sodium solution (1 ml/100 g; Shanghai Reagent Company, Shanghai, China) for general anesthesia.

*2.2. TBPI Model.* Each rat was placed in the supine position. The fur of the surgery area was shaved, and the skin was prepared with iodine. According to the procedure previously reported [26], a supraclavicular transverse incision was made on the left side from the occiput to the scapular angulus superior approximately 4 cm in length to expose $C_5$ to $T_1$ nerve roots. Then, the nerve roots from $C_5$ to $T_1$ were completely avulsed from the spinal cord at the intervertebral foramen level to simulate TBPI. The avulsed nerve roots would be approximately 0.5 cm longer than before, and cerebrospinal fluid would be released to make sure the preganglionic injury. A segment approximately 2 mm in length was removed from each end of the nerves from $C_5$ to $T_1$. No active motion of the affected limb after surgery was considered to indicate successful establishment of the TBPI model.

*2.3. CC7 Nerve Transfer.* After TBPI, CC7 nerve transfer was performed to repair the brachial plexus. First, the proximate portion of the ulnar nerve and median nerve in the left side was explored under the axilla. The distal part of the ulnar

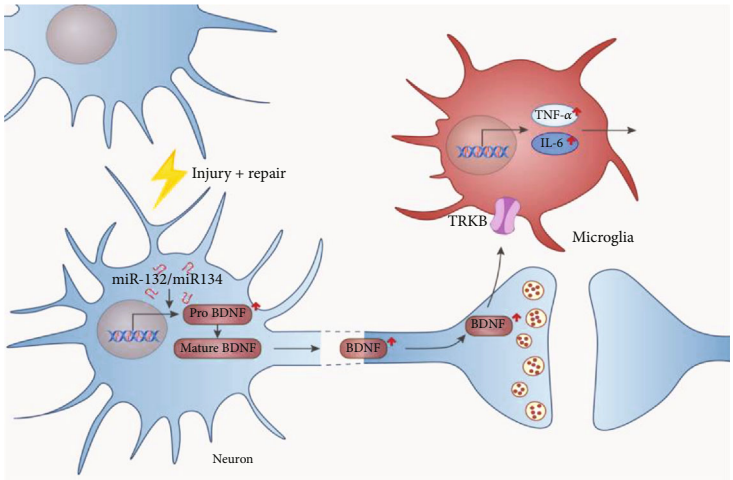


Figure 1: BDNF is reported to be involved in regulating cortical plasticity through activation of microglia, which secreted the proinflammatory factors such as TNF-$\alpha$ and IL-6. After injury and surgical repair of the peripheral nerve, microRNA (miR-132/134) is also reported to regulate the levels of BDNF.

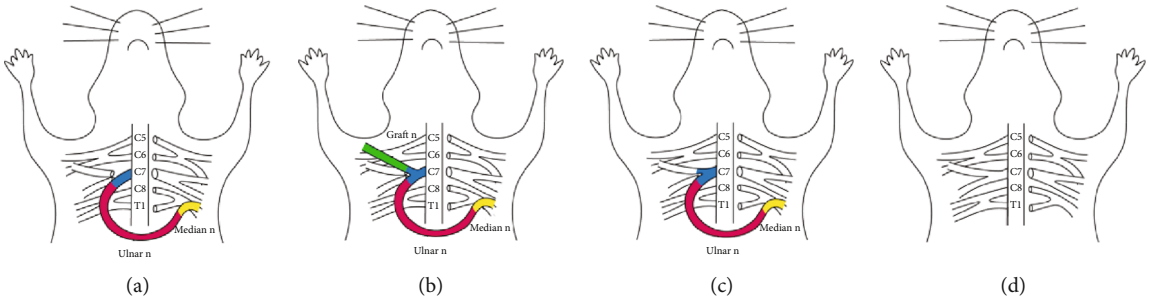


Figure 2: Transfer of entire root, posterior division, and entire root+posterior division. (a) In the entire root group, the entire right CC7 nerve root was transected at the trunk to the division level to be coapted with the ulnar nerve in the left side with no intension by 11-0 microsutures. (b) In the entire root+posterior division group, the entire right CC7 nerve roots were transected at the division level and only the posterior division was coapted with the ulnar nerve in the left side with no intension by 11-0 microsutures. The anterior division was transferred to the pectoralis major bridged by the medial antebrachial cutaneous nerve on the affected side. (c) In the posterior division group, only the posterior division of the right CC7 nerve root was transected and coapted with the ulnar nerve in the left side with no intension by 11-0 microsutures. (d) In the blank control group, the total left brachial plexus was avulsed and the right brachial plexus was only exposed with no operation done.

nerve in the wrist was sectioned and moved through the subcutaneous tissue of the front chest to the contralateral body. Then, the whole CC7 nerve root was explored at the trunk to division level. Epineurotomy was performed to show the anterior and posterior division of the CC7 nerve. As per the situations in different groups, the CC7 nerve root was transected differently as noted for each group. In the entire root group, the entire root was transected and coped with the distal part of the left ulnar nerve. In the posterior division group, only the posterior division of the CC7 nerve root was transected and coped with the distal part of the left ulnar nerve. In the entire root+posterior division group, the entire root of the CC7 nerve was transected, and only the posterior division was coped with the distal part of the left ulnar nerve. The anterior division was transferred to the pectoralis major and bridged by the medial antebrachial cutaneous nerve on the left side, which could block the anterior division and avoid the anterior division growth into the ulnar nerve. Finally, in the above groups, the proximate portion of the left ulnar nerve was coped with the proximate portion of the left median nerve.

*2.4. Obtaining Primary Motor Cortex Samples.* All rats were sacrificed by decapitation under anesthesia at different time points from week 4 to week 40 after the above operations. After decapitation, intact brains were rapidly removed from the skull en bloc (all cortical layers) at ice temperature. Brain tissues between 5 mm anterior and 1 mm posterior to the Bregma and from 0.5 mm lateral to the midline to 4 mm to the midline, which are commonly recognized as the primary motor cortex (PMC), were isolated quickly for the future tests. All tissue samples were shock frozen in liquid nitrogen and stored at −80°C until use.

*2.5. Western Blot.* After the tissues of the brain were harvested for western blot, PMC areas were lysed and extracted in a radioimmunoprecipitation (RIPA) buffer containing protease (Protease Inhibitor Cocktail Set I; Calbiochem,

Darmstadt, Germany) and phosphatase inhibitors according to the manufacturer's instructions at 4°C. Then, the protein concentrations were determined by the BCA standard. After the preparation of PAGE gels, we loaded the samples, markers, and the loading control according to the comparison demand. Then, protein samples were separated by SDS-PAGE in 12% polyacrylamide gels and electroblotted onto a nitrocellulose membrane (Millipore, USA). After blocking in buffer for 2 h at room temperature, membranes were incubated with rabbit anti-BDNF antibody (1 : 1000) from Abcam, UK. Then, after being washed with PBST for 3 times, membranes were incubated at room temperature for 2 h with the corresponding horseradish peroxidase-conjugated secondary antibody diluted 1 : 1000 in blocking buffer. After washing, signals were detected by enhanced chemiluminescence (ECL Plus; Amersham Biosciences) on Kodak Biomax Light films. The housekeeping gene glyceraldehyde-3-phosphate dehydrogenase (GAPDH) levels were used as the loading control. The assays were performed thrice independently.

*2.6. Enzyme-Linked Immunosorbent Assay (ELISA).* For ELISA, rat PMC tissues were weighed and homogenized with an eightfold volume of RIPA buffer containing proteinase and phosphatase inhibitors, sonicated, and centrifuged at 14,000 g for 10 min to obtain the supernatant. Lysate protein concentrations were measured using a BCA protein assay kit (Pierce, Rockford, Illinois, USA). TNF-$\alpha$ and IL-6 levels in the rat PMC were determined using commercially available rat ELISA kits for TNF-$\alpha$ (R&D Systems, Minneapolis, Minnesota, USA) and IL-6 (R&D Systems), respectively, according to the manufacturer's instructions. The brief procedures included firstly obtaining a 96-well plate, rinsing 3 times with PBS, adding 50 $\mu$l of 1 mg/ml of antigen, and incubating for 30 min at 37°C. Then, add 50 $\mu$l of antibody and incubate 30 min at 37°C. After incubation, we added 50 $\mu$l of goat anti-mouse IgG conjugate with alkaline phosphatase. Then, samples were incubated 30 min at 37°C and rinsed 3 times with HPLC water and 0.05% Tween 80 in 0.01 M PBS, pH 7.4. The last step was adding 50 $\mu$l of color development reagent and checking enzyme and color product. The minimum detectable concentrations were less than 12.5 pg/ml for TNF-$\alpha$ and less than 62.5 pg/ml for IL-6. The assays were performed thrice independently.

*2.7. Quantitative Polymerase Chain Reaction.* Total RNA was extracted using TRIzol reagent (Life Technologies, Grand Island, NY) and precipitated in ethanol. Purity and concentration were assessed by agarose gel electrophoresis and ultraviolet (UV) spectrophotometry. After treatment with 10 U DNase I (TaKaRa, Shiga, Japan) at 37°C for 30 min, 2 mg total RNA was reverse-transcribed into cDNA at 42°C for 1 h using SuperScript reverse transcriptase (Invitrogen, CA) with random hexaprimers (TaKaRa, Shiga, Japan) according to the manufacturer's protocol. The GAPDH gene was used as an internal control. Rat miR-132/134 primers were purchased from RiboBio Co., Ltd. The primer sequences were as follows: rat BDNF, forward: 5′-TCATACTTCGGTTGCATGAAGG-3′; rat BDNF reverse: 5′-AGACCTCTCGAACCTGCCC-3′; GAPDH, forward: 5′-TGTTGCCATCAATGACCCCTT-3′; GAPDH reverse: 5′-CTCCACGACATACTCAGCA-3′. For polymerase chain reaction, 2 ml of 10-fold dilutions of the cDNA products was assayed using a TaKaRa Ex-Taq R-PCR kit (TaKaRa) with annealing for 5 min at 94°C, followed by 40 cycles of 94°C for 10 s, 55°C for 20 s, and 72°C for 30 s. The relative expression levels were calculated using the following formula: $2^{-\Delta CT}$($\Delta$Ct = Ct target gene – Ct GAPDH). The assays were performed thrice independently.

*2.8. Immunofluorescence Analysis.* Each rat was perfused through the heart with heparinized PBS (0.01 mol/l, pH 7.35) or 0.9% normal saline followed by 4% paraformaldehyde under sodium pentobarbital anesthetized to obtain tissue samples for immunofluorescence analysis. The brain tissue was excised, fixed in 4% paraformaldehyde overnight, and dehydrated in 20% and 30% sucrose at 4°C. Next, the brain was cut into 10 $\mu$m thick sections and those containing the PMC area were collected. After three washes in PBS, sections were blocked with immunofluorescent blocking agent (Beyotime) for 1 h at 20–25°C and then incubated with primary rabbit polyclonal antibodies: ionized calcium-binding adaptor molecule 1 (Iba-1) overnight at 4°C and then incubated with fluorescein isothiocyanate-conjugated secondary antibodies for 2 h at room temperature in the dark. Measuring and imaging were performed by using a Leica fluorescence microscope (Leica DFC350 FX camera).

*2.9. Statistical Analysis.* Statistical calculations and data handling were performed using SPSS version 20.0 and GraphPad Prism5 (San Diego, California, USA). An analyst who was blind to animal injury performed statistical calculations and data handling. Data were expressed as the mean ± SD. The statistical significance of the data from each biomarker (BDNF, miR-132/134, TNF-$\alpha$, and IL-6) in the motor cortex among different subgroups was determined by one-way ANOVA. Difference between the left and right sides was compared by the Student $t$-test. Least significance difference (LSD) was used for multiple comparison. The Shapiro-Wilk test was used to test data normality. Nonnormal data were analyzed using the Mann-Whitney test. Significance was set at $P = 0.05$.

## 3. Results

*3.1. BDNF Levels in the Rat PMC after CC7 Nerve Root Transfer.* First, western blot showed the dynamic change in BDNF levels in four groups after CC7 nerve transfer. In all groups, BDNF levels in the left hemisphere increased from week 4 to 24 and then decreased until week 40 (Figure 3). Right hemisphere results showed a similar trend. BDNF levels in the right hemisphere increased from week 4 to 16 and then decreased until week 40 (Figure 4).

Comparisons in the left PMC between different groups showed no significant difference between the entire root and entire root+posterior division groups from week 8 to 40 ($P > 0.05$). The relative amount of BDNF levels normalized to GAPDH in the entire root group was 0.67 ± 0.009, 0.84 ± 0.01, 0.97 ± 0.02, 1.00 ± 0.02, 1.11 ± 0.02, 1.03 ± 0.01, and 0.82 ± 0.004 at weeks 4, 8, 12, 16, 24, 32, and 40,

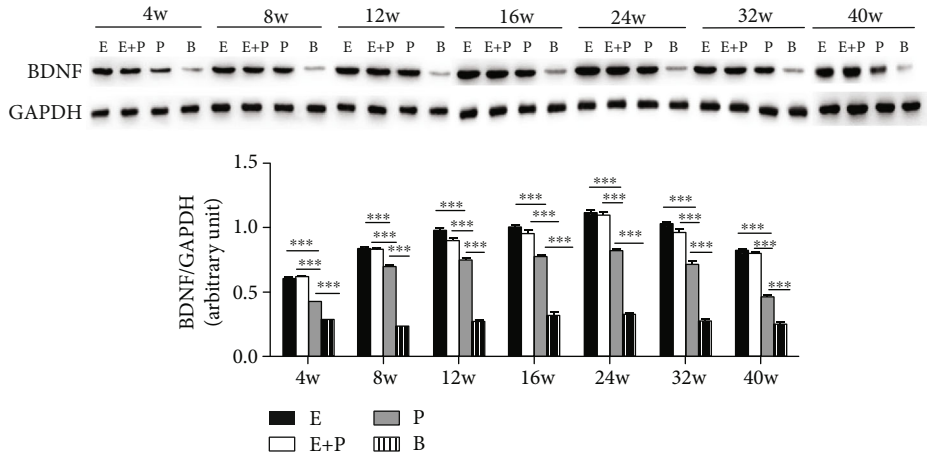


Figure 3: Western blot analysis of BDNF protein levels (normalized to GAPDH) in three groups in the left hemispheres. E: entire root group; E+P: entire root+posterior division group; P: posterior division group; B: blank control group. Data are expressed as mean ± SD; $^{***}P < 0.001$ (one-way ANOVA followed by LSD).

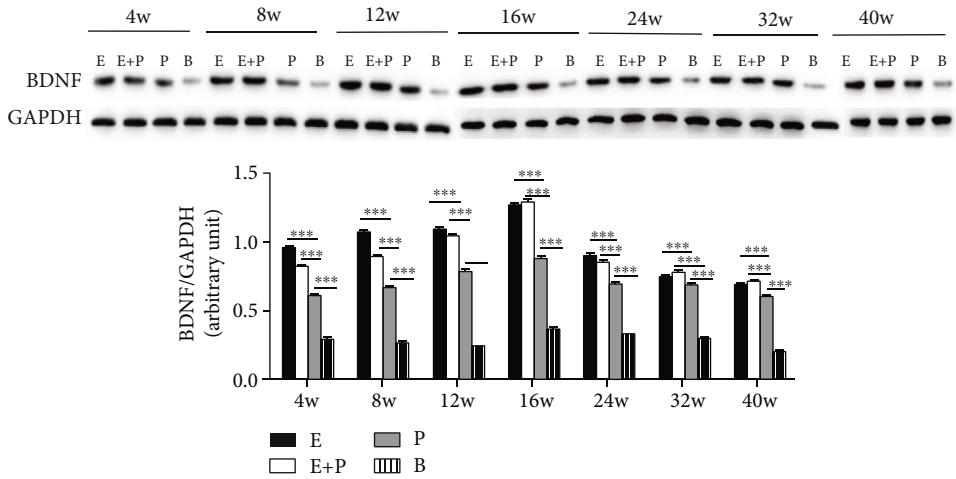


Figure 4: Western blot analysis of BDNF protein levels (normalized to GAPDH) in three groups in the right hemispheres. E: entire root group; E+P: entire root+posterior division group; P: posterior division group; B: blank control group. Data are expressed as mean ± SD; $^{***}P < 0.001$ (one-way ANOVA followed by LSD).

respectively, and 0.62 ± 0.007, 0.83 ± 0.01, 0.90 ± 0.01, 0.96 ± 0.02, 1.10 ± 0.01, 0.96 ± 0.02, and 0.80 ± 0.003 in the entire root+posterior division group, respectively. However, BDNF levels in the above two groups were significantly increased compared with those in the posterior division group and the blank control group at all weeks analyzed after surgery ($P < 0.001$). BDNF levels in the posterior division group were 0.43 ± 0.004, 0.70 ± 0.006, 0.75 ± 0.008, 0.77 ± 0.01, 0.82 ± 0.01, 0.72 ± 0.02, and 0.46 ± 0.004, respectively, which were greater than those in the blank control group ($P < 0.001$) (Figure 3). BDNF levels in the blank control group were 0.29 ± 0.014, 0.23 ± 0.006, 0.27 ± 0.010, 0.31 ± 0.034, 0.32 ± 0.015, 0.27 ± 0.013, and 0.25 ± 0.008, respectively. We obtained similar results for the right PMC (Figure 4). No significant difference in the relative amount of BDNF levels normalized to GAPDH in the right PMC was observed between the entire root group and the entire root+posterior division group ($P > 0.05$), and these levels were significantly increased compared with those in the posterior division group ($P < 0.001$). The BDNF levels normalized to GAPDH in the right PMC in the posterior division group were also greater than those in the blank control group ($P < 0.001$).

Figure 5 also showed comparisons of BDNF levels between the left and right hemispheres and no significant difference of two hemispheres was noted at each time point after the operation ($P > 0.05$).

As shown in Figure 6(a), BDNF mRNA levels in the left PMC of rats revealed no significant difference between the entire root group and the entire root+posterior division group at all weeks analyzed after surgery ($P > 0.05$). BDNF gene expression levels increased 1.02-, 1.48-, 3.29-, 8.03-, 15.03-, 15.55-, and 12.34-fold at weeks 4, 8, 12, 16, 24, 32, and 40, respectively, in the entire root group and increased 0.93-, 1.35-, 3.02-, 7.98-, 14.68-, 15.47-, and 12.45-fold in the entire

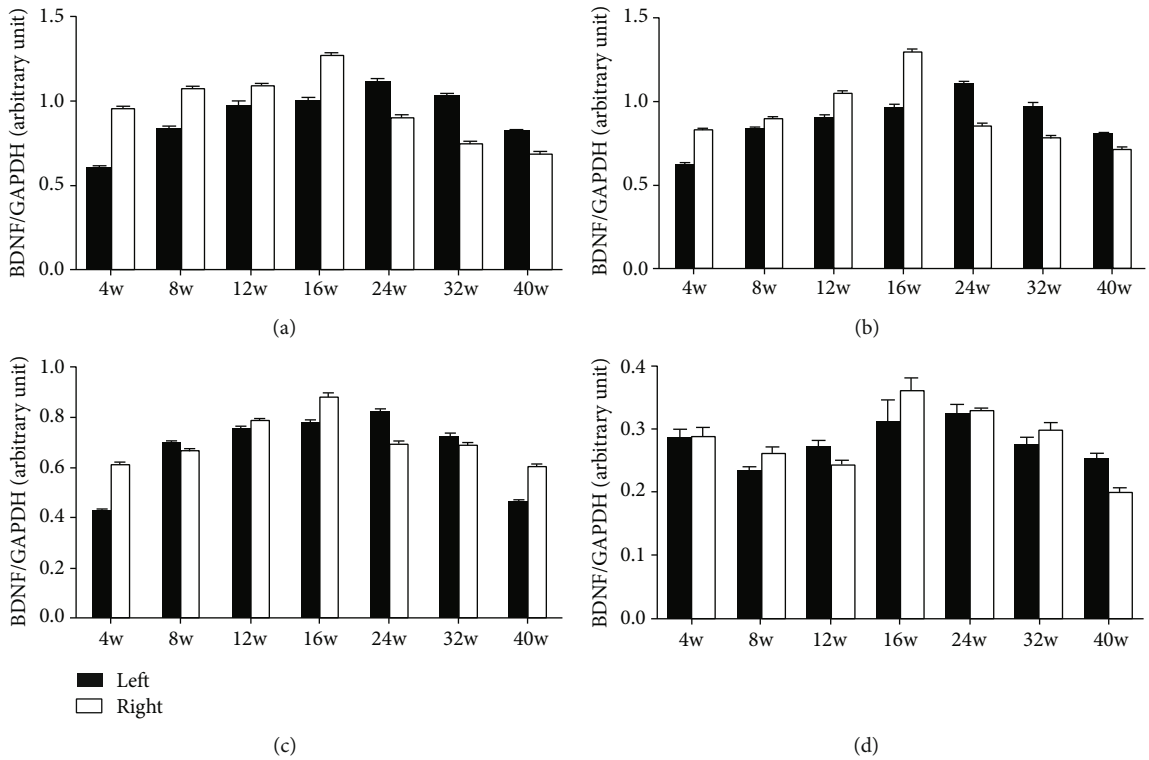


Figure 5: Western blot shows the comparison of the BDNF protein levels (normalized to GAPDH) between the left and right hemispheres. No significant difference was found between the left and right hemispheres. Data are expressed as mean ± SD (Student's $t$-test): (a) entire root group, (b) entire root+posterior division group, (c) posterior division group, and (d) blank control group.

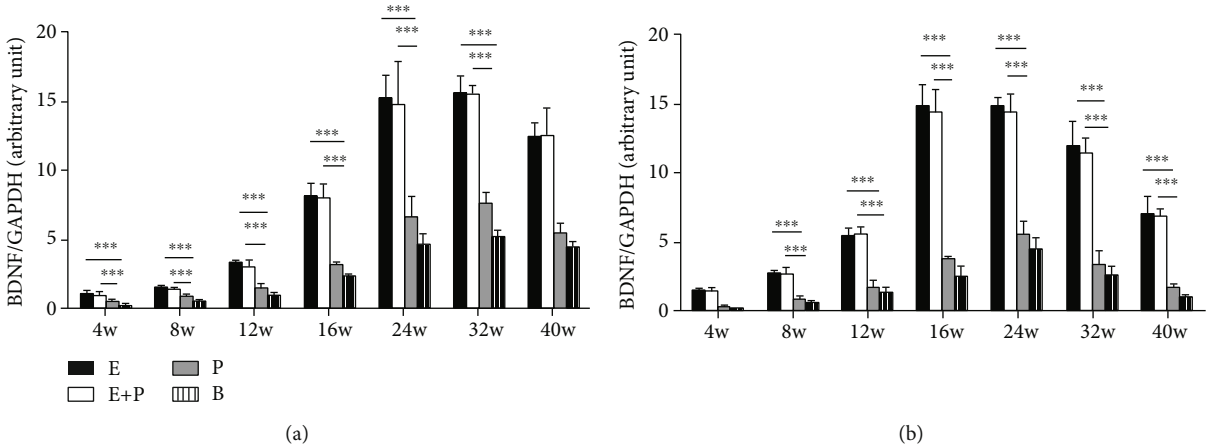


Figure 6: RT-PCR analysis of BDNF gene fold change levels (normalized to GAPDH) in different groups. E: entire root group; E+P: entire root+posterior division group; P: posterior division group; B: blank control group. (a) Left hemisphere; (b) right hemisphere. $^{***}P < 0.001$. Data are expressed as mean ± SD (one-way ANOVA followed by LSD).

root+posterior division group. Significantly lower BDNF gene expression was observed from week 4 to week 32 in the posterior division group and the blank control group. Levels of the posterior division group increased 0.44-, 0.80-, 1.36-, 3.12-, 6.58-, and 7.53-fold, respectively ($P < 0.001$). We also obtained similar results in the right PMC of rats (Figure 6(b)).

*3.2. MiR-132 and miR-134 Levels in the Rat PMC after CC7 Nerve Root Transfer.* Comparisons of miR-132 levels between different groups revealed no significant difference between the entire root and entire root+posterior division groups ($P > 0.05$). Specifically, miR-132 levels in the right PMC in the entire root group increased 1.08-, 2.74-, 6.80-, 10.80-, 15.02-, 16.68-, and 13.95-fold at weeks 4, 8, 12, 16, 24, 32, and 40, respectively, and increased 1.17-, 2.62-, 6.97-, 11.22-, 15.50-, 16.98-, and 13.47-fold in the entire root+posterior division group. The expression levels in these two groups were greater than those in the posterior division

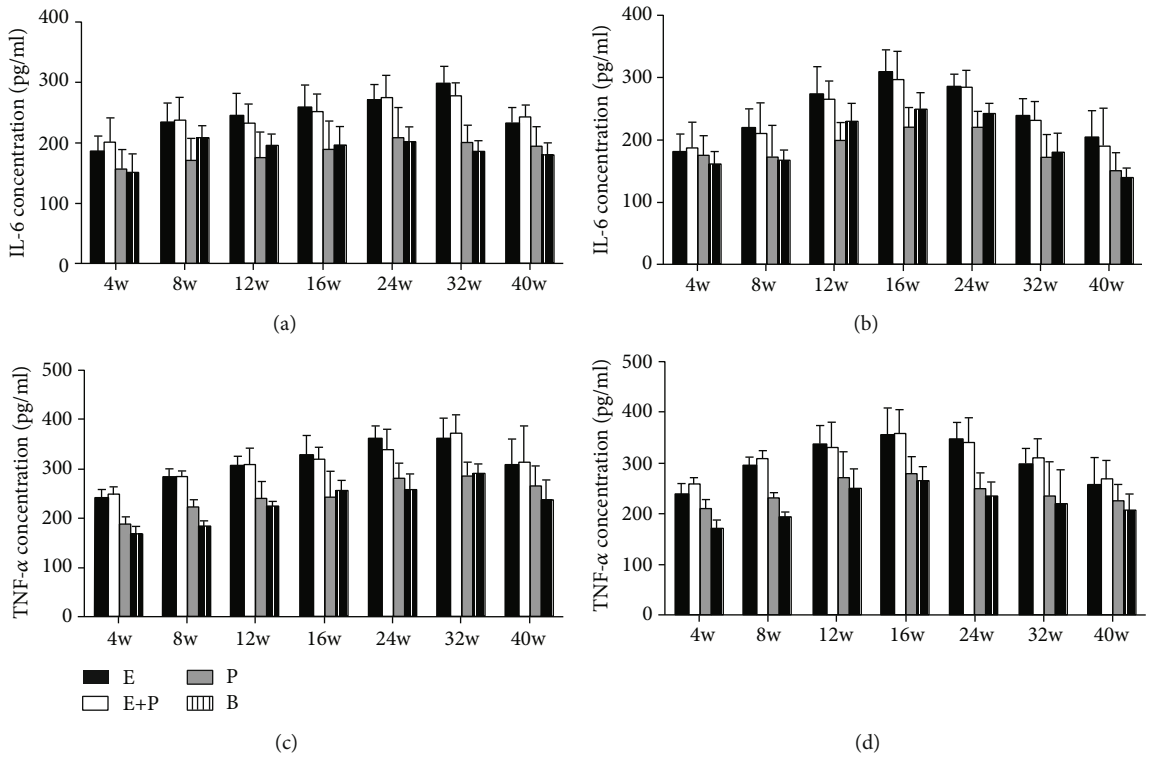


Figure 7: RT-PCR analysis of miR-132 and miR-134 (normalized to U6) in different groups. (a) miR-132 level of the left hemisphere. (b) miR-132 level of the right hemisphere. (c) miR-134 level of the left hemisphere. (d) miR-134 level of the right hemisphere. E: entire root group; E+P: entire root+posterior division group; P: posterior division group; B: blank control group. $^{***}P < 0.001$. Data are expressed as mean ± SD (one-way ANOVA followed by LSD).

group and the blank control group at all weeks analyzed after surgery. The relative levels of miR-132 were 0.33-, 1.29-, 2.42-, 4.59-, 5.82-, 6.25-, and 5.39-fold, respectively, in the posterior division group and 0.21-, 0.93-, 1.70-, 3.02-, 3.67-, 4.98-, and 4.33-fold change in the blank control group (Figure 7(a)). However, significant differences were only noted at weeks 12, 16, 24, 32, and 40 ($P < 0.001$). RT-PCR of miR-132 also showed similar results in the left PMC (Figure 7(b)).

In addition, miR-134 levels were compared between the entire root group and the entire root+posterior division group, and no significant difference between them was observed ($P > 0.05$). Specifically, miR-134 levels in the right PMC in the entire root group increased 1.02-, 4.26-, 6.66-, 8.18-, 12.42-, 13.71-, and 10.65-fold at weeks 4, 8, 12, 16, 24, 32, and 40, respectively, and increased 1.11-, 4.22-, 6.74-, 8.43-, 11.77-, 13.37-, and 10.16-fold in the entire root+posterior division group, respectively. Reduced miR-134 expression was observed in the posterior division group and the blank control group (Figure 7(c)). The relative levels were 0.57-, 1.96-, 3.41-, 4.69-, 5.94-, 6.91-, and 5.14-fold in the posterior division group and 0.33-, 1.30-, 2.11-, 2.98-, 3.78-, 4.98-, and 4.26-fold in the blank control group, respectively. However, significant differences were only noted at weeks 8 and 16 ($P < 0.001$). Similar results were also observed in the left PMC (Figure 7(d)).

*3.3. TNF-α and IL-6 Levels in the Rat PMC after CC7 Nerve Root Transfer.* No significant difference of IL-6 levels was observed between the entire root group and the entire root +posterior division group in the left PMC ($P > 0.05$). IL-6 levels were 184.5 ± 25.1, 231.7 ± 32.7, 243.5 ± 36.9, 257.2 ± 36.8, 268.0 ± 26.6, 296.2 ± 28.6, and 230.1 ± 26.5 in the entire root group and 200.8 ± 39.0, 236.4 ± 37.2, 230.5 ± 32.2, 251.4 ± 27.7, 274.6 ± 35.5, 277.0 ± 20.9, and 241.0 ± 20.4 in the entire root+posterior division group at weeks 4, 8, 12, 16, 24, 32, and 40, respectively (unit: pg/ml). IL-6 levels in the two groups were increased compared with those in the posterior division group and the blank control group. The levels in the posterior group were 165.0 ± 31.5, 219.0 ± 36.8, 206.5 ± 41.8, 207.5 ± 46.9, 216.5 ± 50.4, 199.4 ± 28.3, and 192.7 ± 31.6, respectively (unit: pg/ml) (Figure 8(a)). However, the difference was not significant ($P > 0.05$). Similar results in the right PMC were observed (Figure 8(b)).

No significant difference in TNF-α levels was observed between the entire root group and the entire root+posterior division group in the left PMC ($P > 0.05$). TNF-α levels were 249.5 ± 17.9, 291.2 ± 18.2, 302.7 ± 22.0, 326.4 ± 40.1, 347.8 ± 47.9, 369.7 ± 41.6, and 307.4 ± 51.8 in the entire root group and 258.4 ± 14.2, 274.3 ± 10.4, 306.2 ± 33.5, 319.5 ± 23.1, 328.1 ± 41.4, 390.3 ± 37.7, and 322.4 ± 73.1 in the entire root+posterior division group at weeks 4, 8, 12, 16, 24, 32, and 40, respectively (unit: pg/ml). TNF-α levels in the two groups were increased compared with those in the posterior division group and the blank control group. The levels of the posterior division group were 205.8 ± 16.3, 251.8 ± 13.2, 267.7 ± 35.3, 280.7 ± 52.6, 299.5 ± 30.8, 323.6 ± 28.9, and 274.6 ± 40.9 (unit: pg/ml) (Figure 8(c)). However, the difference was also not

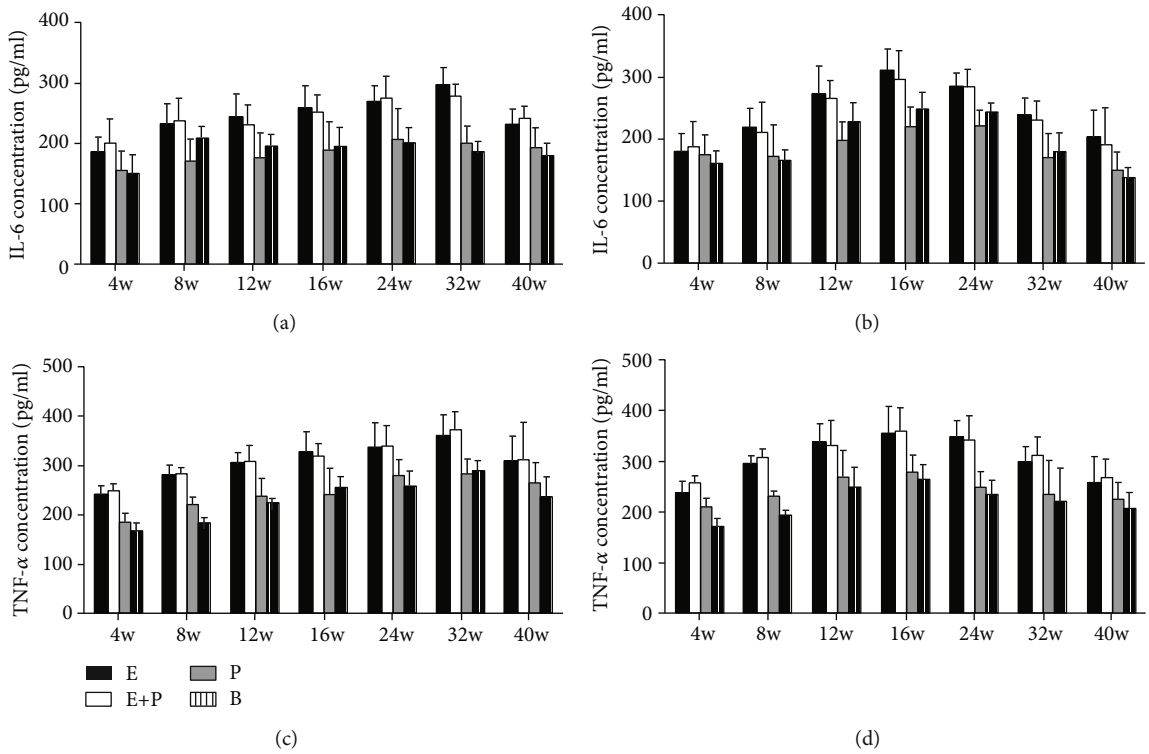


Figure 8: ELISA analysis of IL-6 and TNF-$\alpha$ concentration in different groups. (a) IL-6 concentration of the left hemisphere. (b) IL-6 concentration of the right hemisphere. (c) TNF-$\alpha$ concentration of the left hemisphere. (d) TNF-$\alpha$ concentration of the right hemisphere. Samples were obtained from rats subjected to different divisions of CC7 nerve root at 4 w, 8 w, 12 w, 16 w, 24 w, 32 w, and 40 w postsurgery. E: entire root group; E+P: entire root+posterior division group; P: posterior division group; B: blank control group. Data are expressed as mean ± SD (one-way ANOVA followed by LSD).

significant ($P > 0.05$). Similar results in the right PMC were obtained (Figure 8(d)).

*3.4. Microglia Cell Counting.* Although no significant difference was found in terms of proinflammatory factors, we have also investigated the microglia cells in the PMC in different groups through the immunofluorescence analysis. Considering that the contralateral brain cortical eventually took control of the injured arm in rats, we chose the right PMC in 16 w and 24 w after surgery to compare the microglia cells in different groups. Images showed that there was no significant difference in terms of the positive rates of microglia cells between the entire root group and the entire root+posterior division group, which were greater than the posterior division group and the blank control group ($P < 0.001$) (Figure 9).

## 4. Discussion

Peripheral nerve injury is also related to the central nervous system, especially for the TBPI. On the one hand, some patients are accompanied with the central nervous system injury. On the other hand, the signals received from the peripheral system are altered after the TBPI. Functional cortical reorganization occurring in the central nervous system is considered an important factor influencing the surgery efficacy [9, 17, 20, 27, 28]. The present study provides insight into the possible relationship between different division modes of CC7 nerve root and cortical reorganization by comparing the dynamic levels of these molecules, such as neurotrophins, miR-RNA, and the inflammatory cytokines. To our knowledge, this is the first study exploring the underlying mechanism of this phenomenon.

BDNF is highly expressed in the central nervous system and involved in numerous neuroplasticity processes, such as neuronal survival and neurogenesis [16, 29, 30]. In our experiments, we first analyzed the dynamic levels of BDNF after CC7 nerve transfer. In all groups and hemispheres, BDNF levels exhibited an increasing trend that peaked at weeks 16 to 24 and decreased until week 40. This finding was consistent with the cortical reorganization and demonstrated that BDNF represents an indicator of functional cortical reorganization. During the early phase after the surgery, the peripheral neural route was built, and the signals received from the peripheral stimuli were gradually strengthened. BDNF levels increased with the changes in neuroplasticity and functional cortical reorganization. During the late phase, functional cortical reorganization was almost complete, and some negative regulators start to inhibit BDNF overexpression [17, 31]. Thus, BDNF levels decreased during the late phase.

BDNF levels were also compared between different CC7 division modes. No significant differences were noted between the entire root group and the entire root+posterior division group. Comparing the two groups, the way of CC7 nerve transection was identical, but nerve fiber amount used

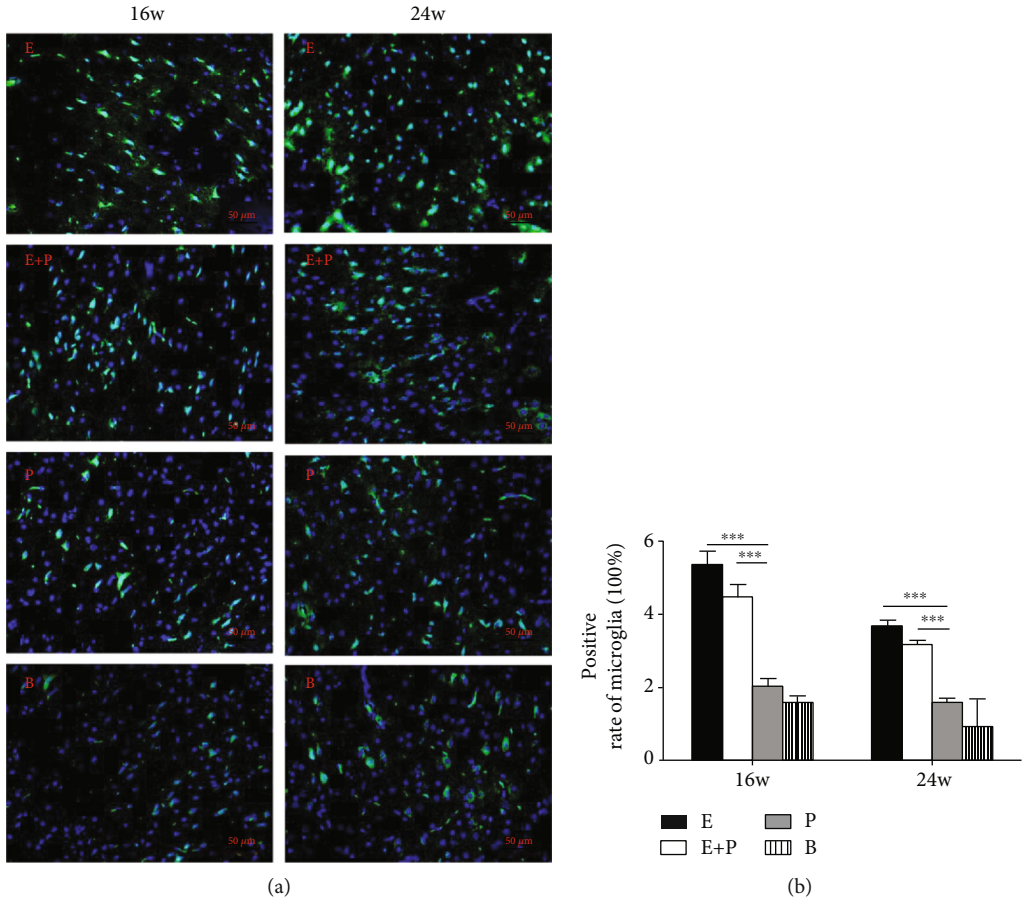


Figure 9: Immunofluorescence staining assay of microglia in the right PMC in 16 w and 24 w after surgery in different groups. (a) Immunofluorescence staining of Iba-1 (green). Scale bar = 50 $\mu$m. (b) Positive rate of microglia cells in different groups. E: Iba-1 expression of the entire root group; E+P: Iba-1 expression of the entire root+posterior division group; P: Iba-1 expression of the posterior division group; B: Iba-1 expression of the blank control group. $^{***}P < 0.001$. Data are expressed as mean ± SD (one-way ANOVA followed by LSD).

as the donor nerve differed. According to previous studies, BDNF is an important biomarker of cortical reorganization [16, 17, 32, 33]. We could infer that the same CC7 transection method yielded the same level of cortical reorganization, and no significant differences in the surgical efficacy were noted. However, BDNF levels of them were all greater than those of the posterior division group. When we compared the entire root+posterior division group and the posterior division group, we found that the number of donor nerve fibers in both groups was similar, but the mode of CC7 transection differed. In the posterior division group, only the posterior division was transected. In the entire root+posterior division group, the entire nerve root was transected. Given the role of BDNF in cortical reorganization, we could infer that different methods of CC7 transection yielded different levels of cortical reorganization and eventually changed the surgical efficacy. We also found that BDNF levels of the posterior division group were greater than those in the blank control group (TBPI), which meant that BDNF levels were upregulated after the surgery to repair the injury and the cortical reorganization did happen after the CC7 nerve transfer.

Then, we compared BDNF levels in both hemispheres at every time point after surgery. No significant difference was noted between both hemispheres. However, we observed that the peak times of the right and left hemispheres were not the same. The peak time point of the right hemisphere was week 16, which was earlier than that noted for the left one at week 24. It is possible that after surgery, the right hemisphere first accepted the peripheral signals for the nerve injury and then the left hemisphere gradually took charge of the affected limb for the rerouted neural pathway [9, 27, 34].

In addition to BDNF, a large body of evidence demonstrates that proinflammatory cytokines play an important role in transhemispheric functional reorganization [19] [20]. In our experiments, these two proinflammatory cytokines were compared between different groups. No significant difference was noted between the entire root group and the entire root+posterior division group, and the values in these groups were increased compared with those in the posterior division and blank control groups. TNF-$\alpha$ and IL-6 results were similar to those noted for BDNF, and these results also revealed the relationship between the type of CC7 division and functional cortical reorganization. Besides,

the dynamic change of TNF-$\alpha$ and IL-6 may also be accounted for the underlying mechanism that BDNF was involved in transhemispheric functional reorganization. Upon nerve injury, inflammatory cells are activated in the neural network and synaptic junctions in the central nervous system. In our experiment, immunofluorescence analysis showed that the microglia cells were activated in the entire root group and the entire root+posterior division group in 16 w and 24 w. The activated inflammatory cells secrete inflammatory cytokines or mediators that act on neurons and regulate the development of cortical reorganization [35–37]. When more CC7 nerve was harvested, more corresponding representations in the motor cortex were replaced and more inflammatory cytokines were secreted [38, 39]. TNF-$\alpha$ and IL-6 in turn play potential roles in the neural circuitry and synaptic plasticity, which may facilitate the cortical reorganization and functional recovery of the affected limb [40, 41]. Although the statistical analysis indicated that the difference was not significant, we believed more research about the relationship between proinflammatory cytokines and the cortical reorganization after CC7 nerve root transfer should be performed.

miR-132 and miR-134 are brain-enriched miRNAs with a well-documented function in neuronal plasticity [22, 42–44]. Dynamic miR-132 and miR-134 levels were similar to BDNF, providing additional evidences indicating that differences in cortical reorganization after different CC7 nerve root divisions modulated surgery efficacy. Studies have shown that miR-132 expression is activity dependent, which may contribute to the long-lasting proteomic changes required for experience-dependent neuronal plasticity [45]. Our results further supported the association between BDNF and miR-134. In our study, we reported that BDNF levels were related with the division mode of the CC7 nerve transfer. However, the underlying mechanism whereby CC7 nerve division regulates BDNF levels remains unknown. Previous studies reported that miR-132 and miR-134 are involved in BDNF regulation [39, 46, 47]. They may also be associated with BDNF expression after the CC7 nerve root transfer. However, the hypothesis must be proven based on additional experiments.

Moreover, we have noticed that biomarkers of the right motor cortex were not fairly consistent among groups although the left avulsion injuries were identical among groups. The results were in accordance with the process of transcortical reorganization which includes both hemispheres. The contralateral cortex firstly lost the control of the injured side and then the ipsilateral cortex took over the control after the connection of CC7 nerve transfer. Then, after the process of reorganization, the contralateral cortex finally regained the control of the injured arm.

Many factors influenced the final efficacy of CC7 transfer including the target muscle, transfer route, donor nerve, and functional cortical reorganization. Functional cortical reorganization occurring after CC7 nerve transfer is a much complex biological process involving many regulators. In the current study, we have found the evidence that division mode could affect the surgery efficacy not only by donor nerve fibers but also by the functional cortical reorganization and these correlated biomarkers could be the targets of future investigation to fully utilize the potential efficacy of the CC7 nerve transfer.

## 5. Conclusion

In conclusion, the present study compared the different levels of BDNF, TNF-$\alpha$, IL-6, and miR-132/134 in rat PMC after CC7 nerve root transfer in different division groups. Results demonstrated that different divisions of CC7 nerve may result in different surgical effects through the modulation of the cortical reorganization. Additional studies are required to further elucidate the further role of these biomarkers in cortical reorganization and their surgical effects.

## Data Availability

The underlying data supporting the results of our study could be obtained by contacting the corresponding author whose email has been provided in the manuscript.

## Conflicts of Interest

The authors declare that they have no conflicts of interest.

## Authors' Contributions

Jinding Guo is the first author and responsible for the conception and design of the study, completion of the animal experiments, data collection and analysis, and manuscript writing. Xin Zhao contributed in critical revision of the manuscript. Jie Lao contributed in data collection and analysis and critical revision of the manuscript. Kaiming Gao is the corresponding author and responsible for the conception and design of the study, critical revision of the manuscript, and final approval of the manuscript.

## Acknowledgments

This study was funded by a grant from the National Natural Science Foundation of China, grant no. 81501871.

## References

[1] Y. D. Gu, G. M. Zhang, D. S. Chen, J. G. Yan, X. M. Cheng, and L. Chen, "Seventh cervical nerve root transfer from the contralateral healthy side for treatment of brachial plexus root avulsion," *Journal of Hand Surger*, vol. 17, no. 5, pp. 518–521, 1992.

[2] D. C. Chuang, "Neurotization procedures for brachial plexus injuries," *Hand Clinics*, vol. 11, no. 4, pp. 633–645, 1995.

[3] K. M. Gao, J. Lao, X. Zhao, and Y. D. Gu, "Outcome of contralateral C7 nerve transferring to median nerve," *Chinese Medical Journal*, vol. 126, no. 20, pp. 3865–3868, 2013.

[4] Y. K. Tu, Y. J. Tsai, C. H. Chang, F. C. Su, C. K. Hsiao, and J. S. Tan, "Surgical treatment for total root avulsion type brachial plexus injuries by neurotization: a prospective comparison study between total and hemicontralateral C7 nerve root transfer," *Microsurgery*, vol. 34, no. 2, pp. 91–101, 2014.

[5] D. M. Sammer, M. F. Kircher, A. T. Bishop, R. J. Spinner, and A. Y. Shin, "Hemi-contralateral C7 transfer in traumatic brachial plexus injuries: outcomes and complications," *The*

*Journal of Bone and Joint Surgery. American Volume*, vol. 94, no. 2, pp. 131–137, 2012.

[6] P. Songcharoen, S. Wongtrakul, B. Mahaisavariya, and R. J. Spinner, "Hemi-contralateral C7 transfer to median nerve in the treatment of root avulsion brachial plexus injury," *The Journal of Hand Surgery*, vol. 26, no. 6, pp. 1058–1064, 2001.

[7] J. K. Terzis and Z. T. Kokkalis, "Selective contralateral c7 transfer in posttraumatic brachial plexus injuries: a report of 56 cases," *Plastic and Reconstructive Surgery*, vol. 123, no. 3, pp. 927–938, 2009.

[8] K. M. Gao, J. Lao, W. J. Guan, and J. J. Hu, "Is it necessary to use the entire root as a donor when transferring contralateral $C_7$ nerve to repair median nerve?," *Neural Regeneration Research*, vol. 13, no. 1, pp. 94–99, 2018.

[9] A. Yu, S. Wang, X. Cheng et al., "Functional connectivity of motor cortical network in patients with brachial plexus avulsion injury after contralateral cervical nerve transfer: a resting-state fMRI study," *Neuroradiology*, vol. 59, no. 3, pp. 247–253, 2017.

[10] M. B. Calford and R. Tweedale, "Interhemispheric transfer of plasticity in the cerebral cortex," *Science*, vol. 249, no. 4970, pp. 805–807, 1990.

[11] H. Thoenen, "Neurotrophins and neuronal plasticity," *Science*, vol. 270, no. 5236, pp. 593–598, 1995.

[12] K. F. Valyear, B. A. Philip, C. M. Cirstea et al., "Interhemispheric transfer of post-amputation cortical plasticity within the human somatosensory cortex," *NeuroImage*, vol. 206, article 116291, 2020.

[13] A. Chemnitz, A. Weibull, B. Rosén, G. Andersson, L. B. Dahlin, and A. Björkman, "Normalized activation in the somatosensory cortex 30 years following nerve repair in children: an fMRI study," *The European Journal of Neuroscience*, vol. 42, no. 4, pp. 2022–2027, 2015.

[14] T. Li, X. Y. Hua, M. X. Zheng et al., "Different cerebral plasticity of intrinsic and extrinsic hand muscles after peripheral neurotization in a patient with brachial plexus injury: a TMS and fMRI study," *Neuroscience Letters*, vol. 604, pp. 140–144, 2015.

[15] F. Pan, H. F. Wei, L. Chen, and Y. D. Gu, "Different functional reorganization of motor cortex after transfer of the contralateral C7 to different recipient nerves in young rats with total brachial plexus root avulsion," *Neuroscience Letters*, vol. 531, no. 2, pp. 188–192, 2012.

[16] V. Nikoletopoulou, K. Sidiropoulou, E. Kallergi, Y. Dalezios, and N. Tavernarakis, "Modulation of autophagy by BDNF underlies synaptic plasticity," *Cell Metabolism*, vol. 26, no. 1, pp. 230–242.e5, 2017, e235.

[17] H. F. Wei, B. F. Zeng, Y. F. Chen, L. Chen, and Y. D. Gu, "BDNF and GAP43 contribute to dynamic transhemispheric functional reorganization in rat brain after contralateral C7 root transfer following brachial plexus avulsion injuries," *Neuroscience Letters*, vol. 500, no. 3, pp. 187–191, 2011.

[18] K. Inoue and M. Tsuda, "Microglia in neuropathic pain: cellular and molecular mechanisms and therapeutic potential," *Nature Reviews Neuroscience*, vol. 19, no. 3, pp. 138–152, 2018.

[19] Y. K. Kim, K. S. Na, A. M. Myint, and B. E. Leonard, "The role of pro-inflammatory cytokines in neuroinflammation, neurogenesis and the neuroendocrine system in major depression," *Progress in Neuro-Psychopharmacology & Biological Psychiatry*, vol. 64, pp. 277–284, 2016.

[20] M. J. Yang, S. Li, C. S. Yang, X. J. Wang, S. M. Chang, and G. X. Sun, "Dynamic alterations of the levels of tumor necrosis factor-$\alpha$, interleukin-6, and interleukin-1$\beta$ in rat primary motor cortex during transhemispheric functional reorganization after contralateral seventh cervical spinal nerve root transfer following brachial plexus avulsion injuries," *Neuroreport*, vol. 28, no. 5, pp. 279–284, 2017.

[21] M. T. Manners, Y. Tian, Z. Zhou, and S. K. Ajit, "MicroRNAs downregulated in neuropathic pain regulate MeCP2 and BDNF related to pain sensitivity," *FEBS Open Bio*, vol. 5, no. 1, pp. 733–740, 2015.

[22] X. H. Wang, L. J. Li, G. X. Sun, Z. P. Wu, J. F. Li, and Y. D. Gu, "Expressions of miR-132, miR-134, and miR-485 in rat primary motor cortex during transhemispheric functional reorganization after contralateral seventh cervical spinal nerve root transfer following brachial plexus avulsion injuries," *Neuroreport*, vol. 27, no. 1, pp. 12–17, 2016.

[23] A. Krug, M. Wöhr, D. Seffer et al., "Advanced paternal age as a risk factor for neurodevelopmental disorders: a translational study," *Molecular Autism*, vol. 11, no. 1, p. 54, 2020.

[24] C. Saraiva, M. Esteves, and L. Bernardino, "MicroRNA: basic concepts and implications for regeneration and repair of neurodegenerative diseases," *Biochemical Pharmacology*, vol. 141, pp. 118–131, 2017.

[25] Y. Qian, J. Song, Y. Ouyang et al., "Advances in roles of miR-132 in the nervous system," *Frontiers in Pharmacology*, vol. 8, p. 770, 2017.

[26] L. Wang, Y. Jiang, J. Lao, and X. Zhao, "Contralateral C7 transfer to lower trunk via the prespinal route in the repair of brachial plexus injury: an experimental study in rats," *Journal of Plastic, Reconstructive & Aesthetic Surgery*, vol. 67, no. 9, pp. 1282–1287, 2014.

[27] R. Kakinoki, S. F. M. Duncan, R. Ikeguchi et al., "Motor and sensory cortical changes after contralateral cervical seventh nerve root (CC7) transfer in patients with brachial plexus injuries," *The Journal of Hand Surgery (Asian-Pacific Volume)*, vol. 22, no. 2, pp. 138–149, 2017.

[28] B. M. Baldassarre, A. Lavorato, P. Titolo et al., "Principles of cortical plasticity in peripheral nerve surgery," *Surgical Technology International*, vol. 36, pp. 444–452, 2020.

[29] S. Cocco, M. Rinaudo, S. Fusco et al., "Plasma BDNF levels following transcranial direct current stimulation allow prediction of synaptic plasticity and memory deficits in 3×Tg-AD mice," *Frontiers in Cell and Development Biology*, vol. 8, p. 541, 2020.

[30] T. Yang, Z. Nie, H. Shu et al., "The role of BDNF on neural plasticity in depression," *Frontiers in Cellular Neuroscience*, vol. 14, p. 82, 2020.

[31] H. Kashiba and E. Senba, "Up- and down-regulation of BDNF mRNA in distinct subgroups of rat sensory neurons after axotomy," *Neuroreport*, vol. 10, no. 17, pp. 3561–3565, 1999.

[32] A. Petzold, L. Psotta, T. Brigadski, T. Endres, and V. Lessmann, "Chronic BDNF deficiency leads to an age-dependent impairment in spatial learning," *Neurobiology of Learning and Memory*, vol. 120, pp. 52–60, 2015.

[33] E. Edelmann, V. Lessmann, and T. Brigadski, "Pre- and postsynaptic twists in BDNF secretion and action in synaptic plasticity," *Neuropharmacology*, vol. 76, pp. 610–627, 2014.

[34] R. P. Sammons and T. Keck, "Adult plasticity and cortical reorganization after peripheral lesions," *Current Opinion in Neurobiology*, vol. 35, pp. 136–141, 2015.

[35] M. B. Orr and J. C. Gensel, "Spinal cord injury scarring and inflammation: therapies targeting glial and inflammatory

responses," *Neurotherapeutics*, vol. 15, no. 3, pp. 541–553, 2018.

[36] Y. Mo, Y. Y. Sun, and K. Y. Liu, "Autophagy and inflammation in ischemic stroke," *Neural Regeneration Research*, vol. 15, no. 8, pp. 1388–1396, 2020.

[37] A. D. Greenhalgh, S. David, and F. C. Bennett, "Immune cell regulation of glia during CNS injury and disease," *Nature Reviews. Neuroscience*, vol. 21, no. 3, pp. 139–152, 2020.

[38] J. B. Stephenson, R. Li, J. G. Yan, J. Hyde, and H. Matloub, "Transhemispheric cortical plasticity following contralateral C7 nerve transfer: a rat functional magnetic resonance imaging survival study," *The Journal of Hand Surgery*, vol. 38, no. 3, pp. 478–487, 2013.

[39] K. N. Corps, T. L. Roth, and D. B. McGavern, "Inflammation and neuroprotection in traumatic brain injury," *JAMA Neurology*, vol. 72, no. 3, pp. 355–362, 2015.

[40] S. L. Patterson, "Immune dysregulation and cognitive vulnerability in the aging brain: interactions of microglia, IL-1$\beta$, BDNF and synaptic plasticity," *Neuropharmacology*, vol. 96, Part A, pp. 11–18, 2015.

[41] K. Riazi, M. A. Galic, A. C. Kentner, A. Y. Reid, K. A. Sharkey, and Q. J. Pittman, "Microglia-dependent alteration of glutamatergic synaptic transmission and plasticity in the hippocampus during peripheral inflammation," *The Journal of Neuroscience*, vol. 35, no. 12, pp. 4942–4952, 2015.

[42] S. Aten, K. F. Hansen, K. Snider et al., "miR-132 couples the circadian clock to daily rhythms of neuronal plasticity and cognition," *Learning & Memory*, vol. 25, no. 5, pp. 214–229, 2018.

[43] S. Karabulut, K. Korkmaz Bayramov, R. Bayramov et al., "Effects of post-learning REM sleep deprivation on hippocampal plasticity- related genes and microRNA in mice," *Behavioural Brain Research*, vol. 361, pp. 7–13, 2019.

[44] I. Puig-Parnau, S. Garcia-Brito, N. Faghihi et al., "Intracranial self-stimulation modulates levels of SIRT1 protein and neural plasticity-related microRNAs," *Molecular Neurobiology*, vol. 57, no. 6, pp. 2551–2562, 2020.

[45] S. Bicker, M. Lackinger, K. Weiß, and G. Schratt, "MicroRNA-132, -134, and -138: a microRNA troika rules in neuronal dendrites," *Cellular and Molecular Life Sciences*, vol. 71, no. 20, pp. 3987–4005, 2014.

[46] W. Huang, F. Meng, J. Cao, X. Liu, J. Zhang, and M. Li, "Neuroprotective role of exogenous brain-derived neurotrophic factor in hypoxia-hypoglycemia-induced hippocampal neuron injury via regulating Trkb/MiR134 signaling," *Journal of Molecular Neuroscience*, vol. 62, no. 1, pp. 35–42, 2017.

[47] X. Gu, X. Su, C. Jia et al., "Sprouty1 regulates neuritogenesis and survival of cortical neurons," *Journal of Cellular Physiology*, vol. 234, no. 8, pp. 12847–12864, 2019.

Hindawi
Neural Plasticity
Volume 2020, Article ID 8814239, 13 pages
https://doi.org/10.1155/2020/8814239

*Research Article*

# Exosomes Derived from CXCR4-Overexpressing BMSC Promoted Activation of Microvascular Endothelial Cells in Cerebral Ischemia/Reperfusion Injury

**Xutong Li**,[1] **Ye Zhang**,[2] **Yong Wang**,[1] **Dan Zhao**,[2] **Chengcheng Sun**,[2] **Shaoting Zhou**,[3] **Dongsheng Xu**,[4,5,6] **and Jing Zhao**[1]

[1]*Department of Neurology, Minhang Hospital, Fudan University, Shanghai, China*
[2]*Department of Rehabilitation, Tongji Hospital, Tongji University, Shanghai, China*
[3]*Department of Rehabilitation, Dongfang Hospital, Tongji University, Shanghai, China*
[4]*Rehabilitation Center, Yueyang Hospital of Integrated Traditional Chinese and Western Medicine, Shanghai, China*
[5]*College of Rehabilitation Science, Shanghai University of Traditional Chinese Medicine, Shanghai, China*
[6]*Engineering Research Center of Traditional Chinese Medicine Intelligent Rehabilitation, Ministry of Education, Shanghai, China*

Correspondence should be addressed to Dongsheng Xu; dxu0927@tongji.edu.cn and Jing Zhao; zhao_jing@fudan.edu.cn

Xutong Li, Ye Zhang, and Yong Wang contributed equally to this work.

Received 1 September 2020; Revised 27 October 2020; Accepted 3 December 2020; Published 18 December 2020

Academic Editor: Zhongyu Li



*Background*. Ischemic stroke is a severe acute cerebrovascular disease which can be improved with neuroprotective therapies at an early stage. However, due to the lack of effective neuroprotective drugs, most stroke patients have varying degrees of long-term disability. In the present study, we investigated the role of exosomes derived from CXCR4-overexpressing BMSCs in restoring vascular function and neural repair after ischemic cerebral infarction. *Methods*. BMSCs were transfected with lentivirus encoded by CXCR4 ($BMSC^{CXCR4}$). Exosomes derived from $BMSC^{CXCR4}$ ($Exo^{CXCR4}$) were isolated and characterized by transmission electron microscopy and dynamic light scattering. Western blot and qPCR were used to analyze the expression of CXCR4 in BMSCs and exosomes. The acute middle cerebral artery occlusion (MCAO) model was prepared, $Exo^{CXCR4}$ were injected into the rats, and behavioral changes were analyzed. The role of $Exo^{CXCR4}$ in promoting the proliferation and tube formation for angiogenesis and protecting brain endothelial cells was determined *in vitro*. *Results*. Compared with the control groups, the $Exo^{CXCR4}$ group showed a significantly lower mNSS score at 7 d, 14 d, and 21 d after ischemia/reperfusion ($P < 0.05$). The bEnd.3 cells in the $Exo^{CXCR4}$ group have stronger proliferation ability than other groups ($P < 0.05$), while the CXCR4 inhibitor can reduce this effect. Exosomes control ($Exo^{Con}$) can significantly promote the migration of bEnd.3 cells ($P < 0.05$), while there was no significant difference between the $Exo^{CXCR4}$ and $Exo^{Con}$ groups ($P > 0.05$). $Exo^{CXCR4}$ can further promote the proliferation and tube formation for the angiogenesis of the endothelium compared with $Exo^{Con}$ group ($P < 0.05$). In addition, cobalt chloride (COCl2) can increase the expression of $\beta$-catenin and Wnt-3, while $Exo^{Con}$ can reduce the expression of these proteins ($P < 0.05$). $Exo^{CXCR4}$ can further attenuate the activation of Wnt-3a/$\beta$-catenin pathway ($P < 0.05$). *Conclusions*. In ischemia/reperfusion injury, $Exo^{CXCR4}$ promoted the proliferation and tube formation of microvascular endothelial cells and play an antiapoptotic role via the Wnt-3a/$\beta$-catenin pathway.

## 1. Introduction

Stroke is an acute cerebrovascular disease caused by local cerebral blood circulation disorder, which is the second cause of global human death [1]. According to the report published by the World Health Organization in 2017, about 6.24 million people die of stroke every year [2]. Among the surviving stroke patients, over 70% of them have varying degrees of

long-term disability [3]. Stroke includes ischemic and hemorrhagic stroke, and the former is the most common subtype, accounting for 87% of all cerebrovascular accidents [4]. Currently, intravenous alteplase and mechanical thrombectomy are recommended effective treatments for patients with acute ischemic stroke. However, these two treatments have many limitations, especially the narrow time window, which largely limits their clinical use [5]. Thus, it is necessary to find alternative therapeutics for patients with acute ischemic stroke.

The brain microvascular endothelium is a thin layer of connected and anchorage-dependent cells, which constitutes the interface between the bloodstream and the deformable solid vascular wall [6]. This vascular endothelium is a highly active metabolic system that synthesizes various vascular regulatory factors to adjust the microcirculation of the cerebral tissue [7]. The brain microvascular endothelium cells are now recognized as a highly active metabolic system that synthesizes various materials to nourish nerves and regulate vasomotor function [8]. As is well known, effective collateral circulation can protect brain tissue after cerebral ischemia by increasing blood perfusion in the ischemic penumbra (IP) [9]. It has been demonstrated that microvascular integrity and cerebrovascular angiogenesis may stabilize brain perfusion thereby promoting neuronal survival, brain plasticity, and neurologic recovery [10–13]. Thus, enhancing angiogenesis in ischemic brain tissue is considered to be an emerging opportunity for potential therapeutic strategies.

Bone marrow mesenchymal stem cells (BMSCs) are able to secrete a variety of trophic factors promoting cell repair and growth [14]. Many studies indicated that stem cells can inhibit inflammation and promote angiogenesis in the ischemic area. Therefore, stem cell therapy is considered to be one of the most promising treatments for ischemic stroke [15, 16]. CXC motif chemokine receptor type 4 (CXCR4) belongs to G-protein-coupled receptor superfamily, which is involved in the homing of a variety of cells. The ligand of CXCR4 is stromal cell-derived factor 1 (SDF-1 or CXCL12) belonging to CXC chemokine family. The expression of CXCL12 is significantly increased in ischemic brain tissue [17] because of the activation of hypoxia-inducible factor-1 (HIF-1). Previous studies have shown that plasma CXCL12 will increase in poststroke patients, which indicated that the concentration gradient of CXCL12 will form in the blood when it is released from the ischemic area [18, 19]. To verify the angiogenic roles of CXCL12 *in vivo*, our previous study utilized the chicken chorioallantoic membrane (CAM) assay. We found that CXCL12 in doses of 50 and 100 ng/ml induced neovessel formation, which indicated that CXCL12 enhanced the capacity for angiogenesis *in vivo* [20]. CXCL12 can bind to the CXCR4 on CXCR4-expressing cells, including brain microvascular endothelial cells (EC). This promotes the migration of cerebral microvascular endothelial cells to ischemic tissues improving the brain tissue repair. Vessel sprouting demands migration and polarization of ECs in response to cytokines [21]. Our previous study indicated that CXCR4 may be involved in the migration and polarization of human umbilical vein endothelial cells in the stripe assay [20]. Collectively, these results are the foundation of the present study to investigate the role of CXCR4 in promoting angiogenesis and protecting brain endothelial cells.

Exosomes are small cell membrane vesicles with a diameter of 30-100 nm; the contents are lipids, proteins, RNA, miRNAs, and mRNAs [22, 23]. Exosomes are carriers of intercellular signal transmission, playing an important role in intercellular communication. The improvement of neural function depends on the entire neurovascular unit, including neurons, astrocytes, vascular endothelial cells, basement membrane, and extracellular matrix. A signal transduction network between cells plays an important role in tissue reconstruction after cerebral ischemia [24]. Increasing evidence is demonstrating that exosomes of mesenchymal stem cells can promote vascular remodeling in the ischemic zone after cerebral ischemia [25]. However, whether the exosomes deprived from CXCR4-overexpressing BMSCs play a role in the angiogenesis is still unclear.

In the present study, we hypothesized that exosomes derived from BMSCs could effectively regulate cell survival, promote angiogenesis, protect nerve cells, and improve stroke outcome in the acute stage of stroke, through upregulating CXCR4 in exosomes of BMSCs. We aim to investigate the role of exosomes derived from CXCR4-overexpressing BMSCs in restoring vascular function and neural repair after ischemic cerebral infarction and to clarify the mechanism of these exosomes in promoting angiogenesis and protecting endothelial cells, so as to provide new ideas for the treatments and further mechanism research of stroke.

## 2. Materials and Methods

*2.1. Chemicals and Reagents.* The chemicals and reagents used in the present study include RIPA lysis buffer (Beyotime Biotechnology, Shanghai), bicinchoninic acid assay (BCA) protein assay kit (Beyotime Biotechnology, Shanghai), sodium dodecyl sulfate-polyacrylamide gel electrophoresis (SDS-PAGE; Beyotime Biotechnology, Shanghai), enhanced chemiluminescence (ECL; Beyotime Biotechnology, Shanghai), 4′,6-diamidino-2-phenylindole (DAPI; Thermo, USA), protein marker (Thermo, USA), Tris-buffered saline tween (TBST; Solarbio, Beijing), phosphate-buffered saline (PBS; Solarbio, Beijing), methanol (Sinopharm, Beijing), anhydrous ethanol (Sinopharm, Beijing), pentobarbital (Sinopharm, Beijing), Dulbecco's modified Eagle medium (DMEM; Gibco, USA), PHK26 (Sigma, USA), 6-0 coated with silicon nylon monofilament suture (Beijing Cinontech Co., Ltd., Beijing), fetal bovine serum (FBS; Beyotime Biotechnology, Shanghai), normal saline (NS; Beyotime Biotechnology, Shanghai), Trizol reagent (Invitrogen, United States), the PrimeScript™ RT reagent Kit (TAKARA, Japan), SYBR Premix Ex Taq™II (TAKARA, Japan), rabbit anti-SQSTM1/p62 (D1Q5S) antibody (1 : 1000 dilution; CST, Boston), rabbit anti-LC3A/B (D3U4C) XP antibody (1 : 1000 dilution; CST, Boston), rabbit anti-BAX antibody (1 : 1000 dilution; Abcam, Cambridge, MA), goat anti-CXCR4 (1 : 1000 dilution; Abcam, Cambridge, MA) antibody, mouse anti-$\beta$-tubulin (1 : 1000 dilution; Sigma, USA) antibody, rabbit anti-TSG101 (1 : 1000 dilution; CST, Boston) antibody, rabbit anti-CD9 (1 : 1000 dilution; Abcam, Cambridge, MA) antibody, mouse anti-Alix (1 : 1000 dilution; CST, Boston) antibody, mouse anti-Bcl2 (1 : 1000

dilution; Abcam, Cambridge, MA) antibody, rabbit anti-PARP (1 : 1000 dilution; CST, Boston) antibody, rabbit anti-Wnt-3a (1 : 1000 dilution; Wanleibio, Shenyang) antibody, rabbit anti-$\beta$-catenin (1 : 1000 dilution; Millipore, Billerica, MA) antibody, mouse anti-$\beta$-actin (1 : 1000 dilution; Proteintech, Chicago) antibody, rabbit anti-CD105 (BD biosciences, San Diego) antibody, rabbit anti-CD44 (BD biosciences, San Diego) antibody, rabbit anti-CD73 (BD biosciences, San Diego) antibody, and rabbit anti-CD90 (BD biosciences, San Diego) antibody.

*2.2. Cell Culture.* The BMSCs were taken from the bone marrow cavity of rat femur. Sprague-Dawley (SD) rats weighing 200 g were anesthetized with excessive pentobarbital intraperitoneally, and the femurs on both sides were removed. The femoral bone marrow cavity was washed repeatedly with low-glucose complete medium to prepare cell suspension, and the primary cells were cultured in a low-glucose DMEM (Gibco, USA) supplemented with 10% FBS. The 3rd to 6th generation BMSCs were used in the following experiments. Mouse brain microvascular endothelial cells (bEnd.3) were purchased from the American Type Strain Collection Center (ATCC CRL-2299). bEnd.3 cells were cultured in DMEM (Gibco, USA) supplemented with 10% FBS in a 5% $CO_2$-humidified atmosphere at 37°C. All animal studies were approved by the Institutional Animal Care and Use Committee (IACUC) of Shanghai Fu Dan University, Shanghai, China.

*2.3. Flow Cytometry.* BMSCs were washed twice with PBS to collect 1 to $5 \times 10^5$ cells. $1 \times$ binding buffer was added to resuspend cells, and the cell concentration was adjusted to $10^6$/ml cells. Antibodies of CD105 (BD biosciences, San Diego), CD44 (BD biosciences, San Diego), CD73 (BD biosciences, San Diego), and CD90 (BD biosciences, San Diego) were added to cell suspension, mixed well, and reacted at room temperature for 15 min in the dark. Various data analyses of the flow cytometer were performed using CELLQuest software to adjust the FSC, SSC, and voltage; adjust the fluorescence compensation according to the standard fluorescein; and set the gate to detect the percentage of positive cells.

*2.4. Lentiviral Transfection.* The main chain of lentivirus vector, pGreenPuro shRNA (pGP), was purchased from Novobio Scientific Co., Ltd., Shanghai, China. Firstly, 293T cells (System Biosciences, USA) were transiently transfected with pGP Sir and pGP null to produce a large number of viruses with the use of pPACKH1 HIV lentivirus packaging kits (System Biosciences, USA). Secondly, the virus supernatant was isolated and purified and was then added to the 3rd to 6th generations BMSCs for 72 hours. The lentivirus was transfected under different multiplicity of infection (MOI) values (10, 30, 60, 80, and 100), and the most suitable MOI value was determined by immunofluorescence. Finally, the lentivirus genome was integrated into the BMSCs genome by virus transfection with MOI = 80. The transfection efficiency was detected by immunofluorescence. BMSCs were divided into two groups: (1) BMSCs transfected with empty lentivirus vectors ($BMSC^{Con}$) and (2) BMSCs transfected with CXCR4 lentivirus vectors ($BMSC^{CXR4}$).

*2.5. Exosome Isolation and Identification.* After 24 h of incubation in a serum-free medium, the BMSC supernatant was collected and subjected to 300g for 10 min, 3000g for 20 min, 10,000g for 30 min, and 100,000g for 2 h of ultracentrifugation at 4°C. Exosomes were obtained and stored at -80°C.

The exosomes were resuspended in PBS and were spread evenly over the copper grid. Then, they were negatively stained with the phosphotungstic acid for 10 min and were observed using a transmission electron microscopy.

The number and size of exosomes were assessed using the NanoSight NS300 system (Malvern Instruments, UK). The supernatant was diluted in PBS, and 1 ml of the solution was used for NanoSight analysis. Each sample was analyzed for 5 times, 10 s for each time. Western blot was used to detect the expression of Alix, TSG101, and CD9 proteins of the exosomes.

*2.6. Cell Uptake of Exosomes.* The exosomes were labeled with PHK26 (Sigma, USA) and were incubated with bEnd.3 in DMEM supplemented with 10% FBS for 48 hours. Then, they were washed with PBS to stop the cell absorption and fixed in 4% paraformaldehyde. Finally, the outcome of cell absorption was observed using the Olympus BX41 microscope equipped with a CCD camera.

*2.7. Quantitative Reverse Transcription Polymerase Chain Reaction (qPCR).* Total RNA of BMSCs transfected with lentiviral was isolated using Trizol reagent (Invitrogen, United States). RNA samples from each group were reverse transcribed into cDNA using the PrimeScript™ RT reagent Kit (TAKARA, Japan). qPCR was performed on a Light Cycler thermal cycler system (Bio-Rad, United States) using SYBR Premix Ex Taq™II (TAKARA, Japan) and gene-specific primers. Gene-specific primers used are as follows: CXCR4—forward 5′-CGCAAATGGGCGGTAGGCGTG-3′ and reverse 5′-CATAGCGTAAAAGGAGCAACA-3′, and GAPDH—forward 5′-CCGCATCT TCTTGTGCA GTG-3′ and reverse 5′-ACCAGC TTCCCATTCTCAGC-3′.

*2.8. Middle Cerebral Artery Occlusion in Rats.* Twenty-four male adult SD rats weighing 250-270 g were divided into 4 groups with 6 rats in each group: the sham-operated group (sham group), the acute middle cerebral artery occlusion model (MCAO) rats injected with PBS group (control group), the MCAO rats injected with exosomes derived from $BMSC^{Con}$ group (Exo group), and the MCAO rats injected with exosomes derived from $BMSC^{CXCR4}$ group ($Exo^{CXCR4}$ group). Rats were anesthetized with 1% pentobarbital intraperitoneally and then received an operation according to the modified Zea Longa method [26]. Briefly, a 6-0 coated with silicon nylon monofilament suture (Beijing Cinontech Co., Ltd., Beijing, China) was introduced into external carotid artery lumen and then gently advanced into the internal carotid artery in order to block the origin of the middle cerebral artery. For the rats in the sham-operated group, the suture was inserted into external carotid artery lumen

but not advanced into the internal carotid artery. After 90 min occlusion, the suture was withdrawn to allow the reperfusion. A 5-point scale [26] was used to assess the neurological deficiency score, and the rats with a score between 1 and 3 were considered as a success of MCAO.

*2.9. Exosome Transplantation.* Exosome transplantation was conducted at 24 h after the establishment of MCAO. The injection was performed as described previously [27]. At a speed of 5 $\mu$l/min, 100 $\mu$g Exo, $Exo^{CXCR4}$, or the same volume of PBS was injected into the lateral ventricle of the affected hemisphere ($X = -0.5$ mm, anterior-posterior; $Y = 1.5$ mm, medial-lateral; and $Z = -3.5$ mm, dorsal-ventral). The observation of vocalization, seizures, hemiplegia, and body weight was continued after surgery.

*2.10. Triphenyl Tetrazolium Chloride (TTC) Staining.* Rats were anesthetized with 2% pentobarbital intraperitoneally at 3 d after ischemia/reperfusion (I/R), and the brains were removed after profusion with NS. A brain slicer was used to coronally section the brains at 2 mm intervals from the frontal pole. The slices were incubated with 1% TTC solution for 15 minutes at 37°C in the dark and then were immersed with 4% paraformaldehyde.

*2.11. Modified Neurological Severity Score.* Rats were examined with modified neurological severity score (mNSS) at 1 d, 3 d, 7 d, 14 d, and 21 d after I/R. This evaluation was performed by a blinded tester. mNSS consists of motor (muscle status, abnormal movement), sensory (visual, tactile, and proprioceptive), reflex, and balance test. Scores ranged from 0 to a maximum of 14. The extent of neurological deficits was assessed as follows: 1-5 scores, mild deficits; 6-9 scores, moderate deficits, and 10-14 scores, severe deficits.

*2.12. Adhesive Removal Test.* The adhesive remove test was used to assess the integration of motor and sensory of rats at 1 d, 3 d, 7 d, 14 d, and 21 d after I/R. This evaluation was performed by a blinded tester. For each rat, an adhesive paper with the size of 1 × 1 cm was pasted on the surface of its forelimb plantar, and the time of removing the adhesive paper was recorded.

*2.13. CCK8 Detects Cell Proliferation.* The bEnd.3 cells were seeded in a 96-well plate at a density of $1 \times 10^4$ cells per well, and 5 wells were set as one group. In the experiment of exosomes promoting the proliferation of bEnd.3 cells, the bEnd.3 cells were divided into 5 groups according to the concentrations of exosome (0, 5, 10, 15, and 20 $\mu$g/ml); in the experiment of cobalt chloride inhibiting the proliferation of bEnd.3 cells, the bEnd.3 cells were divided into 5 groups according to the concentrations of cobalt chloride (0, 100, 200, 400, and 600 $\mu$mol/l). Fresh medium containing 10% CCK8 solution was added into the wells and cultured in a 5% $CO_2$-saturated humidity incubator at 37°C for 0.5 to 4 h. The absorbance value (OD value) of bEnd.3 cells at a wavelength of 450 nm was detected by a microplate reader.

*2.14. Edu Staining Assay Detects Cell Proliferation.* The bEnd.3 cells were divided into 4 groups: the bEnd.3 cells cultured with exosomes derived from $BMSC^{Con}$ group ($Exo^{Con}$ group); the bEnd.3 cells cultured with exosomes derived from $BMSC^{CXCR4}$ group ($Exo^{CXCR4}$ group); the bEnd.3 cells cultured with exosomes derived from $BMSC^{CXCR4}$ and AMD3100 group ($Exo^{CXCR4}$ + AMD3100 group), and the bEnd.3 cell control group. 50 $\mu$mol/l Edu was added to the medium of bEnd.3 cells in each group and then cultured in a 5% $CO_2$ incubator at 37°C. All cell nuclei were stained blue, while the proliferating cell nuclei were also stained red, which were quantified by the fluorescence microscope.

*2.15. Cell Migration Assay.* Cell migration was measured by a Transwell cell chamber. Conditioned medium with 15 $\mu$g/ml $Exo^{Con}$ or $Exo^{CXCR4}$ was added to the lower chamber, while $1 \times 10^5$ bEnd.3 cells were cultured in the upper chamber. After 24 h, the cells were fixed with formaldehyde and then stained with crystal violet (Sigma, USA). Migratory bEnd.3 cells were quantified by a microscope.

*2.16. Tube Formation Assay.* The bEnd.3 cells were incubated with a medium containing exosome or not for 24 h were collected. Cells in each group were seeded in 48-well plates ($5 \times 10^3$ cells per well) coated with matrix glue, and each group was established in three holes. After 6 h, the vascular tubular morphogenesis was observed in at 100x magnification by the inverted optical microscope. The number of vascular lumen structures in 5 random visual field was recorded by ImageJ software.

*2.17. Western Blot.* The total protein of the cells or exosomes was separated by SDS-PAGE. After electrophoretic transfer to polyvinyldifluoridene (PVDF) membranes (Millipore, Billerica, MA), the proteins were treated with SQSTM1/p62 (D1Q5S) (1 : 1000 dilution; CST, Boston), LC3A/B (D3U4C) XP (1 : 1000 dilution; CST, Boston), BAX (1 : 1000 dilution; Abcam, Cambridge, MA), CXCR4 (1 : 1000 dilution; Abcam, Cambridge, MA), $\beta$-tubulin (1 : 1000 dilution; Sigma, USA), TSG101 (1 : 1000 dilution; CST, Boston), CD9 (1 : 1000 dilution; Abcam, Cambridge, MA), Alix (1 : 1000 dilution; CST, Boston), Bcl2 (1 : 1000 dilution; Abcam, Cambridge, MA), PARP (1 : 1000 dilution; CST, Boston), Wnt-3a (1 : 1000 dilution; Wanleibio, Shenyang), $\beta$-catenin (1 : 1000 dilution; Millipore, Billerica, MA), and $\beta$-actin (1 : 1000 dilution; Proteintech, Chicago) overnight at 4°C followed by a horseradish peroxidase-linked secondary anti-mouse or anti-rabbit antibody (1 : 5000 dilution; ICL Lab, Portland Oregon). Finally, the antigen-antibody complexes were photographed by Pierce ECL Western Blotting Substrate.

*2.18. Statistical Analysis.* SPSS 20.0 software (IBM Corporation, NY, USA) and GraphPad Prism 7.0 (GraphPad Software Inc., CA, USA) were used for data analyses; all data were expressed as the mean ± standard deviation (SD). All sample data conformed to the normal distribution by the Kolmogorov-Smirnov test ($P > 0.05$). Differences between multiple groups were analyzed by one-way analysis of variance (ANOVA) test, and then, multiple comparisons were performed using Bonferroni post hoc test. Values of $P < 0.05$ are considered statistically significant.

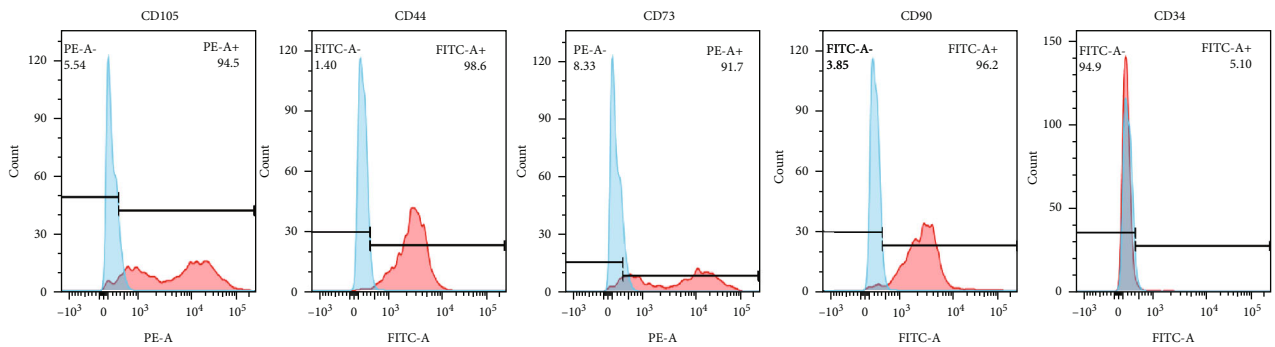


(a)

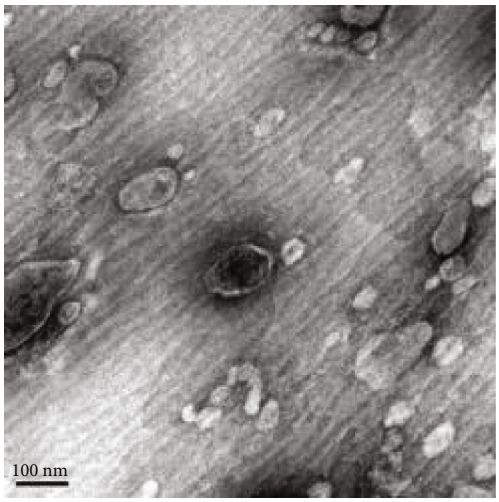


(b)

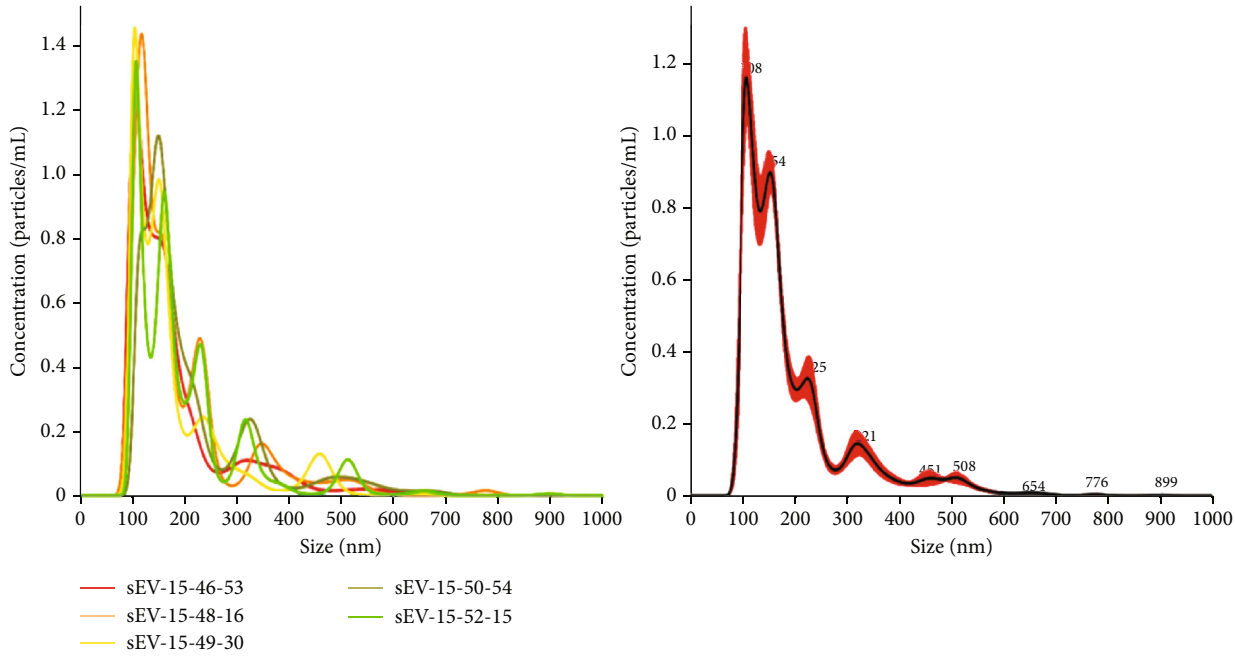


(c)

Figure 1: Continued.

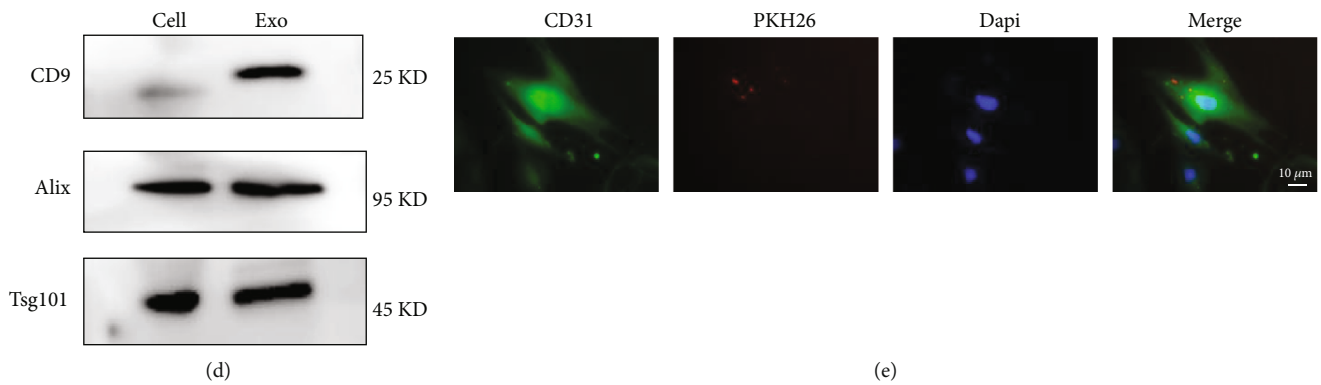


Figure 1: Identification of BMSCs and BMSC exosomes. (a) Identification of BMSC markers CD105(+), CD44(+), CD73(+), CD90(+), and CD34(-) by flow cytometry. (b) Transmission electron microscopy results for exosome ultrastructure. Scale bar = 100 nm. (c) Nanometer diameter range, average size, and concentration of the exosomes were detected by NanoSight. (d) Exosomes were isolated from normalized volumes of BMSC supernatants after 24 h of cell culture. Immunoblotting showed that the isolated exosome expressed CD9, TSG101, and Alix. (e) CD31-labeled bEnd.3 cells (green) were incubated with PKH26-labeled Exo (red) for 2 h, and Exo were swallowed by the bEnd.3 cell. Scale bars = 10 $\mu$m.

## 3. Results

*3.1. Identification of BMSCs and Exosomes.* BMSCs were isolated from SD rats, and the expression of immune markers in the third generation of them was identified by flow cytometry. As shown in Figure 1(a), the CD105 (94.5%), CD44 (98.6%), CD73 (91.7%), and CD90 (96.2%) were found to be positive, while the CD34 (5.10%) were found to be negative, which indicated the high purity of BMSCs.

The shape of the exosomes derived from BMSCs was a classic cup shape under transmission electron microscopy (Figure 1(b)). NTA tracking was used to analyze the size of exosomes, which indicated that the diameter distribution ranged from 50 nm to 600 nm, with a peak at 100 nm (Figure 1(c)). In addition, the expression of exosome protein markers was detected by Western blot. As shown in Figure 1(d), CD9, TSG101, and Alix were expressed in the exosomes. When exosomes labeled with the fluorescent PKH26 were incubated with bEnd.3 cells, the recipient cells—bEnd.3 cells—exhibited high uptake efficiency, as demonstrated by a fluorescence microscopy (Figure 1(e)).

*3.2. Increased Expression of CXCR4 in Exosomes Derived from BMSCs Transfected with Lentivirus.* The lentivirus conveying control vector and CXCR4-overexpressing vector were constructed and transfected into BMSCs. Compared with control groups, the protein and RNA expression of CXCR4 increased in the BMSCs which were transfected with lentivirus encoded by CXCR4 (Figures 2(a)–2(c)). As shown in Figures 2(d), the expression of Alix protein was similar between the $Exo^{Con}$ and $Exo^{CXCR4}$ groups, which indicated the similar concentration of exosome in both groups. Compared with the $Exo^{Con}$ group, the expression of CXCR4 protein was significantly increased in the $Exo^{CXCR4}$ group ($P < 0.05$, Figure 2(e)).

*3.3. Injection of $Exo^{CXCR4}$ Improved Neurobehavioral Outcome in MCAO Rats.* The neurobehavior outcomes of the rats were measured for day 1, day 3, day 7, day 14, and day 21 (Figure 3(a)). We measured the cerebral infarction volume of the rats for day 3 by TTC staining in both the sham and MCAO groups and found that the cerebral infarct volumes were significantly different among the 2 groups ($n = 6$, Figure 3(b)). As shown in Figure 3(c), compared with the control group and $Exo^{Con}$ group, the $Exo^{CXCR4}$ group showed a significantly lower mNSS score at 14 d after I/R ($P < 0.05$, $n = 6$, Figure 3(c)). For the time of removing sticky papers, there was no significant difference among each groups ($P > 0.05$, $n = 6$, Figure 3(d)).

*3.4. The Role of $Exo^{CXCR4}$ in the Proliferation, Migration, and Tube Formation of bEnd.3 Cells.* $Exo^{Con}$ were added to bEnd.3 cells. It was found that the proliferation of bEnd.3 cells was enhanced with increasing exosome concentrations. The proliferative ability of bEnd.3 cells reached its peak at the exosome concentration of 15 $\mu$g/ml, which was used in the following experiments (Figure 4(b)). Then, bEnd.3 cells were cultured with $Exo^{Con}$, $Exo^{CXCR4}$, or $Exo^{CXCR4}$ plus AMD3100, and the Edu staining and CCK8 were used to detect the proliferation of bEnd.3 cells. As shown in Figures 4(a), 4(c), and 4(d), the bEnd.3 cells in the $Exo^{CXCR4}$ group have stronger proliferation ability than other groups ($P < 0.05$), while the CXCR4 inhibitor (AMD3100) can reduce this effect. As for the migration of bEnd.3 cells, $Exo^{Con}$ can significantly promote the migration compared with the control group ($P < 0.05$), while there was no significant difference between the $Exo^{CXCR4}$ and $Exo^{Con}$ groups ($P > 0.05$, Figures 5(a) and 5(b)). As indicated in Figures 5(c) and 5(d), compared with the control group, $Exo^{Con}$ can promote the angiogenesis of the endothelium ($P < 0.05$). Additionally, the $Exo^{CXCR4}$ can further promote the angiogenesis of the endothelium compared with the $Exo^{Con}$ group ($P < 0.05$). The addition of AMD3100 will seriously affect the tube formation.

*3.5. $Exo^{CXCR4}$ Can Reduce Cell Apoptosis Caused by Cobalt Chloride ($COCl_2$).* Western blot was used to assess the

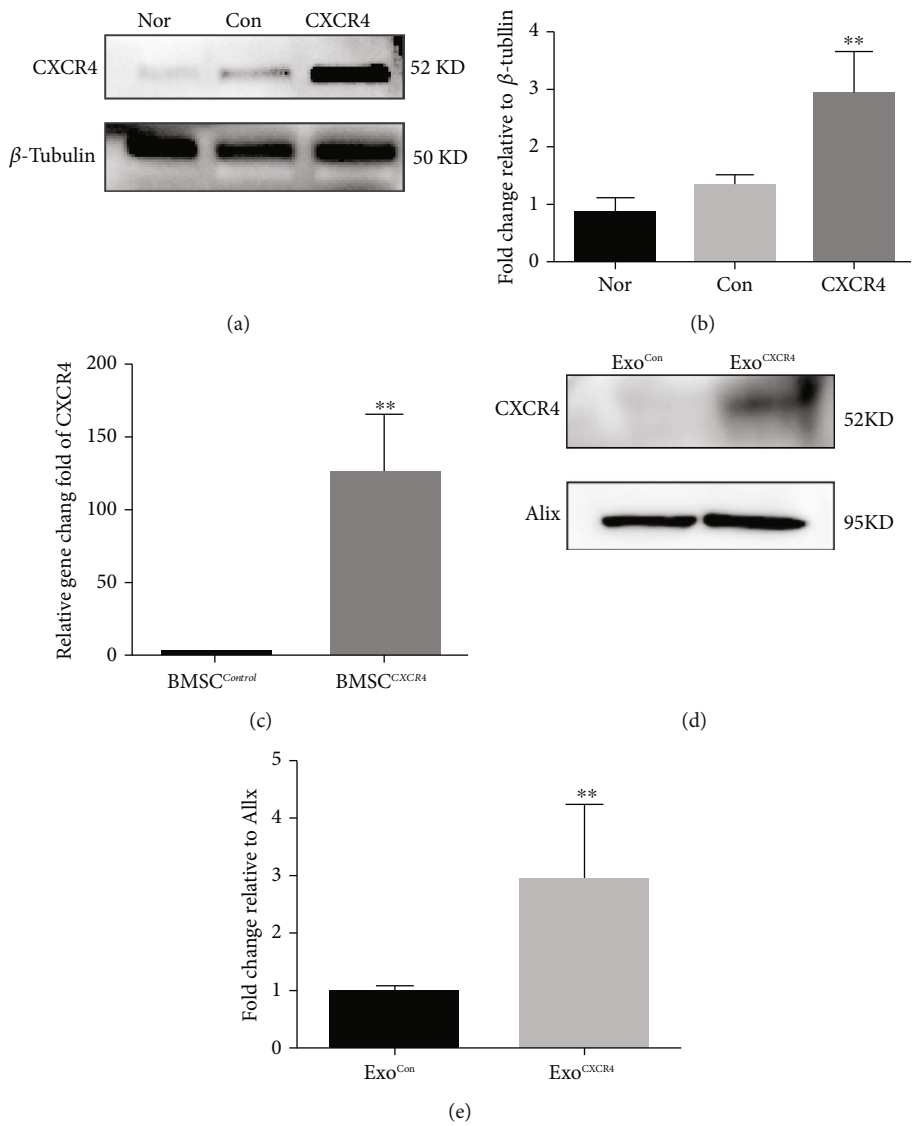


Figure 2: CXCR4 overexpression by BMSCs and exosomes. (a) Western blot results for expression of CXCR4 protein in BMSCs under normal conditions, transfection of control virus, and overexpression of CXCR4. (b) Expression statistics for CXCR4 proteins in BMSCs under normal conditions, transfection of control virus, and overexpression of CXCR4. (c) qPCR was used to detect mRNA after transfection of control virus and CXCR4-encoded virus. (d) Western bolt results for exosome expression. (e) Statistics for exosome CXCR4 protein expression. $^{*}P < 0.05$, $^{**}P < 0.05$, and $^{***}P < 0.01$ vs. the control group.

expression of the proapoptotic protein BAX and antiapoptotic proteins Bcl-2 and PARP. As shown in Figures 6(a) and 6(c), compared with the control group, $COCl_2$ can significant increase the expression of BAX and reduce the expression of Bcl-2 and PARP ($P < 0.05$). Compared with the $COCl_2$ group, the expression of Bcl-2 and PARP in the $COCl_2$ + Exo$^{Con}$ group was higher, while the expression of BAX was lower ($P < 0.05$). In addition, Exo$^{CXCR4}$ can further reduced cell apoptosis caused by $COCL_2$.

Finally, the potential mechanism of antiapoptosis effect of Exo$^{CXCR4}$ was detected by Western blot. As shown in Figures 6(b), 6(d), and 6(e), $COCl_2$ can increase the expression of $\beta$-catenin and Wnt-3, while Exo$^{Con}$ can reduce the expression of these proteins. Additionally, Exo$^{CXCR4}$ can further attenuate the activation of the Wnt-3a/$\beta$-catenin pathway. This indicated that the antiapoptosis effect of Exo$^{CXCR4}$ was related to the Wnt-3a/$\beta$-catenin pathway.

## 4. Discussion

The present study takes advantage of the important role of the CXCL12/CXCR4 axis in the recovery of cerebral infarction. The expression of CXCL12 was significantly upregulated after cerebral ischemia, leading to chemotaxis of endothelial progenitor cells expressing CXCR4 [28]. Additionally, hours after cerebral infarction, CXCL12 expression was elevated in both astrocytes and endothelial cells [29]. Compared to CXCR7, another receptor for CXCL12,

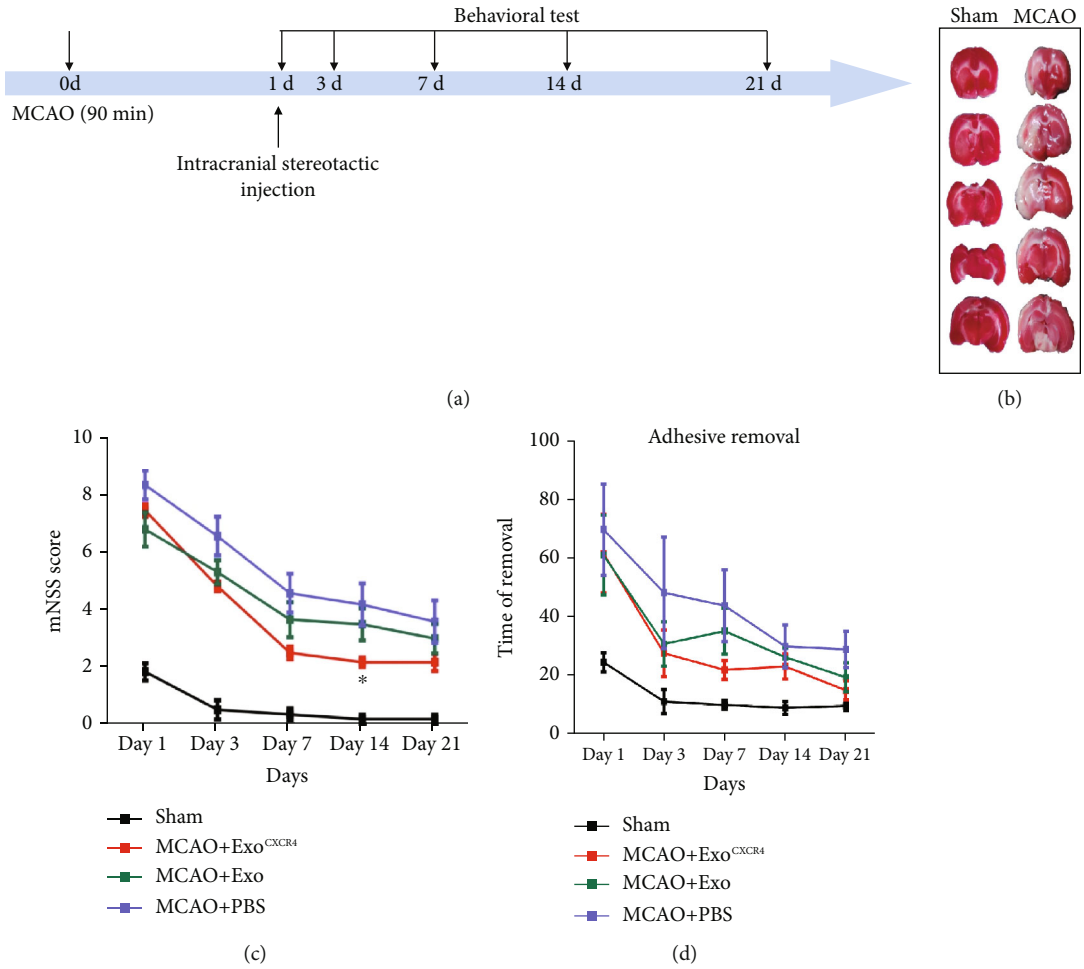


Figure 3: BMSC$^{CXCR4}$-derived exosomes improved neurobehavioral outcome in MCAO rats. (a) Experimental design. Middle cerebral artery was blocked for 90 minutes; 100 $\mu$g of exosomes or the same volume of PBS was stereotactically injected into the ipsilateral lateral ventricle of a rat's brain; (b) TTC staining for rats in sham and MCAO groups ($n = 6$); (c) mNSS score for rats in each group ($n = 6$); (d) times of adhesive removal from rats' right paws in each group ($n = 6$).

CXCR4, is mostly expressed on the cell membrane [30]. Exosomes are vesicles that are packaged by the cell membrane for information transmission [31]. Therefore, it was hypothesized that by increasing CXCR4 on the cell membranes, the amount of CXCR4 on exosomes could be increased. In the present study, BMSCs were genetically modified to overexpress CXCR4 with the help of lentiviral transfection and the exosomes secreted by BMSCs were isolated. According to the results of Western blot and qPCR, CXCR4 was detectable on the Exo$^{CXCR4}$ group, while very little CXCR4 expression was found on Exo$^{Con}$ from BMSCs transfected with no-load virus. Additionally, the recipient cells, bEnd.3 cells, exhibited high uptake efficiency of exosomes as demonstrated by a fluorescence microscopy. These results provided foundation for the research of exosomes in *vivo* and *vitro*.

In *in vivo* experiments, TTC staining was firstly used to assess the cerebral infarction volume of the rats for day 3 to make sure the success of the conduction of MCAO model. Then, the mNSS score and adhesive removal test were used to assess the recovery of the MCAO rats. The results of these tests shown that the injection of exosomes can accelerate the recovery of the MCAO rats, and the rats in the Exo$^{CXCR4}$ group recovered the fastest. This indicated that CXCR4 might promote the positive effect of exosomes in ischemia reperfusion injury.

In *in vitro* experiments, Exo$^{CXCR4}$ were able to promote the proliferation and tube formation of brain microvascular endothelial cells. These effects were all offset by AMD3100, a CXCR4 inhibitor. This evidence does not only prove that BMSC exosomes can promote the angiogenesis in brain tissues after ischemia but also indicates that CXCR4 can improve this effect. However, Exo$^{CXCR4}$ did not promote cell migration better than ordinary BMSC exosomes. This may be because the taken-up exosomes did not completely transfer the CXCR4 to the cell membrane. Besides, the CXCR4 content transferred by exosomes is obviously lower than the CXCR4 content of the cell surface itself, so the total amount of CXCR4 on the cell surface did not change significantly.

BMSCs have a significant inhibitory effect on inflammation. Previous studies have injected BMSCs into animals with central nervous system damage and found that BMSCs can

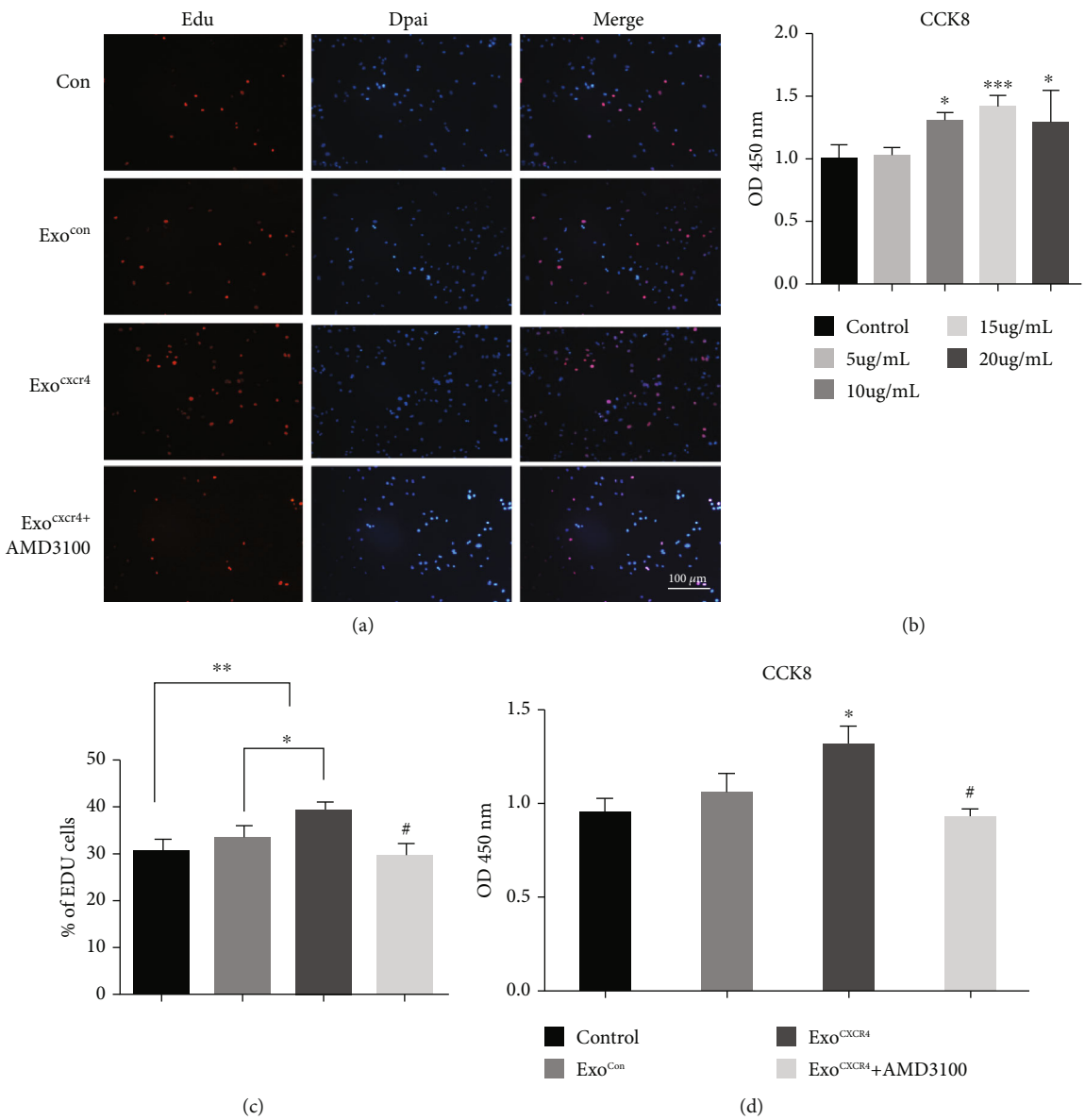


Figure 4: Effect of BMSC$^{CXCR4}$-derived exosomes on endothelial cell proliferation. (a) Edu immunofluorescence staining; (b) CCK8 detects the effects of different exosomes concentrations on proliferation; (c) Edu cell count; (d) CCK8 detects the proliferation for each group. $^{*}P < 0.05$, $^{**}P < 0.05$, and $^{***}P < 0.01$ vs. the control group. Scale bars = 100 $\mu$m.

survive and migrate to damaged tissues and ultimately improve neural function [15, 32]. The CXCL12/CXCR4 axis plays an important role in the treatment of ischemic stroke with transplanting BMSCs [33]. Previous studies have shown that expression of CXCL12 in astrocytes is upregulated within 7 days after cerebral ischemia in newborn mice [29]. CXCR4 is expressed on the surface of BMSCs, which may be an important reason that helps BMSCs migrate to the ischemic area. However, most intravascularly injected BMSCs migrate to the lungs, probably due to insufficient expression of CXCR4 in BMSCs [34, 35]. Therefore, many studies have attempted injection of BMSCs with high expression of CXCR4 or stereotactic injection of BMSCs [36, 37]. Different from BMSCs, exosomes were small with low immunogenicity. It is not easy for exosomes to block blood vessels and easy to store [25, 38]. They are now increasingly used for the exploration of various diseases. Exosomes have been introduced into regenerative medicine as an alternative to BMSCs [39]. However, how to efficiently deliver exosomes to the ischemic area remains unclear. Similar to BMSCs, there are only a few CXCR4 on the surface of exosomes. Most of the exosomes circulate in the body during intravenous injection and their utilization efficiency is uncertain [40]. Therefore, in the present study, exosomes were derived from BMSCs which were transfected with lentivirus encoded by CXCR4. *In vivo* experiments determined that functional recovery of rats in the Exo$^{CXCR4}$ group was significantly improved compared with rats injected with ordinary exosomes.

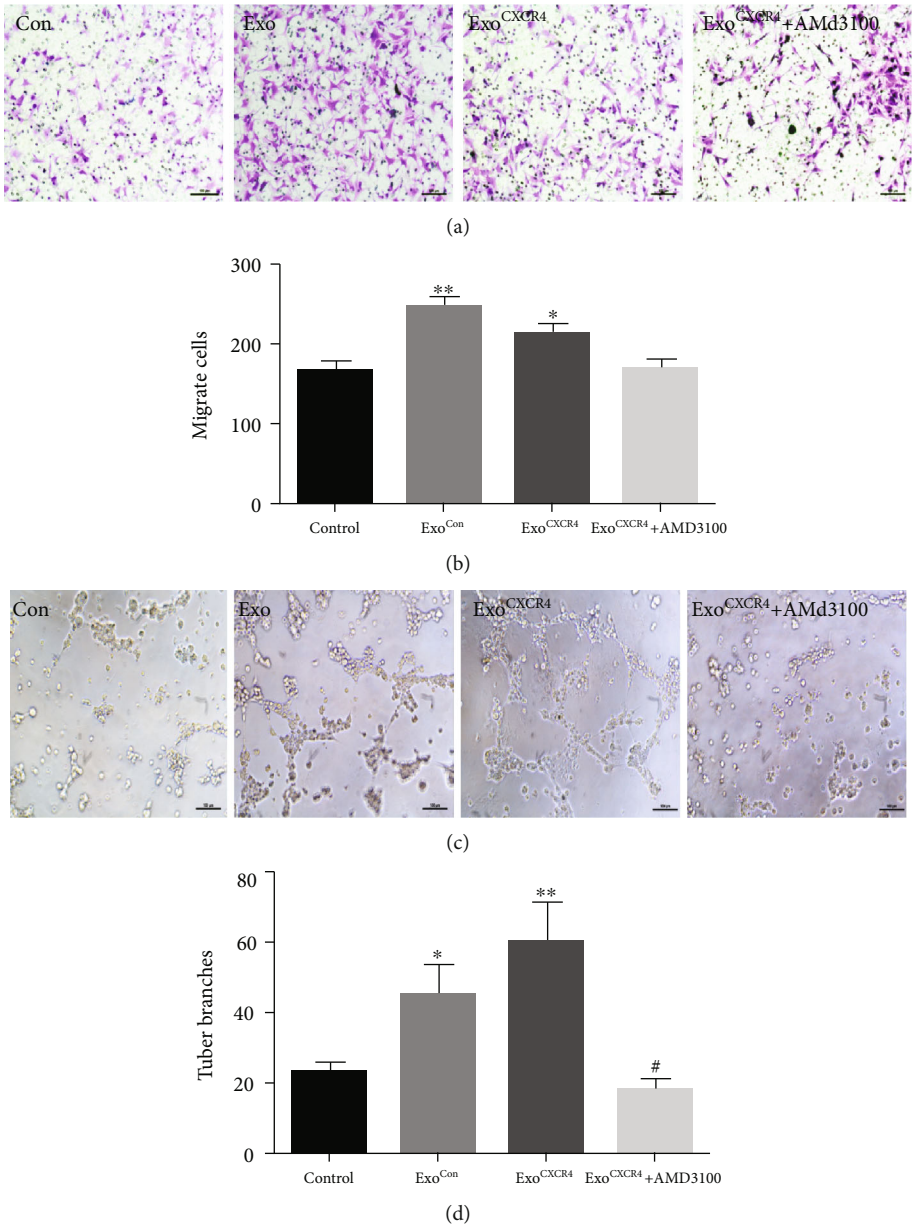


Figure 5: Effect of BMSC$^{CXCR4}$-derived exosomes on endothelial cell migration and lumen formation. (a) Transwell assay detects the effect of exosomes on migration; (b) quantitative migration data for each group on migration; (c) exosome effect on angiogenesis; (d) quantitative data for each group's effect on angiogenesis. $^{*}P < 0.05$, $^{**}P < 0.05$, and $^{***}P < 0.01$ vs. the control group.

After blood clot formation during ischemic stroke, endothelial cells undergo apoptosis due to lack of nutrients, which will destroy the blood-brain barrier, cause brain tissue edema, and aggravate disease progression [41, 42]. The promotion of new vessels in the ischemic region is important for improving the outcome of cerebral infarction. Data have shown that in the 21 days after ischemia, new blood vessels are formed at the edge of the ischemic area, which gradually extends to the ischemic center through budding [9]. Previous studies have shown that CXCL12/CXCR4 can promote the stabilization of endothelial cells and improve the outcome of atherosclerotic diseases by antiapoptotic *in vivo* protein [43]. $COCl_2$ can cause hypoxia in cells, leading to autophagy and apoptosis of cells [44]. In the present study, $COCl_2$ can significantly increase the expression of proapoptotic protein BAX and reduce the expression of antiapoptotic proteins Bcl-2 and PARP, while Exo$^{Con}$ can reverse this effect caused by $COCl_2$. Exo$^{CXCR4}$ can further reduce cell apoptosis caused by $COCL_2$. Additionally, $COCl_2$ can increase the expression of $\beta$-catenin and Wnt-3, while Exo$^{Con}$ can reduce the expression of these proteins. Exo$^{CXCR4}$ can further attenuate the activation of the Wnt-3a/$\beta$-catenin pathway. Thus, the present study shows that Exo$^{CXCR4}$ can promote the proliferation and tube formation of microvascular endothelial cells and plays an antiapoptotic role via the Wnt-3a/$\beta$-catenin pathway, which is consistent with the previous results.

However, this study mainly investigated the effect and mechanism of exosomes derived from BMSCs in promoting

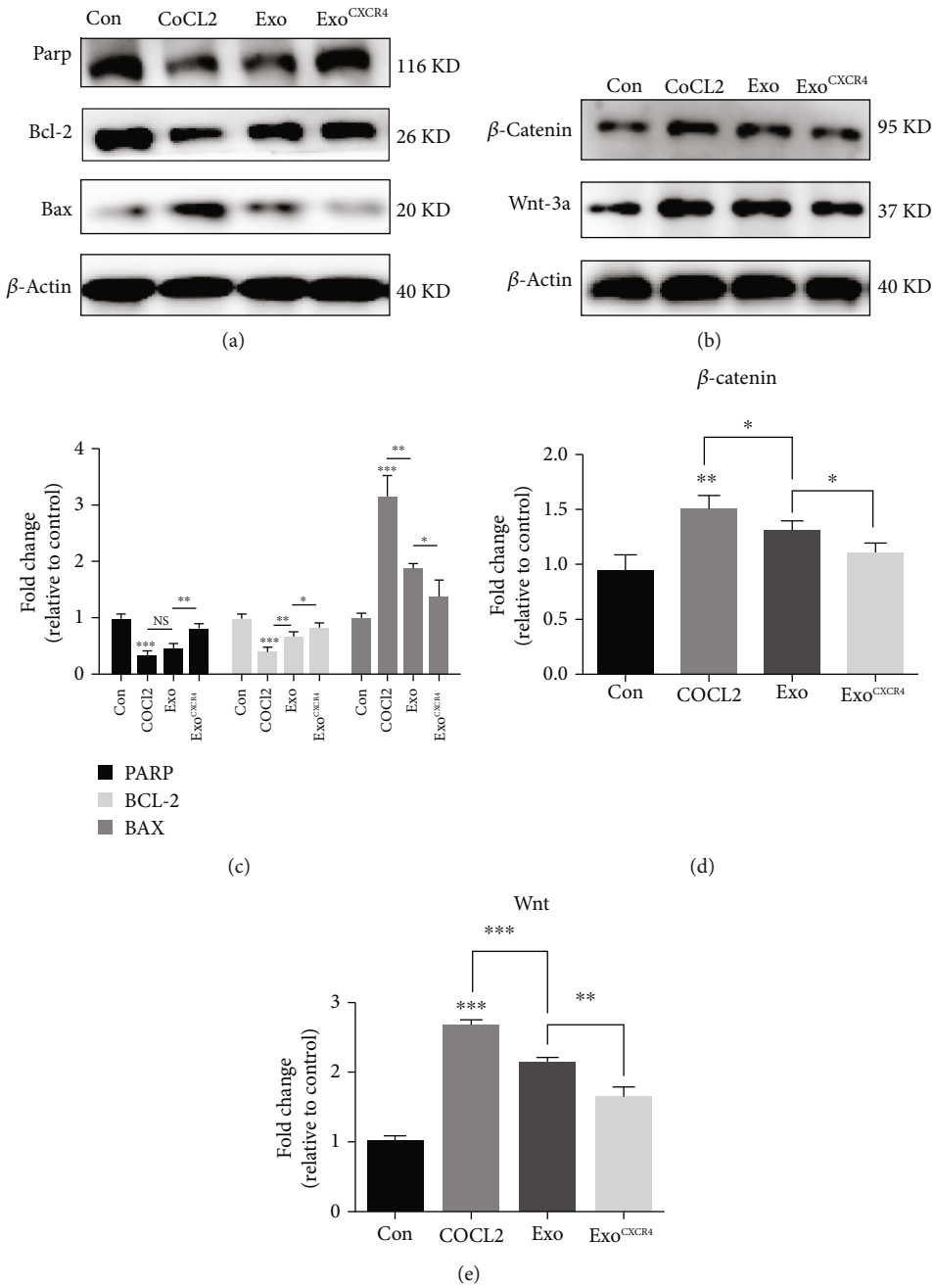


Figure 6: Effect of exosomes derived from BMSC$^{CXCR4}$ on apoptosis. (a) Western blot was used to examine the effect of each group on apoptosis induced by COCl2; (b) $\beta$-catenin and Wnt-3a expression level in bEnd.3 cells was analyzed by Western blot; (c–e) statistics for each group. $^{*}P < 0.05$; $^{**}P < 0.01$.

angiogenesis in ischemia/reperfusion injury, without further research into the specific components of BMSC exosome by which promoted angiogenesis. This is the limitation in this study as well as our future research directions.

## 5. Conclusion

In ischemia/reperfusion injury, Exo$^{CXCR4}$ can promote the proliferation and tube formation of microvascular endothelial cells and play an antiapoptotic role via the Wnt-3a/$\beta$-catenin pathway.

## Data Availability

The raw data supporting the conclusions of this manuscript will be made available by the authors, without undue reservation, to any qualified researcher.

## Conflicts of Interest

The authors declare that there is no conflict of interests regarding the publication of this paper.

## Authors' Contributions

XTL, YZ, DSX, and JZ conceived and designed the experiments. XTL and YZ performed all the experiments. XTL, YZ, and YW analyzed the data. XTL, YZ, YW, DXS, and JZ prepared the figures. ZD, CCS, and STZ contributed the reagents/materials/analysis tools. XTL and YW wrote the paper. YW, DSX, and JZ revised the manuscript. All authors have read and approved the final manuscript. Xutong Li, Ye Zhang, and Yong Wang contributed equally as co-first authors.

## Acknowledgments

The work was supported by the National Key R&D Program of China (grant no. 2020YFC2004202) and the National Nature Science Foundation of China (grant nos. 81772453, 81974358, and 81973157).

## References

[1] M. Naghavi, A. A. Abajobir, C. Abbafati et al., "Global, regional, and national age-sex specific mortality for 264 causes of death, 1980-2016: a systematic analysis for the Global Burden of Disease Study," *The Lancet*, vol. 390, no. 10100, pp. 1151–1210, 2016.

[2] World Health Organization, *The Top 10 Causes of Death*, 2017, https://www.who.int/zh/news-room/fact-sheets/detail/.

[3] G. J. Hankey, "Review: after stroke or TIA, adding clopidogrel to aspirin for ≤1 month reduces recurrence and MACE," *Annals of Internal Medicine*, vol. 171, no. 4, p. JC14, 2019.

[4] E. J. Benjamin, M. J. Blaha, S. E. Chiuve et al., "Heart Disease and Stroke Statistics-2017 update: a report from the American Heart Association," *Circulation*, vol. 135, no. 10, pp. e146–e603, 2017.

[5] Y. Zhou, T. Yang, Y. Gong et al., "Pre-hospital delay after acute ischemic stroke in central urban China: prevalence and risk factors," *Molecular Neurobiology*, vol. 54, no. 4, pp. 3007–3016, 2017.

[6] Q.-j. Yu, H. Tao, X. Wang, and M.-c. Li, "Targeting brain microvascular endothelial cells: a therapeutic approach to neuroprotection against stroke," *Neural Regeneration Research*, vol. 10, no. 11, pp. 1882–1891, 2015.

[7] J. Gracia-Sancho, R. Maeso-Díaz, and J. Bosch, "Pathophysiology and a rational basis of therapy," *Digestive Diseases*, vol. 33, no. 4, pp. 508–514, 2015.

[8] X. Wang, X. Yu, C. Xie et al., "Rescue of brain function using tunneling nanotubes between neural stem cells and brain microvascular endothelial cells," *Molecular Neurobiology*, vol. 53, no. 4, pp. 2480–2488, 2016.

[9] J. Liu, Y. Wang, Y. Akamatsu et al., "Vascular remodeling after ischemic stroke: mechanisms and therapeutic potentials," *Progress in Neurobiology*, vol. 115, pp. 138–156, 2014.

[10] L. Ruan, B. Wang, Q. ZhuGe, and K. Jin, "Coupling of neurogenesis and angiogenesis after ischemic stroke," *Brain Research*, vol. 1623, pp. 166–173, 2015.

[11] Y. Yang and M. T. Torbey, "Angiogenesis and Blood-Brain Barrier Permeability in Vascular Remodeling after Stroke," *Current Neuropharmacology*, vol. 18, no. 12, pp. 1250–1265, 2020.

[12] J. Martí-Fàbregas, J. Crespo, R. Delgado-Mederos et al., "Endothelial progenitor cells in acute ischemic stroke," *Brain and Behavior*, vol. 3, no. 6, pp. 649–655, 2013.

[13] J. Yan, A. Manaenko, S. Chen et al., "Role of SCH79797 in maintaining vascular integrity in rat model of subarachnoid hemorrhage," *Stroke*, vol. 44, no. 5, pp. 1410–1417, 2013.

[14] V. Bucan, D. Vaslaitis, C.-T. Peck, S. Strauß, P. M. Vogt, and C. Radtke, "Effect of exosomes from rat adipose-derived mesenchymal stem cells on neurite outgrowth and sciatic nerve regeneration after crush injury," *Molecular Neurobiology*, vol. 56, no. 3, pp. 1812–1824, 2019.

[15] Y. Tang, C. Zhang, J. Wang et al., "MRI/SPECT/fluorescent tri-modal probe for evaluating the homing and therapeutic efficacy of transplanted mesenchymal stem cells in a rat ischemic stroke model," *Advanced Functional Materials*, vol. 25, no. 7, pp. 1024–1034, 2015.

[16] L. Hao, Z. Zou, H. Tian, Y. Zhang, H. Zhou, and L. Liu, "Stem cell-based therapies for ischemic stroke," *BioMed Research International*, vol. 2014, Article ID 468748, 17 pages, 2014.

[17] T. Bogoslovsky, M. Spatz, A. Chaudhry et al., "Stromal-Derived Factor-1$\alpha$ Correlates With Circulating Endothelial Progenitor Cells and With Acute Lesion Volume in Stroke Patients," *Stroke*, vol. 42, no. 3, pp. 618–625, 2011.

[18] Y. Wang, J. Huang, Y. Li, and G.-Y. Yang, "Roles of chemokine CXCL12 and its receptors in ischemic stroke," *Current Drug Targets*, vol. 13, no. 2, pp. 166–172, 2012.

[19] U. M. Selvaraj, S. B. Ortega, R. Hu et al., "Preconditioning-induced CXCL12 upregulation minimizes leukocyte infiltration after stroke in ischemia-tolerant mice," *Journal of Cerebral Blood Flow & Metabolism*, vol. 37, no. 3, pp. 801–813, 2017.

[20] M. Zhang, L. Qiu, Y. Zhang, D. Xu, J. C. Zheng, and L. Jiang, "CXCL12 enhances angiogenesis through CXCR7 activation in human umbilical vein endothelial cells," *Scientific Reports*, vol. 7, no. 1, p. 8289, 2017.

[21] S. P. Herbert and D. Y. Stainier, "Molecular control of endothelial cell behaviour during blood vessel morphogenesis," *Nature reviews Molecular Cell Biology*, vol. 12, no. 9, pp. 551–564, 2011.

[22] E. J. Goetzl, J. B. Schwartz, M. Mustapic et al., "Altered cargo proteins of human plasma endothelial cell-derived exosomes in atherosclerotic cerebrovascular disease," *The FASEB Journal*, vol. 31, no. 8, pp. 3689–3694, 2017.

[23] S. R. Baglio, K. Rooijers, D. Koppers-Lalic et al., "Human bone marrow- and adipose-mesenchymal stem cells secrete exosomes enriched in distinctive miRNA and tRNA species," *Stem Cell Research & Therapy*, vol. 6, no. 1, 2015.

[24] C. Iadecola, "The neurovascular unit coming of age: a journey through neurovascular coupling in health and disease," *Neuron*, vol. 96, no. 1, pp. 17–42, 2017.

[25] Z. G. Zhang, B. Buller, and M. Chopp, "Exosomes-beyond stem cells for restorative therapy in stroke and neurological injury," *Nature Reviews Neurology*, vol. 15, no. 4, pp. 193–203, 2019.

[26] E. Z. Longa, P. R. Weinstein, S. Carlson, and R. Cummins, "Reversible middle cerebral artery occlusion without craniectomy in rats," *Stroke*, vol. 20, no. 1, pp. 84–91, 1989.

[27] Y. Zhang, M. Chopp, Z. G. Zhang et al., "Systemic administration of cell-free exosomes generated by human bone marrow derived mesenchymal stem cells cultured under 2D and 3D conditions improves functional recovery in rats after traumatic

brain injury," *Neurochemistry International*, vol. 111, pp. 69–81, 2017.

[28] N. Kawaguchi, T. T. Zhang, and T. Nakanishi, "Involvement of CXCR4 in normal and abnormal development," *Cells*, vol. 8, no. 2, p. 185, 2019.

[29] W. D. Hill, D. C. Hess, A. Martin-Studdard et al., "SDF-1 (CXCL12) is upregulated in the ischemic penumbra following stroke: association with bone marrow cell homing to injury," *Journal of Neuropathology and Experimental Neurology*, vol. 63, no. 1, pp. 84–96, 2004.

[30] T. Chu, L. B. E. Shields, Y. P. Zhang, S.-Q. Feng, C. B. Shields, and J. Cai, "CXCL12/CXCR4/CXCR7 chemokine axis in the central nervous system: therapeutic targets for remyelination in demyelinating diseases," *The Neuroscientist*, vol. 23, no. 6, pp. 627–648, 2017.

[31] J. Chen and M. Chopp, "Exosome therapy for stroke," *Stroke*, vol. 49, no. 5, pp. 1083–1090, 2018.

[32] P. Rowart, P. Erpicum, O. Detry et al., "Mesenchymal stromal cell therapy in ischemia/reperfusion injury," *Journal of Immunology Research*, vol. 2015, Article ID 602597, 8 pages, 2015.

[33] H. Shichinohe, S. Kuroda, S. Yano, K. Hida, and Y. Iwasaki, "Role of SDF-1/CXCR4 system in survival and migration of bone marrow stromal cells after transplantation into mice cerebral infarct," *Brain Research*, vol. 1183, pp. 138–147, 2007.

[34] R. H. Lee, A. A. Pulin, M. J. Seo et al., "Intravenous hMSCs improve myocardial infarction in mice because cells embolized in lung are activated to secrete the anti-inflammatory protein TSG-6," *Cell Stem Cell*, vol. 5, no. 1, pp. 54–63, 2009.

[35] S. Kalimuthu, J. M. Oh, P. Gangadaran et al., "In vivo tracking of chemokine receptor CXCR4-engineered mesenchymal stem cell migration by optical molecular imaging," *Stem Cells International*, vol. 2017, Article ID 8085637, 10 pages, 2017.

[36] S.-Z. Wu, Y.-L. Li, W. Huang et al., "Paracrine effect of CXCR4-overexpressing mesenchymal stem cells on ischemic heart injury," *Cell Biochemistry and Function*, vol. 35, no. 2, pp. 113–123, 2017.

[37] X.-B. Zheng, X.-W. He, L.-J. Zhang et al., "Bone marrow-derived CXCR4-overexpressing MSCs display increased homing to intestine and ameliorate colitis-associated tumorigenesis in mice," *Gastroenterology Report*, vol. 7, no. 2, pp. 127–138, 2019.

[38] Z. G. Zhang and M. Chopp, "Exosomes in stroke pathogenesis and therapy," *The Journal of Clinical Investigation*, vol. 126, no. 4, pp. 1190–1197, 2016.

[39] W. Wang, Z. Li, and J. Feng, "The potential role of exosomes in the diagnosis and therapy of ischemic diseases," *Cytotherapy*, vol. 20, no. 10, pp. 1204–1219, 2018.

[40] T. Tian, H.-X. Zhang, C.-P. He et al., "Surface functionalized exosomes as targeted drug delivery vehicles for cerebral ischemia therapy," *Biomaterials*, vol. 150, pp. 137–149, 2018.

[41] Y. Serlin, I. Shelef, B. Knyazer, and A. Friedman, "Anatomy and physiology of the blood-brain barrier," *Seminars in Cell & Developmental Biology*, vol. 38, pp. 2–6, 2015.

[42] M. D. Sweeney, Z. Zhao, A. Montagne, A. R. Nelson, and B. V. Zlokovic, "Blood-brain barrier: from physiology to disease and back," *Physiological Reviews*, vol. 99, no. 1, pp. 21–78, 2019.

[43] Y. Döring, H. Noels, E. P. C. van der Vorst et al., "Vascular CXCR4 limits atherosclerosis by maintaining arterial integrity: evidence from mouse and human studies," *Circulation*, vol. 136, no. 4, pp. 388–403, 2017.

[44] J.-P. Piret, D. Mottet, M. Raes, and C. Michiels, "CoCl2, a chemical inducer of hypoxia-inducible factor-1, and hypoxia reduce apoptotic cell death in hepatoma cell line HepG2," *Annals of the New York Academy of Sciences*, vol. 973, no. 1, pp. 443–447, 2002.

Hindawi
Neural Plasticity
Volume 2020, Article ID 8875915, 9 pages
https://doi.org/10.1155/2020/8875915

*Review Article*

# Comparison of Different In Vivo Animal Models of Brachial Plexus Avulsion and Its Application in Pain Study

**Hang Xian**,[1,2] **Rougang Xie**,[2] **Ceng Luo**,[2] **and Rui Cong**[1]

[1]*Department of Orthopedics, Xijing Hospital, Fourth Military Medical University, Xi'an 710032, China*
[2]*Department of Neurobiology, School of Basic Medicine, Fourth Military Medical University, Xi'an 710032, China*

Correspondence should be addressed to Ceng Luo; luoceng@fmmu.edu.cn and Rui Cong; congrui@fmmu.edu.cn

Received 16 September 2020; Revised 26 October 2020; Accepted 29 October 2020; Published 12 November 2020

Academic Editor: Zhongyu Li



Brachial plexus injuries (BPIs) are high-energy trauma that can result in serious functional problems in the affected upper extremities, and brachial plexus avulsion (BPA) could be considered the most severe type of them. The booming occurrence rate of BPA brings up devastating impact on patients' life. Complications of muscle atrophy, neuropathic pain, and denervation-associated psychological disorders are major challenges in the treatment of BPA. Animal models of BPA are good vehicles for this kind of research. Full understanding of the current in vivo BPA models, which could be classified into anterior approach avulsion, posterior approach avulsion, and closed approach avulsion groups, could help researchers select the appropriate type of models for their studies. Each group of the BPA model has its distinct merits and demerits. An ideal BPA model that can inherit the advantages and make up for the disadvantages is still required for further exploration.

## 1. Introduction

Brachial plexus injury (BPI), which is usually found as the result of posttrauma due to accelerated attacks of the head, neck, and upper limbs, often causes serious functional problems in the affected upper extremities, along with other concomitant injuries to adjacent structures [1, 2]. Most brachial plexus injuries in children that occur during delivery as a result of a traumatic childbirth are known as obstetric brachial plexus palsy (OBPP). The incidence of OBPP ranges from 0.42 to 3 per 1000 live births in Europe as reported [3], while the incidence of adult BPI is still unknown [4]. One retrospective study identified 54 patients of BPI in 4538 (1.2%) patients presenting to a regional trauma facility [5]. The mean age of the patients was 29 years with a male predominance of 89%, while motorcycle and snowmobile accidents were two major causes of adult BPI. Therefore, a distinction between adult versus obstetric BPI should be made for different treatment strategies.

BPI may be described as a traction, rupture, or avulsion injury [6–8]. In a traction injury, the nerve is stretched but not torn from the spinal cord. The degree of injury could vary from neurapraxia and axonotmesis to neurotmesis. In a rupture injury, the nerve is severely stretched and partially or completely torn, which leaves the rupture part outside the spinal column but not the spinal cord, while the attachment of the dorsal root ganglion (DRG) is still intact to the spinal cord (postganglionic lesion) in this type. When the attachment of nerve rootlets is directly torn from the spinal cord, an avulsion injury (preganglionic lesion) happened. This type of avulsion injury is the most serious type of BPI anatomically.

Brachial plexus avulsion (BPA) always requires a tremendous amount of stretching force and is often combined with multiple injuries of the affected limb or others, which is considered the most severe type injury of the upper limb [9]. The occurrence rate of avulsion of one or more roots from the spinal cord, which can be defined as brachial plexus root avulsion, reaches up to approximately 70% in BPA [1]. Because of the concomitant injury to adjacent structures, especially to the spinal cord or principal arteries, prehospital emergency treatment and advanced life support are always needed in the management of this devastating injury. Due to which, early diagnosis of BPA has often been masked.

Motor dysfunction and skin anesthesia of the upper limb are the main symptoms of BPA, and total loss of these functions is often observed on the global avulsion patients who are carrying paralyzed upper limbs. As both of peripheral and central nervous systems are involved in this root avulsion injury, BPA may pose its unique characteristics during the whole pathophysiological process.

Muscle atrophy due to chronic denervation and misdirection of regenerating axons, which finally results in poor motor function of the affected limb, is still the main complication of BPA, although much effort has been made in the treatment procedure of nerve reconstruction [10]. The lack of adequate proximal intraplexus donors (roots) in continuity with the spinal cord is still a thorny issue that the reconstructive surgeons must face [11]. Dorsal root avulsion brings up permanent impairment of sensory functions due to disconnection between the peripheral and central nervous system. The frequency of the development of neuropathic pain after BPA is also another great issue that brings a devastating consequence to BPA patients. The features, such as systemic mechanical and thermal hyperalgesia, which appear immediately after the injury and produce long-lasting pain behavior, and the following pathological plasticity of the central and peripheral nervous systems are triggered by a series of cytokine cascades [12–14]. All the reactivity above will finally achieve a stable and long-lasting neuropathic pain, and the BPA patients are more susceptible to such neuropathic pain with an incidence rate of 50% in BPIs up to 90% in BPAs according to epidemic data [8, 15, 16].

Big challenges on the process of BPA treatment including prevention of nerve degeneration, recovery of limb sensation, and management of neuropathic pain still exist, although lots of efforts have been made. To address these issues, several animal models have been established with attempts to simulate the injury mechanisms of BPA, and most of them are useful in the experimental studies of the pathological process of this injury. Animal models have made great contributions to the field of spotting a novel treatment target and characterizing specific medications. Among the current BPA models, different species, including rat, mice, and rabbit, are well designed to mimic the avulsion mechanism and pathological state like those in BPA patients. These models could be classified into three categories according to different surgical approaches, which include the anterior approach avulsion, the posterior approach avulsion, and the closed approach avulsion. It is very difficult for researchers to select a consummate model to match their experiments, so special attention has been paid in this review to the merits and demerits of each approach of the in vivo BPA models.

## 2. The Anatomy of the Brachial Plexus

The basic feature of the brachial plexus is formed by the anterior spinal nerves from the four lowest cervical roots and the first thoracic root despite significant intra- and interindividual variability [17]. After punch out from the intervertebral foramen, these five nerve roots (C5-T1) form the brachial plexus between the scalenus anterior and the scalenus medius muscles. The brachial plexus could be divided into five different segments according to specific anatomy landmarks, which are roots, trunks, divisions, cords, and branches [18]. The spinal roots unite to form three trunks including the upper trunk (C5 and C6), middle trunk (C7), and lower trunk (C8 and T1). Two terminal nerve branches emerge at the root level including the dorsal scapular nerve (C4-5) and the long thoracic nerve (C5-7), which supplies the levator scapulae and rhomboid muscles, and the serratus anterior muscle, respectively. After travelling posterior to the clavicle, each trunk then divides into two divisions including anterior division and posterior division. Two terminal nerve branches emerge at the trunk level including the suprascapular nerve (C5-6) and the nerve to the subclavius muscle (C5-6). The suprascapular nerve arises from the superolateral aspect of the upper trunk, the location of which is referred to as Erb's point. After the brachial plexus has become infraclavicular distal to the clavicle, the anterior divisions of the upper and middle trunks form the lateral cord, while the lower trunk becomes the medial cord. The posterior divisions of every trunk form the posterior cord by contributing different proportions of spinal roots. The anatomic relationship among the cords and the second part of the axillary artery is the reference standard of the naming of them, and all of them are located posterior to the pectoralis minor muscle. Finally, five main terminal branches including radial nerve, axillary nerve, ulnar nerve, musculocutaneous nerve, and median nerve are formed to govern the motor and sensation of the upper limb.

Anatomically speaking, one species of animal, which could be the most suitable one in BPA modeling, should firstly meet the similarity of the anatomical structure with that of a human being. Bogusch [19] has reported that mice have similar brachial plexus anatomy as humans, which is also built up by spinal nerves C5-C8 and T1. Even if there is some anatomical variation, constant nerve root composition of the mouse brachial plexus is adequate for research use. A rat's brachial plexus also has similar anatomic structure as that of humans, which has been verified by researchers [20, 21]. Similar work has been done on rabbits, and the anatomy results are similar to those of mice and rats [22]. Secondly, an easier operation performance seems to be another issue in animal model selection. During the process of mouse modeling, all procedures should be completed under a microscope for higher precision. This kind of difficulty may not exist in bigger rodents like rats or rabbits. Finally, an easy animal acquisition and convenient management are also of great importance in animal selection. Nevertheless, mouse and rat models are still the most popular BPA models in the field of BPA researches, which will be fully reviewed in the latter parts.

## 3. Three Approaches of the Animal Avulsion Modeling Procedure

### *3.1. Anterior Approach Avulsion*

*3.1.1. Procedure.* One representative surgical method of the anterior approach avulsion is from the research of Rodrigues-Filho et al. [23] in 2003, which is a lower trunk

(C8-T1) rat BPA model. Briefly, the rat was placed on an operating table in supine position after intraperitoneally injecting anesthesia. A horizontal incision parallel to the clavicle, which ran from the sternum to the axillary region, was made for a clear view of the right brachial plexus. The cephalic vein should be carefully protected after the pectoralis major muscle was displaced. The division and cord part of the brachial plexus, which was wrapped in an axillary sheath together with a brachial artery, could be observed after a deeper anatomy in the anterior margin of the pectoralis minor. Trace to the proximal end till the vertebral foramen where the C5-C8 and T1 branches were exited, and the lower trunk of the brachial plexus was carefully identified and dissected. The lower trunk was grasped with forceps and extracted from the spinal cord by steady moderate traction. Tissue layers were finally brought together, and the skin was sutured. The mark of a successful avulsion is the visibility of the corresponding DRGs of the nerve roots. A similar BPA model procedure adapted for mice was performed by Quintão et al. [24] in their research.

*3.1.2. Current Research Focus.* On the BPA model exploration part, single lower trunk avulsion may not meet the clinical and scientific needs for further studies. Li et al. [25] reported a global avulsion of the brachial plexus by using a similar method above for the study of motor neuron apoptosis. Thereafter, a novel BPA rat model of the upper trunk was designed by Liu et al. [26], which showed a persistent neuropathic pain behavior in ipsilateral and contralateral limbs, and may be a suitable animal model for neuropathic pain research. One C7 root avulsion by forceps of a rat model was invented to study the neuroprotective effect of minocycline via different routes [27]. On the research exploration part, BPA models are widely used in the study of BPA-induced neuropathic pain. Avulsion of the brachial plexus in a rat produces persistent mechanical and cold allodynia and mechanical hyperalgesia, all of which are the characteristics of neuropathic pain [23, 28]. Quintão et al. [13] found that neurotrophic factor blockers might represent a new and interesting option for the management of neuropathic pain. Paszcuk et al. [29] reported that cannabinoid agonists could inhibit neuropathic pain induced by BPA which could be a new analgesic target. Similar work has been done by Kobayashi et al. [30] on the application of the p75NTR inhibitory antibody and Zhao and Wu [31] on histone deacetylase inhibition to suppress neuropathic pain after BPA. Recent work on level changes of microRNA could supply other new ideas in BPA-induced neuropathic pain treatment [32], and enhancer of zeste homolog 2 (EZH2) was proven to be a novel regulator of neuroinflammation and neuropathic pain via the mTOR signaling pathway in the anterior cingulate cortex, which could be another target of pain treatment [33]. In other words, an anterior approach BPA model of mice or rats at any trunk of the brachial plexus could be implemented and become a good model of related research, especially on the research in the neuropathic pain field.

*3.1.3. Merits and Demerits.* In this group, the first merit is that the whole anterior procedure could be completed through a smaller incision with little hemorrhage and high security. Second, this approach could get a better view of the total brachial plexus roots, especially the middle and lower trunks, which could help the researchers perform the avulsion procedure conveniently. Then, the force direction of avulsion in this position could well simulate the injury of BPA patients, and whether the avulsion is successful or not could be evaluated by the vision of corresponding DRGs directly during the modeling procedure. Meanwhile, there are also some demerits. Forceps are used to hold the trunk before avulsion, and this kind of clamping force could cause the first step injury to the nerves. Whether this kind of force has an effect on model assessment or not remains inconclusive. In terms of pain behavioral tests, all the tests are performed on other extremities except the avulsion one. Whether this indirect pain response can represent the real pain state of BPA models is still unknown.

To compensate for the shortcomings above, our research group has designed a novel anterior approach BPA model of mice, which is the seventh cervical nerve root (C7) avulsion model. This novel C7 single root avulsion mouse model could not only well mimic the mechanism of the avulsion injury like that in patients but also show a persistent pathological status of neuropathic pain like that in the anterior avulsion models used above. During avulsion operation, we replaced the forceps by a soft silk thread to hook the C7 nerve root and then performed the avulsion, which eliminated the first step injury to the nerves (Figure 1). The behavioral tests including mechanical allodynia and cold hyperalgesia of the ipsilateral fore paw, contralateral fore paw, and ipsilateral hind paw showed that this pain state could last for 28 days after modeling without affecting the grasp force of the fore paw [34]. This direct pain detection and evaluation through tests of the affected fore paw could supply more direct evidence of the neuropathic pain status induced by BPA than other anterior approach models.

### 3.2. Posterior Approach Avulsion

*3.2.1. Procedure.* Primarily, a posterior approach of BPA is introduced for the research of root reimplantation into the spinal cord for repair of the avulsed brachial plexus nerve roots [21]. The procedure is described briefly as follows. The rat was placed on an operating table in prone position after intraperitoneally injecting anesthesia. A 3-5 cm length skin incision through the dorsal midline of the rat was made, and the paraspinal muscles were segregated with a pair of ophthalmic scissors. The prominent spinous process of the C7 vertebrae was used as a landmark; the hemilaminectomy from C4 to T1 on the right was performed to expose the spinal cord through a posterior surgical approach. After adequate hemostasis, the target roots (like C5-T1) of the brachial plexus is identified and confirmed. Then, target roots were avulsed from the spinal cord with a micronerve hook. A successful avulsion could be directly observed under the naked eyes or microscope. Tissue layers were finally brought together, and the skin was sutured after adequate hemostasis again. The ventral and/or dorsal roots of each spinal nerve could be observed clearly in this posterior approach, so a

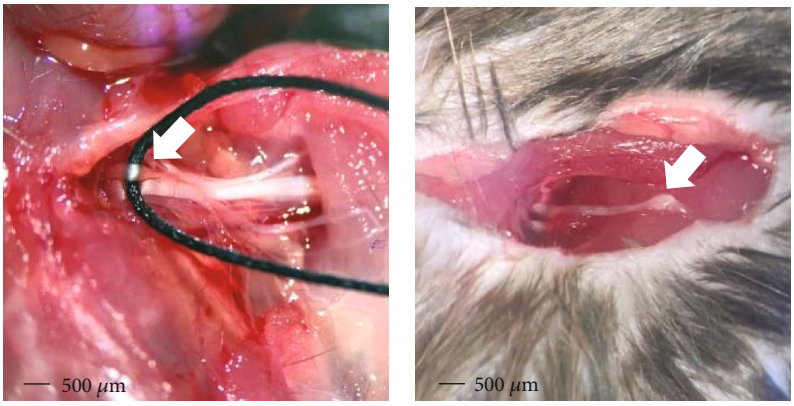


(a) (b)

Figure 1: Surgical procedure of the novel C7 single root avulsion mouse model through an anterior approach: (a) a soft silk thread was used to hook the C7 nerve root for the preparation of avulsion injury (white arrow); (b) the avulsed C7 nerve root where the DRG of this root could be observed (white arrow).

precise ventral or dorsal root level of avulsion also could be achieved through it.

*3.2.2. Current Research Focus.* Similar to an anterior approach, there are also different root combination avulsion by this posterior approach, as Muñetón-Gómez et al. [35] reported a rat model of global BPA through a posterior approach which was used to evaluate the regeneration and reparative therapy of BPA. More precise avulsion of rats' C7 root by Sim et al. [36] and C8 root by Gu et al. [37] was used to evaluate the neuroprotective effect of paclitaxel in the prevention of motoneuron death and mitochondrial dysfunction and to investigate the survival, regeneration, and functional recovery of motor neuron by reimplantation of the ventral root method. Another pediatric pig avulsion model of upper and middle trunks through this approach was used to describe the functional and neuropathological outcome following BPA, with or without spinal cord injury [38]. Similar rat or mouse models of upper-middle trunk and global trunk avulsion were successively reported to expound the mechanism of motor neuron degeneration and/or to evaluate different repair and reconstruction methods [39–41]. A most recent research of Huang et al. [42] reported that the temperature-sensitive quercetin-loaded PLGA-PEG-PLGA hydrogel sustained-release system could promote nerve regeneration and motor function recovery during the early stage of BPA due to its intrinsic function of anti-inflammation, which had a good prospect from bench to bedside translation. Meanwhile, the posterior approach models also could be used in the field of neuropathic pain research according to recent work. Hou and Xu [43] reported that the activation of astrocytes and microglia in the spinal cord played a key role in a rat model of global BPA. Meng et al. [44] found that reduced lncRNA Malat1 expression might induce neuropathic pain by increasing neuronal excitability in the spinal cord via regulation of calcium flux, and Huo et al. [45] reported the beneficial effects of electroacupuncture for relieving neuropathic pain in global BPA rats and also explored its function in brain plasticity. It appears that more and more researches on higher central nervous systems based on this kind of BPA models are emerging to further elucidate the networks of sensory information processing [15, 46]. While the search for the improvement of such models have not stopped, Fang et al. [47] invented a new method through using a weight attached to the forceps or hook during avulsion to achieve a better conditional homogeneity and the initial results were preferable. In a word, a posterior approach BPA model of mice or rats appears to be more popular in exploration of the motor neuron-associated mechanisms and reconstruction procedure evaluation.

*3.2.3. Merits and Demerits.* In this group, the avulsion roots could be definitely confirmed by boney landmarks of cervical vertebrae, and more precise ventral and/or dorsal root avulsion could be easily achieved through this approach. Then, root replantation or other reconstruction operations could be implemented through this approach. Despite the merits above, there are still some demerits. Bigger incision and wound of this approach increase the risk of hemorrhage and cerebrospinal fluid leakage. The hemilaminectomy performed not only can affect the stability of the spinal cord but also can bring up serious complications like paraplegia and death of animals. The avulsion through this approach cannot well simulate the avulsion injury of BPA patients, which may be the reason that studies based on this kind of models are more in the field of motor neuron degeneration and reconstruction compared with the anterior approach ones.

### *3.3. Closed Approach Avulsion*

*3.3.1. Procedure.* In 2000, Spinner et al. [48] established a rat model of BPA using passive acceleration, which could be classified as the closed avulsion approach. In brief, the rat was placed on its right side within a specially designed tube (6 cm in diameter) after intraperitoneally injecting anesthesia. The right forelimb protruded from an oval cutout on the undersurface of the tube. The limb made an approximately vertical angle with the front and back of the torso in this position. Then, the elbow was placed in a designed metal

sleeve which was tightly fixed to a lever arm. The force was applied four times in distance from the fulcrum as the sleeve so that the forelimb supported the weight of the lever arm. An instantaneous force was applied to the limb by dropping a precast test weight down the guide rod from a height (about 30 cm) onto the lever to simulate the injury mechanism like that in patients. The animals were sacrificed to confirm the effect of avulsion. A similar close avulsion rat model was established by Yang et al. [49] through using a specially made model making apparatus.

*3.3.2. Current Research Focus.* Closed avulsion models seem to be the ideal in vivo models of BPA, and they may well simulate the injury mechanism like that in BPA patients. Nevertheless, there is still little research on the mechanism study by using this noninvasive models, and the existing models are confined only to rat species. Further studies are called for on this model with an expectation on producing reliable preclinical evidence in the field of therapeutic strategy exploration and assessment of BPA.

*3.3.3. Merits and Demerits.* Compared with the invasive group above, this noninvasive approach method could be considered the unique merit of this group. The force pattern that induces the avulsion injury could perfectly mimic the avulsion force like the injury experiences of BPA patients. This closed approach requires a series of avulsion facilities and complicated operations which may bring up a longer learning curve of this technique. Precise avulsion of any specific trunk is difficult to be achieved during modeling, and definite avulsion level of roots or trunks is difficult to be evaluated after modeling, both of which may be the obvious demerits of this avulsion approach.

For the detailed overview of the in vivo models of brachial plexus avulsion, refer to Table 1.

## 4. BPA-Induced Neuropathic Pain and Treatment

As the injury mechanisms of BPA is different from other kinds of BPI, in which both the peripheral nervous system and the central nervous system are directly involved at the initial avulsion, therefore, the complications following BPA should be treated differently. Neuropathic pain often develops after the lesion or disease affecting the somatosensory nervous system [50, 51], which could be of central or peripheral origin depending on the location of the lesion or disease [52]. The main clinical symptoms of neuropathic pain include spontaneous pain, hyperalgesia, and allodynia of the affected limb [53], which does not usually respond to general analgesics or which responds only to a small extent. This kind of chronic pathological pain state often not only represents a challenge to clinical practice and basic science but also brings up devastating impact on patients' life [54]. Pain following avulsion injury of the brachial plexus has been early recognized [55], which is considered the most distressing complications of it. It is reported that the incidence of chronic pain following BPI is as high as 50% [56, 57] and even up to 80% [58], and similar incidence rate was also reported in BPAs [59, 60]. The underlying various physiological and pathological mechanisms of the BPA injury are far to be elucidated which may be the main reason for its intractable management.

Previous studies suggested that this neuropathic pain induced by BPA might be alleviated through surgeries including successful nerve transfer procedures to restore limb functions and dorsal root entry zone (DREZ) lesions. As reported by Berman et al. [61], pain reduction might anticipate functional recovery following nerve transfer strategies for BPA and the underlying mechanism might include successful regeneration and/or restoration of peripheral connections prior to their function, especially in the muscle. BPA models of the posterior approach are widely used in this area to investigate the underlying mechanism of motor neuron degeneration and pain and test the treatment effect of different reconstruction strategies and its profound mechanisms [37, 40, 41]. Multiple evidences of experimental and clinical background suggest that the spinal dorsal horn (SDH) is at least the partial location of the pain generator after BPA occurred due to deafferentation [62, 63], so surgeries targeting the location of SDH, especially the DREZ, are supposed to be effective in the treatment of neuropathic pain after BPA. It is reported that neuropathic pain induced by the dorsal horn deafferentation by cervical posterior rhizotomy was successfully relieved through microsurgical DREZ rhizotomy/coagulation [64]. A long-term follow-up study in patients with deafferentation pain due to BPA showed pain relief gradually decreased over 5 years after surgery [65], and similar satisfactory treatment effect has been achieved in other studies [66, 67]. Other therapeutic attempts through surgical procedures also emerged in recent years, which include motor cortex stimulation, thalamic deep brain stimulation, spinal cord stimulation, and DRG stimulation [68–72], and the treatment effects seem satisfying as far as it goes.

The current analgesic treatment for neuropathic pain according to the guidelines include the calcium channel acting as anticonvulsants pregabalin and gabapentin, tricyclic antidepressants, and serotonin-noradrenalin-reuptake inhibitors (duloxetine, venlafaxine), which are the first-line treatment recommendations [52, 73], while the search for better chemical compounds to treat neuropathic pain is still going on. The analgesic effect of the reported researches is still ambiguous [74], which may be due to the reason that the mechanisms of neuropathic pain are a complex pathophysiological process involving multiple anatomy levels that remains to be elucidated. In vivo BPA models are ideal carriers in the field of treatment target selection and assessment. As reported by Quintão and his colleagues [12], selective $B_1R$ antagonists might well represent valuable tools for neuropathic pain management. Our previous work has been done on the molecules, including cyclic GMP-dependent protein kinase-I (PKG-1), CCL2/CCR2, and canonical transient receptor potential channels (TRPC) [75–78], which showed the potential on the treatment of neuropathic pain, but whether this kind of molecules shares the same pathophysiological functions in different BPA-induced neuropathic pain still needs further studies. Therapeutic strategies for the treatment of neuropathic pain are always limited by its elusive

Table 1: Detailed overview of the in vivo models of brachial plexus avulsion.

| Surgical approach | Authorship | Publication year | Species | Type of avulsion | Research field | Refs |
|---|---|---|---|---|---|---|
| Anterior avulsion approach | Rodrigues-Filho et al. | 2003 | Rats | C8-T1 roots | Neuropathic pain | [23] |
| | Quintão et al. | 2008<br>2006 | Mice | C8-T1 roots | Neuropathic pain | [13, 24] |
| | Li et al. | 2015 | Rats | C5-T1 roots | SC motor neuron apoptosis | [25] |
| | Liu et al. | 2016 | Rats | C5-C6 roots<br>C5-T1 roots | Neuropathic pain | [26] |
| | Tan et al. | 2017 | Rats | C7 root | Neuroprotective effect | [27] |
| | Wang et al. | 2015 | Rats | C5-T1 roots | Neuropathic pain | [28] |
| | Paszcuk et al. | 2011 | Mice | C8-T1 roots | Neuropathic pain | [29] |
| | Kobayashi et al. | 2015 | Rats | C8-T1 roots | Neuropathic pain | [30] |
| | Zhao et al. | 2018 | Rats | C8-T1 roots | Neuropathic pain | [31] |
| | Liu et al. | 2018 | Rats | C5-T1 roots | Neuropathic pain | [32] |
| | Meng et al. | 2020 | Rats | C5-T1 roots | Neuropathic pain | [33] |
| | Zhang et al. | 2020 | Mice | C7 root | Neuropathic pain | [34] |
| Posterior avulsion approach | Cao et al. | 2003 | Rats | N. S. | Anatomic and technical exploration | [21] |
| | Muñetón-Gómez et al. | 2004 | Rats | C3-T3 roots | Nerve regeneration | [35] |
| | Sim et al. | 2015 | Rats | C7 root | SC motor neuron protection | [36] |
| | Gu et al. | 2004 | Rats | C8 root | SC motor neuron regeneration | [37] |
| | Zarina et al. | 2016 | Pigs | C5-C7 roots | Neuropathological characteristics | [38] |
| | Zhang et al. | 2017 | Rats | C5-T1 roots | Motor cortical reorganization | [39] |
| | Chen et al. | 2019 | Mice | C5-C7 roots | SC motor neuron protection | [40] |
| | Zhang et al. | 2019 | Rats | C5-C7 roots | SC motor neuron protection and reconstruction methods | [41] |
| | Huang et al. | 2020 | Rats | C5-C7 roots | Nerve regeneration | [42] |
| | Hou et al. | 2018 | Rats | C5-T1 roots | Neuropathic pain | [43] |
| | Meng et al. | 2019 | Rats | C5-T1 roots | Neuropathic pain | [44] |
| | Huo et al. | 2020 | Rats | C5-T1 roots | Neuropathic pain | [45] |
| | Wang et al. | 2019 | Rats | C5-T1 roots | Neuropathic pain | [15] |
| | Shen et al. | 2019 | Rats | C5-T1 roots | Neuropathic pain | [46] |
| | Fang et al. | 2017 | Rats | C5-T1 roots | SC motor neuron protection | [47] |
| Closed avulsion approach | Spinner et al. | 2000 | Rats | N. S. | Model establishment | [48] |
| | Yang et al. | 2015 | Rats | N. S. | Model establishment | [49] |

N. S. refers to the idea that there is no specific root avulsion statement or the ratio of different types of avulsion roots was analyzed in the articles. SC: spinal cord.

mechanisms and the incomplete understanding of nervous system plasticity after the initial injury [79], so we still need to search for different targets to treat this pain. Researches targeting the gene level have emerged with the development of genomics, and the results of the preliminary investigations seemed promising based on BPA models [32, 33, 44], which may be another novel route of the BPA treatment.

Personally speaking, I still call for further improvement of the innovation in BPA modeling to inherit the advantages and make up for the disadvantages. In terms of the existing models, studies on mouse models are relatively scarce. Operations on mouse models may require a higher micromanipulation technique, but characteristics of mouse gene polymorphism, which allows us to use genetic tools and to conduct experiments at the gene therapy level, could make up for its shortcomings to a great extent. In terms of neuropathic pain, models that could well simulate the characteristics of BPA-induced neuropathic pain which could be directly detected and evaluated by associated tests on the affected extremity will better help us in understanding its mechanism and finally guide the choice of treatment. Although there is not absolutely the same model, the accurate reproduction of models is also an issue that needs to be seriously considered during new model design.

## 5. Conclusion

Brachial plexus avulsion injuries are defined as devastating life-altering injuries which could cause multiple complications like extremity disabilities, intractable pain, and negative

emotions. The underlying elusive mechanisms make it difficult to be cured. Selecting suitable in vivo animal models that share an extremely similar injury mechanism, pathophysiological process, and recovery potential as humans not only can help us clarify the mechanisms better but also can facilitate the translation of basic science to the clinical settings. The current in vivo animal models of BPA could meet the initial requirements of both scientific and clinical researches, while there is still need for more advanced BPA models in the future to best match the needs to help researchers explore the further prognosis of the avulsion injuries and finally benefit the BPA patients.

## Abbreviations

BPI: Brachial plexus injury
OBPP: Obstetric brachial plexus palsy
DRG: Dorsal root ganglion
BPA: Brachial plexus avulsion
DREZ: Dorsal root entry zone
PKG-1: Cyclic GMP-dependent protein kinase-I
CCL2: C-C motif ligand 2
CCR2: C-C chemokine receptor type 2
TRPC: Canonical transient receptor potential.

## Data Availability

All data used in this study are available from the corresponding authors by request at "congrui@fmmu.edu.cn" and "luoceng@fmmu.edu.cn."

## Conflicts of Interest

The authors declare no conflict of interest, financial or otherwise.

## Authors' Contributions

Hang Xian and Rougang Xie contributed equally to this work.

## Acknowledgments

This work was supported by grants from the National Natural Science Foundation of China (No. 81870867) and National Science Foundation of Shaanxi Province of China (2019SF-071) to R.G.X., NSFC grants (31671088, 31471059) and grants from the National Science Foundation of Shaanxi Province of China (No. 2017ZDJC-01) to C.L., and grants from the National Natural Science Foundation of China (No. 82072526) and Key Research and Development Projects of Shaanxi Province (No. 2017ZDXMSF062) to R.C.

## References

[1] S. Zhao, Y. Pang, R. W. Beuerman, H. W. Thompson, and D. G. Kline, "Expression of c-Fos protein in the spinal cord after brachial plexus injury: comparison of root avulsion and distal nerve transection," *Neurosurgery*, vol. 42, no. 6, pp. 1357–1362, 1998.

[2] S. S. Noland, A. T. Bishop, R. J. Spinner, and A. Y. Shin, "Adult traumatic brachial plexus injuries," *Journal of the American Academy of Orthopaedic Surgeons*, vol. 27, no. 19, pp. 705–716, 2019.

[3] K. W. Chang, D. Justice, K. C. Chung, and L. J. Yang, "A systematic review of evaluation methods for neonatal brachial plexus palsy," *Journal of Neurosurgery Pediatrics*, vol. 12, no. 4, pp. 395–405, 2013.

[4] Á. B. Cho, A. C. Guerreiro, C. H. V. Ferreira, L. Y. Kiyohara, and L. Sorrenti, "Epidemiological study of traumatic brachial plexus injuries," *Acta Ortopédica Brasileira*, vol. 28, no. 1, pp. 16–18, 2020.

[5] R. Midha, "Epidemiology of brachial plexus injuries in a multitrauma population," *Neurosurgery*, vol. 40, no. 6, pp. 1182–1189, 1997.

[6] S. Arzillo, K. Gishen, and M. Askari, "Brachial plexus injury," *The Journal of Craniofacial Surgery*, vol. 25, no. 4, pp. 1200–1206, 2014.

[7] W. Pondaag and M. J. A. Malessy, "Intercostal and pectoral nerve transfers to re-innervate the biceps muscle in obstetric brachial plexus lesions," *The Journal of Hand Surgery, European Volume*, vol. 39, no. 6, pp. 647–652, 2014.

[8] M. J. Teixeira, M. G. S. da Paz, M. T. Bina et al., "Neuropathic pain after brachial plexus avulsion - central and peripheral mechanisms," *BMC Neurology*, vol. 15, no. 1, 2015.

[9] A. G. Coran, A. Simon, F. Heimberg, and N. Beberman, "Avulsion injury of the brachial plexus," *American Journal of Surgery*, vol. 115, no. 6, pp. 840–842, 1968.

[10] W. Sulaiman and T. Gordon, "Neurobiology of peripheral nerve injury, regeneration, and functional recovery: from bench top research to bedside application," *The Ochsner Journal*, vol. 13, no. 1, pp. 100–108, 2013.

[11] J. K. Terzis, M. D. Vekris, and P. N. Soucacos, "Brachial plexus root avulsions," *World Journal of Surgery*, vol. 25, no. 8, pp. 1049–1061, 2001.

[12] N. L. M. Quintao, G. F. Passos, R. Medeiros et al., "Neuropathic pain-like behavior after brachial plexus avulsion in mice: the relevance of kinin B1 and B2 receptors," *The Journal of Neuroscience*, vol. 28, no. 11, pp. 2856–2863, 2008.

[13] N. L. Quintão, A. R. Santos, M. M. Campos, and J. B. Calixto, "The role of neurotrophic factors in genesis and maintenance of mechanical hypernociception after brachial plexus avulsion in mice," *Pain*, vol. 136, no. 1, pp. 125–133, 2008.

[14] H. Xian, Y. Jiang, H. Zhang, S. B. Ma, R. Zhao, and R. Cong, "CCL2-CCR2 axis potentiates NMDA receptor signaling to aggravate neuropathic pain induced by brachial plexus avulsion," *Neuroscience*, vol. 425, pp. 29–38, 2020.

[15] S. Wang, Z. Z. Ma, Y. C. Lu et al., "The localization research of brain plasticity changes after brachial plexus pain: sensory regions or cognitive regions?," *Neural Plasticity*, vol. 2019, Article ID 7381609, 10 pages, 2019.

[16] P. Ciaramitaro, M. Mondelli, F. Logullo et al., "Traumatic peripheral nerve injuries: epidemiological findings, neuropathic pain and quality of life in 158 patients," *Journal of the Peripheral Nervous System*, vol. 15, no. 2, pp. 120–127, 2010.

[17] G. Blaauw, R. S. Muhlig, and J. W. Vredeveld, "Management of brachial plexus injuries," *Advances and Technical Standards in Neurosurgery*, vol. 33, pp. 201–231, 2008.

[18] R. Limthongthang, A. Bachoura, P. Songcharoen, and A. L. Osterman, "Adult brachial plexus injury," *The Orthopedic Clinics of North America*, vol. 44, no. 4, pp. 591–603, 2013.

[19] G. Bogusch, "Innervation of the dermatomes in the neck of the mouse," *Cells Tissues Organs*, vol. 129, no. 4, pp. 275–278, 1987.

[20] E. C. Greene, "Anatomy of the rat," *The American Journal of the Medical Sciences*, vol. 27, no. 6, pp. 1–370, 1968.

[21] X. C. Cao and L. J. Ling, "Anatomic basis and technical aspects of a new brachial plexus avulsion injury model in the rat," *Plastic and Reconstructive Surgery*, vol. 111, no. 7, pp. 2488–2490, 2003.

[22] P. Reichert, Z. Kiełbowicz, P. DziĘgiel et al., "The rabbit brachial plexus as a model for nerve repair surgery-histomorphometric analysis," *The Anatomical Record*, vol. 298, no. 2, pp. 444–454, 2015.

[23] R. Rodrigues-Filho, A. R. S. Santos, J. A. Bertelli, and J. B. Calixto, "Avulsion injury of the rat brachial plexus triggers hyperalgesia and allodynia in the hindpaws: a new model for the study of neuropathic pain," *Brain Research*, vol. 982, no. 2, pp. 186–194, 2003.

[24] N. L. Quintão, D. Balz, A. R. Santos, M. M. Campos, and J. B. Calixto, "Long-lasting neuropathic pain induced by brachial plexus injury in mice: role triggered by the pro-inflammatory cytokine, tumour necrosis factor alpha," *Neuropharmacology*, vol. 50, no. 5, pp. 614–620, 2006.

[25] K. Li, R. J. Cao, X. J. Zhu, X. Y. Liu, L. Y. Li, and S. S. Cui, "Erythropoietin attenuates the apoptosis of adult neurons after brachial plexus root avulsion by downregulating JNK phosphorylation and c-Jun expression and inhibiting c-PARP cleavage," *Journal of Molecular Neuroscience*, vol. 56, no. 4, pp. 917–925, 2015.

[26] Y. Liu, L. Wang, C. Meng, Y. Zhou, J. Lao, and X. Zhao, "A new model for the study of neuropathic pain after brachial plexus injury," *Injury*, vol. 48, no. 2, pp. 253–261, 2017.

[27] Y. C. Tan, S. S. Kiat, H. G. Faizul, W. Wu, and J. M. Abdullah, "The effects of minocycline on spinal root avulsion injury in rat model," *Malaysian Journal of Medical Sciences*, vol. 24, no. 1, pp. 31–39, 2017.

[28] L. Wang, L. Yuzhou, Z. Yingjie, L. Jie, and Z. Xin, "A new rat model of neuropathic pain: complete brachial plexus avulsion," *Neuroscience Letters*, vol. 589, pp. 52–56, 2015.

[29] A. F. Paszcuk, R. C. Dutra, K. A. B. S. da Silva, N. L. M. Quintão, M. M. Campos, and J. B. Calixto, "Cannabinoid agonists inhibit neuropathic pain induced by brachial plexus avulsion in mice by affecting glial cells and MAP kinases," *PLoS One*, vol. 6, no. 9, article e24034, 2011.

[30] T. Kobayashi, K. Yamauchi, Y. Matsuura, K. Kuniyoshi, K. Takahashi, and S. Ohtori, "The effects of generally administered anti–nerve growth factor receptor (p75NTR) antibody on pain-related behavior, dorsal root ganglia, and spinal glia activation in a rat model of brachial plexus avulsion," *The Journal of Hand Surgery*, vol. 40, no. 10, pp. 2017–2025, 2015.

[31] Y. Zhao and T. Wu, "Histone deacetylase inhibition inhibits brachial plexus avulsion-induced neuropathic pain," *Muscle & Nerve*, vol. 58, no. 3, pp. 434–440, 2018.

[32] Y. Liu, L. Wang, J. Lao, and X. Zhao, "Changes in microRNA expression in the brachial plexus avulsion model of neuropathic pain," *International Journal of Molecular Medicine*, vol. 41, no. 3, pp. 1509–1517, 2018.

[33] X. L. Meng, P. Fu, L. Wang et al., "Increased EZH2 levels in anterior cingulate cortex microglia aggravate neuropathic pain by inhibiting autophagy following brachial plexus avulsion in rats," *Neuroscience Bulletin*, vol. 36, no. 7, pp. 793–805, 2020.

[34] F. L. Zhang, H. Xian, C. Liang, C. Luo, and R. Cong, "A study on the model of neuropathic pain in mice induced by C7 root avulsion," *Chinese Journal of Hand Surgery*, vol. 36, no. 3, pp. 216–220, 2020.

[35] V. Muñetón-Gómez, J. S. Taylor, S. Averill, J. V. Priestley, and M. Nieto-Sampedro, "Degeneration of primary afferent terminals following brachial plexus extensive avulsion injury in rats," *Biomédica*, vol. 24, no. 2, pp. 183–193, 2004.

[36] S. K. Sim, Y. C. Tan, J. H. Tee, A. A. Yusoff, and J. M. Abdullah, "Paclitaxel inhibits expression of neuronal nitric oxide synthase and prevents mitochondrial dysfunction in spinal ventral horn in rats after C7 spinal root avulsion," *Turkish Neurosurgery*, vol. 25, no. 4, pp. 617–624, 2015.

[37] H. Y. Gu, H. Chai, J. Y. Zhang et al., "Survival, regeneration and functional recovery of motoneurons in adult rats by reimplantation of ventral root following spinal root avulsion," *The European Journal of Neuroscience*, vol. 19, no. 8, pp. 2123–2131, 2004.

[38] Z. S. Ali, V. E. Johnson, W. Stewart et al., "Neuropathological characteristics of brachial plexus avulsion injury with and without concomitant spinal cord injury," *Journal of Neuropathology and Experimental Neurology*, vol. 75, no. 1, pp. 69–85, 2015.

[39] J. Zhang, L. Chen, and Y. D. Gu, "Changes in expressions of major histocompatibility complex class I, paired-immunoglobulin-like receptor B, and cluster of differentiation 3ζ in motor cortical representations of the brachial plexus after avulsion in rats," *World Neurosurgery*, vol. 106, pp. 211–218, 2017.

[40] S. Chen, Y. Hou, Z. Zhao et al., "Neuregulin-1 accelerates functional motor recovery by improving motoneuron survival after brachial plexus root avulsion in mice," *Neuroscience*, vol. 404, pp. 510–518, 2019.

[41] X. Zhang, X. D. Liu, Y. F. Xian et al., "Berberine enhances survival and axonal regeneration of motoneurons following spinal root avulsion and re-implantation in rats," *Free Radical Biology & Medicine*, vol. 143, pp. 454–470, 2019.

[42] C. Huang, C. Fu, Z. P. Qi et al., "Localised delivery of quercetin by thermo-sensitive PLGA-PEG-PLGA hydrogels for the treatment of brachial plexus avulsion," *Artificial Cells, Nanomedicine, and Biotechnology*, vol. 48, no. 1, pp. 1010–1021, 2020.

[43] A. L. Hou and W. D. Xu, "A model of neuropathic pain in brachial plexus avulsion injury and associated spinal glial cell activation," *Journal of Pain Research*, vol. 11, pp. 3171–3179, 2018.

[44] C. Meng, X. Yang, Y. Liu et al., "Decreased expression of lncRNA Malat1 in rat spinal cord contributes to neuropathic pain by increasing neuron excitability after brachial plexus avulsion," *Journal of Pain Research*, vol. 12, pp. 1297–1310, 2019.

[45] B. B. Huo, M. X. Zheng, X. Y. Hua, J. Shen, J. J. Wu, and J. G. Xu, "Brain metabolism in rats with neuropathic pain induced by brachial plexus avulsion injury and treated via electroacupuncture," *Journal of Pain Research*, vol. 13, pp. 585–595, 2020.

[46] J. Shen, B. B. Huo, M. X. Zheng et al., "Evaluation of neuropathic pain in a rat model of total brachial plexus avulsion from behavior to brain metabolism," *Pain Physician*, vol. 22, no. 3, pp. E215–E224, 2019.

[47] J. Fang, J. Yang, Y. Yang et al., "A novel rat model of brachial plexus injury with nerve root stumps," *Journal of Neuroscience Methods*, vol. 295, pp. 1–9, 2018.

[48] R. J. Spinner, A. Khoobehi, S. Kazmi et al., "Model for avulsion injury in the rat brachial plexus using passive acceleration," *Microsurgery*, vol. 20, no. 2, pp. 94–97, 2000.

[49] J. Yang, X. Li, Y. Hou et al., "Development of a novel experimental rat model for brachial plexus avulsion injury," *Neuroreport*, vol. 26, no. 9, pp. 501–509, 2015.

[50] R. Baron, C. Maier, N. Attal et al., "Peripheral neuropathic pain," *Pain*, vol. 158, no. 2, pp. 261–272, 2017.

[51] N. B. Finnerup, S. Haroutounian, P. Kamerman et al., "Neuropathic pain," *Pain*, vol. 157, no. 8, pp. 1599–1606, 2016.

[52] J. Gierthmühlen and R. Baron, "Neuropathic pain," *Seminars in Neurology*, vol. 36, no. 5, pp. 462–468, 2016.

[53] J. Bruxelle, V. Travers, and J. B. Thiebaut, "Occurrence and treatment of pain after brachial plexus injury," *Clinical Orthopaedics and Related Research*, vol. 237, pp. 87–95, 1988.

[54] Z. C. Sun, S. B. Ma, W. G. Chu, D. Jia, and C. Luo, "Canonical transient receptor potential (TRPC) channels in nociception and pathological pain," *Neural Plasticity*, vol. 2020, Article ID 3764193, 13 pages, 2020.

[55] C. B. Parry, "Pain in avulsion lesions of the brachial plexus," *Pain*, vol. 9, no. 1, pp. 41–53, 1980.

[56] A. Subedi, P. Chaudakshetrin, H. Chotisukarat, and S. Mandee, "Effect of co-morbid conditions on persistent neuropathic pain after brachial plexus injury in adult patients," *Journal of Clinical Neurology*, vol. 12, no. 4, pp. 489–494, 2016.

[57] J. L. Giuffre, S. Kakar, A. T. Bishop, R. J. Spinner, and A. Y. Shin, "Current concepts of the treatment of adult brachial plexus injuries," *The Journal of Hand Surgery*, vol. 35, no. 4, pp. 678–688, 2010.

[58] S. Brill and I. G. Aryeh, "Neuromodulation in the management of pain from brachial plexus injury," *Pain Physician*, vol. 11, no. 1, pp. 81–85, 2008.

[59] J. A. Bertelli and M. F. Ghizoni, "Pain after avulsion injuries and complete palsy of the brachial plexus: the possible role of nonavulsed roots in pain generation," *Neurosurgery*, vol. 62, no. 5, pp. 1104–1114, 2008.

[60] J. A. Bertelli and M. F. Ghizoni, "Use of clinical signs and computed tomography myelography findings in detecting and excluding nerve root avulsion in complete brachial plexus palsy," *Journal of Neurosurgery*, vol. 105, no. 6, pp. 835–842, 2006.

[61] J. S. Berman, R. Birch, and P. Anand, "Pain following human brachial plexus injury with spinal cord root avulsion and the effect of surgery," *Pain*, vol. 75, no. 2, pp. 199–207, 1998.

[62] J. D. Loeser and A. A. Ward, "Some effects of deafferentation on neurons of the cat spinal cord," *Archives of Neurology*, vol. 17, no. 6, pp. 629–636, 1967.

[63] H. B. Brinkhus and M. Zimmermann, "Characteristics of spinal dorsal horn neurons after partial chronic deafferentation by dorsal root transection," *Pain*, vol. 15, no. 1, pp. 221–236, 1983.

[64] M. Guenot, J. Bullier, and M. Sindou, "Clinical and electrophysiological expression of deafferentation pain alleviated by dorsal root entry zone lesions in rats," *Journal of Neurosurgery*, vol. 97, no. 6, pp. 1402–1409, 2002.

[65] B. Prestor, "Microcoagulation of junctional dorsal root entry zone is effective treatment of brachial plexus avulsion pain: long-term follow-up study," *Croatian Medical Journal*, vol. 47, no. 2, pp. 271–278, 2006.

[66] M. Samii, S. Bear-Henney, W. Lüdemann, M. Tatagiba, and U. Blömer, "Treatment of refractory pain after brachial plexus avulsion with dorsal root entry zone lesions," *Neurosurgery*, vol. 48, no. 6, pp. 1269–1277, 2001.

[67] N. D. Tomycz and J. J. Moossy, "Follow-up 26 years after dorsal root entry zone thermocoagulation for brachial plexus avulsion and phantom limb pain," *Journal of Neurosurgery*, vol. 114, no. 1, pp. 196–199, 2011.

[68] J. P. Lefaucheur, X. Drouot, P. Cunin et al., "Motor cortex stimulation for the treatment of refractory peripheral neuropathic pain," *Brain*, vol. 132, no. 6, pp. 1463–1471, 2009.

[69] E. A. Pereira, S. G. Boccard, P. Linhares et al., "Thalamic deep brain stimulation for neuropathic pain after amputation or brachial plexus avulsion," *Neurosurgical Focus*, vol. 35, no. 3, article E7, 2013.

[70] V. Abreu, R. Vaz, V. Rebelo et al., "Thalamic deep brain stimulation for neuropathic pain: efficacy at three years' follow-up," *Neuromodulation*, vol. 20, no. 5, pp. 504–513, 2017.

[71] M. Kretzschmar, M. Reining, and M. A. Schwarz, "Three-year outcomes after dorsal root ganglion stimulation in the treatment of neuropathic pain after peripheral nerve injury of upper and lower extremities," *Neuromodulation*, vol. 23, pp. 1–8, 2020.

[72] T. R. Deer, N. Mekhail, D. Provenzano et al., "The appropriate use of neurostimulation of the spinal cord and peripheral nervous system for the treatment of chronic pain and ischemic diseases: the Neuromodulation Appropriateness Consensus Committee," *Neuromodulation: Technology at the Neural Interface*, vol. 17, no. 6, pp. 515–550, 2014.

[73] N. B. Finnerup, N. Attal, S. Haroutounian et al., "Pharmacotherapy for neuropathic pain in adults: a systematic review and meta-analysis," *The Lancet Neurology*, vol. 14, no. 2, pp. 162–173, 2015.

[74] J. Katz, N. Finnerup, and R. Dworkin, "Clinical trial outcome in neuropathic pain: relationship to study characteristics," *Neurology*, vol. 70, no. 4, pp. 263–272, 2008.

[75] V. Gangadharan, X. Wang, and C. Luo, "Cyclic GMP-dependent protein kinase-I localized in nociceptors modulates nociceptive cortical neuronal activity and pain hypersensitivity," *Molecular Pain*, vol. 13, 2016.

[76] C. Luo, V. Gangadharan, K. K. Bali et al., "Presynaptically localized cyclic GMP-dependent protein kinase 1 is a key determinant of spinal synaptic potentiation and pain hypersensitivity," *PLoS Biology*, vol. 10, no. 3, article e1001283, 2012.

[77] R. G. Xie, Y. J. Gao, C. K. Park et al., "Spinal CCL2 promotes central sensitization, long-term potentiation, and inflammatory pain via CCR2: further insights into molecular, synaptic, and cellular mechanisms," *Neuroscience Bulletin*, vol. 34, no. 1, pp. 13–21, 2018.

[78] W. G. Chu, F. D. Wang, Z. C. Sun et al., "TRPC1/4/5 channels contribute to morphine-induced analgesic tolerance and hyperalgesia by enhancing spinal synaptic potentiation and structural plasticity," *The FASEB Journal*, vol. 34, no. 6, pp. 8526–8543, 2020.

[79] K. Meacham, A. Shepherd, D. P. Mohapatra, and S. Haroutounian, "Neuropathic pain: central vs. peripheral mechanisms," *Current Pain and Headache Reports*, vol. 21, no. 6, 2017.